

# Thermal Energy Transport in Oxide Nuclear Fuel

David H. Hurley,\* Anter El-Azab, Matthew S. Bryan, Michael W. D. Cooper, Cody A. Dennett, Krzysztof Gofryk, Lingfeng He, Marat Khafizov, Gerard H. Lander, Michael E. Manley, J. Matthew Mann, Chris A. Marianetti, Karl Rickert, Farida A. Selim, Michael R. Tonks, and Janelle P. Wharry



Cite This: *Chem. Rev.* 2022, 122, 3711–3762



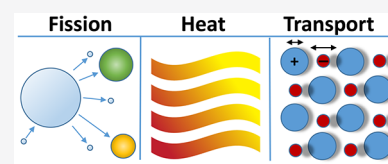
Read Online

ACCESS |

Metrics & More

Article Recommendations

**ABSTRACT:** To efficiently capture the energy of the nuclear bond, advanced nuclear reactor concepts seek solid fuels that must withstand unprecedented temperature and radiation extremes. In these advanced fuels, thermal energy transport under irradiation is directly related to reactor performance as well as reactor safety. The science of thermal transport in nuclear fuel is a grand challenge as a result of both computational and experimental complexities. Here we provide a comprehensive review of thermal transport research on two actinide oxides: one currently in use in commercial nuclear reactors, uranium dioxide ( $\text{UO}_2$ ), and one advanced fuel candidate material, thorium dioxide ( $\text{ThO}_2$ ). In both materials, heat is carried by lattice waves or phonons. Crystalline defects caused by fission events effectively scatter phonons and lead to a degradation in fuel performance over time. Bolstered by new computational and experimental tools, researchers are now developing the foundational work necessary to accurately model and ultimately control thermal transport in advanced nuclear fuels. We begin by reviewing research aimed at understanding thermal transport in perfect single crystals. The absence of defects enables studies that focus on the fundamental aspects of phonon transport. Next, we review research that targets defect generation and evolution. Here the focus is on ion irradiation studies used as surrogates for damage caused by fission products. We end this review with a discussion of modeling and experimental efforts directed at predicting and validating mesoscale thermal transport in the presence of irradiation defects. While efforts in these research areas have been robust, challenging work remains in developing holistic tools to capture and predict thermal energy transport across widely varying environmental conditions.



## CONTENTS

1. Introduction	3712	2.2.4. Computing Thermal Transport from Phonons and Their Interactions	3718
1.1. Origins of Phonon Thermal Conductivity	3713	2.2.5. First-Principles Calculations on $\text{UO}_2$ and $\text{ThO}_2$	3718
2. Thermal Transport in Perfect Single Crystals	3714	2.3. Thermophysical Properties	3719
2.1. Inelastic Neutron and X-ray Scattering	3714	2.3.1. Introduction	3719
2.1.1. Phonon Dispersion and Thermal Conductivity	3714	2.3.2. Heat Capacity	3719
2.1.2. Techniques for Measuring Phonons	3715	2.3.3. Thermal Conductivity	3719
2.1.3. Triple-Axis Neutron Measurements of the Phonon Lifetimes in $\text{UO}_2$	3715	2.3.4. Elastic Constants and Thermal Expansion	3720
2.1.4. Inelastic X-ray Measurements of Phonons in Irradiated Epitaxial Thin Films of $\text{UO}_2$	3716	2.4. Crystal Growth	3720
2.1.5. Time-of-Flight Neutron Measurements Reveal Nonlinear Modes in $\text{ThO}_2$ and $\text{UO}_2$	3716	2.4.1. Challenges in Growing Single Crystals	3720
2.2. First-Principles Thermal Transport in Perfect Crystals	3716	2.4.2. Bulk Crystal Growth Techniques	3720
2.2.1. General Considerations	3716	2.4.3. Epitaxial Thin Films	3721
2.2.2. First-Principles Approaches for Crystals beyond DFT	3717	2.5. Outlook	3722
2.2.3. Computing Phonons and Their Interactions from First Principles	3717	3. Crystalline Defect Generation, Evolution, and Characterization	3722

Received: June 13, 2021

Published: December 17, 2021



3.1. Intrinsic Point Defects	3723
3.1.1. Characterization Techniques	3723
3.1.2. Intrinsic Point Defects: Characterization and Modeling	3725
3.2. Irradiation-Induced Defects	3727
3.2.1. Characterization Techniques	3727
3.2.2. Irradiation-Induced Point Defects	3728
3.2.3. Dislocation Loops	3729
3.2.4. Cavities and Precipitates	3730
3.3. Modeling of Defect Clustering	3731
3.3.1. Simple Rate Theory Model of Defect Evolution	3731
3.3.2. Cluster Dynamics Approach to Defect Evolution	3732
3.4. Grain Boundaries	3733
3.4.1. Intrinsic Grain Boundaries	3733
3.4.2. Restructured Grain Boundaries	3733
3.5. Outlook	3734
4. Thermal Conductivity under Irradiation	3735
4.1. Fuel Performance Codes and Thermal Conductivity	3735
4.2. Experimental Measurement of Thermal Conductivity	3736
4.3. Boltzmann Transport Framework	3737
4.3.1. Phonon Scattering	3737
4.3.2. Klemens–Callaway–Debye Approximation	3738
4.3.3. Single-Mode Relaxation Time Approximation	3739
4.4. Molecular Dynamics Simulations of Thermal Conductivity	3740
4.4.1. Bulk Thermal Conductivity	3740
4.4.2. Point-Defect Scattering Using Molecular Dynamics	3741
4.4.3. Extended Defects	3742
4.5. Impact of Grain Boundaries and Porosity	3742
4.6. Comparison between Experiment and Modeling	3742
4.6.1. Impact of Point Defects in Low-Temperature Low-Dose-Irradiated UO <sub>2</sub>	3742
4.6.2. Impact of Dislocation Loops in High-Temperature Proton-Irradiated CeO <sub>2</sub>	3743
4.6.3. Mixed Impact of Point Defects and Loops in ThO <sub>2</sub>	3743
4.6.4. Impact of Grain Boundaries	3744
4.7. Future Outlook	3745
5. Concluding Remarks	3745
Author Information	3745
Corresponding Author	3745
Authors	3745
Author Contributions	3745
Notes	3745
Biographies	3745
Acknowledgments	3747
References	3747

## 1. INTRODUCTION

Currently, about 73% of the electricity in the world is generated using heat engines.<sup>1</sup> This includes heat generated by burning fossil fuels (coal, gas, oil), by concentrated solar energy, and by nuclear fission. On the surface, the anatomy of a heat-engine power plant looks similar regardless of the heat source. Heat

extracted by passing a coolant over the heat source is used to create steam, which is then converted to electricity using a steam turbine. For a fossil-fuel-powered plant, the heat source (i.e., exhaust gas) moves, allowing additional heat to be extracted by increasing the length of the heat exchanger. A nuclear plant is fundamentally different in this regard: heat is generated by nuclear fission in a crystalline solid and must be conducted through the fuel and transferred to the coolant, as shown in Figure 1. This perspective illustrates the close connection between conduction of thermal energy (heat) and electricity generation in nuclear power plants.

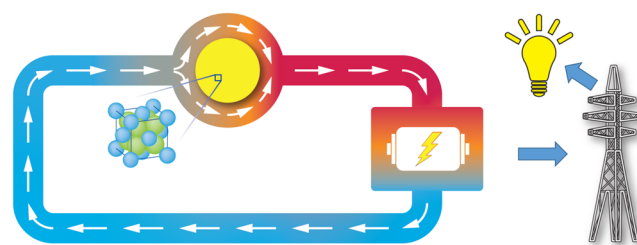


**Figure 1.** Schematic of a nuclear energy plant. The heat extracted from the solid fuel is used to drive a steam turbine and generate electricity.

Nuclear reactors operating in the world today primarily use actinide oxides (uranium dioxide, UO<sub>2</sub>, and mixed oxides containing UO<sub>2</sub> and plutonium dioxide, PuO<sub>2</sub>) as fuel materials. These oxide fuels have a high energy density (a single commercial reactor fuel pellet weighing about 10 g stores the same amount of energy as 1.4 tons (~1300 kg) of coal, 285 gallons (~1 m<sup>3</sup>) of oil, or 38 800 cubic feet (~150 m<sup>3</sup>) of natural gas<sup>2</sup>), and electricity generation does not involve the release of greenhouse gases. In nuclear fuel, a fissile nuclide absorbs a neutron, becomes unstable, and splits, creating at least two new atoms (called fission fragments), producing  $\gamma$  rays and neutrons, and imparting about 200 MeV of kinetic energy into those fission fragments (as illustrated in Figure 2).<sup>3</sup> The transfer of this kinetic energy to the crystalline lattice of the fuel generates thermal energy that must be conducted through the fuel and transferred to the coolant for eventual conversion to electricity. The thermal energy is conducted through the fuel almost entirely by lattice waves or phonons because of the scarcity of free electrons in oxide fuels.<sup>4</sup> The rapid transfer of the kinetic energy from the fission event to the lattice also produces defects (vacancies, interstitials, and extended defects), with deposition of fission fragments as impurity atoms. These defects effectively scatter phonons, reducing the capacity of the fuel to conduct heat. Over the lifetime of the fuel in a reactor, the thermal conductivity decreases by as much as 70%.<sup>5</sup>

However, in some cases a cooperative influence between multiple defect types has a positive effect by increasing the lattice thermal conductivity over that expected if the defects acted in isolation. For example, in the high-burnup structure (HBS) of nuclear fuels, where considerable irradiation-driven restructuring greatly increases the grain boundary surface area<sup>6</sup> and decreases the lattice defect concentration because of segregation to grain boundaries,<sup>7</sup> the thermal conductivity is higher than that in similar fuel that has not formed HBS.<sup>8,9</sup> The myriad defect types and interactions in nuclear fuel under irradiation have motivated researchers to consider improving function by controlling defect evolution and structure. Examples include the use of dopants to control defect concentrations by modification of the grain size,<sup>10–13</sup> simulation of HBS using

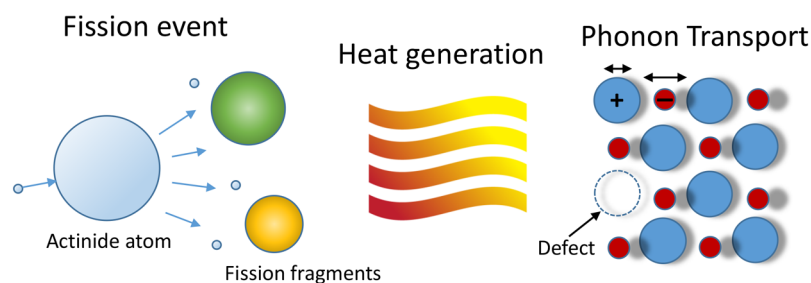


**Figure 2.** Nuclear fission is used to generate heat. Fission fragments create damage and are deposited as chemical impurities. Heat is carried by phonons in oxide nuclear fuels.

nanocrystalline  $\text{UO}_2$  to improve fission gas retention and mechanical properties,<sup>14,15</sup> and direct addition of other materials to  $\text{UO}_2$  to raise the thermal conductivity.<sup>16–24</sup> Expediting progress toward tailoring defects and microstructure to bring about desired thermal properties will require further development of fundamental predictive models of phonon transport in actinide oxide fuels containing irradiation-induced defects.<sup>25–29</sup>

This desire to understand and tailor the thermal properties of fuels to improve the efficiency, safety, and reliability of electricity generation has driven a great deal of fundamental research over the past 60 years. Our current understanding of thermal transport in actinide oxides can be traced back to early work involving phonon transport in semiconductors and insulators. This work, using analytical expressions to represent conductivity, provided a mechanistic understanding of phonon thermal transport in the presence of defects.<sup>30–33</sup> More recently, a first-principles theoretical approach has produced accurate results for simple semiconductors with no adjustable parameters.<sup>34–36</sup> Similar work using the Green's function T-matrix approach has been used to calculate phonon scattering rates for simple lattice defects from first principles.<sup>37–39</sup> On the experimental side, this effort has included phonon structure measurements using bright neutron and X-ray sources and spatially resolved thermal conductivity measurements.<sup>40–42</sup> Extending these approaches to actinide oxides containing irradiation-induced defects remains a grand challenge for several reasons, including challenges associated with the fabrication of high-quality single-crystal samples for phonon structure measurements, complexities encountered in accurate treatment of electron correlation in 5f electron systems, seeding samples with specific defect populations found in reactor fuel, accurate characterization of the spectrum of defects, and measurement of thermal transport on length scales commensurate with defect accumulation.

Here we review the current understanding of phonon thermal transport in oxide nuclear fuels, highlighting the above-mentioned challenges. Specifically, we provide a comprehensive review of previous work on two actinide oxides: one currently in use in commercial nuclear reactors,  $\text{UO}_2$ , and one advanced fuel candidate material, thorium dioxide ( $\text{ThO}_2$ ).  $\text{ThO}_2$  additionally acts as a surrogate material for  $\text{UO}_2$ , as it lacks the complexity of electron correlation effects. We also provide a narrower review of other oxide materials relevant to  $\text{UO}_2$  and  $\text{ThO}_2$  research. Our focus is primarily on defects produced by ion irradiation, as ions provide a convenient and expedient approach to inject defects that are found in real fuel specimens. Emphasis is placed on identifying remaining knowledge gaps and revealing new opportunities to improve thermal transport in reactor fuels.

### 1.1. Origins of Phonon Thermal Conductivity

In nuclear fuel, thermal transport can be viewed from both a macroscopic viewpoint and an atomistic viewpoint. On the macroscopic scale, thermal transport is treated within a continuum framework to obtain the temperature distribution in a fuel pellet. On an atomistic scale, thermal transport is treated within a quantum-mechanical framework to obtain an expression for the thermal conductivity, which controls the temperature distribution. Phonon thermal conductivity is most often calculated using one of two methods: (1) molecular dynamics (MD) simulations using empirical interatomic potentials (EIPs) or interatomic potentials derived from first principles (FIPs) and (2) seeking solutions to the linearized Boltzmann transport equation (BTE) for phonons (see Figure 3).

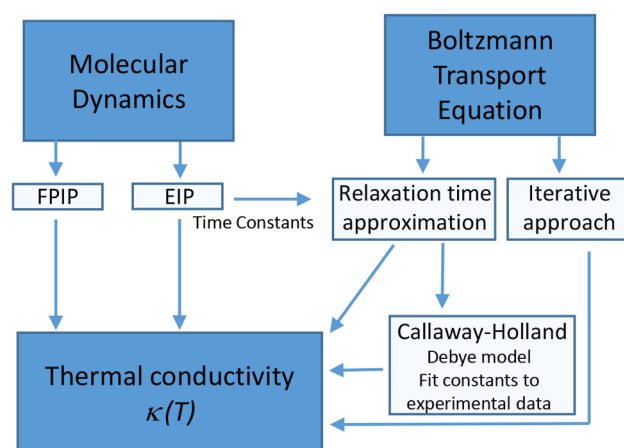


**Figure 3.** Different ways to calculate thermal conductivity.

While this review will cover studies using both methods, this section provides an overview of the Boltzmann framework, as this best illustrates the motivation for the organization of this review. In crystals, vibrational energy is exchanged between phonon modes. In thermal equilibrium, the average number of modes with energy  $\hbar\omega$  is given by the Planck distribution:

$$N(\omega) = \frac{1}{\exp(\hbar\omega/k_B T) - 1} \quad (1)$$

The number of modes of a particular energy increases with increasing temperature. Another way of stating this is that phonons are created by increasing the temperature and destroyed by decreasing the temperature (i.e., the number of phonons is not conserved). The strong temperature dependence

of the thermal conductivity in insulators and semiconductors partially results from this lack of conservation. A thermal gradient imposed by an external heat source will force the system away from equilibrium. The thermal conductivity depends on the extent to which the phonon distribution can deviate from equilibrium for a specific thermal gradient.

The time–space evolution of  $N(\omega)$  is governed by the BTE for phonons. This equation is in general difficult to solve. The two solution methods that will be discussed in this review are the exact iterative solution<sup>43,44</sup> and the relaxation time approximation (RTA).<sup>45</sup> Iterative solution of the BTE is well-suited for calculation of the thermal conductivity of perfect single crystals but remains too computationally expensive to model crystals with nontrivial defects. For the RTA, lattice dynamics is not required to compute relaxation times, as they can also be calculated using molecular dynamics. It is this aspect that makes the RTA well-suited for treatment of thermal transport in crystals containing a range of defects from point defects to extended defect clusters.

Under the RTA, the thermal conductivity,  $\kappa$ , can be represented as

$$\kappa = \frac{1}{3} \sum_{\mathbf{q}s} C_{\mathbf{q}s} v_{\mathbf{q}s}^2 \tau_{\mathbf{q}s} \quad (2)$$

where  $s$  enumerates the possible phonon modes for a given phonon wave vector  $\mathbf{q}$ . The right-hand side of this equation contains the branch-specific phonon lifetime ( $\tau_{\mathbf{q}s}$ ), the phonon velocity ( $v_{\mathbf{q}s}$ ), and the specific heat ( $C_{\mathbf{q}s}$ ), the latter two of which are functions only of the phonon dispersion (the relation between frequency and wave vector,  $\omega(\mathbf{q})$ ). The lifetime is determined by phonon scattering, which ultimately limits the thermal conductivity. Above cryogenic temperatures, in nearly perfect single crystal materials the phonon scattering is dominated by scattering with other phonons mediated by lattice anharmonicity (third- and higher-order terms in the interatomic potential).

Structural defects caused by irradiation also influence the lifetime by introducing phonon scattering sites. Both scattering

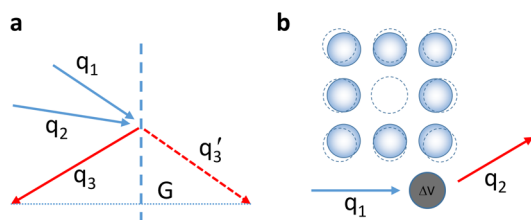


**Figure 4.** Phonon scattering: (a) anharmonic three-phonon Umklapp scattering does not conserve total momentum and plays an outsized role in limiting the conductivity; (b) phonon defect scattering.

processes are illustrated in Figure 4. With Matthiessen's rule, the total phonon lifetime can be written as

$$\tau_{\mathbf{q}s}^{-1}(\omega) = \tau_{\text{anharmonic}}^{-1} + \tau_{\text{defect1}}^{-1} + \tau_{\text{defect2}}^{-1} + \dots \quad (3)$$

to account for scattering from multiple mechanisms, both intrinsic (anharmonic) and extrinsic (defects). This Boltzmann transport framework provides a template that is used to organize the material presented in this review. Section 2, Thermal Transport in Perfect Single Crystals, addresses the input to eq 2 in terms of phonon dispersion and lifetime and discusses

previous work aimed at understanding thermal transport in perfect single crystals. Section 3, Defect Generation Evolution, and Characterization, discusses the body of work involving the generation and evolution of defects in actinide oxides using energetic ion irradiation. Section 4, Thermal Conductivity under Irradiation, reports on the output of eq 2, reviewing modeling and experimental efforts directed at predicting and validating thermal conductivity in the presence of defects.

## 2. THERMAL TRANSPORT IN PERFECT SINGLE CRYSTALS

The absence of defects enables studies that focus on the fundamental aspects of phonon transport, including the impact of strong electron correlation. Experimentally, prior efforts ranging from synthesis of single crystals to inelastic neutron and X-ray scattering are discussed. Computationally, previous work aimed at the application of advanced electronic structure calculations to systems that exhibit strong electron correlation is reviewed. In keeping with the scope delineated in the Introduction, the emphasis of this section and the sections to follow is on providing a review of key discoveries, highlighting fundamental mechanisms, and identifying remaining knowledge gaps.

### 2.1. Inelastic Neutron and X-ray Scattering

#### 2.1.1. Phonon Dispersion and Thermal Conductivity.

Measurements of the phonon dispersion curves in a material offer a unique window into the microscopic mechanisms controlling phonon thermal transport (see Figure 5). These

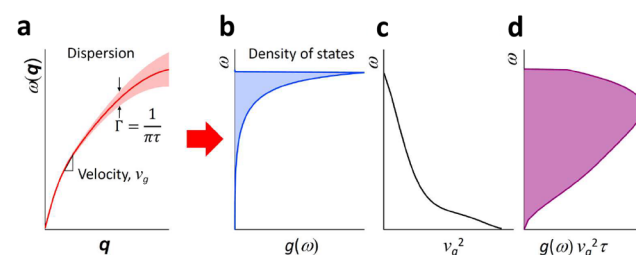


**Figure 5.** Relationship between phonon dispersion and thermal conductivity. (a) Phonon dispersion curve for a typical acoustic mode. The slope provides the phonon group velocity,  $v_g$ , and the line width,  $\Gamma$ , is inversely related to the phonon lifetime,  $\tau$ , as indicated. (b) The mode partial phonon density of states scales as  $g(\omega) \propto q^2(\omega)(dq/d\omega)$ . (c) Phonon group velocity squared,  $v_g^2 = (d\omega/dq)^2$ . (d) The product of the density of states, group velocity squared, and lifetime gives a distribution for the contributions to the thermal conductivity tensor assuming full thermal occupation ( $k_B T \gg \hbar\omega_{\text{max}}$ ), where each mode contributes equally to the heat capacity. At low temperatures the higher-frequency phonons thermally depopulate and no longer contribute as much heat.

dispersion curves relate the phonon wave vector,  $\mathbf{q}$ , to the frequency,  $\omega$ , through the interatomic force constants. In principle, thermal conductivity can be represented using the measured dynamical structure factor.<sup>46</sup> The mode partial phonon density of states,  $g(\omega)$ , is evaluated by differentiation of the phonon branches<sup>47</sup> and can be used to evaluate the heat capacity and vibrational entropy per mode.<sup>48</sup> The slope of a measured dispersion curve determines the phonon group velocity,  $v_g$ , and the line width of the curve is inversely related to the phonon lifetime. As illustrated in Figure 5b, for a typical acoustic phonon, the partial density of states available to carry heat becomes very small for states near the zone center ( $\mathbf{q} = 0$ ).

Consequently, even though the velocities (see Figure 5c) and lifetimes are large in this region, the contributions to the thermal conductivity can still be small. At high temperatures, with full thermal occupation ( $k_B T \gg \hbar \omega_{\max}$ ), the heat capacity term in eq 2 follows the density of states, and the contributions to thermal conductivity are more broadly distributed over the curve (Figure 5d), peaking in importance near the middle of the curve. Similar arguments can be made for dispersive optical phonons. For this reason, understanding the thermal conductivity at high temperatures requires measurements of the full set of dispersion curves, including line widths, and this requires neutron or X-ray scattering techniques at large user facilities.

**2.1.2. Techniques for Measuring Phonons.** The earliest measurements of the phonon dispersion curves of the actinide oxides  $\text{UO}_2$ <sup>49</sup> and  $\text{ThO}_2$ <sup>50</sup> were performed using the reactor-based triple-axis neutron scattering technique (Figure 6a) that was first established for measuring phonon dispersion curves by

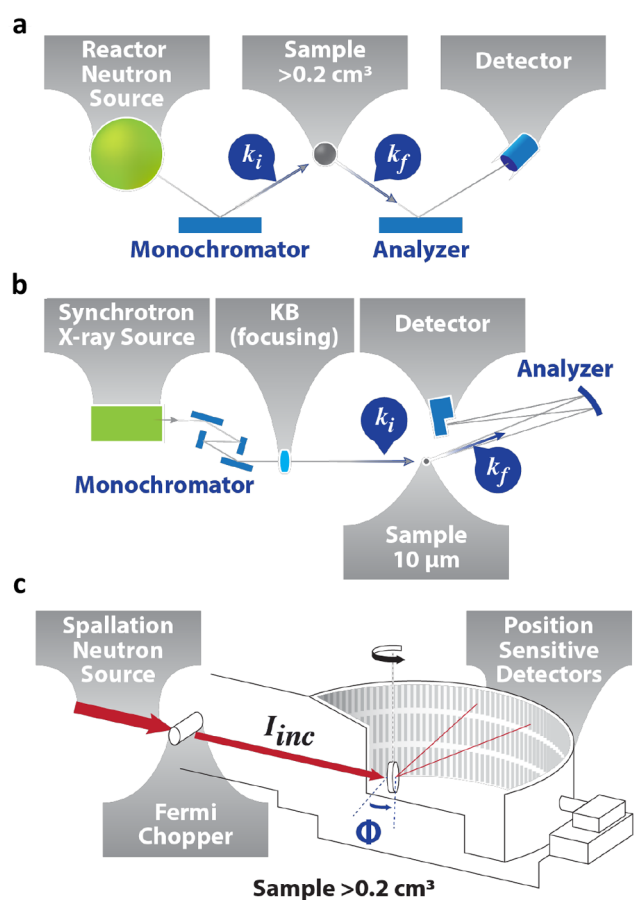


**Figure 6.** Important scattering techniques for measuring phonon dispersion curves in actinides. (a) Triple-axis neutron scattering spectrometer at a reactor source. A monochromator fixes the incident neutron wave vector,  $k_i$ , and an analyzer crystal selects the final wave vector,  $k_f$ , from which momentum transfer,  $\mathbf{Q} = \mathbf{k}_i - \mathbf{k}_f$ , and energy transfer,  $\hbar\omega = \hbar^2(k_i^2 - k_f^2)/2m$ , can be selected to measure the phonon dispersion curves. (b) Inelastic X-ray scattering at a synchrotron. This is similar to a triple-axis instrument in operation but has a more selective monochromator to extract  $\sim 1$  meV resolution from an  $\sim 20$  keV beam. (c) Time-of-flight direct-geometry inelastic neutron scattering spectrometer. The incident energy is selected using a chopper, and the final energies and wave vectors are determined by the times of flight of the scattered neutrons arriving at a wide-angle detector bank, allowing for a broad sampling of energy–momentum space.

Brockhouse.<sup>51,52</sup> However, the early work on actinide oxides primarily focused on determining the phonon dispersion curves or density of states and left out the phonon lifetimes, which are more difficult to measure but crucial for understanding the thermal conductivity. Additionally, because of large neutron absorption cross sections and crystal size requirements ( $>0.2$   $\text{cm}^3$ ), certain actinide oxides (e.g., plutonium dioxide) remained impractical to measure with neutrons.

The situation changed with the advent of high-energy-resolution synchrotron-based inelastic X-ray scattering (IXS) spectrometers<sup>53–56</sup> (Figure 6b), which have no isotope requirements and can handle crystal sizes as small as a few micrometers.<sup>57</sup> This allows the measurements of individual crystal grains within a polycrystalline sample. The first measured phonon dispersion curves for plutonium metal<sup>58</sup> and the first phonon density of states of  $\text{PuO}_2$ <sup>59</sup> were both obtained using IXS rather than neutron scattering. IXS also opened up measurements of phonons at high pressures and in thin films using grazing incidence. Actinides are particularly well-suited to IXS measurements in small geometries since the X-ray scattering per atom increases as the square of the atomic number. However, there are a limited number of facilities available for these measurements, and like triple-axis neutron scattering, it takes considerable beamtime to map a full set of phonon dispersion curves. A full set of phonon dispersion curves takes about 2 weeks to map, which may require multiple experimental cycles. An example is the recent phonon dispersion curves for  $\text{NpO}_2$  taken from a very small crystal with X-rays at the European Synchrotron Radiation Facility (ESRF).<sup>60</sup>

Another important advance in measuring phonons in actinide oxides came with the wide-angle-range time-of-flight spectrometers at next-generation spallation neutron sources such as the Spallation Neutron Source (SNS) at Oak Ridge National Laboratory,<sup>61</sup> which came online in the mid to late 2000s (Figure 6c). These instruments and sources enable measurements of higher-energy modes than are normally accessible with reactor-based triple-axis measurements and provide a sampling of a large volume of energy–momentum space in a single measurement, allowing full mapping of the dispersion curves. These two advantages have proven useful in the discovery of new high-energy dynamical features.<sup>62</sup> These measurements, however, also require large samples.

**2.1.3. Triple-Axis Neutron Measurements of the Phonon Lifetimes in  $\text{UO}_2$ .** Building on the pioneering work of Dolling et al.,<sup>49</sup> Pang et al.<sup>27,63</sup> have shown using triple-axis inelastic neutron scattering (Figure 7) that the principal contribution to the thermal conductivity of  $\text{UO}_2$  comes from the acoustic phonons together with a steep and relatively low energy longitudinal optical phonon,  $\text{LO}_1$  (see Figure 7a).

In most crystalline insulators, the majority of thermal heat transport is carried by the acoustic phonons, since they typically have the largest group velocities and the longest lifetimes. However, the triple-axis measurements<sup>27</sup> indicate that the steep longitudinal optical mode carries the largest amount of heat by branch at 295 K in  $\text{UO}_2$  (see Figure 7b), which was not expected. It was also not predicted in previous simulations<sup>64</sup> because they underestimated the group velocities and lifetimes of the  $\text{LO}_1$  phonon compared with experiment,<sup>27</sup> rendering it less important in the simulated thermal conductivity. The steeply dispersing  $\text{LO}_1$  phonon is a general feature of the fluorite crystal structure and thus is likely to be important in the thermal conductivities of all of the actinide oxides considered herein.

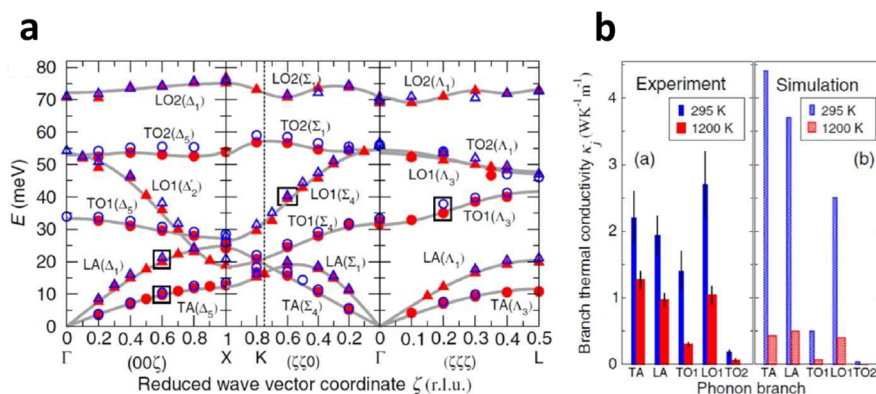


**Figure 7.** Phonon dispersion curves and branch thermal conductivity of  $\text{UO}_2$ . (a) Phonon dispersion curves measured using triple-axis neutron scattering at 295 K (blue) and 1200 K (red). (b) Phonon branch thermal conductivity derived from the measured phonon dispersion and lifetimes (“Experiment”) and from calculations (“Simulation”). Adapted with permission from ref 27. Copyright 2013 American Physical Society.

**2.1.4. Inelastic X-ray Measurements of Phonons in Irradiated Epitaxial Thin Films of  $\text{UO}_2$ .** The focus of this section thus far has been on neutron scattering measurements on perfect or nearly perfect single crystals. However, as mentioned previously, IXS can provide phonon structure information on thin films using grazing-incidence methods. Here we extend our focus momentarily to consider IXS on ion-irradiated  $\text{UO}_2$  thin films, as this gives a phonon-level description on the impact of irradiation. An experiment by Rennie et al.<sup>65</sup> involved 300 nm thick epitaxial films of  $\text{UO}_2$  that were irradiated with 2.1 MeV  $\text{He}^{2+}$  ions to 0.15 dpa, resulting in homogeneous damage and a lattice swelling of  $\Delta a/a \approx 0.6\%$ . The film was then examined by grazing-incidence X-ray inelastic scattering using synchrotron radiation (Figure 6b) to measure whether the acoustic phonons showed any change under these conditions.

The results showed that the frequency of the phonons was not changed, but their widths  $\Gamma$  (Figure 5a) were substantially increased. Although it is difficult to measure optical phonons with this technique, the results with acoustic phonons are consistent with the drop in the thermal conductivity for this level of radiation damage.<sup>66</sup> These experiments confirm that the effects of irradiation in  $\text{UO}_2$  are intrinsic to the microscopic structural changes caused by the damage and result in shorter lifetimes of the acoustic phonons. The negligible impact of irradiation damage on the phonon velocity will provide important information for studies discussed in subsequent sections that are aimed at the forward problem of predicting the thermal conductivity in defective oxides using the BTE formalism.

**2.1.5. Time-of-Flight Neutron Measurements Reveal Nonlinear Modes in  $\text{ThO}_2$  and  $\text{UO}_2$ .** The vibrational motions in crystalline solids are typically phonons, equivalent to the normal modes of classical mechanics. The total number of phonon modes in a system with  $N$  atoms in the primitive cell is  $3N$ . In the case of fluorite-structured  $\text{ThO}_2$  and  $\text{UO}_2$ ,  $N = 3$ , giving a total of nine phonon branches. Recent inelastic neutron scattering measurements observed all nine branches.<sup>67</sup> However, in addition to the nine phonon modes expected, a dispersing mode has been observed in this system at energies above the highest-energy phonon mode, which is called the nonlinear propagating mode (NPM). This mode is observed in  $\text{UO}_2$  and  $\text{ThO}_2$  as well as in natural fluorite,  $\text{CaF}_2$ . It is observable at temperatures ranging from 5 to 1200 K. The observed dispersion and line width are comparable to a typical

phonon dispersion and line width in this system. It also repeats with the same symmetry as the phonon modes, providing evidence that the NPM propagates with the same periodicity as the phonons.

Additional degrees of freedom can lead to additional modes, but this is unlikely given the wide range of observations and no evidence of a phase transition leading to the absence or appearance of the NPM. Nonlinear terms in the equations of motion, which result because the interatomic potential is not perfectly harmonic, can also produce additional modes, as observed previously.<sup>68</sup> It has been argued that this is the source of the mode in these materials with support from first-principles calculations.<sup>68</sup>

The high group velocity of the NPM suggests that it may make a positive contribution to the thermal conductivity. However, the high energy of the mode indicates that this could only be the case at high temperatures (80 meV corresponds to about 930 K). The mode may also act as an additional scattering channel for normal phonons, decreasing thermal conductivity, so the impact of NPMs on the thermal conductivity remains an open question. A full accounting of the phonons and NPMs from first principles is needed to resolve this question.

## 2.2. First-Principles Thermal Transport in Perfect Crystals

$\text{ThO}_2$ , a band insulator, does not have ground state f-shell electrons, while  $\text{UO}_2$  has a partially filled f shell and is a Mott insulator. Thus, in addition to being of interest to the nuclear fuels community, these materials are model systems for understanding the role of electron correlation. We begin by generically considering the state of first-principles computations of electronic and lattice properties of crystals compared to experimental measurements on high-purity single crystals. After the general discussion, we critically review the literature concerning application of first-principles computation to thermal transport in  $\text{ThO}_2$  and  $\text{UO}_2$ , highlighting main findings and identifying open issues.

**2.2.1. General Considerations.** The foundation of any first-principles prediction of thermal transport in crystals begins with the computation of the various quasiparticles that will be carriers of heat (e.g., electrons, phonons, etc.), requiring the approximate solution to the many-body Schrödinger equation for electrons interacting with some symmetric arrangement of nuclei. Fortunately, we have elegant mathematical formalisms, such as density functional theory (DFT),<sup>69–73</sup> which have allowed us to make substantial progress in obtaining

approximate solutions to this many-body problem that represents the forefront of mathematical and computational physics. Furthermore, first-principles computations of various sorts will then be needed to calculate the intrinsic scattering mechanisms of the respective quasiparticles, and we will focus on phonon–phonon interactions in the subsequent sections.

### 2.2.2. First-Principles Approaches for Crystals beyond DFT.

**2.2.2.1. Hybrid Functionals and DFT+U.** Hybrid functionals mix standard DFT exchange–correlation functionals with some fraction of Hartree–Fock exchange.<sup>74</sup> Generically speaking, this approach has been very successful for correcting ground- and excited-state properties in atoms and molecules,<sup>75,76</sup> weakly correlated band insulators,<sup>74</sup> defect energetics,<sup>77</sup> and strongly magnetic insulators.<sup>78–81</sup> However, hybrid functionals can be unreliable for metals<sup>82</sup> and can fail completely for strongly correlated electron materials. For example, the Heyd–Scuseria–Ernzerhof hybrid functional<sup>83</sup> is qualitatively wrong for the classical material VO<sub>2</sub>,<sup>84</sup> where the undistorted rhombohedral phase is predicted to be insulating<sup>85</sup> whereas it is known to be metallic;<sup>84</sup> the dimerized monoclinic phase is predicted to be higher in energy than the rhombohedral phase in addition to being a magnetic insulator,<sup>85</sup> whereas it is experimentally known to be the ground-state structure<sup>84</sup> and nonmagnetic (i.e., no local moments observed);<sup>86</sup> and the predicted band gap of 2.23 eV is in poor comparison with the experimental value of 0.6–0.8 eV.<sup>87</sup> A further limitation of hybrid functionals is the rather large computational cost when a plane-wave basis set is used, scaling approximately as the cube of the number of atoms in the unit cell.<sup>88</sup>

DFT+U<sup>89</sup> bears many similarities to hybrid functionals, in that DFT+U can be viewed as a sort of local hybrid functional. The connection between DFT+U and hybrid functionals has indeed received attention from a methodological perspective.<sup>90,91</sup> While DFT+U does not contain the nonlocal aspects of a hybrid functional, it does account for the important local aspects present in many strongly correlated materials. More importantly, the computational cost of DFT+U is considerably smaller than that of hybrid functionals. Additionally, while DFT+U has more empirical parameters than hybrid functionals (i.e.,  $U$ ,  $J$ , and double counting in DFT+U vs the  $\alpha$  mixing parameter in hybrids), this is not entirely a disadvantage because it facilitates an empirical exploration of the various components of the functional. Altogether, DFT+U is a very efficient theory that can operate in the same spirit as DFT, performing full structural relaxations and exploring a wide phase space of possibilities.

**2.2.2.2. DFT + Dynamic Mean-Field Theory.** All known implementations of DFT break down in certain strongly correlated electron materials, illustrating the difficulty of developing sufficiently robust approximations for the exchange–correlation functional. Instead of creating functionals of the density, one can choose to create functionals of other observables, which might be more sensitive to capturing the physics of strong correlations, such as the single-particle Green's functions.<sup>92–94</sup> In such approaches, there is an analogy to the exchange–correlation functional, which embodies the unknown portion of the energy as a functional of the Green's function, and the functional derivative of this quantity with respect to the Green's function is the well-known self-energy. Dynamical mean-field theory (DMFT) can be viewed as a tool that allows for the approximate computation of the self-energy.<sup>95</sup>

DMFT was created in the context of the Hubbard model,<sup>96–98</sup> which is one of the simplest models of interacting electrons on a lattice, consisting of an on-site Coulomb repulsion and a nearest-

neighbor hopping parameter to embody both the kinetic energy and some external potential. The Hubbard model cannot be solved in general, but it can be solved in one dimension using the Bethe ansatz<sup>99,100</sup> and in infinite dimensions in conjunction with DMFT.<sup>101</sup> DMFT maps the Hubbard model to an effective Anderson impurity model (AIM), where the bath is determined via the DMFT self-consistency condition. Some other approach is then needed to solve the AIM, and most prevalent approaches to the many-body problem have been applied.<sup>101,102</sup> Because the AIM is still a tractable many-body problem, DMFT allows the exact numerical solution of the infinite-dimensional Hubbard model using techniques such as quantum Monte Carlo.<sup>103,104</sup> However, these numerically exact techniques are computationally expensive and limited to finite temperatures and may face minus sign problems.<sup>105</sup>

While DMFT can clearly capture the physics of the Mott transition in the infinite-dimensional Hubbard model, it is not tractable for treating all of the electrons in a strongly correlated electron material. Fortunately, it is only a subset of electrons in real materials that give rise to strongly correlated electron behavior—typically d and f electrons. It is then natural to combine the best aspects of both DFT and DMFT by constructing an energy functional of two variables: the density and the local Green's function of the correlated orbitals.<sup>102</sup> This functional is then approximated using some exchange–correlation functional for DFT along with DMFT, yielding the so-called DFT+DMFT approach. DFT+DMFT has been placed on the same footing as DFT, allowing for detailed total energy calculations of complex materials, for which DFT sometimes qualitatively breaks down.<sup>106–111</sup>

Upon executing a DFT+DMFT calculation, one needs some approach to solve the effective AIM of the DMFT portion of the calculation, and there is always a balance between accuracy and computational cost. The impurity solver with the smallest computational expense is Hartree–Fock, and this leads to the well-known DFT+U approach. It is worth noting that DFT+U<sup>112</sup> was developed around the same time as DMFT, and therefore, DFT+U greatly preceded DFT+DMFT. Therefore, it is often not appreciated that DFT+U is a special case of DFT+DMFT.<sup>102</sup>

### 2.2.3. Computing Phonons and Their Interactions from First Principles.

Computing phonons and their interactions from first principles amounts to computing the Taylor series expansion of the Born–Oppenheimer potential of a given first-principles approach with respect to the nuclear displacements of the crystal. A crystal is infinite in extent, and therefore, the computed Taylor series at each order must be truncated at some maximum range in real space or density in reciprocal space. Sufficient resolution needs to be obtained at each order such that the observable at hand is converged to within a sufficient tolerance, and therefore, the necessary resolution will vary depending on which observable is being considered. For a comprehensive review of computing phonons and their interactions from first principles, we refer the reader to ref 113.

There are two basic approaches for computing derivatives of a Born–Oppenheimer potential:<sup>114,115</sup> perturbative approaches and finite displacements. We use the latter term broadly to include any approach that explicitly displaces the nuclear coordinates and solves the Schrödinger equation of the displaced structure, including usual finite-difference approaches or more complicated fitting procedures based on finite displacements. The nature of the perturbative approach and

the order to which it can be carried out will depend on the particular first-principles approach that is being used. Finally, these two approaches are naturally combined, using a perturbative approach to obtain some low-order derivatives (e.g., Hellman–Feynman forces) and finite displacements for higher-order derivatives, allowing many derivatives to be simultaneously measured in a given finite-displacement calculation.<sup>113,116,117</sup>

**2.2.4. Computing Thermal Transport from Phonons and Their Interactions.** The anharmonic vibrational Hamiltonian poses a nontrivial many-body problem of interacting bosons, and exactly evaluating the thermal conductivity is highly nontrivial. The most common approach is the linearized BTE.<sup>118</sup> The inputs to the BTE are the phonon eigenvalues and eigenvectors, the phonon velocities, and typically the cubic phonon interactions. The BTE may be numerically solved without approximation using iterative techniques<sup>44</sup> and variational approaches,<sup>119</sup> with the latter guaranteeing numerical convergence. Solutions of the BTE based on phonons and phonon interactions have been executed over a large number of material systems,<sup>120,121</sup> often resulting in impressive agreement with experiment, though most of the systems that have been studied are band insulators.

Typical approaches to the Boltzmann equation have numerous limitations. For example, most studies account only for scattering via cubic phonon interactions and do not account for thermal expansion of the crystal, and both of these assumptions are valid only at sufficiently low temperatures. Several recent studies have attempted to go beyond these limitations by including quartic phonon interactions<sup>122–125</sup> and thermal expansion<sup>125</sup> when solving the Boltzmann equation. If one only needs results in the classical regime, another approach is to use Kubo–Green linear response in conjunction with classical molecular dynamics.<sup>126,127</sup> A potential advantage of this route in conjunction with first-principles molecular dynamics is to retain phonon interactions to all orders and include all possible allowed scattering processes.

**2.2.5. First-Principles Calculations on UO<sub>2</sub> and ThO<sub>2</sub>.** The ground-state and thermodynamic properties of ThO<sub>2</sub>, including the phonons, are reasonably well described by DFT,<sup>128–131</sup> as expected for a band insulator. A recent study<sup>132</sup> compared the accuracy of three different exchange–correlation functionals to experimental results (see Figure 8).

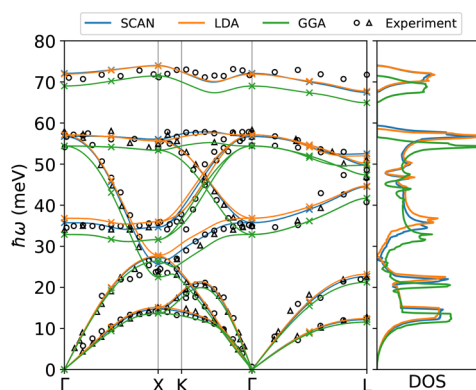


**Figure 8.** (left) Phonon dispersion for ThO<sub>2</sub> computed using DFT with three different exchange–correlation functionals (LDA, GGA, and SCAN) and measured using inelastic neutron scattering. (right) Phonon density of states. From ref 132. CC BY 4.0.

Overall, the strongly constrained and appropriately normed (SCAN) functional and the local density approximation (LDA) show better agreement with experiment than the generalized gradient approximation (GGA). UO<sub>2</sub> nominally contains two electrons in the uranium f shell, as the remaining four uranium valence electrons will be transferred to the oxygen atoms. However, in reality, hybridization substantially alters this nominal charge counting. The partially filled f shell gives rise to a low-energy Hamiltonian that exhibits a competition between the strong on-site Coulomb repulsion and delocalization, resulting in the “actinide Hamiltonian”,<sup>133</sup> which is a combination of the well-known Hubbard and periodic Anderson models. Therefore, one is faced with a challenging many-body problem with the potential for strongly correlated electron behavior. Moreover, the physics of UO<sub>2</sub> is further complicated by the relatively strong spin–orbit coupling in uranium.

A large number of DFT, DFT+*U*, hybrid functional, DFT+DMFT, and other first-principles calculations have been performed on UO<sub>2</sub>.<sup>134</sup> The LDA and GGA qualitatively fail, producing a metallic state.<sup>135</sup> The PBE0 and HSE hybrid functionals both produce an antiferromagnetic insulator.<sup>136,137</sup> DFT+*U* also produces an antiferromagnetic insulator and can even capture the proper 3k structure;<sup>138–141</sup> reasonable agreement with the spin-wave spectra is also obtained.<sup>142</sup> DFT+*U* calculations can provide moderate agreement with the experimental phonon spectrum.<sup>143,144</sup> Of course, DFT+*U* is confined to ordered states, and DFT+DMFT will be needed for extension to the paramagnetic state.

DFT+DMFT calculations for UO<sub>2</sub> have been executed using a variety of different approximations to solve the DMFT impurity problem, including exact diagonalization for a small bath,<sup>145</sup> the Hubbard-I approximation,<sup>146</sup> and continuous-time quantum Monte Carlo (CTQMC).<sup>146</sup> It is straightforward for DFT+DMFT to capture the paramagnetic insulating state in all cases. Studying small energy details with DFT+DMFT is still challenging because of the severe trade-off between precision and computational expense in solving the DMFT impurity problem. Precise techniques such as CTQMC will inherently hit a computational wall at sufficiently low temperatures, while inexpensive techniques such as Hubbard-I are not terribly reliable. A technique that is well-suited to the paramagnetic state at zero temperature for UO<sub>2</sub> is rotationally invariant slave boson theory,<sup>147</sup> which finds UO<sub>2</sub> to be an orbitally selective Mott insulator. However, the shortcoming of this approach is that it provides only a semiquantitative characterization of Mott physics, and more precise methods are needed to further investigate these findings.

With these approaches for the lattice properties of UO<sub>2</sub> and ThO<sub>2</sub>, thermal conductivity has been computed for both materials at various levels of approximation. The lowest-level approximation includes only the anharmonicity at the level of the mode-averaged Grüneisen parameter in conjunction with the Slack equation,<sup>148</sup> and this has been executed for ThO<sub>2</sub> using various DFT functionals<sup>129–131,149</sup> and for UO<sub>2</sub> using DFT-(GGA)+*U*<sup>150</sup> in addition to DFT+DMFT, where the DMFT impurity problem is solved via exact diagonalization using a truncated bath.<sup>64</sup> The next level of approximation is direct computation of the cubic phonon interactions from first principles and computation of the phonon lifetimes from perturbation theory followed by use of the RTA. This has been executed for ThO<sub>2</sub> using DFT<sup>151,152</sup> and UO<sub>2</sub> using DFT+*U*,<sup>27</sup> where the latter demonstrated rather substantial deviation from experiment. The next level of approximation goes beyond the

RTA and fully solves the BTE, which has been executed for  $\text{ThO}_2$ .<sup>153,154</sup> It should be noted that quantitative differences were found in the two aforementioned studies, despite the fact that the calculations were nominally very similar, highlighting some sort of methodological shortcomings.

### 2.3. Thermophysical Properties

**2.3.1. Introduction.** In addition to thermal conductivity, the heat capacity, thermal expansion, and elastic constants are all directly determined by the phonon structure. The thermophysical properties of actinide oxides have been a subject of many studies during the last 70 years. This fundamental research, initiated by the Manhattan Project, started various systematic studies of actinide oxides that led, among others, to the discovery of phase transitions in both  $\text{UO}_2$ <sup>155</sup> and  $\text{NpO}_2$ <sup>156</sup> at temperatures below 50 K. Neutron diffraction experiments established the antiferromagnetism (AF) in  $\text{UO}_2$  below 30 K,<sup>157,158</sup> but the situation in  $\text{NpO}_2$  remained a mystery for many years. The AF of  $\text{UO}_2$  was originally thought to be a simple type I AF single-k (1k), but work by Burlet et al.<sup>159</sup> strongly suggested that the ordering was of a 3k nature, and this was confirmed unambiguously by Blackburn and co-workers.<sup>160</sup> In such a magnetic structure, the moment directions are noncollinear but point along alternate  $\langle 111 \rangle$  directions. At the same time, resonant X-ray experiments<sup>161</sup> had established that the ordering at 25 K in  $\text{NpO}_2$  was of the electric quadrupoles, and they were also found soon after in  $\text{UO}_2$ .<sup>162</sup> Many of these complications and the associated theory are reviewed in ref 163, and the latest excitation spectra of  $\text{UO}_2$ , as measured with polarized neutrons, were published in 2011.<sup>164</sup> Hints of the elusive quadrupolar excitations<sup>165</sup> were found in this study, but an unambiguous proof of their existence remains a challenge. A more recent (shorter) review of these challenges in  $\text{UO}_2$  appeared in 2020.<sup>166</sup>

Our focus here is on studies that target thermophysical properties at low temperature (room temperature and below). This is in keeping with our later discussion of thermal transport in the presence of defects. In investigations of the influence of irradiation defects, it is often advantageous to freeze out phonon–phonon interactions by conducting experiments at low temperatures.

**2.3.2. Heat Capacity.** The low-temperature heat capacity of  $\text{ThO}_2$  has been measured on both polycrystalline samples and single crystals.<sup>29</sup> As expected for a diamagnetic insulator, the heat capacity does not show any sign of phase transitions, and its temperature dependence is governed by the acoustic and optical contributions, which can be described using the DFT harmonic approximation (see Figure 9).  $\text{UO}_2$  orders antiferromagnetically (noncollinear 3k magnetic structure) below the Néel temperature ( $T_N = 30.5$  K), as discussed above. In  $\text{UO}_2$  the transition is accompanied by a Jahn–Teller distortion of the oxygen atoms, discovered in 1976,<sup>167</sup> and electric quadrupolar ordering (3k type).<sup>142,163</sup> Because of that, the heat capacity shows a large first-order-type anomaly at the transition (see Figure 9).

Anharmonic effects, which were first observed in diffraction experiments by Willis and Hazell,<sup>173</sup> are important in describing the heat capacity in this oxide family. In  $\text{UO}_2$ , the observation of a small anharmonic specific heat contribution is the result of relatively large energy-dependent anharmonic effects that have opposite signs, leading to a total contribution near zero.<sup>168</sup> As might be expected, there have been much fewer studies on the specific heats of  $\text{NpO}_2$  and  $\text{PuO}_2$ .  $\text{NpO}_2$  has electric quadrupole ordering at 25.5 K<sup>161</sup> and a complex ordering of a higher-order magnetic multipoles.<sup>163,174–176</sup> Similar to  $\text{ThO}_2$ , the temper-

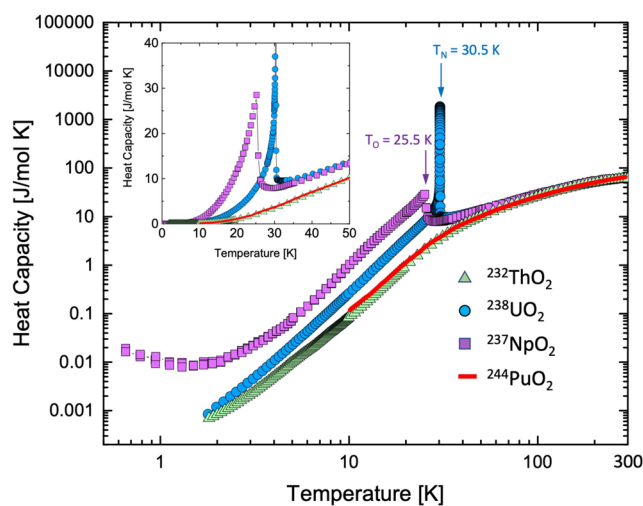


**Figure 9.** Heat capacities of  $\text{ThO}_2$  (green triangles),<sup>29</sup>  $\text{UO}_2$  (blue circles),<sup>168</sup> and  $\text{NpO}_2$  (purple squares)<sup>169</sup> single crystals and polycrystalline  $\text{PuO}_2$  (red line).<sup>170,171</sup> In the case of  $\text{UO}_2$ , a large first-order-type anomaly is observed at 30.5 K as a result of Jahn–Teller structural distortion and antiferromagnetic ordering. For  $\text{NpO}_2$ , the transition at 25.5 K is caused by ordering of high-order magnetic multipoles. The increase in heat capacity below 3 K in various neptunium systems is usually associated with a nuclear Schottky term due to the splitting of the  $I = 5/2$  nuclear ground level of the  $^{237}\text{Np}$  nuclei by the hyperfine field. In  $\text{NpO}_2$ , however, the origin of the anomaly is unclear since the nuclear contribution seems to be too small to explain the difference.<sup>172</sup>

ature dependence of the specific heat of  $\text{PuO}_2$  (polycrystalline samples) shows no anomaly, in agreement with a temperature-independent Pauli paramagnetic state,<sup>170,171,177</sup> which arises from the singlet ground state established for this  $\text{Pu}^{4+}$  ( $5f^4$ ) material.<sup>178</sup> The similarity in the behavior of the heat capacity in these oxides agrees with the similarity in the phonon dispersions observed in these materials. Also, the low-temperature electronic contribution to the specific heat can be extrapolated to zero at  $T = 0$ , in perfect agreement with their Mott-insulating ground state.

**2.3.3. Thermal Conductivity.** Despite the importance of  $\text{ThO}_2$  as a nuclear fuel material, the thermal conductivity of  $\text{ThO}_2$  single crystals has been measured only recently.<sup>179</sup> Overall, the temperature dependence of the thermal conductivity of  $\text{ThO}_2$  is typical for diamagnetic insulators, with a characteristic maximum below 40 K. Its behavior can be described by phonon thermal transport by taking into account boundary, defect, and Umklapp phonon–phonon scattering mechanisms.<sup>180</sup> In contrast, uranium dioxide shows anomalous behavior with a double-peak structure (see Figure 10) and a low magnitude of  $\kappa(T)$ .

That behavior cannot simply be explained by different strengths of defect or grain boundary scattering processes present in different materials, as the thermal conductivity of  $\text{UO}_2$  is similar for stoichiometric pellets, polycrystals, and single crystals.<sup>181</sup> To explain that discrepancy, it has been suggested that the reduction of the thermal conductivity in  $\text{UO}_2$  is due to strong resonant scattering of phonons and electronic degrees of freedom, such as spins, with characteristic energies on the order of 10 meV.<sup>180</sup> Similar behavior has also been suggested to describe the  $\kappa(T)$  behavior in other magnetic materials.<sup>182–184</sup> Furthermore, the thermal conductivity of  $\text{UO}_2$  appears to exhibit anisotropic behavior (Figure 10b), with slightly smaller ( $\sim 10\%$ )

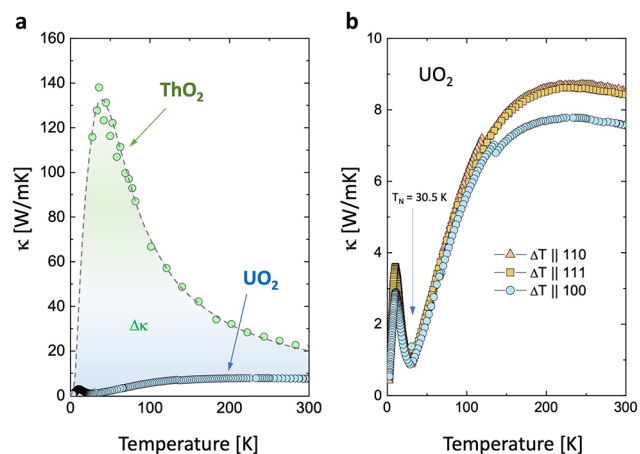


**Figure 10.** (a) Thermal conductivities of ThO<sub>2</sub> (green circles) and UO<sub>2</sub> (blue circles) single crystals measured along the  $\langle 100 \rangle$  crystallographic direction. The significant differences in  $\kappa(T)$  and its magnitude between ThO<sub>2</sub> and UO<sub>2</sub> should be noted. (b) Temperature dependence of the thermal conductivity of a UO<sub>2</sub> single crystal measured in the  $\langle 100 \rangle$ ,  $\langle 110 \rangle$ , and  $\langle 111 \rangle$  crystallographic directions. The ThO<sub>2</sub> data were taken from ref 179. The UO<sub>2</sub> data were taken from ref 180.

heat conduction along the  $\langle 100 \rangle$  direction.<sup>180</sup> If confirmed, this unusual behavior for the second-rank thermal conductivity tensor indicates that there is some “hidden” anisotropic behavior (in certain phonon interactions or couplings) that break the cubic symmetry in this material and lead to anisotropic thermal transport. Some microscopic evidence to support these macroscopic measurements has come from measurements of the low-temperature phonon line widths with IXS.<sup>185</sup> A strong anisotropy is found in that the line widths are strongly broadened over the energy range 5–15 meV in the  $\langle 100 \rangle$  direction, whereas no effects are observed in the  $\langle 011 \rangle$  direction. Further study is needed to definitively connect these phonon features and macroscopic thermophysical properties.

**2.3.4. Elastic Constants and Thermal Expansion.** Elastic constants have been studied experimentally using a pulse-echo technique on single crystals of ThO<sub>2</sub> and UO<sub>2</sub> at room temperature.<sup>186,187</sup> The thermal expansion of UO<sub>2</sub> single crystals was measured by Brandt and Walker in 1967.<sup>188,189</sup> That was the first direct demonstration that the phase transition is first-order in the lattice properties. The volume collapse at  $T_N$  was first observed in 1974<sup>190</sup> and, more recently, by X-ray diffraction.<sup>191</sup> Furthermore, the measurements of elastic constants versus temperature have not only exhibited changes at the magnetic transition but also confirmed that the elastic properties at high temperature (up to room temperature) are much more complicated than anticipated. Similar indications have come from susceptibility measurements<sup>192</sup> and polarized neutron studies<sup>193</sup> that showed short-range order up to at least 200 K. Elastic constants are directly related to low-frequency dispersion of the three acoustic phonon modes. In cubic systems, there are three independent elastic constants,  $C_{11}$ ,  $C_{12}$ , and  $C_{44}$ . In UO<sub>2</sub>, the temperature dependence of  $C_{44}$  (shear along the  $\langle 111 \rangle$  crystallographic direction—the cube diagonal) is highly anomalous<sup>188,189</sup> and indicative of a considerable interaction between the lattice and spins even well above the Néel temperature (see Figure 11). The strong spin–phonon coupling and magnetoelastic interactions have also been confirmed by inelastic neutron scattering experiments.<sup>194,195</sup>

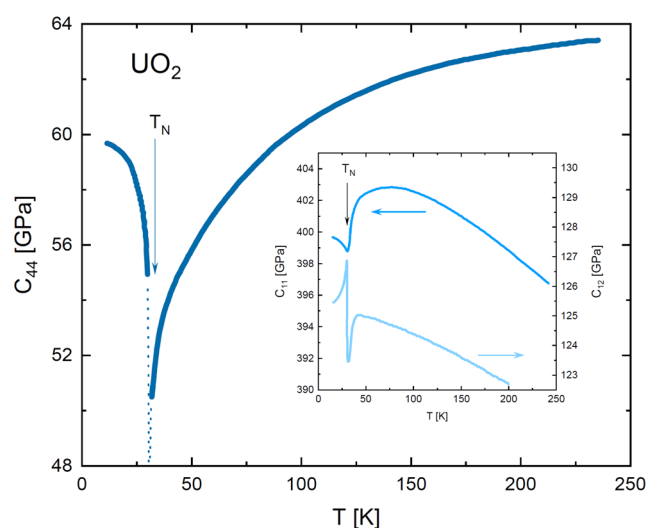


**Figure 11.** Change in elastic constants with temperature for UO<sub>2</sub>. The data were taken from ref 188.

This is more completely discussed in a recent neutron inelastic scattering study,<sup>164</sup> a review article,<sup>163</sup> and the 2020 review.<sup>166</sup>

Recently, the thermal expansion of UO<sub>2</sub> has been studied under a high magnetic field. It was found that UO<sub>2</sub> becomes a piezomagnet when the magnetic field is applied along the  $\langle 111 \rangle$  direction in the antiferromagnetic state and exhibits a peculiar memory effect due to a partial domain reorientation.<sup>196</sup> These effects are due to the strong magnetoelastic interactions and the symmetry of the noncollinear 3k antiferromagnetic order in this material, which allows the appearance of piezomagnetism in UO<sub>2</sub>.<sup>197</sup>

## 2.4. Crystal Growth

**2.4.1. Challenges in Growing Single Crystals.** Many of the experimental efforts discussed herein either require single crystals or perform best when single crystals are analyzed. However, the AO<sub>2</sub> (A = Ce, Th, U, Pu) family is extremely challenging to grow as single crystals because the high melting points (2470–3377 °C)<sup>198–201</sup> exceed those of the containers used in melt growth syntheses and the solubilities are low in most industrially feasible solvent systems.<sup>202–205</sup> Overviews of the successful growth techniques have been published elsewhere,<sup>206–210</sup> but herein the discussion focuses on how each successful growth technique maximizes some of the desired attributes while having shortcomings in other aspects. As a result, in approaching a study of the AO<sub>2</sub> family or even any individual member, compromises must typically be made on the basis of what single-crystal properties are of highest importance. The main areas where this trade-off occurs are in the crystal purity, growth speed, structural quality, and size. The various oxidation states that are available for U and Pu further complicate crystal production.<sup>211</sup>

**2.4.2. Bulk Crystal Growth Techniques.** The cornerstone of large (>1 m), high purity ( $\gg 99.9\%$ ), high-quality crystal growth in the semiconductor industry is the pulled melt crystal growth methodology, such as that employed in the Czochralski method. However, maintaining a feedstock of molten AO<sub>2</sub> is infeasible because their melting points exceed those of widely used containment vessels. As a result, the AO<sub>2</sub> family has been the subject of more exotic crucible methods, such as the cold crucible technique (ThO<sub>2</sub> and UO<sub>2</sub>)<sup>212</sup>, closed capsule zone melting (UO<sub>2</sub>)<sup>213</sup>, and use of a floating zone furnace

( $\text{UO}_2$ <sup>214,215</sup>). An alternative route to avoid crucible destruction is to have much more rapid melt growth, such as in arc melting ( $\text{UO}_2$ <sup>214,216–218</sup> and  $\text{ThO}_2$ <sup>219–223</sup>), a solar furnace ( $\text{UO}_2$ <sup>224</sup> and  $\text{ThO}_2$ <sup>225</sup>), or the Verneuil method ( $\text{UO}_2$ <sup>226</sup>). Although many of these techniques yield large ( $>1\text{ cm}^3$ ) products, they are never single crystals for the  $\text{AO}_2$  family. Rather, agglomerates of multiple single crystals that are sintered together are produced.<sup>227</sup>

Samples used for analysis are often cut from these large domains in such a way that a single crystal is acquired. This means that all of the single crystals thus obtained have been mechanically altered, which in the case of  $\text{A} = \text{U}$  or  $\text{Pu}$  could mean that the surface adopts a new cation-to-anion ratio. Furthermore, the production of large crystal domains signifies that orientation control is difficult for melt growth of these refractive oxides. The presence of these large domains indicates that the growth conditions are quite heterogeneous, suggesting that the crystal quality might vary within a single given domain, but experimental investigations have rarely been performed to assess this.

If melt growth is eschewed because of these assorted shortcomings, the next most common growth techniques dissolve the feedstock under conditions well below the melting point and then crystallize out the feedstock from the solution. Chemical vapor deposition (CVD) or chemical transport ( $\text{UO}_2$ <sup>228–231</sup>,  $\text{U}_x\text{Th}_{1-x}\text{O}_2$ <sup>232</sup> and  $\text{U}_{1-x}\text{Pu}_x\text{O}_2$ <sup>233</sup>), flux ( $\text{CeO}_2$ <sup>234–241</sup>,  $\text{ThO}_2$ <sup>220,223,234–238,242–247</sup>,  $\text{UO}_2$ <sup>217,248,249</sup>,  $\text{U}_x\text{Th}_{1-x}\text{O}_2$ <sup>249</sup> and  $\text{PuO}_2$ <sup>242,250–253</sup>), and hydrothermal or solvothermal synthesis ( $\text{CeO}_2$ <sup>254</sup>,  $\text{ThO}_2$ <sup>29,67,179,255–262</sup>,  $\text{U}_{1-x}\text{Th}_x\text{O}_2$ <sup>262–264</sup>,  $\text{UO}_2$ <sup>256–258,264–267</sup> and  $\text{PuO}_2$ <sup>268</sup>) fall into this category and have been employed for the entire  $\text{AO}_2$  family. High-quality, well-faceted single crystals of  $\text{ThO}_2$  and  $\text{UO}_2$  produced using the hydrothermal method are shown in Figure 12. Whereas melt crystal growth is largely a physical growth

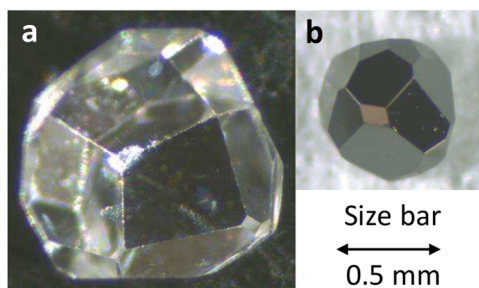


**Figure 12.** High-quality, well-faceted single crystals of (a)  $\text{ThO}_2$  and (b)  $\text{UO}_2$  produced using the hydrothermal method.

method (although oxidation, reduction, and crucible contamination can become major chemical factors), solution-based growth techniques are truly chemical growth methods. This complicates matters in that the solvent–reactant, solvent–product, and solvent–container interactions all become variables in addition to chemical species and oxidation/reduction. The added complexity means that large, high-quality single crystals can be grown, but the development of a reliable, large-scale technique is often a cumbersome undertaking. Furthermore, solvent contamination is an inherent challenge, frequently resulting in measurable impurities in single crystals produced via these pathways. In some cases, however, ideal solvents can be found, such as how the highest-purity  $\text{CeO}_2$  single crystals have been fabricated by the hydrothermal

technique in a  $\text{KF}$  solution with impurities of only 100 ppm  $\text{K}$  and 10 ppm  $\text{F}$ .<sup>254</sup> Despite the purity, the 100  $\mu\text{m}$  size somewhat limits their utility. Seeded growth can be performed easily in most of these techniques (provided a suitable seed can be procured), enabling orientation control and iteratively improving the crystal quality.

There are a few techniques that fall outside of the purview of both melt techniques and transport-assisted growth methods, including sublimation in vacuum or from a plasma ( $\text{ThO}_2$ <sup>269</sup> and  $\text{UO}_2$ <sup>217,269,270</sup>), thermal decomposition ( $\text{UO}_2$ <sup>271</sup> and  $\text{PuO}_2$ <sup>272</sup>), electrodeposition ( $\text{UO}_2$ <sup>273–276</sup>), and high-temperature sintering ( $\text{UO}_2$ <sup>217</sup>). Sublimation has to date only yielded crystals (4 to 12 mm) of  $\text{AO}_2$  with purities that are often worse than that of the starting material. Thermal decomposition, where something other than  $\text{AO}_2$  (e.g.,  $\text{AOCl}_2$ ) is the feedstock for flux growth, maintains the same drawbacks of flux growth with the added complication that the starting material itself is a source of impurities. Electrodeposition suspends two electrodes in a molten flux containing the feedstock material, repeating the same shortcomings of flux growth and enhancing them with the possibility of electrode contamination. High-temperature sintering is essentially limited by the growth time, as grains will slowly enlarge, but the atomic mobility is extremely low compared with fluid or gas growth mechanisms. Despite these challenges, high-quality crystals have been produced by these techniques, but they are often small, contain impurities, or both.

In the techniques discussed here, some type of trade-off is necessitated among the crystal purity, growth speed, structural quality, or size. Even with these compromises, however, at present there is not a direct route to make large ( $>1\text{ cm}^3$ ) single crystals of any member of the  $\text{AO}_2$  family. Growth procedures are discussed that report larger crystals, but these often have grain boundaries or large domains, so the term “single crystal” cannot readily be applied. As of now, however, there are some leaders in the crystal growth of each  $\text{AO}_2$  member. Dark-brown  $\text{CeO}_2$  crystals with edges of up to 8 mm, for example, were grown with a (100) cubic morphology using a flux mixture of  $\text{Pb}_3\text{P}_2\text{O}_8$ ,  $\text{PbF}_2$ ,  $\text{Al}_2\text{O}_3$ ,  $\text{NaF}$ ,  $\text{MgF}_2$ , and  $\text{V}_2\text{O}_5$ .<sup>235</sup> The crystal purity might be low, however, as similar flux solutions displayed  $>1\text{ wt } \%$   $\text{Pb}$  inclusions in  $\text{CeO}_2$ .<sup>240</sup> Adjusting the flux to  $\text{Li}_2\text{WO}_4$  resulted in lower impurity concentrations (200 ppm  $\text{W}$  and  $<50$  ppm  $\text{Li}$ ), but the size decreased to a maximum edge size of 2 mm.<sup>239</sup> For  $\text{ThO}_2$ , a 18.92 mm  $\times$  9.69 mm  $\times$  0.85 mm single crystal with a (100) cubic morphology was grown by the hydrothermal technique,<sup>67</sup> and the bulk purity ( $>99$  atom % for cation content) was higher than that of the starting  $\text{ThO}_2$  feedstock material.<sup>29</sup> However, the first 50 nm of the surface had a high concentration of impurities, demonstrating that the impurities from the starting  $\text{ThO}_2$  feedstock were purified out of the bulk material and then deposited on the sample during the final cooling cycle.  $\text{UO}_2$  crystals with side lengths approaching 10 mm and a variety of crystal morphologies were synthesized with electrolytic decomposition in a molten flux.<sup>274</sup> Altering the conditions decreased the size to 3 mm per side but afforded crystals with a highly defined cuboctahedral morphology and a decrease of  $\sim 33\%$  of the impurities present in the starting material.<sup>273</sup> The radiological concerns of  $\text{PuO}_2$  make its crystal growth a rare endeavor, but 2 mm  $\times$  2 mm  $\times$  3 mm single crystals with a (111) octahedral morphology were grown from a  $\text{Li}_2\text{Mo}_4\text{O}_7$  flux with a relatively low concentration of impurities (the highest was  $\text{Fe}$  at 200 ppm).<sup>251</sup>

**2.4.3. Epitaxial Thin Films.** Epitaxial thin films of  $\text{AO}_2$  ( $\text{CeO}_2$ <sup>277</sup>,  $\text{ThO}_2$ <sup>278</sup>,  $\text{UO}_2$ <sup>211,279,280</sup> and  $\text{PuO}_2$ <sup>211</sup>) produced via

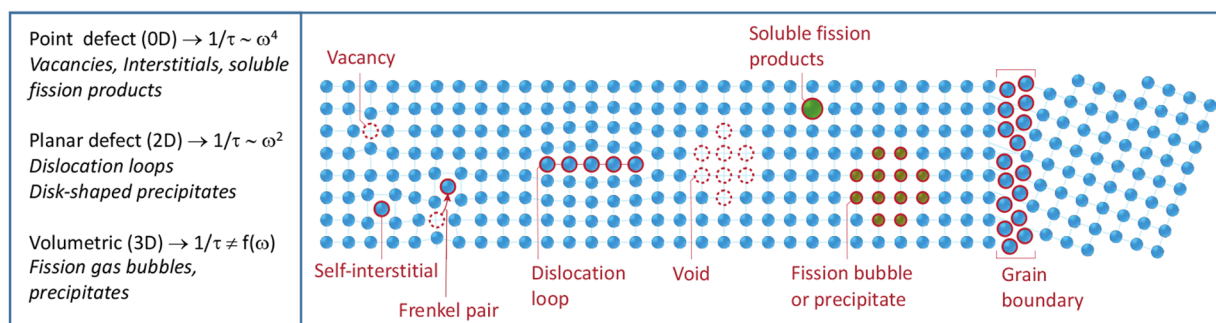


**Figure 13.** Illustration of irradiation defects found in oxide nuclear fuels. The phonon scattering rate is sensitive to the dimensionality of the defect.

reactive magnetron sputtering, polymer-assisted deposition, and sol–gel techniques represent an alternative route to the synthesis of bulk single crystals. While much remains to be done before samples of the quality used in the semiconducting industry are available, this field has started to pay dividends. For example, antiferromagnetism of  $\text{UO}_2$  thin films on different substrates has been studied<sup>281</sup> and showed the effect of strain induced by the substrate–film interaction.

Currently, films are commonly produced using a commercially available substrate such as  $\text{LaAlO}_3$ ,  $\text{SrTiO}_3$ , or YSZ, which imparts strain into the grown oxide layer. This explains, in part, why thin films have been shown to have broad X-ray diffraction (XRD) rocking curves,<sup>282</sup> large deviations from bulk lattice parameters,<sup>282</sup> and columnar grains.<sup>283</sup> Nonetheless, tremendous potential exists in this field as suitable single-crystal  $\text{AO}_2$  substrates become available. A start along this line was reported on  $\text{U–UO}_2$  interfaces<sup>284</sup> and  $\text{UO}_2\text{–ThO}_2$  interfaces.<sup>258</sup>

### 2.5. Outlook

Foundational work on phonon transport in nearly perfect single crystals is the first step in developing a comprehensive understanding of thermal transport in oxide nuclear fuels under irradiation. On the experimental side, this portion of the review focused on inelastic X-ray and neutron scattering to obtain detailed information about the phonon structure and measurement of low-temperature thermophysical properties. These studies revealed gaps in understanding that are the source of continued research. Examples include the origin of nonlinear propagating modes found in several fluorite crystal structures, including  $\text{UO}_2$  and  $\text{ThO}_2$ , and the possibility of anisotropic thermal conductivity in  $\text{UO}_2$  due to phonon interactions that locally break cubic symmetry. On the modeling side, electronic structure calculations were reviewed with a focus on strongly correlated materials. The shortcomings of DFT with regard to accurate prediction of the branch-specific contributions to the conductivity in  $\text{UO}_2$  point to new opportunities for DFT +DMFT modeling approaches. Finally, central to all fundamental studies, a short review of growth of actinide oxide single crystals was presented. As new high-quality single-crystal substrates of actinide oxides become available, opportunities exist for the synthesis of epitaxial thin films and interfaces with quality rivaling that found in the semiconductor industry. As mentioned in the introduction, it is thought that interfaces in nuclear fuel play an outsized role in defect evolution and thermal transport. Having access to interfaces with chemical precision would open new frontiers for understanding thermal transport under irradiation.

## 3. CRYSTALLINE DEFECT GENERATION, EVOLUTION, AND CHARACTERIZATION

In line with the main goal of this review, here we present an overview of defects in  $\text{UO}_2$ ,  $\text{ThO}_2$ , and  $\text{CeO}_2$ , which are closely tied to thermal transport. Defects play a critical role in thermal transport because of their ability to scatter phonons. Experiments have shown that the thermal conductivity in  $\text{UO}_2$  under reactor conditions is influenced by (1) irradiation defects, (2) intragranular clustering of fission products, and (3) clustering at existing and newly formed grain boundaries<sup>5,8</sup> (see Figure 13). Until recently, the impact of many of these defects on thermal transport has been treated only empirically, as the concentration, size, and distribution of these defects are controlled by complex mechanisms and are highly dependent upon local irradiation conditions. Accordingly, here we primarily focus on smaller-scale defects that can be introduced in a controlled ion beam environment and where recombination, saturation, and clustering play an outsized role.

In the last several decades, a number of studies have focused on radiation damage in  $\text{UO}_2$ , including dislocation loop formation,<sup>285</sup> radiation-induced lattice expansion,<sup>286–288</sup> HBS development,<sup>6,289</sup> and fission gas release.<sup>290–294</sup> The irradiation microstructure of  $\text{CeO}_2$ , an important surrogate material for oxide nuclear fuels, has started to receive significant attention over the past decade.<sup>28,295–298</sup>  $\text{ThO}_2$  has received sporadic attention since the 1960s but is now receiving more consideration, as it has emerged as a promising advanced nuclear fuel.<sup>299–303</sup>

In this section, we discuss the nature of irradiation-induced defects as revealed in experiments, selected methods for characterization of defects and their evolution, off-stoichiometry and equilibrium point defect disorder in oxides, and the mechanisms of defect clustering and long-term evolution in irradiated oxides and give an outlook on required future developments in understanding defects from the perspective of thermal transport. The primary focus here will be key findings tied to ion beam irradiation studies. Ion beam irradiation has proven to be a flexible tool for the generation of defects found in real fuel.<sup>29,304–328</sup> Although they are beyond the scope of this review, it is noted here that complementary studies involving neutron,<sup>329</sup>  $\alpha$ -particle,<sup>286–288,330</sup> or electron<sup>331</sup> irradiation can be used to judge the efficacy of employing a particular set of ion irradiation conditions (e.g., ion mass, energy, and fluence).

As shown in the left panel of Figure 13, the frequency dependence of the phonon scattering rate,  $\tau^{-1}$ , is sensitive to the dimensionality of the defect with respect to the wavelength of the heat-carrying phonons. Thus, to provide a distinct phonon transport perspective, this section is organized according to the size and dimensionality of the defect. In particular, we introduce

intrinsic point defects first, followed by point defects and defect clusters that form under irradiation and then other extended defects such as defect-decorated grain boundaries and grain boundaries formed as a result of restructuring.

### 3.1. Intrinsic Point Defects

Intrinsic point defects are present in single-crystal oxides under thermodynamic equilibrium in the form of vacancies, interstitials, and native dispersed impurities. The presence of these point defects makes oxides off-stoichiometric. Off-stoichiometry is important in understanding the structural properties, thermokinetic properties, and performance of oxide nuclear fuels. Moreover, carefully accounting for the impact of intrinsic defects on thermal transport is the first step in providing a comprehensive description of thermal transport under irradiation.

**3.1.1. Characterization Techniques.** Accurate characterization of the size and distribution of intrinsic, subnanometer defects remains a challenge. Here, we provide a brief review of two experimental techniques used to glean information about subnanometer defects. Point defects in oxides such as  $\text{UO}_2$ ,  $\text{CeO}_2$ , and  $\text{ThO}_2$  have been extensively characterized using light-source techniques.<sup>322,332–344</sup> This field of study was recently reviewed by Lang et al.<sup>345</sup> However, our focus here will be on positron annihilation spectroscopy (PAS) and optical spectroscopy, which to date have seen limited use in oxide fuels but show particular promise for characterizing the spectrum of point defects and small clusters that reside in ion-irradiated oxide fuels and fuel surrogates. While each technique exhibits demonstrated potential, particular attention must be paid to the characterization of point defects in ion-irradiated oxides.

**3.1.1.1. Positron Annihilation Spectroscopy.** PAS can accurately probe individual atomic vacancies as well as small and large clusters of vacancies with a remarkable sensitivity of less than 1 ppm, providing quantitative information about their size and density.<sup>346</sup> When introduced into a solid, a positron quickly loses its kinetic energy and eventually annihilates with an electron, producing two photons that are emitted in nearly opposite directions. The emitted photons are Doppler-shifted by the longitudinal momentum of the electron. Measurement of this shift has been developed as an effective method known as Doppler broadening spectroscopy (DBS) to provide information about the concentration and characteristics of defects in solids, as the electron momentum sampled by the positron is strongly affected by trapping at defects.

The positron annihilation rate is governed by the overlap between the positron wave function and the electron density at the annihilation site, providing information about the local electron density, which is directly related to the nature and size of the defect. Thus, positron annihilation lifetime spectroscopy (PALS) provides a direct method for measuring the size and density distributions of atomic scale defects. It can discriminate among vacancy clusters ranging from single vacancies to clusters of  $\sim 50$ – $100$  vacancies until they become large enough to be resolvable by transmission electron microscopy (TEM).

While standard PAS techniques are extremely useful, the typical penetration depth is several hundreds of micrometers, and as a consequence, they cannot be applied to ion-irradiated materials, as the damage layer is only a few micrometers thick. In the 1980s, the development of slow positron beams and variable-energy positron techniques made depth-resolved measurements and characterization of ion-irradiated materials possible. The

first studies of depth-resolved PAS were performed on He-ion-irradiated Cu and Ni.<sup>347</sup>

Laboratory-based slow positrons or variable-energy positron beams begin with a positron source having a continuous energy distribution. The most commonly used source is the radioactive isotope  $^{22}\text{Na}$ . Some of the fast positrons emanated from the source are moderated down to  $\sim 75$  meV as they pass through a thin foil (e.g., W and Ni).<sup>347,348</sup> The positrons extracted from the moderator are then guided through a vacuum system to the target using magnetic or electrostatic lenses. The unmoderated positrons are filtered through crossed electric and magnetic fields ( $\mathbf{E} \times \mathbf{B}$  filter) or a magnetic velocity selector. The left side of Figure 14 illustrates the extraction of slow positrons through a

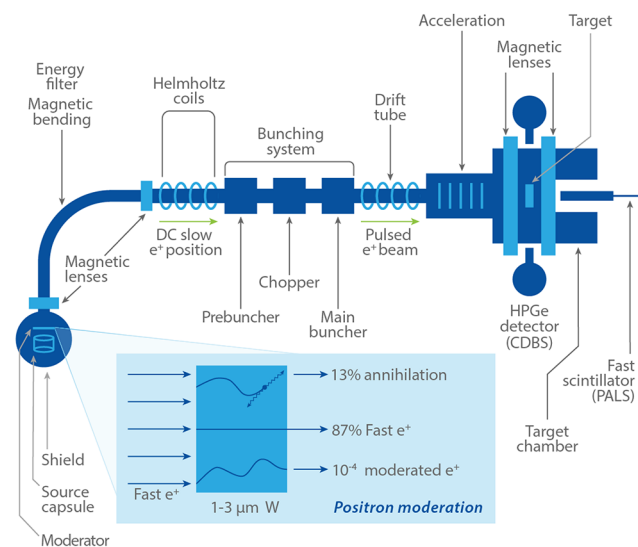


**Figure 14.** Simplified schematic of a magnetically transported slow pulsed positron beam with a positron annihilation lifetime spectrometer and coincident Doppler broadening spectrometer. Vacuum components, high-voltage/current sources, and beam diagnostic tools are not shown.

magnetic velocity selector. The figure also shows the moderation process. After extraction of the slow positrons, the direct current (DC) slow  $e^+$  beam is then accelerated to variable energies, typically up to 30 keV, where variable-energy DBS (VEDBS) can be performed. VEDBS can provide qualitative information about the defect structures and measure the overall defect level in ion-irradiated materials. Such measurements have been applied to ion-irradiated actinide oxides in the last few decades, and the knowledge learned from them will be briefly discussed in the next section. However, the full characterization of radiation-induced defects in terms of size, density, and depth distributions can be extracted only from PALS measurements, which require pulsed positron beams with short pulses on the order of 100–200 ps. In the last several years, reactor- and accelerator-based pulsed positron beams have been developed with sufficient temporal resolution for characterization of small defects induced by ion irradiation in some metals as a function of depth.<sup>349</sup> While these user facility adaptations of positron characterization provide the irradiation materials science community with tremendous new capability, multiple measurement methodologies cannot be easily accommodated. Current efforts directed at developing pulsed positron beams derived from radioactive isotopes (see Figure 14) will usher in a new era in positron characterization by enabling in situ measurements of materials

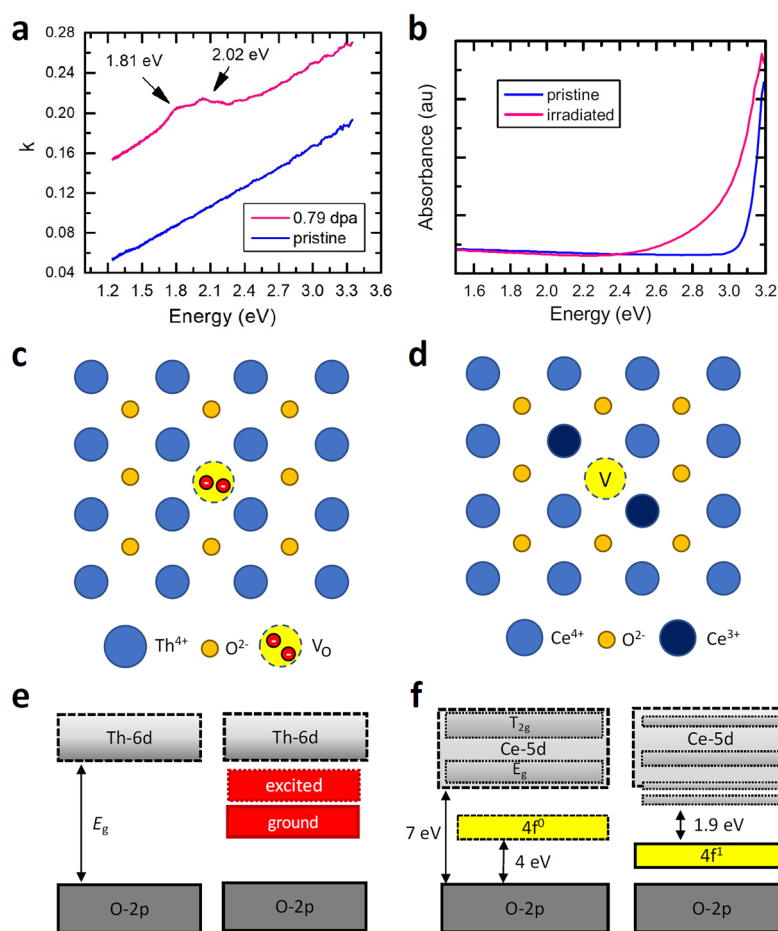


**Figure 15.** Optical characterization of defects in irradiated fluorite oxides. (a, b) Optical absorption in (a) proton-irradiated  $\text{ThO}_2$  and (b) electron-irradiated  $\text{CeO}_2$ . (c, d) Atomic configurations of oxygen vacancies in (c)  $\text{ThO}_2$  and (d)  $\text{CeO}_2$  and (e, f) the corresponding electronic band diagrams. The data were taken from (a) ref 132 and (b) ref 360.

during ion irradiation.<sup>350</sup> Figure 14 shows the incorporation of a bunching system to a magnetically transported beam to convert the DC slow  $e^+$  to pulses that are hundreds of picoseconds in width, making them relevant for PALS measurements in a wide range of ion-irradiated materials. Then DBS and PALS can be done simultaneously, as illustrated in Figure 14.

**3.1.1.2. Optical Spectroscopy.** Optical absorption and luminescence spectroscopy are convenient methods for characterizing point defects in irradiated oxides, as oxygen vacancies have prominent signatures. While these spectroscopies have been applied to characterize a wide range of irradiated oxides,<sup>351–353</sup> application to irradiated actinide oxides is limited. The optical response of oxides depends strongly on the preferred charge state of the cation. We thus start our discussion with  $\text{ThO}_2$ , as Th has only one preferred charge state. We then discuss  $\text{CeO}_2$  and  $\text{UO}_2$ , both of which have multiple charge states.

In  $\text{ThO}_2$ , Th exhibits only the 4+ charge state. Therefore, when one considers an oxygen vacancy, two electrons (in a neutral defect) or one electron (in a positively charged defect) is localized on the vacant site and creates a virtual atom having specific electronic states. Optical induced transitions of an electron within this virtual atom contribute to the emergence of absorption and luminescence bands within the band gap. Because of their impact on the optical permittivity, these defects are called color centers. Figure 15a shows representative spectra

for proton-irradiated  $\text{ThO}_2$  exhibiting absorption peaks at 1.8 and 2.0 eV.<sup>132</sup> The locations of these peaks match previous reports on irradiated  $\text{ThO}_2$ .<sup>219,354</sup> In contrast to  $\text{Al}_2\text{O}_3$  and  $\text{MgO}$ ,<sup>351–353</sup> the number of studies of electronic structure of defects in  $\text{ThO}_2$  has been limited.<sup>149,355</sup> Accordingly, assignment of these absorption/luminescence peaks to defect types will require more systematic studies.

In  $\text{CeO}_2$ , the oxygen-vacancy-induced peaks have a different origin.<sup>356,357</sup> Unlike  $\text{ThO}_2$ ,  $\text{CeO}_2$  does not have color centers, as extra electrons are localized on cerium ions, changing their charge state from 4+ to 3+. The extra electron on the  $\text{Ce}^{3+}$  ion occupies the 4f electron state, which is empty in  $\text{Ce}^{4+}$ . Additionally, it has been reported that 5d-band electrons in  $\text{Ce}^{3+}$  exhibit additional crystal field splitting. In perfect  $\text{CeO}_2$ ,  $\text{Ce}^{4+}$  has octahedral coordination, leading to splitting of the 5d bands into two groups of bands with  $T_{2g}$  and  $E_g$  symmetry (Figure 15e).<sup>358</sup> When defects are present, the symmetry of the crystal structure is reduced, which results in further splitting of the d bands (Figure 15e). Overall, this leads to an emergence of additional absorption bands corresponding to electron transitions from 4f bands into crystal-field-split 5d bands, as shown in the spectra of irradiated  $\text{CeO}_2$  (Figure 15b), which exhibits an additional absorption peak at 2.8 eV.<sup>359</sup> Computationally, there is strong evidence supporting localization of electrons on Ce ions.<sup>355</sup>

The electronic band structure of pristine  $\text{UO}_2$  has been thoroughly investigated experimentally;<sup>361</sup> however, investigation of the electronic structure of defects has been limited to computational efforts involving DFT+ $U$  treatments of electron correlation.<sup>362,363</sup> While in  $\text{ThO}_2$  and  $\text{CeO}_2$  the highest populated level corresponds to 2p bands of oxygen, in  $\text{UO}_2$  it corresponds to 5f bands. In  $\text{ThO}_2$ , the lowest unoccupied state is 5d, whereas in  $\text{CeO}_2$  it is 4f. In  $\text{UO}_2$  an additional effect is present, where the f band is split as a result of strong electron correlation effects, making  $\text{UO}_2$  a Mott insulator.<sup>364</sup> The challenge here involves properly treating electron correlation to accurately assign absorption/luminescence peaks to defect types.

**3.1.1.3. Raman Spectroscopy.** Raman spectroscopy allows the vibrational properties of fluorite crystals to be probed<sup>365–367</sup> and can be used to characterize point defects and small defect clusters. Raman spectra of  $\text{UO}_2$  have been presented in a number of studies,<sup>258,368</sup> while reports on  $\text{ThO}_2$  are more limited.<sup>29,321</sup> An extensive body of literature exists for  $\text{CeO}_2$  and  $\text{ZrO}_2$ .<sup>369,370</sup> Perfect crystal structures of these fluorites exhibit a mode at  $\sim 450\text{ cm}^{-1}$ , characterized as a triply degenerate mode with  $T_{2g}$  symmetry at the  $\Gamma$  point.<sup>371</sup> The other three optical modes at the  $\Gamma$  point (see Figures 7 and 8) have  $T_{1u}$  symmetry and are infrared-active but not Raman-active. Point defects contribute to the emergence of new vibrational modes, some of which are Raman-active.<sup>372–374</sup> The vibrational structures of anion vacancies and interstitial and cation substitutions in fluorites have been analyzed using the Green's function approach for lattice dynamics.<sup>370,372–374</sup> Group theory considerations are used to determine the symmetry of the defect structure and its vibrational modes.<sup>370</sup>

Figure 16a depicts the Raman spectra in proton-irradiated  $\text{UO}_2$ , and Figure 16b depicts the same for  $\text{ThO}_2$ .<sup>29</sup> The observed

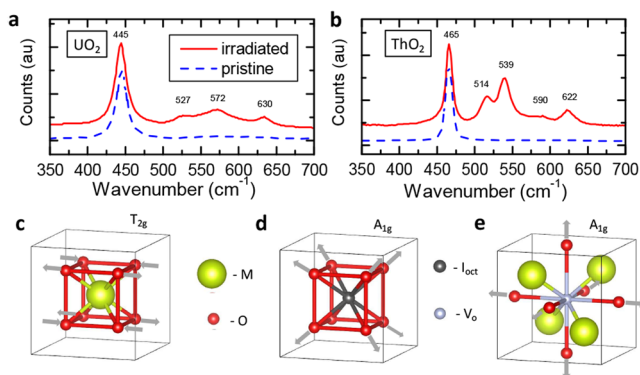


**Figure 16.** Raman spectra in pristine and irradiated (a)  $\text{UO}_2$  and (b)  $\text{ThO}_2$ . (c–e) Cartoon representations of the vibrational modes in perfect and defected fluorite systems. The data in (a) and (b) were taken from ref 368.

defect peaks share features similar to ones in  $\text{CeO}_2$ . In  $\text{CeO}_2$ , the peak at  $560\text{ cm}^{-1}$  is attributed to oxygen vacancies, and the peak  $590\text{ cm}^{-1}$  is associated with substitutions on the cation sublattice.<sup>371,375</sup> In  $\text{UO}_2$ , the peaks at  $630\text{ cm}^{-1}$  have been attributed to cuboctahedral clusters,<sup>376</sup> while the peak at  $570\text{ cm}^{-1}$  corresponds to a mode having  $T_{1u}$  symmetry that is Raman-activated in the presence of disorder.<sup>377</sup> Another feature observed in irradiated fluorites is a broadening and peak shift of  $T_{2g}$  due to a disorder-induced phonon confinement effect.<sup>277,371</sup>

Assignment of the defect peaks in irradiated  $\text{ThO}_2$  is pending further studies.<sup>29</sup>

**3.1.1.4. Correlative Characterization.** It is important to note that the positron and optical characterization methods described above have unique advantages and limitations. While PALS can size-discriminate from single-vacancy-type defects through divacancy to larger-scale clusters, it is not sensitive to interstitial-type defects. In contrast, optical spectroscopy can provide information about both vacancy- and interstitial-type defects, but its ability to size-discriminate is somewhat limited. Thus, there are advantages in combining these techniques. Optical, photoluminescence, and Raman spectroscopies can successfully detect oxygen vacancies, while PAS directly measures cation vacancies and the defect complexes of vacancies and impurities. Combining more than one technique such as PAS and Raman spectroscopy can thus be effective in revealing the variety of different types of defects present in actinide oxides.<sup>378</sup>

### 3.1.2. Intrinsic Point Defects: Characterization and Modeling.

For homogeneously distributed intrinsic defects, standard positron techniques can also be used to characterize vacancy-type point defects and small clusters. PAS measurements have been applied to characterize defects in oxidized uranium metal,<sup>379</sup>  $\text{UO}_2$  and  $\text{ThO}_2$  powders,<sup>380–382</sup> and doped  $\text{UO}_2$ .<sup>383</sup> Changing the U concentration strongly modifies the density and size of U vacancies as revealed from PALS and DBS measurements. There is strong evidence that doping  $\text{UO}_2$  with metal oxides can increase the grain size in fresh fuel, leading to enhanced fission gas retention.<sup>10–13</sup> However, it is not clear whether doping has an influence on intergranular intrinsic point defects. From a phonon transport perspective, the presence of intrinsic point defects is important because they effectively scatter phonons. Chollet et al. used PALS to characterize point defects in Cr- and Al-doped  $\text{UO}_2$ .<sup>383</sup> The PALS measurements presented in Figure 17 reveal that doping with Cr and Al using the Advanced Doped Pellet Technology (ADOPT) leads to a large number of vacancies and complete positron trapping.

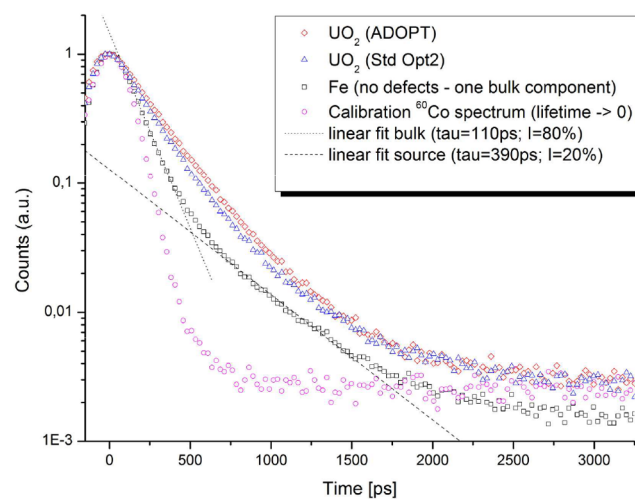


**Figure 17.** Positron lifetime spectra measured for doped and undoped  $\text{UO}_2$  fuel samples, compared with the spectrometer resolution ( $^{60}\text{Co}$  spectrum) and defect-free Fe metal. The doped sample is denoted as the ADOPT (Advanced Doped Pellet Technology) sample, and the undoped sample is denoted as the Std Opt2 (Standard Optima 2) sample. From ref 383. CC BY 4.0.

XRD has proven to be a useful tool to shed light on the nature of point defects in fluorite oxides. Using Vegard's law, which relates the lattice constant to the radius of each ion, the impact of oxygen vacancies in hypostoichiometric  $\text{CeO}_{2-x}$  and trivalent lanthanide (Ln)-doped  $\text{Ce}_{1-x}\text{Ln}_x\text{O}_{2-y}$  on the lattice constant has been well-documented.<sup>384</sup> Similar analysis has been applied to Ln-doped and nonstoichiometric  $\text{UO}_2$ .<sup>385</sup> The ionic radii for different charge states of Ce, U, and Ln agree well with those tabulated.<sup>386</sup> However, because X-ray diffraction provides an average lattice constant, it is often difficult to tell whether off-stoichiometric defects are isolated point defects or combine into larger clusters or even precipitate into different phases. To address these shortcomings, researchers have started to combine XRD with first-principles models to delineate between different scenarios. Recently *ab initio* methods have been implemented to further investigate the impact of the charge state of defects on the relaxation volume of the defected cell, which is expected to be related to the radii of the associated ionic representation of defects.<sup>387</sup> Furthermore, more careful analysis of the lattice constant in nonstoichiometric  $\text{UO}_2$  considering the possibility of different defect charge states using thermodynamics has suggested that uranium vacancies are absent in  $\text{UO}_{2+x}$ .<sup>388</sup>

The impacts of defects in nonstoichiometric and doped  $\text{UO}_2$  on Raman spectra has been investigated in several studies.<sup>377,389,390</sup> Raman spectra of the pristine samples exhibit two primary peaks. The first peak at  $445\text{ cm}^{-1}$  is attributed to phonons with  $T_{2g}$  symmetry that are also visible in neutron scattering measurements. The second peak at  $1150\text{ cm}^{-1}$  is the second-order Raman peak corresponding to the second harmonic of the LO mode located at  $575\text{ cm}^{-1}$  and thus is denoted as the 2LO peak. Upon introduction of trivalent lanthanides into  $\text{UO}_2$ , a broad feature centered around  $560\text{ cm}^{-1}$  was reported.<sup>377</sup> Detailed analysis of this feature suggested the presence of two closely located peaks at  $540$  and  $575\text{ cm}^{-1}$ . The first was attributed to oxygen vacancies that emerged because of the trivalent nature of the dopants and the latter was attributed to Raman activation of the LO mode caused by symmetry breaking. Oxygen-rich  $\text{UO}_2$  and oxidized  $\text{U}_{1-x}\text{Ln}_x\text{O}_{2-y}$  exhibit defect peaks, the most prominent of which is located at  $630\text{ cm}^{-1}$  and is attributed to oxygen interstitials forming cuboctahedral clusters such as in  $\text{U}_4\text{O}_9$ .<sup>389,390</sup> All of these studies suggest that presence of the peaks can be used as an indication of particular defect types and that the peak intensities can be related to the defect concentrations.

The above examples illustrate that the state of defects in oxides can be more complex than just dispersed vacancies, self- or impurity interstitials, and substitutional impurities. The presence of point defects is also often associated with other electronic carriers such as electrons and holes. Thermodynamic modeling of equilibrium defect disorder can capture these carriers simultaneously with the atomic defects themselves. Under irradiation, however, this goal is far from complete. Here we review the equilibrium point defect disorder calculations focusing on  $\text{UO}_2$  and  $\text{ThO}_2$ .

$\text{UO}_2$  can exist in the form  $\text{UO}_{2\pm x}$ , where  $x$  denotes the deviation from the reference stoichiometric state  $\text{UO}_2$ . The finding that  $\text{UO}_2$  can be off-stoichiometric agrees with experimental data on oxygen partial pressure against O/U ratio published by Gúeneau et al.,<sup>391</sup> who calculated O/U ratios of up to 2.2 for temperatures ranging from 800 to 2500 K. For  $\text{ThO}_2$ , the phase diagram reported by Agarwal and Parida<sup>392</sup> based on published data<sup>393–395</sup> shows the oxide system to exist as a hypostoichiometric oxide above 1300 K. Past work by

Murphy et al.<sup>396</sup> and Bergeron et al.<sup>397</sup> investigated the off-stoichiometric properties of  $\text{ThO}_2$  by DFT simulations using the CASTEP code and thermodynamic modeling, respectively, and showed  $\text{ThO}_2$  to exhibit hypostoichiometry.

Point defect disorder models for oxides predict the concentrations of point defects, electrons, and holes under prescribed temperature and oxygen pressure conditions. A typical model is based on minimizing the Gibbs free energy of the defective oxide subject to the constraint of electroneutrality and the prescribed temperature and oxygen pressure. The results of this approach, adapted from Schmalzried,<sup>398</sup> are discussed below.<sup>149,399</sup>

Common Brouwer diagram depictions of oxides show that O vacancy defects dominate the hypostoichiometric regime and are charge-compensated by free electrons. Meanwhile, O interstitial defects dominate the hyperstoichiometric regime and are charge-compensated by free holes in the system.<sup>400</sup> Findings by Hassan et al.<sup>401</sup> on defects in  $\text{UO}_2$  showed domination of U vacancies in the hyperstoichiometric regime of  $\text{UO}_2$  instead of O interstitial defects. Subsequent work by other authors involved further investigation of the specific conditions in which this case occurs. For instance, Cooper et al.<sup>402</sup> found that when vibrational entropy is omitted, O interstitials are predicted to be the dominant mechanism of excess oxygen accommodation over only a small temperature range (1265–1350 K). Conversely, when vibrational entropy is included, O interstitials dominate from 1165 to 1680 K (Busker potential) or from 1275 to 1630 K (CRG potential). Below these temperature ranges, excess oxygen is predicted to be accommodated by U vacancies, while above them the system is hypostoichiometric, with oxygen deficiencies accommodated by O vacancies.<sup>402</sup> A similar deduction was made by Soulié et al.,<sup>403</sup> who found that at high temperature O interstitials are dominant, either in isolated form or in clusters depending on the deviation from stoichiometry. They predicted that at temperatures lower than 1300 K, U vacancies would be dominant in the near-stoichiometric material. As shown in the hyperstoichiometric regime, there is ongoing debate with respect to the defect—U vacancy or O interstitial—that is ultimately responsible for this stoichiometry.

$\text{ThO}_2$  has been found to exist mostly as a hypostoichiometric oxide. Murphy et al.<sup>396</sup> predicted the hypostoichiometric regime to be characterized by O vacancy defects that are charge-compensated by conduction-band electrons. Their simulations also highlighted the importance of the poroxo-oxygen interstitial defect, which is predicted to form with a significantly higher concentration than octahedral O interstitial defects under hyperstoichiometric conditions.  $\text{ThO}_2$  is hypostoichiometric when subjected to high temperatures (2400–2655 K).<sup>399</sup> It was found that the extent of hyperstoichiometry in the (Th,U) $\text{O}_2$  system depends strongly on the temperature and oxygen partial pressure.<sup>399</sup>

In summary, extensive work has been done to study the thermodynamics of oxides. However, there is still much work ahead in this field. For instance, the study of the effect of vibrational entropy is relatively incomplete and has not yet been extended to study the thermodynamics of mixed oxides. Proper calculation of the entropy of formation of defects must take into consideration its temperature dependence. However, this does not seem to be the practice followed in computing the internal energy of formation, where the defect formation energies are often computed at 0 K. Interestingly, the lattice vibrational information used to compute the entropy of formation and its

dependence on temperature can be used to properly compute the same for the internal energy of defect formation.

### 3.2. Irradiation-Induced Defects

The complexity of the radiation environment associated with nuclear fuels brings about a rich spectrum of defects. This includes defects created directly by fast neutron damage<sup>404</sup> and high-energy fission products,<sup>329</sup> defects created by alpha decay of radioactive actinide isotopes,<sup>329,405</sup> and defects created by beta and gamma decay. However, damage caused by high-energy fission fragments is the most significant damage source by orders of magnitude. After the damage event, the lattice contains isolated fission product atoms, point defects, and to a lesser degree small defect clusters.<sup>302</sup> Over time and at temperature, these defect populations evolve to form a rich spectrum of defects ranging from point defects to large clusters. As a surrogate to damage caused by neutrons, ion beam irradiation has proven to be a convenient approach to separate the effects of specific defects on thermal transport. Irradiation with proton (or He) beams provides relatively flat damage profiles over tens of micrometers (or close to 10  $\mu\text{m}$ ) at ion energies of a few megaelectronvolts, which are sufficiently thick for modern thermal transport measurements.<sup>29,42,315,406,407</sup> Moreover, proton irradiation has been shown to be an effective means for producing irradiated microstructures comparable to those produced by neutron irradiation.<sup>408</sup> This is a very rich field of research, and providing a comprehensive, historical review is well beyond the scope of this article. Instead, in this section we present a review of the main findings and open issues, with the intent of identifying new opportunities for impactful research.

**3.2.1. Characterization Techniques.** In section 3.1.1, we discussed two underutilized techniques for characterization of point defects. Here we focus on two techniques that show promise for characterization of larger-scale defects that form due to clustering: analytical TEM and atom probe tomography (APT). For irradiated metals, these two characterization techniques are starting to be used in a correlative fashion. Extending correlative studies to oxides is an area of research with tremendous opportunities.

**3.2.1.1. Analytical Transmission Electron Microscopy.** Conventional TEM has been widely used to study extended defects, dislocation loops, and cavities in irradiated actinide oxides and their nonradioactive surrogates. A variation of conventional TEM, scanning transmission electron microscopy (STEM), involves raster scanning of a tightly focused ( $\sim 0.1$  nm) electron beam over a sample to form an image. This configuration makes STEM suitable for analyzing local chemistry using spectroscopy methods. Electron energy loss spectroscopy (EELS) and energy-dispersive X-ray spectroscopy (EDS) are powerful tools for imaging of radiation-induced defects, phase changes, and small-scale changes in composition. EDS, a relatively simple technique to apply, is well-suited to measure elemental composition and has been used extensively to characterize phases and fission products in nuclear fuels.<sup>328,409,410</sup> However, EDS is not capable of measuring changes in stoichiometry, which is required for understanding how interfaces, such as grain boundaries, influence the local stoichiometry.

EELS has been successfully used to identify the oxidation states of U and Ce in their oxides. Phonon scattering at interfaces such as grain boundaries may significantly affect the thermal transport of materials. The grain boundary chemistry in  $\text{CeO}_2$  has been revealed using STEM/EELS mapping of the  $\text{Ce M}_{4,5}$

edge, which reflects the  $3d \rightarrow 4f$  transitions in Ce.<sup>407,411–414</sup> The relative intensities of  $\text{M}_4$  and  $\text{M}_5$  are characteristic of the  $4f$  shell occupancy and have been used to determine oxidation state of Ce and the O vacancy concentration. The O vacancy concentration at grain boundaries depends on the boundary character: the more distorted the boundary, the more oxygen vacancies it forms. Similarly the U  $\text{M}_{4,5}$  edge, which results from  $3d \rightarrow 5f$  transitions in U, has been used to characterize the oxidation state of U.<sup>415,416</sup> Compared with the Ce  $\text{M}_{4,5}$  edge, the U  $\text{M}_{4,5}$  edge at higher energy loss has a smaller signal, thus requiring long collection times to obtain an appropriate signal-to-noise ratio, which presents experimental difficulties due to beam drifting. This leads to reduced spatial resolution, and the overall ability to measure chemical changes at the nanometer and atomic scales is affected. Recently, atomic-scale EELS for U using the U  $\text{M}_{4,5}$  edge has been achieved thanks to large probe convergence angles, high currents, and small probe sizes in modern aberration-corrected microscopes.<sup>417</sup>

**3.2.1.2. Atom Probe Tomography.** APT relies on field evaporation of the specimen to produce a three-dimensional (3D) reconstruction containing atom-by-atom position-sensitive composition information. The use of a laser (as opposed to the conventional voltage APT mode) is necessary to induce field evaporation in semiconducting and insulating materials.<sup>418</sup> Effective field evaporation in oxides requires uniform laser absorption and efficient dissipation of thermal energy, which are highly dependent upon the optical properties, thermal properties, and surface chemistry of the oxide.<sup>419</sup> The field evaporation parameters must therefore be tailored or optimized in each oxide for accurate chemical quantification.<sup>420–426</sup> Poorly optimized field evaporation parameters can produce thermal artifacts, surface diffusion, and preferential evaporation that ultimately degrade the accuracy of APT quantitative compositional analysis.<sup>427</sup>

There is no clear trend in the optimal APT field evaporation parameters for nuclear fuel oxides and their surrogates. For example,  $\text{CeO}_2$  can yield sufficient field evaporation with low-energy laser pulses,<sup>422</sup> whereas  $\text{UO}_2$  requires moderate laser energies<sup>420</sup> and  $\text{ThO}_2$  requires high laser energies with a low specimen temperature.<sup>255</sup> In  $\text{CeO}_2$ , the use of higher laser energy and lower base temperature results in degradation of the mass spectrum resolution.<sup>422</sup> Recent work has used Bayesian expectation–maximization statistical methods to assign ion identities to data convoluted in thermal tails, enabling accurate quantification of the chemical composition of thermally affected mass spectra in  $\text{ThO}_2$ .<sup>255</sup> While challenges remain for APT characterization of oxides, there exists considerable opportunity to use APT in a correlative fashion with analytical TEM.

**3.2.1.3. Correlative TEM–APT Characterization.** While TEM and APT have several advantages for characterizing composition at the nanoscale, each technique has well-known limitations.<sup>428–432</sup> TEM/STEM is excellent in crystallographic/structural analysis. Grain orientations, phase structure, and defects can be identified or visualized using electron diffraction and high-resolution imaging techniques. The grain orientations may also be measured by APT, but the spatial resolution of APT datasets is determined by the regularity of the field-evaporation sequence. The dependence of field evaporation on the grain orientation and local bonding state may reduce the spatial resolution in the reconstructed 3D atom maps, especially at locations of defects or interfaces.<sup>428,433</sup>

STEM/EDS has been routinely used to quantify local chemical compositions at the nanoscale. The elemental

sensitivity of EDS depends on the atomic number of the element. The quantification of light elements such as O and N is based on low-energy X-rays, and K peaks and their  $k$ -factors depend on X-ray absorption. Because of inaccuracy of the absorption correction due to self-absorption of low-energy X-rays, their poor detection efficiency, and the low fluorescence yield, quantification of light elements is very challenging. Compared with EDS, EELS tends to work better for elements of relatively low atomic number. However, quantification of EELS spectra relies on obtaining single scattering profiles, which can be realized only when very thin samples are used. In thicker samples, multiple inelastic scattering changes the edge shapes and intensities, and therefore, quantification errors can be introduced.<sup>434</sup> When the size of the target defect is smaller than the sample thickness, the measured composition is an effective composition that is an average over the sample thickness and may not be representative of the target defects.

Quantitative elemental analysis at the near-atomic scale using APT is rather robust because ionic species in most cases can be simply identified according to their mass-to-charge ratio, although there are intrinsic challenges associated with quantification of O especially from nanosized features. It is well-known that the concentration of O in materials is strongly dependent on the analysis parameters of APT, such as the laser wavelength, laser pulse energy, and field condition of the specimen.<sup>435,436</sup> For example, at high laser energies, metal atoms are preferentially evaporated, whereas O atoms diffuse and desorb as a result of inhomogeneous thermal absorption of the laser, leading to inaccuracies in the measured composition. In addition, APT measures chemical composition in only a very localized volume of  $\sim 10^6$  nm<sup>3</sup>, in comparison with the volume  $\sim 10^{10}$  nm<sup>3</sup> used for STEM/EDS/EELS measurements in TEM.<sup>430</sup>

Spatially correlated TEM and APT studies are of significance to understand the effects of radiation in nuclear materials. Recently researchers have investigated combining APT and STEM, with the advantages of one technique offsetting the limitations of the other. Wang et al.<sup>432</sup> quantified chemical compositions around nanovoids in NiCoCr solid solution alloys. Figure 18 shows an example of correlative imaging using STEM and APT. Lach et al.<sup>431</sup> characterized the radiation-induced segregation around grain boundaries and dislocation loops together with precipitation in 304 stainless steel. To date, these correlative studies have been applied to metals, and thus, while there is great potential for extending correlative studies to oxides, there exist considerable challenges.

**3.2.2. Irradiation-Induced Point Defects.** Near room temperature in low damage ranges ( $<0.1$  dpa), the formation of extended defects is limited by limited diffusion. Several reports have applied Raman spectroscopy to characterize point defects in irradiated fluorite oxides.<sup>437–439</sup> One notable study investigated depth-resolved radiation damage upon irradiation of UO<sub>2</sub> by 25 MeV He<sup>2+</sup> ions.<sup>438</sup> The ion-impacted region of the cross-sectional scan exhibited a reduction in intensity of the T<sub>2g</sub> peak at 445 cm<sup>-1</sup> and the emergence of new defect peaks at 527, 574, and 634 cm<sup>-1</sup>. The peaks at 527 and 634 cm<sup>-1</sup> were attributed to oxygen vacancies and interstitials, respectively, and the peak at 574 cm<sup>-1</sup> was attributed to activation of the Raman-forbidden LO peak caused by symmetry breaking. A cross-sectional line scan along the incident direction of the implanted He ions was performed and showed that the intensity of the T<sub>2g</sub> peak decreases and the intensity of the defect peak increases proportional to the amount of depth-dependent displacement

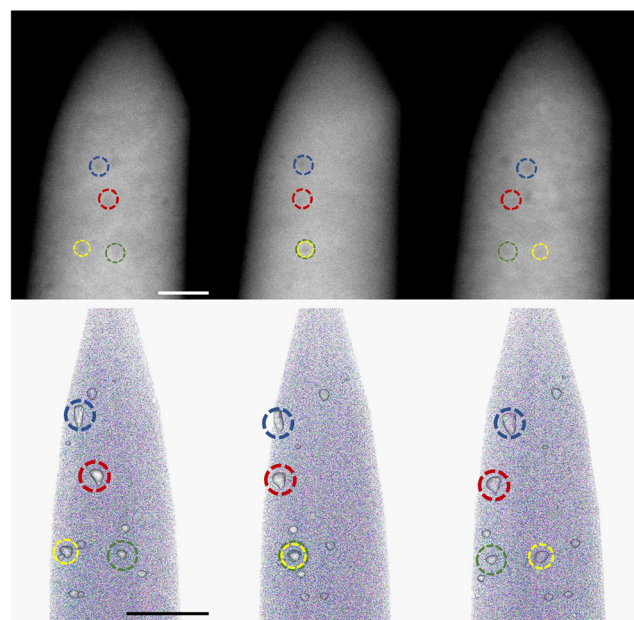


**Figure 18.** STEM and APT images acquired for a needle-shaped NiCoCr specimen at different rotation angles. The scale bar for both sets of images is 40 nm. From ref 432. CC BY 4.0.

damage predicted using Stopping and Range of Ions in Matter (SRIM) calculations.<sup>438</sup> In a more recent report, it was postulated that the LO peak is due to defects on the uranium sublattice and associated with changes in the charge state of uranium from 4+ to either 3+ or 5+.<sup>439</sup>

Similar measurements have been performed in light-ion-irradiated ThO<sub>2</sub>.<sup>29,368</sup> In 2 MeV proton-irradiated ThO<sub>2</sub>, four prominent peaks at 515, 535, 585, and 630 cm<sup>-1</sup> were identified.<sup>29</sup> The latter three are similar to the defect peaks in UO<sub>2</sub>, whereas the peak at 515 cm<sup>-1</sup> has not been reported in other fluorite oxides. Similar peaks were observed at 514, 539, 590, and 622 cm<sup>-1</sup> for ThO<sub>2</sub> irradiated with 21 MeV He<sup>2+</sup>, but they were not identified as Raman peaks by the authors and instead were attributed to luminescence.<sup>368</sup>

XRD has been applied to monitor microstructure evolution in irradiated UO<sub>2</sub>.<sup>287,440</sup> During isochronal annealing of neutron- and  $\alpha$ -particle-irradiated UO<sub>2</sub>, different stages of defect recovery were identified. These stages were attributed to mobility of different defect types. These results enabled the determination of migration barriers and the relaxation volume of Frenkel pairs without clear differentiation between the uranium and oxygen sublattices. Similar measurements have been applied to  $\alpha$ -particle-irradiated CeO<sub>2</sub> and PuO<sub>2</sub>.<sup>286</sup>

For self-irradiation studies involving doping with a radioactive isotope, traditional PAS can be used to measure the vacancy-type defect distribution throughout the bulk. One such example used PALS to characterize the damage generated by  $\alpha$  self-irradiation in UO<sub>2</sub>.<sup>441</sup> This study suggested that the point defects observed using PALS correspond to uranium vacancies. From a phonon transport perspective, defects in the uranium and oxygen sublattices can influence phonon scattering in significantly different ways. In the case of high-energy electron and ion irradiation, defects are generated in the bulk of the samples, and traditional PALS was successfully applied to study defects in CeO<sub>2</sub> and UO<sub>2</sub> using this approach.<sup>442</sup> Additionally, coupling of experimental results to a DFT description revealed detailed information about the structure of vacancy-type defects

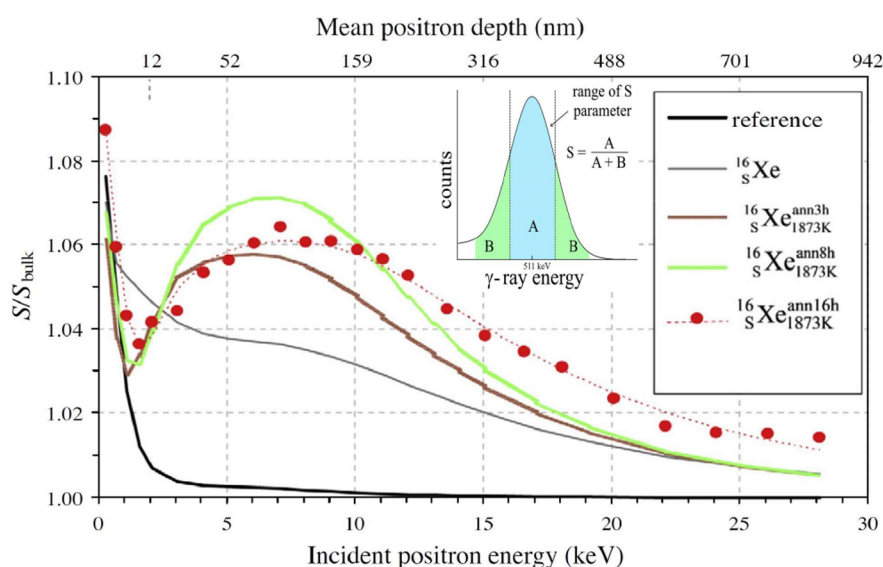


**Figure 19.** Defect parameter  $S$  as a function of depth in  $\text{UO}_2$  for a reference sample, a Xe-implanted sample, and post-Xe-implantation annealed samples. The inset is a schematic illustrating how  $S$  is extracted from the 511 keV peak in DBS. The radiation fluence for the implanted samples, indicated by a superscript “16,” was  $1 \times 10^{16}$  Xe  $\text{cm}^{-2}$ . Adapted with permission from ref 444. Copyright 2012 Elsevier B.V.

in  $\text{UO}_2$ . Wiktor et al.<sup>443</sup> used this approach to reveal that the dominant irradiation-induced defect in 45 MeV alpha-irradiated  $\text{UO}_2$  is a bound Schottky defect of neutral  $\text{V}_\text{U} + 2\text{V}_\text{O}$  trivacancies.

In the early 1990s, researchers first demonstrated the applicability of using slow positrons to perform depth-resolved studies of ion-implanted  $\text{UO}_2$ .<sup>445</sup> More recent studies applied VEDBS to characterize vacancy-type defects in electron- and light-ion-irradiated  $\text{UO}_2$ .<sup>446–449</sup> In one study involving electron irradiation of  $\text{UO}_2$ , the results revealed that U-related vacancies were formed when the irradiation energy was stepped from 1 to 2.5 MeV.<sup>446</sup> In another study involving 1 MeV He implantation, it was found that the nature of the irradiation-induced vacancy-type defects did not change with the fluence.<sup>447</sup> VEDBS was also applied to investigate the depth distributions of defects in Xe-implanted  $\text{UO}_2$ . As an example, Figure 19 depicts the defect parameter  $S$  extracted from DBS measurements as a function of depth for unirradiated  $\text{UO}_2$  (reference sample), a Xe-implanted sample, and post-Xe-implantation annealed samples. The large nonlinear increase in  $S$  indicates the formation of Xe bubbles after annealing.

**3.2.3. Dislocation Loops.** At intermediate temperatures and low damage levels, ion irradiation may create both point defects and dislocation loops.<sup>28,29,315</sup> Detailed TEM and atomic-resolution STEM imaging shows the dislocation loop characteristics of single-crystal  $\text{ThO}_2$  (Figure 20).<sup>303</sup> They are interstitial faulted loops or Frank loops with a Burgers vector,  $\mathbf{b}$ , of  $1/3\langle 111 \rangle$  and a habit plane of  $\{111\}$ . The large extended strain field around faulted loops scatters phonons significantly, leading to a larger reduction in the thermal conductivity compared with perfect loops.<sup>315</sup> In neutron- and ion-irradiated  $\text{UO}_2$ ,  $\text{ThO}_2$ , and  $\text{CeO}_2$ , both faulted loops with  $\mathbf{b} = 1/3\langle 111 \rangle$  and perfect loops with  $\mathbf{b} = 1/2\langle 110 \rangle$  are found. MD simulations<sup>298,303,326</sup> showed that mainly  $1/3\langle 111 \rangle$  Frank loops are energetically favorable when the loop size is small (several nm) and that  $1/2\langle 110 \rangle$  perfect loops are preferred when the loops grow. Thus, there must be an unfauling process of loops under irradiation, and the formation of perfect loops can be ascribed to a reaction between a Frank partial and a Shockley partial.<sup>298,303,326</sup> However, this

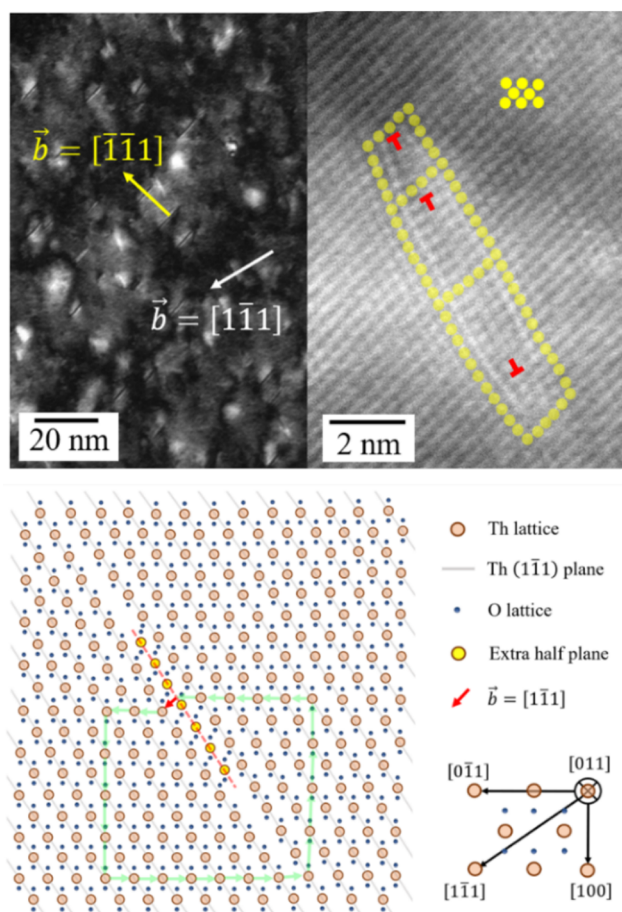


**Figure 20.** (top left) Weak-beam dark-field TEM image and (top right) atomic-resolution STEM image of dislocation loops in  $\text{ThO}_2$ . (bottom) Schematic representation of a  $1/3\langle 111 \rangle$  Frank partial dislocation loop, showing an extra half-plane and the Burgers vector  $\mathbf{b}$  as viewed along the  $[011]$  zone axis. Adapted with permission from ref 303. Copyright 2021 Elsevier B.V.

unfaulting process during loop growth has not been directly observed in actinide oxides and their surrogate, CeO<sub>2</sub>.

In the past decade, the formation and evolution of extended defects, dislocation loops, and bubbles under heavy ion irradiation have also been well-studied using in situ ion irradiation facilities such as the Intermediate Voltage Electron Microscope (IVEM) at Argonne National Laboratory<sup>295,296,312,314</sup> and JANNuS-Orsay in France.<sup>309,317,318,324–326</sup> The size and density of dislocation loops increase with the irradiation dose until the density saturates, after which the dislocation loops start to transform into dislocation segments and tangled networks at higher doses through coalescence and coarsening mechanisms.<sup>295,296,312,313</sup> Both dislocation loops and cavities can nucleate under heavy-ion irradiation at room temperature,<sup>311,314,318</sup> which is different than the case with light-ion (e.g., proton) irradiation. At a low irradiation temperature, some dislocation loops can nucleate directly at the clusters produced in cascades, and such a process does not require U interstitials and U vacancies to be diffusive. Electrons or light ions such as protons produce damage as isolated Frenkel pairs or in small clusters, while heavy ions and neutrons produce damage in large clusters. The direct nucleation of extended defects at small clusters is more difficult than at large clusters, which may explain why loops do not form under proton irradiation at room temperature. For in situ irradiation, it is noted that the TEM samples are very thin (~100 nm) and the surface is a strong sink for irradiation-induced defects, which may impact defect evolution. For those samples prepared by focused ion beam (FIB) milling, FIB damage may contribute to the defect evolution.

**3.2.4. Cavities and Precipitates.** Defects that are large in comparison with the wavelength of the phonons responsible for thermal transport can have a significant impact on thermal conductivity. While voids and bubbles can be formed under heavy-ion irradiation, precipitates can form through coalescence of impurities, doping atoms, and fission products. The formation of these large-scale defects typically requires long-range diffusion. While heavy-ion irradiation has been used to study fission gas diffusion in UO<sub>2</sub>,<sup>310,311,314,317</sup> ThO<sub>2</sub>,<sup>299</sup> and Th<sub>1-x</sub>U<sub>x</sub>O<sub>2</sub>,<sup>300</sup> fission gas bubble nucleation, growth, migration, and self-organization in ThO<sub>2</sub> and Th<sub>1-x</sub>U<sub>x</sub>O<sub>2</sub> have not yet been studied in detail.

**3.2.4.1. Cavities.** Cavities, including voids and fission gas bubbles, have been characterized extensively in UO<sub>2</sub> and CeO<sub>2</sub>. Generally, TEM has been used to characterize bubble sizes and distributions,<sup>308,450–453</sup> while techniques such as secondary ion mass spectroscopy (SIMS)<sup>454</sup> and X-ray absorption spectroscopy (XAS)<sup>455–457</sup> have been used to quantify gas pressures.

Michel et al.<sup>452</sup> performed one of the earliest in situ TEM studies of bubble evolution in UO<sub>2</sub> irradiated using 390 keV Xe ions. Their results confirmed the rapid formation of a population of small (<1 nm) bubbles. The novel result was the fact that the bubble concentration reached a nearly asymptotic value. Although this experiment provided invaluable data against which cluster dynamics models may be assessed, no clear physical explanation was found for saturation of the bubble concentration. Theoretical and experimental work is currently ongoing to elucidate this longstanding conundrum.

Using Kr irradiation, He et al.<sup>311</sup> showed the bubble size to be a weak function of ion dose but strongly dependent on the temperature. Kr bubble formation at room temperature was observed for the first time, indicating either that U vacancies are mobile at room temperature or that Kr bubbles may directly

nucleate at the vacancy clusters produced during cascades, with such a process not requiring Kr and U vacancies to be diffusive. In a similar study involving Xe irradiation of UO<sub>2</sub> single crystals, it was shown that small bubbles (1–2 nm) were formed at room temperature, indicating that bubble formation does not require long-range diffusion of Xe atoms or U vacancies.<sup>314</sup> These studies involving Kr irradiation indicating bubble formation at room temperature are to be contrasted with another study involving gas atom precipitation in CeO<sub>2</sub> at room temperature and 600 °C.<sup>295</sup> In that study, no gas bubbles were observed at room temperature.

In a study by Ye et al.<sup>296</sup> that looked at the effect of Xe irradiation on cavity formation in UO<sub>2</sub> and CeO<sub>2</sub>, it was suggested that implanted Xe ions were trapped in vacancy clusters and aggregated into bubbles at elevated temperature. The size and density of those features are comparable to the fission gas bubbles in low-burnup UO<sub>2</sub> fuel in a similar temperature range. Kinetic Monte Carlo analysis revealed that the O mobility in UO<sub>2</sub>/CeO<sub>2</sub> is substantially higher under hypostoichiometric conditions (MO<sub>2-x</sub>) than under hyperstoichiometric conditions (MO<sub>2+x</sub>).

Void formation has been studied using Au irradiation of thin UO<sub>2</sub> foils. Because most of the Au passes through the foil, this irradiation regime creates only ballistic damage. In one study, Onofri et al.<sup>327</sup> found that void nucleation is a heterogeneous process since new voids do not involve long-range diffusion of point defects and gas atoms. In a related study, Sabathier et al.<sup>458</sup> suggested that heterogeneous nucleation of voids was induced by energetic cascade overlap. Such nanovoids are likely to act as sinks for mobile fission products during reactor operation.

Researchers are now looking beyond TEM methods to characterize fission gas bubbles. One of the early studies in this area involved the use of APT to map the Kr profile in ion-irradiated UO<sub>2</sub> as a function of depth.<sup>311</sup> The Kr concentration measured by APT was considerably smaller than that predicted by SRIM. This was attributed to the gas being lost to the vacuum within the analysis chamber and not registered by the detector. However, using APT to directly characterize bubbles can be problematic. For instance, aberrations are associated with tomographic reconstructions near surfaces (internal and external) and may change the evaporative characteristics of atoms. As mentioned in a [previous section](#), correlative studies that utilize STEM and APT are beginning to demonstrate promising results tied to characterization of bubbles in metallic samples. A recent study by Perrin-Pellegrino et al.<sup>459</sup> extended this approach to oxides. Using APT in concert with TEM revealed the existence of nanoclusters enriched in Xe with a size and density comparable to bubble populations observed with TEM.

Coincidence Doppler broadening spectroscopy (CDBS) is another powerful tool to characterize the chemistry of gas bubbles, identify the chemical environments around vacancies, and probe atomic-scale precipitates.<sup>460</sup> Nagai et al.<sup>461</sup> employed CDBS to detect the ultrafine precipitation of Cu impurities in nuclear reactor pressure vessel (RPV) steel. The work revealed that positrons can be trapped by embedded ultrafine particles to form quantum-dot-like positron states, thus enabling the detection of atomic-scale precipitates. In general, correlative studies using PAS and TEM will be useful to characterize the size, size distribution, and local chemistry of defects ranging from single vacancies to clusters and large voids.<sup>462,463</sup> This will be crucial to understanding defect formation in the early stages and the mechanisms of defect accumulation and recombination.

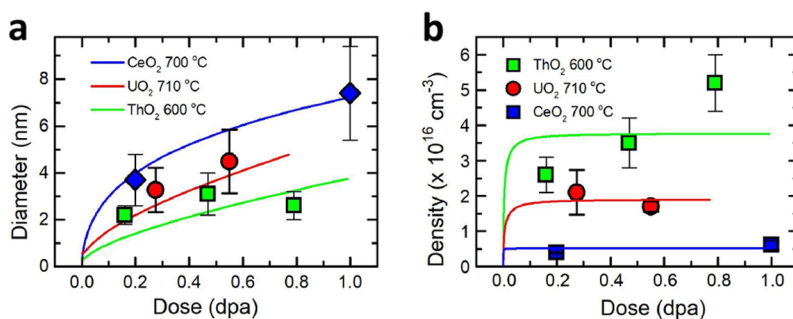


**Figure 21.** Comparison of dislocation loop evolution in proton-irradiated CeO<sub>2</sub>, ThO<sub>2</sub>, and UO<sub>2</sub> obtained using rate theory modeling (solid lines) to the results of experimental measurements (symbols). The UO<sub>2</sub> data were taken from ref 28. The ThO<sub>2</sub> data were taken from ref 132. The CeO<sub>2</sub> data were taken from ref 315.

**3.2.4.2. Precipitates.** Precipitation in irradiated oxide fuels can have a significant impact on physical properties, including swelling, melting point, and thermal conductivity. Moreover, the irradiation-induced aggregation of solute species into precipitates can bring about a cooperative effect wherein the integrated impact on the thermal conductivity of impurity atoms in solution differs from that of precipitates composed of the same elemental species. Characterization of precipitates in oxide fuels and surrogates is commonly performed using TEM, APT, and light-source techniques.

In a recent study involving emulated spent fuel, Jiang et al.<sup>464</sup> used TEM and APT to study thin films of CeO<sub>2</sub> doped with metallic fission products. They found a uniform distribution of doped metals within the as-grown film. Pd particles with sizes of ~3 nm appeared near dislocations after He irradiation. Annealing at 1073 K in air led to the formation of precipitates of Mo and Pd at grain boundaries, and further annealing resulted in precipitate coarsening.

The structure of the precipitate (e.g., crystalline vs amorphous) can have a significant impact on phonon scattering and transmission through the precipitate. In addition to studies that investigated the composition of precipitates, several studies have addressed the structure of precipitates. In one study, the local atomic structure of chromium-bearing precipitates in chromia-doped uranium dioxide was investigated by combining microbeam XRD and XAS.<sup>465</sup> The XRD data indicated that the chromia precipitates contained structural disorder, and  $\mu$ -XAS results provided insight into the oxidation state of the chromium. In a study targeting fission gas bubble formation, Yun et al.<sup>466</sup> found solid Xe precipitates in irradiated 5% La-doped CeO<sub>2</sub>. The fact that these precipitates formed only at very high doses indicated a dose threshold in their formation.

Oxide fuels are also known to exhibit steep radial gradients in burnup, which can have significant implications for chemical clustering and segregation. Bachhav and co-workers<sup>467</sup> recently demonstrated a novel APT-based approach to determine local burnup in irradiated fuels. This method, which relies upon isotopic ratios of <sup>235</sup>U, <sup>236</sup>U, <sup>238</sup>U, <sup>239</sup>Pu, and <sup>237</sup>Np, provides localized understanding of U enrichment and local burnup. In a follow-on study,<sup>468</sup> the team linked burnup to local fission product chemistry. By conducting APT at the center and on the edge of an irradiated UO<sub>2</sub> pellet, they observed burnup-related differences in the irradiation-induced nucleation of metallic fission product Mo–Tc–Ru–Rh–Pd precipitates. The precipitates were larger at the pellet edge than in the center.

### 3.3. Modeling of Defect Clustering

Several methods are used to model defect evolution. MD simulations can be used to investigate defect evolution at very short time scales and provide useful information on initial conditions used for modeling approaches that target long time evolution. For scales of interest to the materials discussed in this review, there are two main modeling methods: kinetic Monte Carlo and rate theory models. While kinetic Monte Carlo retains spatial correlation, all possible events and their rates must be known in advance. Conversely, rate theory does not retain spatial correlation but does exhibit predictive capability. Rate theory models have been used extensively for metallic systems; however, more development is required for application to oxide nuclear fuels. Accordingly, our focus in this section is on reviewing recent work and identifying future opportunities associated with rate theory models.

Two types of rate theory models exist in the literature to model point defect and cluster evolution in irradiated oxides. The first is a simplified model designed to yield the time evolution of point defects interacting with a mean density of features such as loops and voids at an average evolving size. The second, termed cluster dynamics, is one in which the densities of clusters of all sizes evolve simultaneously with point defects. These models are briefly reviewed below.

#### 3.3.1. Simple Rate Theory Model of Defect Evolution.

Simple rate theory models consider three processes: point defect generation by irradiating particles, mutual recombination of interstitial–vacancy pairs, and defect clustering into dislocation loops and voids.<sup>297,328,469</sup> However, for low-dose proton irradiation at intermediate temperatures, void nucleation may be suppressed for kinetic reasons in some oxides (e.g., ThO<sub>2</sub>), and loop nucleation dominates because of the relatively higher mobility of interstitials. A rate theory for such a situation consists of a set of ordinary differential equations describing the time rates of changes in the concentrations  $C_i$  of various defect types:<sup>328</sup>

$$\frac{dC_i}{dt} = G - S_{ij}C_iC_j \quad (4)$$

where  $i$  and  $j$  denote defect types, including interstitial O ( $O_i$ ), oxygen vacancy ( $V_O$ ), interstitial metal ( $M_i$ ), and metal vacancy ( $V_M$ ) monomers as well as loops (L);  $G$  is the generation rate for monomers and the di-interstitial formation rate for loop nucleation; and the  $S_{ij}$  are rate constants for mutual interactions between defects, including recombination for each ( $O_i$ ,  $V_O$ ) and ( $M_i$ ,  $V_M$ ) cation pair and di-interstitial formation for two cation interstitials. These di-interstitials act as the only source of

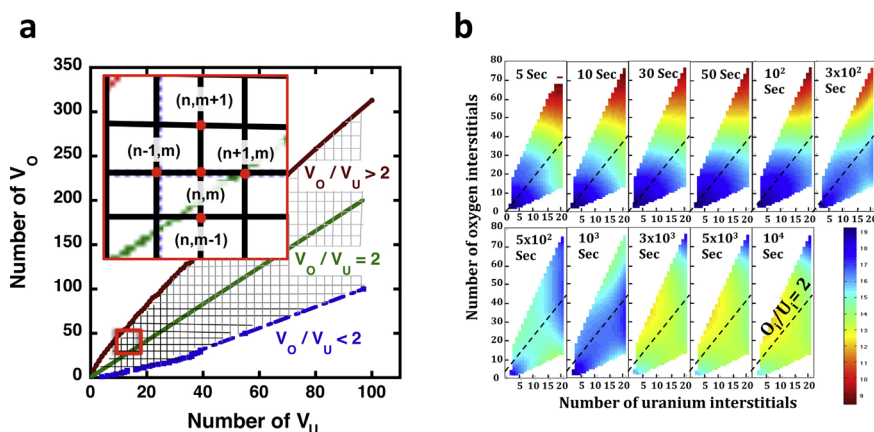


**Figure 22.** (a) CCS for vacancy loops. The blue and brown lines represent the minimum and maximum number of  $V_O$  that can exist in a cluster with a given number of  $V_U$ . The middle green line represents the 2:1 ratio of  $V_O$  to  $V_U$ . (b) Time evolution of SIA cluster density. Adapted with permission from ref 488. Copyright 2017 Elsevier B.V.

dislocation loop nucleation. Terms  $S_{iL}$  capture absorption of monomers by loops and contribute to the loop size evolution,<sup>328</sup> which is given by

$$\frac{d}{dt} \left( \frac{\pi b}{3\Omega_0} R_L^2 C_L \right) = S_{iL} C_i C_L \quad (5)$$

where  $R_L$  is the loop radius,  $b$  is the magnitude of the Burgers vector,  $\Omega_0$  is the volume per atom, and summation over  $i$  and  $j$  are indicated using Einstein notation. The rate constants  $S_{ij}$  depend on monomer diffusion coefficients and geometrical factors that capture the atomic structures of defects. Expressions for these coefficients can be found in ref 328. Figure 21 compares the predicted evolutions of the loop diameter and loop density in proton-irradiated  $\text{CeO}_2$ ,  $\text{ThO}_2$ , and  $\text{UO}_2$ <sup>29,315,328</sup> to the results of experimental measurements. It can be seen that the loop growth rate and loop concentration are inversely correlated and are proportional to the mobility of cation interstitials in this system. Faster cation mobility promotes faster loop growth, but leads to a lower supersaturated concentration of monomers.<sup>470,471</sup> These results indicate that cation interstitial migration is fastest in  $\text{CeO}_2$  and slowest in  $\text{ThO}_2$ .

### 3.3.2. Cluster Dynamics Approach to Defect Evolution.

The formation of extended defects such as dislocation loops and voids under irradiation results from diffusion and interaction of vacancies and interstitials produced by atomic displacements. This dynamic generation and interaction process may be studied using cluster dynamics (CD), an approach based on chemical reaction rate theory.<sup>472,473</sup> In this approach, the temporal evolution of the density of defect clusters in size space is controlled by the emission and absorption of mobile point defects generated in the collision cascade. The CD approach assumes a uniform distribution of defect clusters of varying sizes and considers that the above-mentioned interactions take place continuously in space and time. CD approaches have been used extensively in the study of radiation-induced defect generation and evolution, including spatially dependent approaches that take into account the local configurations of defects of different sizes.<sup>474–477</sup> However, these spatially correlated approaches have to date found wide use in metallic systems, while mean-field approaches lacking spatial correlation have been applied more readily to oxide fuel materials.<sup>478–480</sup> In either case, the rate at which clusters of a specific size accumulate in the material is obtained as a sum of their generation and depletion rates due to

the absorption and emission of point defects by similar- or different-sized clusters. This approach has been used extensively to study defect evolution in materials like Fe,<sup>481</sup> stainless steel,<sup>482,483</sup> and Zr<sup>484</sup> as a robust multiscale method that takes input from atomistic simulations and successfully predicts the evolution of defect densities over extended length and time scales. In multicomponent systems, the CD framework has been used to study precipitation kinetics in binary<sup>485,486</sup> and ternary<sup>485</sup> alloys.

Irradiation of oxides generates charged point defects of different species in the displacement cascade. For instance, in irradiated  $\text{UO}_2$  the point defects obtained are O self-interstitial atoms (O-SIAs), U-SIAs, O vacancies, and U vacancies, denoted with their nominal charge states as  $\text{O}_i^{2-}$ ,  $\text{U}_i^{4+}$ ,  $\text{V}_O^{2+}$ , and  $\text{V}_U^{4-}$ , respectively. The point defects can also have non-nominal charges (e.g.,  $\text{U}_i^{3+}$ ,  $\text{V}_U^{3-}$ , etc.) depending on the stability of individual ionic species in the irradiated oxide.<sup>401</sup> To make a CD approach tractable, some limits must be placed on the charges and spectrum of cluster sizes considered. Skorek et al.<sup>487</sup> studied the evolution of fission gas bubbles in  $\text{UO}_2$  assuming Schottky defects (i.e.,  $\text{U}_i-2\text{O}_i$  and  $\text{V}_U-2\text{V}_O$  defect complexes are generated in the cascade rather than isolated SIAs and vacancies). They further assumed that the Schottky defect complexes are mobile and hence migrate and agglomerate into clusters having stoichiometric compositions, preserving the charge neutrality of the matrix. The clusters trap fission gas atoms, which are otherwise highly mobile, and impede their rate of escape to grain boundaries. Although the simplified CD model was able to predict the experimentally observed release rate of the fission gas, it did not allow for the matrix to become hyperstoichiometric under irradiation. Later, Khalil et al.<sup>488</sup> used a more detailed mean-field approach that allowed for asymmetric (nonstoichiometric) generation of point defects of different species in the displacement cascade due to their varying displacement energies and also for the possibility of agglomeration of point defects into clusters having nonstoichiometric compositions. They defined the cluster composition space (CCS) for loops, as shown in Figure 22a, by counting the respective point defects (i.e.,  $\text{O}_i^{2-}$ ,  $\text{U}_i^{4+}$  for SIA loops and  $\text{V}_O^{2+}$ ,  $\text{V}_U^{4-}$  for vacancy loops) in the fluorite crystal structure of  $\text{UO}_2$ . The mesh points in Figure 22a represent all possible defect compositions, where each point  $(m, n)$  indicates a vacancy cluster with  $m V_U$  and  $n V_O$  and can move either horizontally or

vertically by interaction (absorption or emission) with U and O defects, respectively. Figure 22b gives the time evolution of SIA clusters at 800 °C and a dose rate of  $9.2 \times 10^{-4}$  dpa/s, which shows off-stoichiometric loop growth at higher doses. Vacancy loops evolve similarly, favoring off-stoichiometric compositions with larger loop sizes. This modified CD model gives detailed insight into the wide range of stoichiometries of defect clusters and their evolution with time. However, a significant source of error in this model may lie in the assignment of binding energies for each defect species. These energies are routinely assigned for defect clusters in pure materials using molecular dynamics, although in reality these too may change as a function of stoichiometry.

While the approach described above relies on the input of defect monomers only, MD simulations of primary radiation damage in the mixed  $\text{Th}_{1-x}\text{U}_x\text{O}_2$  oxide system show that small vacancy and SIA clusters may be produced directly in the damage cascade.<sup>302</sup> Thus, in modified next-generation CD models for oxides, the production rates of small clusters should be provided as input parameters, similar to what is done for monomers. Also, the strict assumption that monomers are the only mobile species in the general CD model<sup>478,488</sup> needs to be discarded. Instead, the spatial and temporal evolution of loops and voids driven by the diffusion of small clusters should be targeted directly. Such a modified CD model can be extended to introduce new terms in the cluster evolution equations that govern the migration of vacancy and SIA clusters. As reviewed by Kohnert and co-workers,<sup>489</sup> spatially resolved cluster dynamics has proven to be useful in modeling the evolution of complex metallic microstructures resulting from defect diffusion. Indeed, such spatially correlated methods are the next logical progression for the CD approach applied to oxide fuel materials.

### 3.4. Grain Boundaries

Here we first look at microstructure evolution in the presence of isolated grain boundaries. Characterization of isolated boundaries is a notably easier task than characterization of boundaries in nanocrystalline materials. Moreover, new experimental tools have enabled studies that target the impact of isolated boundaries on thermal transport. These studies of thermal transport can then be compared with predictions in a one-to-one fashion. An important goal for materials scientists will be to translate understanding of isolated boundaries to nanocrystalline restructured oxide fuel.

**3.4.1. Intrinsic Grain Boundaries.** Grain boundaries can significantly influence microstructure evolution in the environments in which nuclear fuels operate. In addition to providing sinks and sources for defects, grain boundaries can accelerate mass diffusion. Numerous studies have identified accelerated mass transport pathways along grain boundaries in  $\text{UO}_2$  for self-diffusion (i.e., U and O species)<sup>490–494</sup> and diffusion of He.<sup>495</sup> In general, grain boundaries in  $\text{UO}_2$  have a higher concentration of mobile charge carriers than the bulk, leading to enhanced oxygen transport along grain boundaries.<sup>493</sup> The result is highly anisotropic ionic diffusion localized along grain boundaries that is dependent upon the temperature, local structure, and grain boundary character.<sup>493,496</sup>

The impact of grain boundary structure in  $\text{UO}_2$  on segregation has also been studied with MD simulations.<sup>497,498</sup> It was found that high-angle grain boundaries are energetically favored to accommodate Xe versus low-angle boundaries. Motivated by this computational study, Valderrama et al.

investigated segregation of Kr at grain boundaries in ion-irradiated  $\text{UO}_2$ . It was found that high-angle grain boundaries contain substantially more Kr than low-angle grain boundaries. They also found that excess Kr grain boundary segregation leads to bubble formation. In another study targeting bubble evolution in Kr-irradiated  $\text{UO}_2$  during annealing,<sup>310</sup> it was found that the size of intergranular bubbles increased more rapidly than the size of intragranular ones, and bubble-denuded zones near grain boundaries formed in all of the annealed samples at 1000 to 1600 °C. The area density of strong segregation sites in the high-angle grain boundaries is much higher than that in the low-angle grain boundaries. The geometric constraints for intergranular bubbles, which are restricted to planar surfaces, result in a much smaller spacing between these large bubbles than between intragranular bubbles.<sup>500</sup> This deviation from a random distribution due to the cooperative behavior of pre-existing grain boundaries and mass transport can have a profound impact on thermal transport properties.<sup>501</sup>

Computational studies have confirmed that the character of the grain boundary has a large impact on both intergranular bubble nucleation and growth. In a study involving the segregation of Xe to a selected group of grain boundaries in  $\text{UO}_2$ ,<sup>496</sup> it was suggested that the segregation properties of grain boundaries may result in different nucleation rates for fission gas bubbles. This was investigated in more detail using random-walk Monte Carlo simulations,<sup>502</sup> which showed that the segregation energy of a grain boundary has a large impact on its intergranular bubble nucleation rate. It was also shown that the interconnection rate of intergranular bubbles depends on the grain boundary character, since the grain boundary energy dictates the contact angle of the bubble with the grain boundary.<sup>503</sup>

Similarly, grain boundary segregation of dopants in  $\text{CeO}_2$ , as a model material or fuel cell component, depends on the character of the grain boundary.<sup>504</sup> Li et al.<sup>505</sup> used APT to investigate segregation of Y in doped  $\text{CeO}_2$ . They found that Y segregates at grain boundaries but is uniformly distributed within the grains. In a similar study involving Gd-doped  $\text{CeO}_2$ ,<sup>506</sup> it was found that Gd strongly segregates at the grain boundary and within nanosized domains within the grains.  $\text{CeO}_2$  accommodates aliovalent dopants such as Gd and Mn through dopant–defect complexes. First-principles studies by Dholabhai et al.<sup>504</sup> suggested that the arrangement of these complexes at grain boundaries strongly influences the stability of oxygen vacancies. However, Sun et al.<sup>507</sup> used atomistic simulations to show that dopant arrangements at a dislocation in  $\text{CeO}_2$ , in concert with the strain field around the dislocation, can slow oxygen ion transport along the dislocation. The reduced ionic conductivity in Gd-doped  $\text{CeO}_2$  is supported by experimental evidence of grain boundary segregation of Gd and the formation of nanosized Gd-rich domains within  $\text{CeO}_2$  grains, as observed by laser-assisted APT.<sup>506</sup>

**3.4.2. Restructured Grain Boundaries.** The formation of HBS in commercial reactor fuel was first observed in the late 1950s and early 1960s.<sup>508,509</sup> This area of research remained relatively untouched until the mid-1980s, when researchers readdressed the subject in response to the industrial trend toward increasing fuel burnup. This structure, characterized by the formation of submicrometer-sized grains and micrometer-sized intergranular fission gas bubbles, forms near the rim of the fuel pellet where the temperature is relatively low and the damage accumulation is relatively high. The high damage rate is

due to the creation of fissile  $^{239}\text{Pu}$  caused by resonant absorption of epithermal neutrons by  $^{238}\text{U}$ . In this region, the fission product concentration and damage levels are significantly higher than the average values. Originally it was thought that the formation of the rim structure would negatively impact the thermal transport, leading to high centerline temperatures and enhanced fission gas transport.<sup>510</sup> In the early 2000s, Spino and Papaioannou<sup>511</sup> speculated that formation of the rim structure would have a net positive impact on the thermal conductivity by removing uniformly distributed intragranular defects (point defects, dislocation loops, and fission products). In 2004, Ronchi et al.<sup>5</sup> provided a systematic study of the impact of HBS on thermal conductivity using a combination of standard commercial reactor fuel and fuel samples irradiated in a test reactor. They found that the formation of HBS has a net beneficial impact on the thermal conductivity, with an intrinsic conductivity gain of 6–7% over fuel irradiated at intermediate temperatures where HBS did not form. Bai et al. used simulations to show that the likely cause of this thermal conductivity gain is the reduction in fission gas within the matrix due to grain boundary segregation.<sup>512</sup> There have been several research efforts aimed at understanding the formation mechanisms and the impact on physical properties using samples exposed to neutron irradiation. Comprehensive reviews of these studies were provided by Rondinella and Wiss<sup>6</sup> and Wiss et al.<sup>513</sup>

Here we focus on ion irradiation studies aimed at investigating the mechanisms responsible for the formation of HBS.<sup>510,514–517</sup> There are two broad groups of theories regarding the formation of HBS.<sup>6</sup> The first involves nucleation and growth at either highly defective sites (e.g., dislocation tangles) or amorphous regions near fission tracks. The second involves polygonization, where grains subdivide along dislocation networks produced by radiation damage. It is generally thought that nucleation and growth will lead to high-angle grain boundaries and that polygonization will lead to low-angle grain boundaries. In an effort to isolate the formation mechanism, researchers in the 1990s started to investigate dislocation produced by heavy-ion irradiation. One of the earlier studies involved Xe irradiation of single-crystal  $\text{UO}_2$  samples to a dose of  $1 \times 10^{17}$  ions/cm<sup>2</sup>.<sup>510</sup> Rutherford channeling and X-ray diffraction measurements showed that a fine-grained polycrystal was formed with a misalignment of a few degrees between grains. Another study in support of the polygonization mechanism involved an investigation of ion tracks in  $\text{UO}_2$  irradiated with 100 MeV Zr and Xe ions.<sup>516</sup> In that study it was argued that overlapping fission tracks led to the formation of subgrains at relatively low temperatures. A more recent study using 84 MeV Xe ion irradiation found that grain polygonization due to accumulation of radiation-induced dislocations caused the fine grains to form.<sup>518</sup> There are many opportunities for new research involving ion studies aimed at unraveling the HBS formation mechanisms. For instance, the role that fission products play in the formation of HBS could be addressed by the use of doped samples. Another area that may provide rich physics involves studies targeting the role of existing grain boundaries. This is especially interesting in light of a recent study<sup>519</sup> using modern electron microscopy techniques, which suggested that the formation of low-angle boundaries is initiated at existing high-angle boundaries.

### 3.5. Outlook

Irradiation produces a wide range of defects in oxide fuels. A clear understanding of the role of these defects requires isolating the individual defects and studying them individually. While proton irradiation at low temperature can generate point defects and very small clusters, intermediate-temperature irradiation can generate loops and point defects. Higher-temperature annealing, however, can be used to eliminate point defects and control the size distribution of loops via coarsening. In the presence of gaseous species such as He, bubbles may also evolve in specimens that have loops. Thus, a hierarchy of irradiation experiments can be used to investigate the different defects one by one for comparison with computational modeling. At high temperature, unfauling of Frank loops can occur in proton-irradiated samples. Since the effects of faulted and unfauling loops on thermal transport are quite different because of strain fields, it is of significance to distinguish loop types and quantify their sizes and densities and also measure the strain fields around them. In situ TEM visualization under irradiation could be used to capture the unfauling process.

There is a common understanding that a nonequilibrium point defect concentration is established under an irradiating particle flux. Most postirradiation measurements are not able to capture this supersaturated state, as by the time the ex situ characterization is done a different distribution of point defects is probed. Evidence for this effect has been demonstrated in several recent in situ measurements of various properties, including thermal conductivity,<sup>520,521</sup> elastic properties,<sup>522–524</sup> vibrational spectra observed using Raman spectroscopy<sup>525</sup> and optical properties.<sup>526,527</sup> Similar approaches can be applied to the material systems considered in this review.

The ongoing efforts to develop in situ PAS techniques that can be used during ion irradiation would offer great opportunities to detect the formation of defects at the very early stages of irradiation and monitor their evolution to larger clusters and voids in actinide oxides. PAS can detect atomic-sized vacancies with a sensitivity of better than 1 ppm, thus providing new capabilities not attained by in situ TEM. Capabilities for the indirect measurement of defect concentrations through their impact on thermophysical properties under ion irradiation are also rapidly being developed through the use of in situ transient grating spectroscopy and other laser-based techniques.<sup>522,528</sup> As thermal transport in oxides is impacted by the in situ defect content, which cannot be predicted from ex situ measurements, gaining insight into defect concentrations while defect generation is ongoing is of high priority.

Computational modeling of defects is important to conduct simultaneously with experiments. Thermodynamic modeling requires ab initio underpinning, especially in fuels containing U and Pu. This type of modeling is not only useful in understanding the dominant defects in the oxide in both the hypo- and hyperstoichiometric regimes but also important in understanding and interpreting self-diffusion data for both cations and anions near thermal equilibrium conditions. Cluster dynamics modeling, on the other hand, is important in yielding the cluster size and composition distributions, which are critical inputs to thermal transport models. While the recent trends in cluster dynamics of oxides paid attention to the cluster composition issues, more research in this area is still required to account for the variability of cluster shapes and the effects of charge on both the energetics and kinetics of clustering in oxides.

#### 4. THERMAL CONDUCTIVITY UNDER IRRADIATION

In this section, we review key studies aimed at modeling and measuring thermal conductivity in the presence of irradiation defects. From the modeling side, we focus on studies that use both the Boltzmann transport framework and molecular dynamics to predict thermal conductivity in  $\text{UO}_2$ ,  $\text{ThO}_2$ , and oxide fuel surrogates, each containing crystalline defects found in reactor fuels. From the experimental side, we focus on work that uses ion beams either to directly emulate the multifeature microstructures found in real fuels or to perform single-effect studies to isolate individual populations of microstructural features.<sup>304,529</sup> The use of ion beam studies has been necessitated by the extreme difficulty associated with measuring the conductivity of reactor-irradiated fuel as well as the challenge of connecting measurements of conductivity to specific microstructural features in multifeature systems (e.g., point defects and defect clusters).<sup>530</sup> Moreover, when paired with new experimental methods for measuring thermal conductivity of thin damaged layers, ion irradiation experiments can be conducted rapidly, enabling researchers to probe a large parameter space of exposure and test conditions. The diagram shown in Figure 23 exemplifies a diverse set of methods that are needed to conduct a comprehensive study of phonon transport in defective crystals.

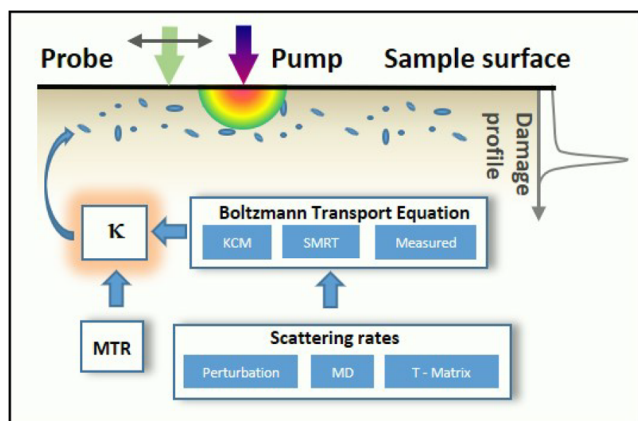


**Figure 23.** Illustration of the methods discussed in this section. Modulated thermal reflectance is used to extract the thermal conductivity of the thin damage layer caused by ion irradiation. Various levels of solutions to the Boltzmann transport equation for phonons are then compared to measured conductivity values.

We begin by discussing the limitations of current fuel performance codes and highlighting the promise of advanced codes currently under development, with an emphasis on thermal conductivity. We then discuss recent experimental efforts that have enabled measurements of thermal conductivity on length scales commensurate with damage accumulation associated with ion irradiation. This is followed by a discussion of atomistic and atomistically informed models of thermal transport in the presence of irradiation-induced microstructure. We end this section by reviewing recent work directed at comparing model predictions to experimental measurements of thermal conductivity in defective single crystals of  $\text{ThO}_2$ ,  $\text{UO}_2$ , and surrogate oxides.

##### 4.1. Fuel Performance Codes and Thermal Conductivity

The safe and efficient operation of commercial nuclear reactors relies on analysis provided by fuel performance codes.<sup>531–533</sup>

The temperature distribution within the fuel, governed by the fuel thermal conductivity, plays a central role in fuel performance. Fuel performance codes must consider thermal conductivity as a time- and space-dependent property that changes dynamically during operation because of fission damage, the buildup of fission gases, and a myriad of other parameters.<sup>5</sup>

Current light-water reactor fuel performance codes based on  $\text{UO}_2$ , such as FRAPCON,<sup>531</sup> TRANSURANUS,<sup>532</sup> and more recently BISON,<sup>534,535</sup> rely on empirical correlations between conductivity, burnup, and temperature.<sup>5,9</sup> Within these codes, the fuel thermal conductivity,  $\kappa$ , is modeled using a simple expression derived from the kinetic theory of gases that approximates a broad phonon spectrum by a narrow phonon band:<sup>536,537</sup>

$$\kappa = \frac{1}{A + BT} \quad (6)$$

In eq 6,  $A$  captures any conductivity reduction due to defects and  $B$  parametrizes the intrinsic conductivity. Fuel performance codes use the functional form of eq 6 to define the thermal conductivity of the fuel by defining  $A$  and  $B$  as functions of fuel burnup and irradiation temperature.<sup>5</sup> In particular,  $A$  can be represented as  $A = A_0 + \sum_i x_i A'_i$ , where the summation is over defects  $i$ ,  $x_i$  is the concentration of defect  $i$ ,  $A'_i$  is the scattering parameter for defect  $i$ , and  $A_0$  is the residual value for a pristine material.<sup>25,530</sup> Recommended values of  $A_0$  and  $B$  for pristine samples of  $\text{UO}_2$ ,  $\text{ThO}_2$ , and  $\text{CeO}_2$  are summarized in Table 1,

**Table 1.** Parameters for High-Temperature Conductivity of Pristine Fluorite Oxides

material	ref	$B$ [m/W]	$A_0$ [m·K/W]
$\text{UO}_2$	544	$2.165 \times 10^{-4}$	0.0375
$\text{ThO}_2$	545	$2.25 \times 10^{-4}$	$4.2 \times 10^{-4}$
$\text{CeO}_2$	407	$1.89 \times 10^{-4}$	$7.84 \times 10^{-4}$

and representative conductivity profiles as functions of temperature are shown in Figure 24. The simplified formulation and minor variations thereof have been used to describe the thermal conductivity of fresh and irradiated  $\text{UO}_2$  fuel,<sup>538,539</sup> mixed uranium–plutonium dioxide (MOX) fuel,<sup>540–542</sup> and rare-earth-doped  $\text{UO}_2$ .<sup>543</sup>

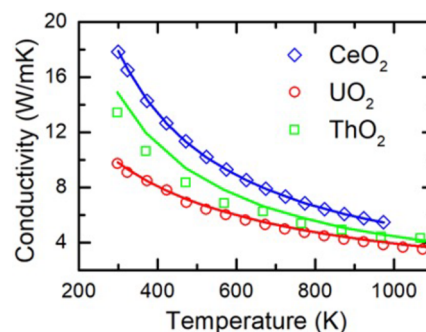


**Figure 24.** High-temperature thermal conductivity of selected fluorite oxides. Solid lines are values predicted using eq 6, and the open symbols are data taken from the literature. The  $\text{CeO}_2$  data (model and experiment) were taken from ref 407. The  $\text{UO}_2$  experimental data were taken from ref 551. The  $\text{ThO}_2$  model data were taken from ref 545. The  $\text{UO}_2$  model data were taken from ref 544. The  $\text{ThO}_2$  experimental data were taken from ref 154.

In these fuel performance codes, the temperature distribution is used to predict important physical properties that impact fuel performance, including the behavior of fission products, swelling, creep, and the release of fission gases.<sup>533</sup> However, the approximate treatment of thermal conductivity leads to increased uncertainty<sup>546</sup> and correspondingly to larger safety margins. Thus, microstructure-based fuel performance codes will be required to expand the application of these codes to higher burnups and/or alternative fuel utilization schemes proposed by new reactor concepts.<sup>547</sup>

In the 1990s, researchers started to develop more advanced mechanistic descriptions of the thermal conductivity of  $\text{UO}_2$ . One of the more notable studies<sup>530</sup> used measurements on simulated fuel (SIMFUEL) to extract the impact of dissolved fission products and large fission gas bubbles on thermal conductivity. Recently, several effective-medium models have been developed to capture the impact of large intergranular fission gas bubbles on the fuel thermal conductivity.<sup>26,501,548</sup> General models that predict the impact of randomly distributed bubbles on the thermal conductivity, such as the Maxwell–Eucken equation,<sup>549</sup> do not accurately describe the impact of the intergranular gas bubbles because they are not randomly distributed; they are aligned on grain boundaries, which also provide some thermal resistance.<sup>501</sup> Initial models were developed by fitting to mesoscale finite-element-method predictions of the thermal conductivity.<sup>501,548</sup> Later, a model was developed that represented the impact of the grain boundary and intergranular bubbles on the fuel thermal conductivity using a network of thermal resistors and predicted an effective thermal resistance of the grain boundary as a function of the fraction of the grain boundary area that was covered by gas bubbles.<sup>26</sup> A later sensitivity analysis showed that the thermal resistor model did not demonstrate the same sensitivities to the average bubble radius as a mesoscale finite-element model,<sup>550</sup> indicating that it may be an oversimplification of the heat transport through fuel with intergranular fission gas bubbles.

Most of the effective-medium modeling approaches have focused on fission gas bubbles, which are typically large in comparison with the wavelength of the phonons responsible for transporting thermal energy. However, it has been recognized for some time that smaller radiation-induced defects such as dislocation loops and sub-TEM-resolution defect clusters contribute significantly to a reduction in thermal conductivity. Until recently, the impact of smaller defects has been neglected, as they are more difficult to characterize and require a more detailed accounting of phonon structure.<sup>29,66,315,552–555</sup>

#### 4.2. Experimental Measurement of Thermal Conductivity

While our focus here is on measuring the thermal conductivity of fuel surrogates, it is important contextually to mention the large amount of work that has been devoted to measuring the thermal conductivity of reactor fuel. Since the early 2000s, researchers primarily in Europe and Japan have sought to investigate thermal conductivity in real fuel specimens that have been reinstrumented with thermocouples and tested in research reactors. These studies illustrate the challenge of truly understanding thermal transport in nuclear fuel under irradiation. Most of the studies performed used two measurements of temperature (fuel centerline and cladding temperature) along with estimates of the magnitude and distribution of the heat source to extract information on the average thermal conductivity of the fuel across the pellet radius.

With these tools, irradiation effects have been measured directly on neutron-exposed samples<sup>8,543</sup> and on simulation fuel, where the irradiation-induced microstructure was emulated through addition of fission products<sup>556,557</sup> and porosity controlled via conventional ceramic processing methods.<sup>558–561</sup> Outside of reactor environments, the thermal conductivities of fresh fuels and their surrogates have been measured extensively using laser flash methods,<sup>407,551,558–560,562,563</sup> direct heat-flow conductivity measurements,<sup>179,180</sup> and recently with femto-second and continuous-wave (CW) laser-based approaches.<sup>320,564</sup> In the following, we review several efforts used to understand thermal conductivity specifically in ion-irradiated fuel and surrogate materials, with a special emphasis on recent efforts targeting single-effect studies employing ion beam irradiation.

In the past decade, to overcome challenges associated with the small damage volumes created by ion beam irradiation, several pump–probe optical techniques relying on photothermal material excitation have been developed. A brief description of the three that have been utilized most frequently—transient grating spectroscopy (TGS), time-domain thermorefectance (TDTR), and modulated thermorefectance (MTR)—is provided here. For each of these methods, the key parameter that must be matched to the ion irradiation conditions is the thermal wave penetration depth,  $L_{\text{th}}$ . Importantly, the range of  $L_{\text{th}}$  values available through these methods spans from  $\sim 0.5$  to  $\sim 30 \mu\text{m}$ . This length scale is commensurate with the damage profile associated with ion irradiation. Schematics of each of these methods at the sample surface are shown in Figure 25.

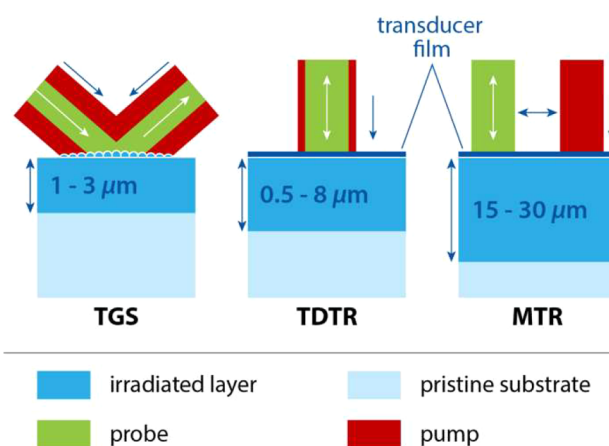


**Figure 25.** Schematics of the TGS, TDTR, and MTR optical geometries at the sample surface. For each case, the irradiated layer thicknesses and corresponding thermal wave depths are given as examples of those used in the literature and do not describe an exhaustive range.

These methods are nondestructive, allowing the thermal transport characteristics to be captured while leaving as-irradiated material available for detailed microstructure characterization when necessary.

TGS utilizes periodic laser excitation generated by crossing two laser pulses from the same source, with the fringe pattern spacing determined by the optical geometry. The resulting periodic thermal and elastic excitation is monitored by the diffraction of a CW probe from the sample.<sup>565</sup> The resulting thermal wave penetration is commonly given as  $L_{\text{th}} = \Lambda/\pi$ , where  $\Lambda$  is the fringe spacing projected onto the sample

surface.<sup>566</sup> The most detailed work to date using TGS to study thermal transport in ion-irradiated materials has focused on metals irradiated with both light and heavy ions.<sup>566,567</sup> In situ ion irradiation capabilities with concurrent TGS property monitoring have also recently been developed.<sup>522,564</sup>

The TDTR methodology most often relies on a train of ultrafast laser pulses that are split into pump and probe beam paths.<sup>406,568</sup> The pump injects high-frequency thermal waves into the sample, and the probe measures the evolution of the temperature field by monitoring small changes in temperature-induced optical reflectivity (thermoreflectance). The simplest form for the thermal wave penetration for the TDTR geometry is given as  $\sqrt{D/(\pi f)}$ , where  $D$  is the diffusivity of the substrate and  $f$  is the pump modulation frequency.<sup>406,569</sup> TDTR has been used to study a variety of ion-irradiated materials, including nuclear fuel,<sup>570</sup> nuclear fuel cladding,<sup>571</sup> silicon carbide,<sup>572</sup> metallic multilayers,<sup>571</sup> silicon,<sup>571,573</sup> sapphire,<sup>574</sup> and diamond,<sup>575</sup> across orders of magnitude in thermal conductivity.

MTR, also called spatial domain or beam-offset thermoreflectance,<sup>576–581</sup> has been used in the majority of studies of ion-irradiated actinide oxides and their surrogates. MTR utilizes modulated CW lasers to inject thermal waves into a sample under investigation. Pump and probe beams generated through either free-space or fiber-coupled CW lasers are focused onto a sample of interest coated with a transducer film.<sup>529</sup> The spatial extent of the thermal wave is measured by scanning either the pump or the probe along the surface of the sample.<sup>578,582</sup> In this geometry,  $L_{th}$  is again controlled by the applied modulation frequency of the pump and given by the same expression as shown above for TDTR. MTR has also been applied to a variety of materials following ion irradiation, including silicon,<sup>583</sup> sapphire,<sup>584</sup> fuel cladding alloys,<sup>585</sup> and a variety of oxide nuclear fuels and surrogates, including  $UO_2$ ,<sup>586</sup>  $CeO_2$ ,<sup>315</sup> and  $ThO_2$ .<sup>29</sup> Recent work has focused on measurements of defect-bearing oxides at cryogenic temperatures in order to discriminate among phonon scattering resulting from multiple types of defects.<sup>132</sup>

Experimental studies focusing on thermal transport in ion-irradiated oxide nuclear fuels and surrogates have found the most success to date using MTR. Of these methods, MTR has the combination of highest spatial resolution—using spot sizes on the order of 1–2  $\mu\text{m}$ —and highest sensitivity to low-conductivity materials. Both of these features are key for interrogation of actinide oxide fuels, as detailed surface preparation is often challenging because of material handling constraints, leaving surfaces to be measured that are not optically smooth over hundreds of micrometers. MTR also retains theoretical sensitivity to both in-plane and cross-plane thermal transport relative to the free surface,<sup>584</sup> which is useful for systems such as  $UO_2$  where intrinsic or imposed thermal anisotropy has been identified.<sup>180</sup> In contrast, the other methods described retain primary sensitivity to only a single direction of transport (TGS, in-plane; TDTR, cross-plane). MTR has a final advantage of requiring simple, compact CW laser sources. This has allowed MTR to be deployed in complex physical environments such as a highly radioactive glovebox for the direct study of spent nuclear fuel.<sup>587</sup>

Example MTR-measured values of thermal conductivity reduction in ion-irradiated  $UO_2$ ,  $CeO_2$ , and  $ThO_2$  are shown in Figure 26.<sup>29,297,315,320,586</sup> A major trend evident in Figure 26 is the inverse correlation between irradiation temperature and thermal conductivity reduction; as the irradiation temperature

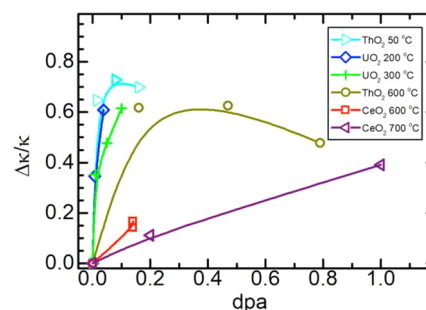


**Figure 26.** Summary of thermal conductivity measurements on ion-irradiated fluorites. For  $T_{irr}/T_m < 0.2$ , the microstructure is point-defect-dominated, whereas for  $T_{irr}/T_m > 0.3$  it is loop-dominated ( $T_{irr}/T_m$  is the ratio of the irradiation temperature to the melting temperature). The 200 °C  $UO_2$  data were taken from ref 320. The 300 °C  $UO_2$  data were taken from ref 586. The  $CeO_2$  data were taken from ref 315. The  $ThO_2$  data were taken from ref 29. The 600 °C  $CeO_2$  data were taken from ref 297.

increases, more conductivity is retained in these fluorite materials. Irradiations performed at lower temperatures cause degradation of the thermal conductivity primarily due to point defects (vacancies, interstitials, and charged defects).<sup>29</sup> With increasing irradiation temperature, point defects become more mobile and mutually recombine at higher rates. This recombination results in a lower density of point defects even at higher irradiation doses. In parallel, however, at higher temperatures the increased point defect mobility also allows dislocation loops to nucleate and grow; these loops tend to dominate the microstructure of fluorite oxides irradiated at elevated temperatures.<sup>29,297,315</sup> A qualitative investigation of data in Figure 26 suggests that dislocation loops contribute to the observed conductivity reduction for irradiations at 600 °C and higher.

### 4.3. Boltzmann Transport Framework

In this section, we review efforts to model thermal transport in actinide fuels and surrogate oxides using the Boltzmann transport equation. Our discussion of Boltzmann transport applied to oxide fuels and surrogates considers only the relaxation time approximation, as it is best suited for treating thermal transport in crystals containing a range of defects from point defects to extended defect clusters. We first discuss phonon scattering by both intrinsic three-phonon processes and defects, as the cross sections defined for these processes can be used for any level of approximation. Within the RTA formalism, individual phonon scattering mechanisms are treated independently and added together using Matthiesen's rule defined previously in eq 3. We pay close attention to the form of the cross section for point defects, as this model has been used frequently to gauge the impact of irradiation on the thermal conductivity in oxide fuels. This is followed by a short discussion of early work aimed at simple analytical solutions to the RTA. We end this section by discussing the single-mode relaxation time (SMRT) approximation, which more accurately captures the phonon structure.

**4.3.1. Phonon Scattering.** The three-phonon scattering processes shown in Figure 4 provide an intrinsic limitation to phonons' ability to conduct heat in anharmonic crystals. They are considered as perturbations to a harmonic oscillation resulting in finite phonon lifetimes. As a result, the three-phonon interactions shown in Figure 4a can be represented by<sup>588</sup>

$$\tau_{\mathbf{q}_s, \text{anh}}^{-1} = P_{\mathbf{q}_s}^{(\text{anh})} N_3(\mathbf{q}_s, \omega) \quad (7)$$

where  $P_{\mathbf{q}_s}^{(\text{anh})}$  is the average anharmonicity parameter and  $N_3(\mathbf{q}_s, \omega)$  is the occupation-weighted density of states that captures the three-phonon scattering phase space, satisfying energy and momentum conservation laws.

Defects act as phonon scattering centers, reducing the phonon lifetimes and mean free paths. Scattering by the core of the defect is due to the atomic mass mismatch and changes in the interatomic force constants. Additionally, defects introduce a strain field that scatters phonons through anharmonic interactions. The general form for the rate of scattering due to phonon interactions with the defect, as depicted in Figure 4b, can be written in a form similar to eq 7:

$$\tau_{\mathbf{q}_s, \text{def}}^{-1} = V_{\mathbf{q}_s}^{(\text{def})} D_2(\mathbf{q}, \omega) \quad (8)$$

where  $V_{\mathbf{q}_s}^{(\text{def})}$  is the defect-induced perturbation to the interatomic potential energy and  $D_2(\mathbf{q}, \omega)$  is the density of states that captures phonon-defect-scattering phase space.<sup>53,6</sup> In the Debye approximation, this perturbation may be carried out to define simple functional forms for defect scattering rates for various types of defects. These are listed in Table 2.

**Table 2. Rates of Phonon Scattering with Various Defects<sup>a</sup>**

defect type	core	strain field
point defect (0D) <sup>30</sup>	$n_x S_c^2 \frac{V_0}{4\pi N v_s^3} \omega^4$	$n_x S_s^2 \frac{V_0}{4\pi N v_s^3} \omega^4$
line defect (screw dislocation) (1D) <sup>30,58,9</sup>	$N_d \frac{V_0^{4/3}}{v_s^4} \omega^3$	$0.06\gamma^2 b^2 N_d \omega$
planar defect (stacking fault) (2D) <sup>59,0</sup>	$\propto \omega^2$	$N_f \frac{0.7a^2\gamma^2}{v_s} \omega^2$
platelet (disk-shaped precipitate) (2D) <sup>591,592</sup>	$N_p \frac{24\pi h^2 R_p^2}{v_s} \omega^2$	N/A
void (3D) <sup>593,594</sup>	$\pi v_s R_v^2 N_v$	N/A

<sup>a</sup>Abbreviations:  $n_x$  is the point-defect concentration of a given species  $x$ ;  $S_c^2 = \frac{\Delta M_i^2}{M^2}$  and  $S_s^2 = 2\left(\frac{\Delta K_i}{K} - 2Q\gamma \frac{\Delta R_i}{R}\right)^2$  are the point-defect core and strain field scattering cross sections, respectively, for that species;  $N_d$  is the dislocation line density;  $N_f$  is the stacking fault density;  $N_p$  and  $R_p$  are the platelet density and radius, respectively; and  $N_v$  and  $R_v$  are the spherical void density and radius, respectively. It should be noted that technically the first term in  $S_s^2$  can be treated as a part of core scattering.

It should be noted that the exponent of the frequency in core scattering scales with the defect dimensionality, which is determined by the density of available states into which a phonon can scatter subject to applicable conservation laws, including energy and the tangential component of the momentum under the assumption that specular reflection occurs.<sup>30</sup> Larger-scale defects, including grain boundaries, large voids and bubbles, precipitates, and macroscale porosity, are most frequently taken into account using effective-medium approaches.<sup>26,53,0</sup> Phonon interactions with point defects require a defect-type-dependent scattering cross section to be defined.

For point defects specifically, the perturbation of the local potential has several components, including changes in atomic mass, force constant, and strain field surrounding the defect. Using second-order perturbation theory, Klemens derived a general expression for a “scattering parameter” or “scattering

strength” for phonon–point defect interactions,  $\Gamma$ , in terms of the mass difference of lattice points ( $\Delta M$ ), the harmonic force constant difference ( $\Delta K$ ), and the elastic strain scattering due to

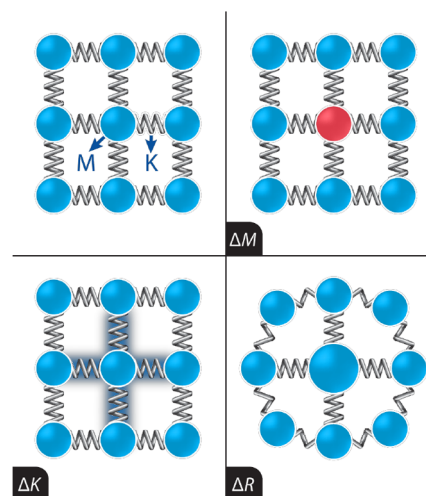


**Figure 27.** Schematic illustrating changes in mass, force constant, and atomic radius resulting from a point defect present in a crystal lattice. Each change is modeled by Klemens’ expression for the scattering strength or scattering cross section for phonon–point defect scattering (eq 9).<sup>30</sup>

the atomic radius change ( $\Delta R$ )<sup>30</sup> (Figure 27). This parameter  $\Gamma$  is given by

$$\Gamma = \sum_i n_i S_i^2 = \sum_i n_i \left[ \frac{\Delta M_i^2}{M^2} + 2 \left( \frac{\Delta K_i}{K} - 2Q\gamma \frac{\Delta R_i}{R} \right)^2 \right] \quad (9)$$

where  $n_i$  is the fractional concentration of the  $i$ th defect type,  $\gamma$  is the Grüneisen anharmonicity parameter, and  $Q$  approximates the number of distorted nearest-neighbor bonds surrounding the point defect (3.2 for substitutional defects and 4.2 for vacancies in the fluorite oxide lattice). However, for significant densities of point defects, the permutations of defect configurations within a unit cell must be taken into account.<sup>407,558,595</sup> Furthermore, Klemens’ original formula assumes a single atom per unit cell, and the treatment of compound materials requires further consideration. Gurunathan et al. provided a detailed description of this and showed that a refined version of Klemens’ general formulation may still be used with careful accounting of the average unit cell mass around defects of different types.<sup>596,597</sup>

#### 4.3.2. Klemens–Callaway–Debye Approximation.

One convenient approximation to the BTE approach is a method generally called the Klemens–Callaway method (KCM),<sup>53,6,598</sup> which approximates phonon branches by a simple Debye model. This allows the summation over  $\mathbf{q}$  space to be replaced by an integral over frequency,  $\omega$ , where the scattering rates are also expressed in terms of frequencies. In the KCM, the thermal conductivity is defined as

$$\kappa = \int_0^{\omega_D} C(\omega, T) v_s^2 \tau^{-1}(\omega) D(\omega) d\omega \quad (10)$$

where  $D(\omega) = 3N\omega^2/V_0\omega_D^3$  is the Debye density of states;  $\omega_D^3 = 6\pi^2 v_s^3 N/V_0$  defines the Debye frequency;  $C(\omega, T)$  is the specific heat defined in terms of the Planck distribution, given by

$C(\omega, T) = \hbar\omega \frac{\partial N^0(\omega, T)}{\partial T}$ , and  $N$  is the number of atoms per primitive cell (for fluorite oxides,  $N = 3$ ). Other parameters are defined, and their values for  $\text{UO}_2$ ,  $\text{ThO}_2$ , and  $\text{CeO}_2$  are listed in Table 3. Phonon scattering rates are calculated using

**Table 3. Parameters for Calculation of Thermal Conductivity Following the KCM Approach**

property	$\text{UO}_2^{320}$	$\text{ThO}_2^{179}$	$\text{CeO}_2^{407}$
velocity, $v_s$ (m/s)	2644	3145	3270
unit cell volume, $V_0$ ( $\text{\AA}^3$ )	163.6	175.2	159.2
Debye frequency, $\omega_D$ (THz)	43	50.2	53.8
Debye temperature, $T_D$ (K)	328	381	409
$B$ ( $10^{-18}$ s/K)	1.6	1.2	1.2
Grüneisen parameter, $\gamma$	1.8	–	2.5

perturbation theory under the assumption that all phonons are represented by a single band. In this approximation, the three-phonon scattering rate is given by  $\tau_{3\text{ph}}^{-1}(T, \omega) = BT\omega^2 \exp(-T_D/3T)$ , where  $B$  is fit from experimental data.<sup>32</sup>

If only point defects are considered in the high-temperature limit, such that they and intrinsic three-phonon scattering are the sole scattering mechanisms present, then eq 10 can be analytically integrated when  $\tau_{3\text{ph}}^{-1}(T, \omega) = \frac{2\gamma^2 k_B}{Mv_s^2 \omega_m} T\omega^2$  is defined in terms of the reduced Debye frequency  $\omega_m^3 = \frac{6\pi^2 v_s^3}{V_0}$  to obtain

$$\kappa_p = \kappa_i \left( \frac{\omega_0}{\omega_m} \right) \text{atan} \left( \frac{\omega_m}{\omega_0} \right) \quad (11)$$

where  $\kappa_i$  is the intrinsic conductivity in the absence of defects, given by

$$\kappa_i = \left( \frac{Mv_s \omega_m^2}{4\pi^2 \gamma^2} \right) \frac{1}{T} \quad (12)$$

Here, the correction due to defects is

$$\left( \frac{\omega_0}{\omega_m} \right)^2 = \left( \frac{4N\gamma^2 k_B T}{3\pi Mv_s^2} \right) \frac{1}{\Gamma} \quad (13)$$

where  $\Gamma$  is computed using eq 9. These analytical forms are useful comparison tools for estimating contributions from individual microstructural features, but more care in accounting for all of the contributions to phonon–defect scattering must normally be taken when the results of a computation are compared to measured thermal conductivity values.

#### 4.3.3. Single-Mode Relaxation Time Approximation.

The simple nature of eq 6 as used in performance codes makes it practical for engineering applications. However, its validity is limited to high temperatures where phonon–phonon scattering dominates. The KCM approach described above is a first step in making more accurate calculations of low-temperature thermal conductivity. However, the Debye approximation is known to underrepresent the role of phonons with long mean free paths, requiring a more accurate representation of phonons across the Brillouin zone.<sup>42,599</sup> As discussed in section 1, numerous phonon modes exist in crystalline solids, each having its own vibrational frequency, velocity, and lifetime. All of these details influence the thermal conductivity of a given material.<sup>536,600,601</sup> Different approaches for calculating thermal conductivity using first principles in defect-free systems were reviewed in section 2. Since it is computationally expensive to follow similar methods

for systems having nontrivial defects, we consider here several levels of simplification that bring both intrinsic anharmonic and defect perturbations to similar levels of complexity.

A simplification in the calculation of the three-phonon scattering phase may be made on the basis of the SMRT approximation,<sup>600</sup> in which the scattering phase space term in eq 8 retains exact phonon dispersion, but the anharmonic interaction term is represented by a single Grüneisen parameter. This method is especially useful for systems like  $\text{UO}_2$ , where the accuracy of current DFT methods is questionable.<sup>27,602</sup> While dispersion curves can be validated by neutron scattering experiments, the data on three-phonon scattering are limited. This approach has been applied recently to  $\text{ThO}_2$ <sup>555</sup> to predict bulk single-crystal thermal conductivity in comparison to measured values.<sup>179</sup> Figure 28 compares some of the notable results from previous studies that considered the thermal conductivity of  $\text{ThO}_2$ .

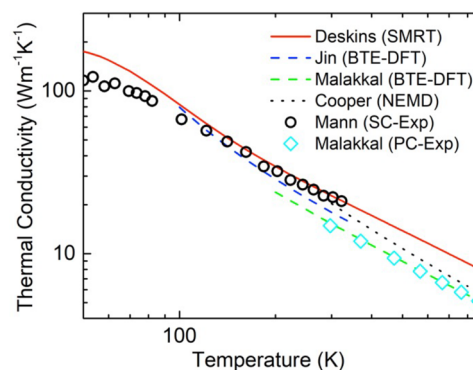


**Figure 28.** Comparison of different methods for calculation of thermal conductivity in  $\text{ThO}_2$ : SMRT results by Deskins et al.<sup>555</sup> (red curve) and bulk  $\text{ThO}_2$ ; NEMD results by Cooper et al.<sup>603</sup> (dotted line); BTE-DFT results by Malakkal et al.<sup>154</sup> (green dashed line) and Jin et al.<sup>152</sup> (blue dashed line). The black circles and cyan diamonds are experimental results for 96.7 TD  $\text{ThO}_2$  single crystals by Mann et al.<sup>179</sup> and polycrystalline  $\text{ThO}_2$  by Malakkal et al.,<sup>154</sup> respectively.

The associated phonon–point defect scattering rate of a phonon with wavenumber  $q$  and polarization  $s$ , accounting for the actual dispersion curves, can be written in terms of the scattering parameter as<sup>596</sup>

$$\tau_{\text{PD},qs}^{-1} = \frac{\Gamma V_0}{4\pi v_{p,qs} v_{g,qs}^2} \omega^4 \quad (14)$$

where  $v_{p,qs}$  is the phonon phase velocity. In the Debye limit, this form reduces to that listed in Table 2 for point defects. Equation 14 takes into account the dispersive nature of the phonon and distinguishes between phonon group velocity ( $v_g$ ) and phase velocity ( $v_p$ ). The expansion of phonon scattering rates in Table 2 to SMRT requires recasting them into a form that accounts for differences between  $v_p$  and  $v_g$ . Using dispersion curves fit to inelastic neutron scattering data,<sup>50</sup> Deskins et al.<sup>555</sup> implemented the SMRT approximation in the case of uranium substitutional defects in  $\text{ThO}_2$  and compared the resulting temperature dependence of the thermal conductivity to measured values<sup>604</sup> and those from MD simulations<sup>603</sup> (Figure 29). This comparison shows that in these fluorite oxide systems, making the SMRT approximation still produces a reasonable description of the thermal conductivity in defect-bearing systems across a wide temperature range through the BTE. As

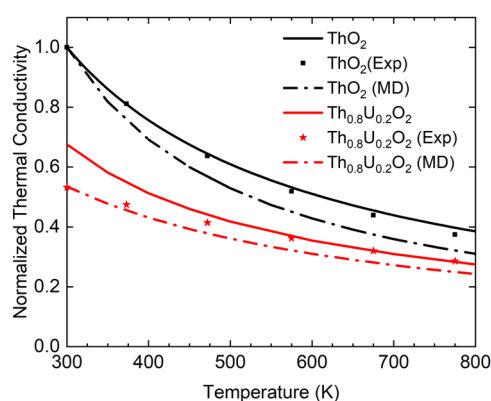


**Figure 29.** Reduction of thermal conductivity presented by Deskins et al. (solid lines) compared to experimental and MD results for  $\text{ThO}_2$  containing 20% uranium substitutional defects. Each value is normalized by the respective value for pure  $\text{ThO}_2$  at 300 K from each study. Adapted with permission from ref 555. Copyright 2021 AIP Publishing.

more accurate first-principles treatments of thermal transport in  $\text{UO}_2$  become available, researchers will be able to revisit assumptions regarding lattice anharmonicity and phonon–defect scattering that are tied to the SMRT approximation.

However, the Boltzmann framework, at any level of approximation discussed here, typically considers only three-phonon processes (cubic phonon interactions) and may be inadequate to describe phonon thermal transport at high temperatures, where four-phonon scattering can become significant.<sup>123,605</sup> An additional limitation of the standard implementation of the BTE at higher temperatures may arise from the fact that materials undergo thermal expansion, resulting in phonon softening. A detailed accounting for this effect would require recalculation of phonon dispersion and relevant anharmonic terms as a function of temperature. Nevertheless, while these higher-order effects are important to the broader community, they do not come into play for work reviewed in this section for two reasons. First, in an effort to isolate the role of defects, experiments are typically carried out at room temperature and below to reduce the obscuring influence of phonon–phonon interactions. Second, measurements on ion-irradiated material at elevated temperature introduce significant complications due to kinetic defect processes such as recombination and agglomeration.

#### 4.4. Molecular Dynamics Simulations of Thermal Conductivity

Molecular dynamics simulations offer an alternative way of calculating thermal conductivity in lattices where defects and other features can be directly specified. It can be applied to defective structures and captures higher-order anharmonic effects, which are too computationally expensive to be implemented within the BTE. The application of additional postprocessing can reveal detailed mechanisms of phonon scattering.

**4.4.1. Bulk Thermal Conductivity.** Classical MD involves solving Newton's equations of motion to determine the trajectories of atoms within a crystal lattice.<sup>606</sup> To approximate an infinite lattice, a structure of many thousands of atoms can be replicated periodically in all dimensions, creating a supercell. The behavior of the system is dictated by the description of interatomic forces using an empirical interatomic potential derived by fitting to experimental material properties or to forces

calculated from DFT. During MD simulations, thermal transport within such an ensemble can be evaluated using either the nonequilibrium MD (NEMD) method or the Green–Kubo equilibrium method.<sup>607</sup>

During NEMD, the system is driven out of its equilibrated state by application of a heat flux (Figure 30), which creates a

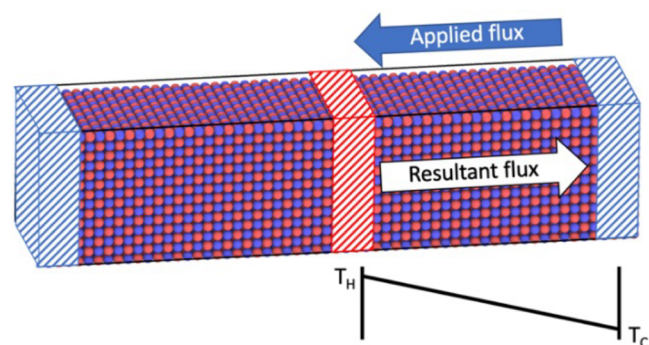


**Figure 30.** Schematic of the NEMD method, whereby a  $\text{UO}_2$  supercell with a large aspect ratio is used. A heat flux is applied, which causes a thermal gradient. This in turn causes a resultant heat flux. At steady state, the applied heat flux and the resultant heat flux are equal and opposite.

thermal gradient,<sup>608</sup> or by application of a thermal gradient, which creates a heat flux.<sup>609</sup> In either case, after a certain amount of time the system will reach a steady state in which the heat flux,  $\mathbf{q}$ , and thermal gradient,  $dT/dx$ , become constant, and the thermal conductivity is defined by Fourier's law:

$$\mathbf{q} = \kappa \frac{dT}{dx} \quad (15)$$

Finite-size effects arise because the separation of the hot and cold regions is shorter than the phonon mean free path.<sup>609–611</sup> In NEMD, the true bulk thermal conductivity,  $\kappa_\infty$ , must be extrapolated from the following relationship:  $\kappa^{-1} = AL_x^{-1} + \kappa_\infty^{-1}$ , where  $\kappa$  is the thermal conductivity of the system with supercell length  $L_x$ .

The Green–Kubo method is carried out on a system in its equilibrium state, whereby the system is held at constant temperature. The thermal conductivity is determined from the ensemble average of the heat current autocorrelation function,  $\langle \mathbf{J}(0) \cdot \mathbf{J}(t) \rangle$ :

$$\kappa = \frac{V}{3k_B T^2} \int_0^\infty \langle \mathbf{J}(0) \cdot \mathbf{J}(t) \rangle dt \quad (16)$$

where  $V$  is the volume of the system,  $T$  is the absolute temperature, and  $k_B$  is the Boltzmann constant. For long simulation times,  $\mathbf{J}(t)$  becomes uncorrelated with respect to  $\mathbf{J}(0)$ , such that  $\langle \mathbf{J}(0) \cdot \mathbf{J}(t) \rangle$  tends to zero, enabling convergence of  $\kappa$ . A benefit of the Green–Kubo method is that finite-size effects appear to be less severe than for the NEMD method; however, long simulation times are required, and the force on an atom due to each of its neighbors must be precisely defined, which is not trivial for many-body empirical potentials.<sup>607,611</sup>

Inherent to both methods are uncertainties regarding the choice of empirical potential and its ability to describe thermal transport in the system being studied. Commonly, pairwise empirical potential forms have been employed for oxides, whereby the interaction energies of U–U, U–O, and O–O atom pairs are independent of the positions of other atoms in the

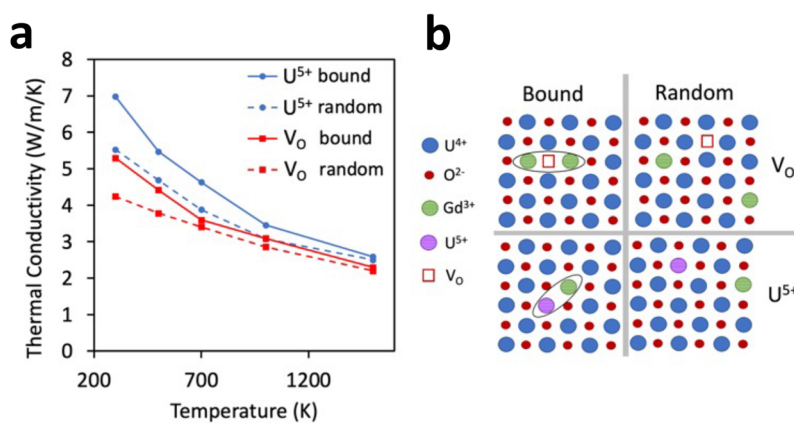


**Figure 31.** (a) Thermal conductivity of  $\text{UO}_2$  containing 5 wt % Gd calculated using NEMD by Qin et al. Each data set corresponds to a different charge-compensating mechanism, as shown by (b) the schematic of atomic configurations. Adapted with permission from ref 635. Copyright 2020 Elsevier B.V.

system. The total system energy is given by a sum over all of the pairwise interactions. Typically, a pair potential consists of long-range Coulomb and short-range interactions. Often partial ionic charges are used, meaning that the degree of ionicity can be used as a fitting parameter. However, the majority of the fitting parameters are still contained within the short-range interactions. Most  $\text{UO}_2$  potentials use a Buckingham form<sup>612</sup> to describe the repulsive force due to the Pauli exclusion principle and intermediate-range dispersive forces due to van der Waals interactions. Additionally, a Morse potential<sup>613</sup> can be included to capture a degree of covalency in  $\text{UO}_2$ , as in the Basak<sup>614</sup> and Yakub<sup>615</sup> potentials. Several  $\text{UO}_2$  potentials, such as the Morelon<sup>616</sup> and Jackson<sup>617</sup> potentials, utilize the four-range formulation of the Buckingham potential, which retains the exponential description of forces at short ranges and the dispersive term at longer distances and uses splines near the potential minima. This approach avoids the unphysical energies at short ranges due to the asymptotic nature of the  $r^{-6}$  dispersion term. A number of potentials account for ionic polarizability using the shell model, representing a deviation from a strictly pairwise description that enables the dielectric constant and the Cauchy violation in the elastic constants to be reproduced.<sup>618</sup> More recently, Cooper, Rusthon, and Grimes (CRG) extended a Coulombic–Buckingham–Morse pair potential form to include many-body interactions through the embedded atom method (EAM), allowing the temperature dependence of the bulk modulus to be captured, and this was also later demonstrated by Soulie et al.<sup>619</sup> for the Sattouy potential.<sup>620</sup> The Sattouy and Li<sup>621</sup> potentials moved beyond a rigid-ion model to include charge transfer between atoms. A number of detailed studies<sup>602,618,622–625</sup> have compared the properties of contemporary potentials to experimental or DFT data, such as thermal expansion, mechanical properties, and defect energies. The ability of a potential to capture such properties is the primary metric used to evaluate the quality of the potential.

Frequently, however, empirical potentials are not fit to the phonon properties of a material, and the ability of a potential to accurately describe thermal transport must be rigorously validated. Notably, classical MD struggles to reproduce the low thermal conductivity of  $\text{UO}_2$ , particularly at low temperatures,<sup>602,626–629</sup> whereas MD potentials tend to perform better for  $\text{ThO}_2$ .<sup>154,630,631</sup> It has been suggested that this is due to spin–phonon resonance associated with low-lying *f* electron states in  $\text{UO}_2$  that cannot be included directly in classical MD.

However, the Klemens–Callaway model accounts for this, greatly improving the comparison between MD and experiment.<sup>25,26,180</sup> Chernatynskiy et al. applied a non-MD lattice dynamics approach and found that several potentials performed reasonably well for  $\text{UO}_2$ ; they suggested an anharmonic correction to improve the results.<sup>632</sup>

Recently, the CRG potential was rigorously assessed for accurate predictions of phonon dispersion, lifetime, and branch-specific conductivity for  $\text{UO}_2$  and  $\text{ThO}_2$ .<sup>152</sup> It was found that the CRG potential captures the dispersion of the acoustic branches well but exhibits significant discrepancies for the optical branches, leading to an overestimate of the phonon lifetime and conductivity for both materials. Similarly, it has been found that several  $\text{UO}_2$  potentials accurately capture the dispersion of the acoustic branches but that inaccuracies in the optical branches result in a poor description of thermal properties.<sup>602</sup> These findings suggest that the empirical potential needs to be further optimized for robust prediction of thermal conductivity both in perfect crystals and in the presence of complex defects. Moreover, the methods discussed here are suitable only for modeling classical thermal transport due to phonons and do not address polaron contributions (which can be significant at high temperatures in semiconductors like  $\text{UO}_2$ <sup>633</sup>) or spin–phonon resonance processes.

**4.4.2. Point-Defect Scattering Using Molecular Dynamics.** Thermal transport in defective crystals can be addressed using the same methods as outlined above. First, the defect-free lattice thermal conductivity should be determined as a baseline. Subsequently, defects can be introduced to the system by adding new atoms at interstitial sites, removing atoms to create vacancies, or substituting one atom for another to create impurity defects.<sup>25,627,634–636</sup> The now-defective system is then allowed to equilibrate before the thermal conductivity assessment of the system is repeated, taking care to treat finite-size effects. This process can be repeated with varying defect concentrations. The phonon thermal conductivity calculated as a function of concentration can be fitted with either the simple model represented by eq 6 or the Klemens–Callaway model to determine the effective phonon scattering cross section for each defect or defect group.<sup>25,28</sup>

Broadly speaking, impurity defects have a lesser impact on the thermal conductivity than interstitials and vacancies, and among the fission products, Xe has the most significant impact on the

thermal conductivity of  $\text{UO}_2$ .<sup>25,26,555</sup> An additional complexity for ionic materials is the fact that scattering due to charge-compensating defects must also be considered. For example, Figure 31 shows the significant impact of a particular charge-compensating mechanism on the thermal conductivity of  $\text{UO}_2$  doped with 5 wt % Gd.<sup>635</sup> If  $\text{U}^{5+}$  substituted at  $\text{U}^{4+}$  sites is used to compensate for Gd impurities, the thermal conductivity is significantly higher than if oxygen vacancies ( $\text{V}_\text{O}$ ) are used, despite the lower concentration of  $\text{V}_\text{O}$  needed to charge-compensate 5 wt % Gd. By reducing the number of phonon scattering centers, binding increases the thermal conductivity with respect to a random distribution of defects. This demonstrates the complexity that must be considered for all defects in oxide nuclear fuels, be they formed by fission product accommodation, irradiation damage, or varying off-stoichiometry. Understanding the scattering due to individual point defects allows the coupling of phenomena such as fission gas behavior or radiation damage to thermal conductivity models.<sup>26,28</sup> Finally, phonon thermal conductivities calculated using either the NEMD or Green–Kubo method can be fitted with either the simple model represented by eq 6 or the Klemens–Callaway model to determine the effective phonon scattering cross section for each case.<sup>25,28</sup>

**4.4.3. Extended Defects.** MD simulations can be employed to simulate the impact of extended defects (e.g., dislocations, grain boundaries, voids, and bubbles) on phonon-mediated thermal conductivity. For example, the reduction in thermal conductivity of  $\text{UO}_2$  for several concentrations of edge dislocations has been predicted to develop an analytical form suitable for use in a fuel performance code.<sup>637</sup> The impact of grain boundaries on  $\text{UO}_2$  thermal conductivity has also been estimated and extrapolated from MD simulations, revealing only a small impact for micrometer-sized grains (as are typically present in fresh fuel).<sup>638–641</sup> However, because grain boundaries serve as sinks for point defects, it is expected that the impediment to thermal transport caused by grain boundaries will increase under irradiation.<sup>407,552</sup> MD simulations have been used to investigate the degradation of thermal conductivity due to porosity<sup>553</sup> and the accumulation of fission gas (Xe)<sup>642</sup> or decay gas (He)<sup>643</sup> into bubbles. As expected, increased porosity reduces the thermal conductivity; however, Chen et al.<sup>642</sup> and Lee et al.<sup>643</sup> both showed a decrease in thermal conductivity as the voids were filled with Xe and He, respectively. For He this was attributed to the resolution of He into the lattice, whereas resolution did not occur for Xe and the decrease was attributed to  $\text{UO}_2$  atom distortion at the bubble– $\text{UO}_2$  interface. Nonetheless, Tonks et al. demonstrated that the thermal conductivity degradation due to dispersed gas in the lattice greatly outweighs that of gas in the bubbles.<sup>26</sup>

#### 4.5. Impact of Grain Boundaries and Porosity

While the impact of atomistic-level defects is best captured using RTA, the effect of multiple grain boundaries on phonon thermal conductivity is better captured using effective-medium approximations. The impact of grain boundaries on the thermal conductivity may be represented using a series resistance model:

$$\frac{1}{\kappa_e} = \frac{1}{\kappa_0} + \frac{R_{\text{GB}}}{d} \quad (17)$$

where the effective thermal conductivity,  $\kappa_e$ , is a function of the single-crystal conductivity,  $\kappa_0$ , the average grain size,  $d$ , and the grain boundary interfacial thermal (or Kapitza) resistance  $R_{\text{GB}}$ . At low temperatures, where the Debye model serves as a good

approximation for the density of states, the acoustic mismatch model and the diffusive mismatch model have been developed to explain the temperature drop across boundaries.<sup>644</sup> Unfortunately, neither model provides good predictive capability across a wide range of grain boundary types. These failures result from interface scattering processes, which depend sensitively on the atomic structure and are difficult to treat in analytical models. Recent studies have used molecular dynamics<sup>552,645</sup> to understand the impact of atomic structure on thermal transport across grain boundaries. One of the first studies involving  $\text{UO}_2$  was performed by Watanabe and co-workers.<sup>552</sup> Their results demonstrated that the calculated value of the grain boundary resistance depends strongly on the choice of interatomic potential. A more recent molecular dynamics study<sup>645</sup> that considered larger grain sizes reported Kapitza resistances that were 50% smaller than those reported by Watanabe. It was suggested that this difference is due to the polycrystalline averaging scheme employed by Watanabe.

Corrections to the thermal conductivity resulting from volumetric porosity have also been taken into account by including a correction factor:

$$\kappa_p = \kappa_f(p, T) \quad (18)$$

using the Loeb expression or the Maxwell–Eucken formula, each of which accounts for fractional volume of porosity, shape factor, and temperature.<sup>530</sup> This expression does not account for pore size and breaks down for nanometer-sized pores that have dimensions on the scale of the phonon mean free path. Clearly, a more accurate accounting of nanovoids requires models that consider the atomic structure of the defects. In parallel with grain boundaries, recent molecular dynamics modeling work has aimed to understand the role of atomic structure at pore–bubble boundaries.<sup>642,646</sup> Zhu et al.<sup>646</sup> used nonequilibrium molecular dynamics to study the impact of Xe bubbles on thermal transport in  $\text{UO}_2$ . They found that many defects are produced at the bubble interface, leading to a substantial increase in the interfacial thermal resistance and an overall decrease in the thermal conductivity.

#### 4.6. Comparison between Experiment and Modeling

In this section, we review efforts to correlate microstructural defects produced by ion irradiation to thermal conductivity using the Boltzmann transport framework and MD. Very little work had been done in this area until recently because of the difficulty in accurately characterizing the range of defects produced by ion irradiation and accurately measuring the thermal conductivities of thin damage layers. As mentioned above, the most recent work in this area has been the experimental measurement of low-temperature conductivity in defect-bearing crystals. At reduced temperatures, the relative contribution of defects to the total scattering is the largest, allowing the most information to be collected on fundamental mechanisms of phonon–defect interactions.

**4.6.1. Impact of Point Defects in Low-Temperature Low-Dose-Irradiated  $\text{UO}_2$ .** One of the first efforts along these lines was the work of Weisensee et al.,<sup>570</sup> who investigated the effect of room-temperature Ar ion irradiation on the thermal conductivity of thin films of  $\text{UO}_2$  using TDTR. While the lattice strain associated with the lattice mismatch between the substrate and film prevented a detailed study of the baseline microstructure, it was suggested that the  $\text{UO}_2$  was slightly hyperstoichiometric. XRD data revealed a broadening of the diffraction peaks and a shift to lower angles, an indication that

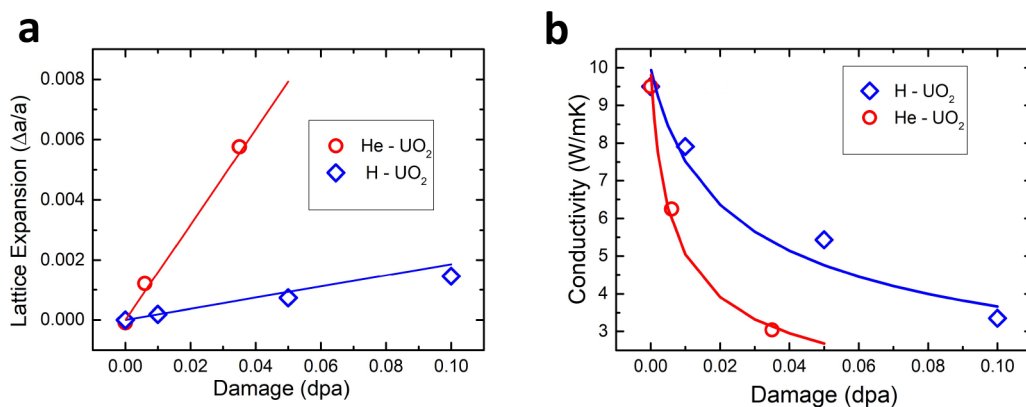


**Figure 32.** Analysis of thermal conductivity degradation in  $\text{H}^+$ - and  $\text{He}^{2+}$ -irradiated  $\text{UO}_2$ . Adapted with permission from ref 28. Copyright 2020 Acta Materialia Inc.

the  $\text{U}_4\text{O}_9$  phase was not formed under irradiation. A simple model of phonon thermal conductivity was used to extract an effective nondimensional scattering strength for point defects in  $\text{UO}_2$ .

In another study targeting the impact of point defects, polycrystalline  $\text{UO}_2$  was irradiated using 2.6 MeV protons and 3.9 MeV helium ions at 300 and 200 °C, respectively.<sup>28</sup> After irradiation, the sample thermal conductivity and lattice constant were measured using MTR and XRD, respectively (Figure 32). The reduction in conductivity and lattice expansion did not follow a similar trend with dose for these two different irradiation conditions. The results were analyzed using simple models for lattice expansion and thermal conductivity reduction informed by atomistic simulations from the literature. It was concluded that microstructure evolution under H and He ion irradiation produced different types of defects as a result of differences in defect clustering and electronic-ionization-induced mobility of the defects.

**4.6.2. Impact of Dislocation Loops in High-Temperature Proton-Irradiated  $\text{CeO}_2$ .** A study targeting the impact of dislocation loops on conductivity by Khafizov et al.<sup>315</sup> involved measuring the conductivity reduction caused by proton irradiation of  $\text{CeO}_2$  at 700 °C. As revealed by TEM analysis, the microstructure was dominated by dislocation loops. A rate theory model parametrized by analyzing two sets of samples irradiated at 600 and 700 °C revealed that the conductivity reduction in the sample irradiated at 700 °C is due to dislocation loops, whereas at 600 °C the reduction is primarily attributable to point defects (Figure 33).<sup>297</sup> One interesting observation that follows from these studies is that thermal conductivity reduction due to loops is unusually high and is attributed to long-range strain fields.<sup>315</sup>

**4.6.3. Mixed Impact of Point Defects and Loops in  $\text{ThO}_2$ .** More recently, efforts have been directed at drawing a closer connection between microstructure and thermal conductivity using more comprehensive defect characterization techniques (discussed in section 3 of this review) and a more complete accounting of the physical mechanisms of phonon transport.

Dennett and co-workers experimentally studied the impact of 2 MeV proton irradiation on thermal transport in single-crystal thorium dioxide grown by the hydrothermal synthesis method using MTR.<sup>29</sup>  $\text{ThO}_2$  was irradiated at 25 °C from 0.016 to 0.16 dpa and at 600 °C from 0.47 to 0.79 dpa. At 25 °C, the thermal conductivity in the irradiated layer dropped to 20% of the

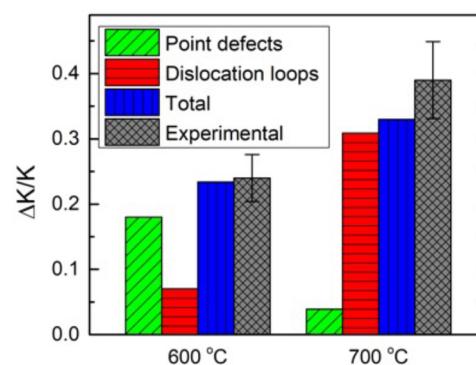


**Figure 33.** Analysis of thermal conductivity degradation due to dislocation loops in proton-irradiated  $\text{CeO}_2$ . Adapted with permission from ref 297. Copyright 2021 Acta Materialia Inc.

pristine value for all doses investigated, while at 600 °C, 40% of the pristine conductivity was retained at both doses. For both temperatures investigated, the thermal conductivity was found to be consistent among all of the doses, suggesting saturation of the defect population imparted via irradiation at these levels. Top-down Raman spectra collected following irradiation suggested the presence of defect clusters in both cases, with a higher density or larger clusters expected at 600 °C on the basis of the higher mobility of defects. The retention of higher thermal conductivity at 600 °C is attributed to the concentration of defects into larger clusters and loops, reducing the total number of phonon scattering sites retained in the lattice.<sup>520,554,583</sup>

Further measurements of the thermal conductivity in defected  $\text{ThO}_2$  single crystals were conducted on a subset of the crystals irradiated at 600 °C over a temperature range of 77 to 300 K using MTR (see Figure 34).<sup>132</sup> These data provide a low-temperature comparison for BTE calculations of defect-affected thermal transport (similar to the 300 K and higher BTE calculation of transport in U-doped  $\text{ThO}_2$  shown in Figure 29). To compute the thermal conductivity of defect-bearing  $\text{ThO}_2$ , dislocation loop characteristics were measured directly using TEM in order to compute scattering rates from stacking-fault-type defects as shown Table 2 (as these loops are observed to be faulted Frank loops). In addition, point-defect contributions to scattering were estimated through the use of a rate theory model for defect generation and evolution<sup>297</sup> and used to seed the calculation of the scattering rates based on eq 14. With the use of fitting parameters only to account for native impurities in the as-

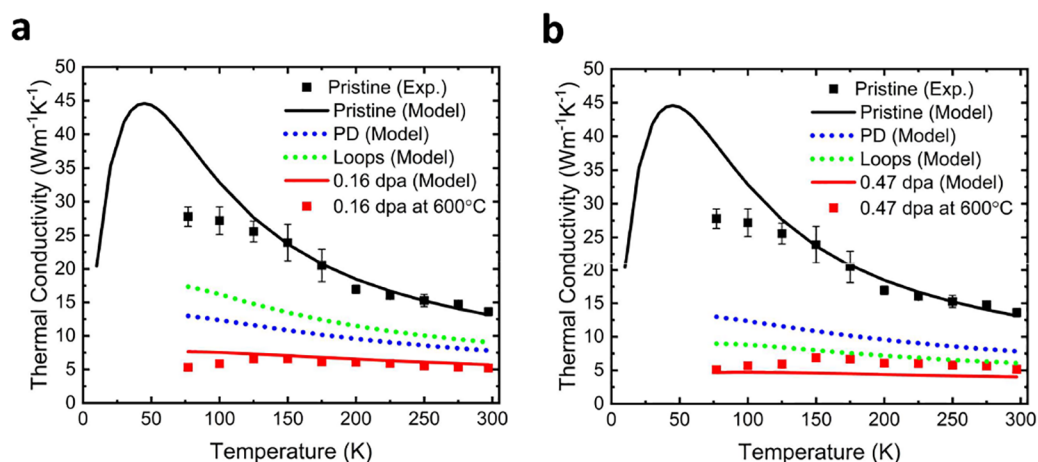


**Figure 34.** Comparison of MTR-measured and BTE-computed thermal conductivities for single-crystal  $\text{ThO}_2$  irradiated with 2 MeV protons at (a) 0.16 dpa at 600 °C and (b) 0.47 dpa at 600 °C. In each panel, computed conductivities considering only one type of extrinsic defect (dislocation loops or point defects) are shown by the dotted lines, while the total conductivity considering both defect populations is shown by the solid red line. From ref 132. CC BY 4.0.

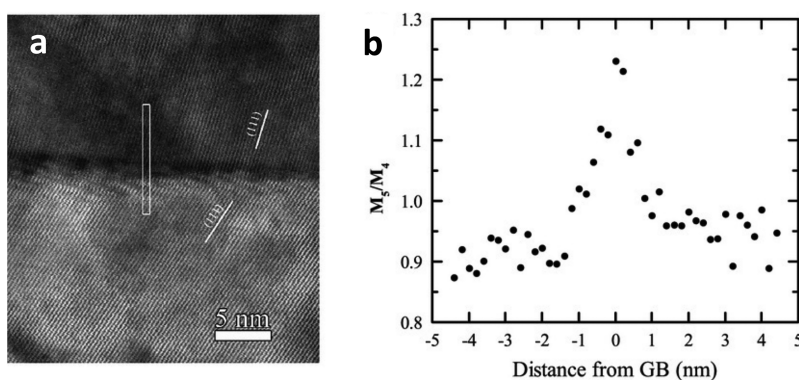


**Figure 35.** Impact of defect segregation on the interface thermal resistance of grain boundaries. Adapted with permission from ref 407. Copyright 2019 The American Ceramic Society.

synthesized crystals, good agreement was found between the MTR-measured conductivity and that computed using the BTE in the SMRT approximation, as shown in Figure 34 for  $\text{ThO}_2$  irradiated to 0.16 and 0.47 dpa.

**4.6.4. Impact of Grain Boundaries.** The segregation of defects at grain boundaries is thought to have a significant impact on thermal conductivity in the HBS. Generally, the HBS corresponds to a rim in the nuclear fuel where the fuel remains coldest and has the highest amount of damage due to a higher fission rate. In this region, extensive damage is accommodated by grain subdivision and subsequent defect segregation. The net beneficial effect on the intrinsic thermal conductivity suggested by Rondinella and Wiss<sup>6</sup> has motivated recent work that has looked at understanding the role of interfaces in phonon transport in fuel surrogates.

Hua et al.<sup>647</sup> reported the Kapitza resistance for grain boundaries in large-grained  $\text{CeO}_2$  using an investigative approach first developed for Si bicrystals.<sup>648,649</sup> That study provided a correlation between the measured Kapitza resistance and the misorientation angle between grain boundaries. To form this correlation, it was assumed that the plane of the grain boundaries coincided with the surface normal. In another study involving  $\text{UO}_2$ , experimental measurements of thermal conductivity were performed on a series of polycrystalline samples having grain sizes ranging from  $\sim 100$  nm to several micro-

meters.<sup>650</sup> By the use of eq 17, it was found that the extracted Kapitza resistance was considerably larger than that calculated using molecular dynamics.<sup>552,645</sup> It was suggested that the difference between the measurement and the model may be due to local changes in oxygen stoichiometry near the boundary.

Another study by Khafizov et al.<sup>407</sup> that has a more direct connection to thermal transport behavior in the HBS involved measurement of the thermal conductivity in highly non-stoichiometric nanocrystalline ceria.<sup>407</sup> In that study, it was found that the measured thermal conductivity was much higher than that predicted assuming that the oxygen defects were uniformly distributed. Electron energy loss spectroscopy revealed that oxygen defects segregated at grain boundaries, leaving the grain interior relatively defect-free (Figure 35). The authors speculated that the increase in the grain boundary resistance due to segregation was more than offset by a reduction in phonon scattering by intragranular oxygen defects. This supposition has since been supported by MD and multiscale modeling studies on  $\text{UO}_2$ .<sup>512,552</sup> Watanabe et al. found that the grain boundary thermal resistance was 2 orders of magnitude higher than that expected from pristine interfaces calculated using molecular dynamics simulations,<sup>552</sup> while Bai et al. found that grain boundary segregation leads to higher intragranular thermal conductivity.<sup>512</sup>

#### 4.7. Future Outlook

While the works described above have shown some success in connecting models of varying complexity to experimental measurements of thermal transport in defected actinide oxides, gaps still exist in the ability to capture the unique influence of the entire spectrum of radiation-induced defects on phonon scattering. Models beyond the RTA are needed to accurately treat conductivity at sufficiently low temperatures where normal processes dominate over Umklapp processes. Furthermore, the RTA can be problematic in certain classes of materials that introduce symmetries not found in the bulk, such as epitaxial films. MD models may help address the shortcomings of the RTA but require interatomic potentials that accurately capture phonon transport properties. First-principles descriptions of the details of the phonon band structure can provide important benchmarks for developing new, more accurate interatomic potentials. While the computational tools needed to perform this task are available, this will no doubt be a challenge for strongly electron-correlated materials.

Currently, the Green's function T-matrix method is the most fundamental approach to capture the impact of defects on phonon scattering rates.<sup>651,652</sup> Work using this method has demonstrated the shortcomings of using perturbation theory to treat the impact of vacancies in diamond, silicon carbide, and boron arsenide. These methods are currently finding applications in predicting scattering rates of phonons with extended defects such as clusters and dislocation loops.<sup>653,654</sup> However, extending these approaches to materials that exhibit strong electron correlation remains a difficult task for first-principles calculations.

#### 5. CONCLUDING REMARKS

This review has focused primarily on phonon thermal transport in two actinide oxides: one currently in use in commercial nuclear reactors, UO<sub>2</sub>, and one advanced fuel candidate material, ThO<sub>2</sub>. A comprehensive understanding of phonon transport in these actinide oxides under irradiation remains a grand science challenge. This area of research contains rich physics, including the 5f electron challenge, defect generation and evolution, and the development of experimentally validated mesoscale models of thermal conductivity in the presence of defects. New computational tools such as DFT+DMFT and new experimental tools enabled by new synthesis capabilities are ushering in a new era, enabling scientists to study in exquisite detail the fundamental mechanisms that control phonon transport.

Meeting this challenge will provide new opportunities for the nuclear fuels community. For example, accurate calculations of electronic structure in 5f systems will provide the scientific community with key information for constructing accurate interatomic potentials required for high-throughput compositional screening of advanced fuels. The development of a comprehensive understanding of thermal energy transport, while intimately connected to advanced nuclear fuels, can provide opportunities for energy-related technologies beyond nuclear energy. Examples include tailoring electron scattering in textured nanocrystals to enhance the thermal conductivity of metal interconnects, simultaneously controlling electron and phonon transport across interfaces in thermoelectric devices, specifying the interaction of electrons with dislocations in topological insulators, and harnessing strong electron correlation to realize new paradigms for quantum materials.

#### AUTHOR INFORMATION

##### Corresponding Author

David H. Hurley – Idaho National Laboratory, Idaho Falls, Idaho 83415, United States; [orcid.org/0000-0002-1845-1518](https://orcid.org/0000-0002-1845-1518); Email: david.hurley@inl.gov

##### Authors

- Anter El-Azab – School of Materials Engineering, Purdue University, West Lafayette, Indiana 47907, United States
- Matthew S. Bryan – Materials Science and Technology Division, Oak Ridge National Laboratory, Oak Ridge, Tennessee 37831, United States
- Michael W. D. Cooper – Materials Science and Technology Division, Los Alamos National Laboratory, Los Alamos, New Mexico 87545, United States
- Cody A. Dennett – Idaho National Laboratory, Idaho Falls, Idaho 83415, United States
- Krzysztof Gofryk – Idaho National Laboratory, Idaho Falls, Idaho 83415, United States; [orcid.org/0000-0002-8681-6857](https://orcid.org/0000-0002-8681-6857)
- Lingfeng He – Idaho National Laboratory, Idaho Falls, Idaho 83415, United States; [orcid.org/0000-0003-2763-1462](https://orcid.org/0000-0003-2763-1462)
- Marat Khafizov – Department of Mechanical and Aerospace Engineering, The Ohio State University, Columbus, Ohio 43210, United States; [orcid.org/0000-0001-8171-3528](https://orcid.org/0000-0001-8171-3528)
- Gerard H. Lander – European Commission, Joint Research Center, D-76125 Karlsruhe, Germany
- Michael E. Manley – Materials Science and Technology Division, Oak Ridge National Laboratory, Oak Ridge, Tennessee 37831, United States
- J. Matthew Mann – U.S. Air Force Research Laboratory, Sensors Directorate, Wright Patterson AFB, Ohio 45433, United States
- Chris A. Marianetti – Department of Applied Physics and Applied Mathematics, Columbia University, New York, New York 10027, United States
- Karl Rickert – KBR, Dayton, Ohio 45431, United States; [orcid.org/0000-0003-1056-0637](https://orcid.org/0000-0003-1056-0637)
- Farida A. Selim – Department of Physics and Astronomy, Bowling Green State University, Bowling Green, Ohio 43403, United States; [orcid.org/0000-0001-8367-3785](https://orcid.org/0000-0001-8367-3785)
- Michael R. Tonks – Department of Materials Science and Engineering, University of Florida, Gainesville, Florida 32611, United States
- Janelle P. Wharry – School of Materials Engineering, Purdue University, West Lafayette, Indiana 47907, United States

Complete contact information is available at:  
<https://pubs.acs.org/10.1021/acs.chemrev.1c00262>

##### Author Contributions

The manuscript was written through contributions of all authors. All of the authors approved the final version of the manuscript.

##### Notes

The authors declare no competing financial interest.

##### Biographies

David H. Hurley is a Laboratory Fellow and a group lead in the Materials Science and Engineering Department at Idaho National Laboratory (INL). He received his Ph.D. in Materials Science and Engineering from Johns Hopkins University in 1999. He was a Japanese

Society for the Promotion of Science Postdoctoral Fellow in the Applied Solid State Physics Laboratory at Hokkaido University. He is the recipient of the INL Outstanding Innovation Award for development of a hot-cell-compatible instrument for nanoscale thermal transport measurements. Currently he is the founding director of the Center for Thermal Transport under Irradiation (TETI), an Energy Frontier Research Center funded by the U.S. Department of Energy, Office of Basic Energy Sciences.

Anter El-Azab is a Professor of Materials Science and Engineering at Purdue University and the Science Question Lead for TETI. Prior to coming to Purdue, he was a Professor of Computational Science and Materials Science at Florida State University and a research scientist at Pacific Northwest National Laboratory. He obtained his doctorate at the University of California, Los Angeles. His research and teaching focus on microstructure complexity in materials.

Matthew S. Bryan is a postdoctoral researcher in the Materials Science and Technology Division at Oak Ridge National Laboratory. He obtained his Ph.D. in Physics from Indiana University in 2019. His work focuses on using inelastic neutron and X-ray scattering to study phonon dispersion, line widths, and density of states and how these measurements relate to thermal transport in actinide-bearing materials.

Michael W. D. Cooper is currently a Scientist in the Materials Science and Technology Division at Los Alamos National Laboratory, where he was also a postdoctoral researcher from 2015 to 2018. He obtained a Ph.D. in Materials Science from Imperial College London in 2015. His research interests focus on the application of classical molecular dynamics and density functional theory to understanding the atomic-scale processes that govern nuclear fuel behavior. In particular, he derives parameters for defects, fission products, and thermophysical properties relevant to ceramic fuels of various forms, such as oxides, nitrides, and silicides.

Cody A. Dennett is currently an Applied Physicist in the Materials Science and Engineering Department at Idaho National Laboratory. He obtained his Ph.D. from the Massachusetts Institute of Technology in 2019. He was the recipient of the INL Russell L. Heath Distinguished Postdoctoral Fellowship, and before coming to INL he was a U.S. Department of Energy National Nuclear Security Administration Stewardship Science Doctoral Fellow. His work focuses on laser-based measurements of thermophysical properties in dynamic or extreme environments to understand defect kinetics and transport phenomena in metals and ceramics.

Krzysztof Gofryk is a distinguished staff scientist and a group lead for actinide science in the Irradiated Fuels and Materials Department at Idaho National Laboratory. He obtained his Ph.D. from the Institute of Low Temperature and Structure Research of the Polish Academy of Sciences in 2006. Before joining INL, he worked at Los Alamos and Oak Ridge National Laboratories. He is a recipient of the DOE Early Career Award, the Presidential Early Career Award for Scientists and Engineers, and INL's Exceptional Achievement Award. His work focuses on strongly correlated electron systems at low temperatures and strong magnetic fields, including transport and magnetism in 5f electron materials, quantum criticality, heavy fermion physics, and spin-orbit-coupled systems.

Lingfeng He is a distinguished staff scientist and High-Resolution Materials Characterization Group leader in the Advanced Characterization Department at Idaho National Laboratory and the deputy director of the TETI. He received his Ph.D. in Materials Science at the Chinese Academy of Sciences in 2009. He worked as a postdoctoral research associate and assistant scientist at Nagaoka University of Technology in Japan and the University of Wisconsin-Madison before

joining INL in 2014. He is the recipient of the INL Laboratory Director's 2020 Exceptional Scientific Achievement Award.

Marat Khafizov is an associate professor in Mechanical and Aerospace Engineering at The Ohio State University. He received his Ph.D. in Physics from the University of Rochester in 2008. He was a postdoctoral research associate and R&D scientist at Idaho National Laboratory in 2010–2014 before joining OSU in 2014. His research focus is on understanding the impact of defects and radiation damage on physical properties of materials. He is a Phonon Transport Thrust Lead for TETI.

Gerard H. Lander obtained his Ph.D. at the University of Cambridge in 1967. He worked for 19 years at Argonne National Laboratory and for the last 5 years was the director of Argonne's Pulsed Neutron Source. In 1986 he returned to Europe to work at the EU Transuranium Institute in Karlsruhe, Germany, where he was director from 2002 to 2006, when he retired. He is a Fellow of the APS, was a John Wheatley Fellow at LANL and a consultant to the Japanese Atomic Energy Commission, was awarded an Honorary Professorship by the Polish Academy of Sciences, and received the Walter Halg Prize from the European Neutron Scattering Association in 2011. He is now a Visiting Professor at Bristol University in the U.K.

Michael E. Manley is a Senior Researcher at Oak Ridge National Laboratory in the Materials Science and Technology Division. He received his Ph.D. in Materials Science from the California Institute of Technology in 2001 and was awarded the 18th Louis Rosen Prize for his thesis. He was a Director's Postdoctoral Fellow at Los Alamos National Laboratory before being promoted to Technical Staff Member. He moved to Lawrence Livermore National Laboratory in 2006 and then to his current position at Oak Ridge in 2012. He won the 2021 TMS FMD Distinguished Scientist Award for his research on the thermophysical properties of materials and the discovery of intrinsic localized modes in anharmonic materials. He is Science Question Lead for TETI.

J. Matthew Mann is a Senior Research Chemist for the Sensors Directorate with the Air Force Research Laboratory. He received his Ph.D. in Inorganic Chemistry from Clemson University in 2009. He was the recipient of the 2019 Dr. Brian Kent Award for his innovative research in the area of neutron detection. His current research interests include crystal growth and characterization of radioactive materials, neutron detectors, novel laser hosts, and next-generation high-powered electronics.

Chris A. Marianetti is an Associate Professor of Materials Science and Applied Physics and Applied Mathematics at Columbia University. His research focuses on computing the behavior of crystalline materials using first-principles quantum mechanics. Applications span the periodic table, with particular emphasis on materials with strong electronic correlations. He received a Ph.D. in Materials Science and Engineering from MIT in 2004 and a B.S./M.S. from The Ohio State University. He held postdoctoral positions in the Department of Physics at Rutgers University and at Lawrence Livermore National Laboratory and was a recipient of the NSF CAREER and DARPA Young Faculty Awards.

Karl Rickert is currently a Senior Chemist at KBR, contracted to the Sensors Directorate at the Air Force Research Laboratory. Prior to this, he was an Oak Ridge Institute for Science and Education Postdoctoral Fellow at the Air Force Institute of Technology after receiving his Ph.D. from Northwestern University in 2016. His work focuses on the growth and characterization of actinide oxides and their implementation in detection devices.

Farida A. Selim is an Associate Professor of Physics and a member of the Center for Photochemical Science at Bowling Green State University. She obtained her Ph.D. in a joint program between Harvard and Alexandria University in Egypt. She is the lead of Thrust 1 “Point Defects” for the Center for Fundamental Understanding of Transport under Reactor Extremes, an Energy Frontier Research Center funded by the U.S. Department of Energy, Office of Basic Energy Sciences. She is known for inventing a new positron annihilation spectroscopy technique (gamma-induced positron spectroscopy). Her research spans a wide range of areas in defect studies, exploring novel electronic phenomena in wide-band-gap oxides and developing new instrumentation for defect and photoemission studies.

Michael R. Tonks is a Professor and Alumni Professor of Materials Science and Engineering and Nuclear Engineering at the University of Florida. He received his Ph.D. in Mechanical Engineering from the University of Illinois at Urbana–Champaign in 2008. Before coming to UF he was a staff scientist at Idaho National Laboratory for 6 years and an Assistant Professor at Penn State for 2 years. He is a recipient of the Presidential Early Career Award for Scientists and Engineers and the INL Early Career Exceptional Achievement Award. His work uses multiscale modeling and simulation to investigate the coevolution of microstructure and properties in materials in harsh environments.

Janelle P. Wharry is an Associate Professor in the School of Materials Engineering at Purdue University. Her research aims to understand structure–property–functionality relationships in irradiated materials, with an emphasis on deformation mechanisms and mechanical behavior at the nano/microscale. She is a recipient of the U.S. Department of Energy Early Career Award and the National Science Foundation CAREER Award. She is an Editor of *Materials Today Communications*. She received her Ph.D. from the University of Michigan in 2012.

## ACKNOWLEDGMENTS

D.H.H., A.E.-A., M.S.B., C.A.D., K.G., L.H., M.K., M.E.M., C.A.M., J.M.M., K.R. and J.P.W. acknowledge support from the Center for Thermal Energy Transport under Irradiation (TETI), an Energy Frontier Research Center funded by the U.S. Department of Energy, Office of Science, Office of Basic Energy Sciences. F.A.S. acknowledges support from Fundamental Understanding of Transport under Reactor Extremes (FUTURE), an Energy Frontier Research Center funded by the U.S. Department of Energy, Office of Science, Office of Basic Energy Sciences. M.R.T. and M.W.D.C. acknowledge support from the Nuclear Energy Advanced Modeling and Simulation (NEAMS) Program funded by the U.S. Department of Energy, Office of Nuclear Energy.

## REFERENCES

- (1) *Statistical Review of World Energy*. BP, 2020. <https://www.bp.com/en/global/corporate/energy-economics/statistical-review-of-world-energy.html> (accessed 2021-03-01).
- (2) *Energy Density Calculations of Nuclear Fuel*. <https://whatisnuclear.com/energy-density.html> (accessed 2021-03-01).
- (3) Lamarsh, J. R.; Baratta, A. J. *Introduction to Nuclear Engineering*; Prentice Hall, 2001; p 117.
- (4) Ronchi, C.; Sheindlin, M.; Musella, M.; Hyland, G. J. Thermal Conductivity of Uranium Dioxide up to 2900 K from Simultaneous Measurement of the Heat Capacity and Thermal Diffusivity. *J. Appl. Phys.* **1999**, *85*, 776–789.
- (5) Ronchi, C.; Sheindlin, M.; Staicu, D.; Kinoshita, M. Effect of Burn-Up on the Thermal Conductivity of Uranium Dioxide up to 100 MWd<sup>-1</sup>. *J. Nucl. Mater.* **2004**, *327*, 58–76.

- (6) Rondinella, V. V.; Wiss, T. The High Burn-Up Structure in Nuclear Fuel. *Mater. Today* **2010**, *13*, 24–32.
- (7) Lassmann, K.; Walker, C. T.; Van de Laar, J.; Lindström, F. Modelling the High Burnup UO<sub>2</sub> Structure in LWR Fuel. *J. Nucl. Mater.* **1995**, *226*, 1–8.
- (8) Walker, C.T.; Staicu, D.; Sheindlin, M.; Papaioannou, D.; Goll, W.; Sontheimer, F. On the Thermal Conductivity of UO<sub>2</sub> Nuclear Fuel at a High Burn-Up of Around 100 MWd/kgHM. *J. Nucl. Mater.* **2006**, *350*, 19–39.
- (9) Roostaii, B.; Kazeminejad, H.; Khakshournia, S. Including High Burnup Structure Effect in the UO<sub>2</sub> Fuel Thermal Conductivity Model. *Prog. Nucl. Energy* **2021**, *131*, 103561.
- (10) Sawbridge, P. T.; Baker, C.; Cornell, R. M.; Jones, K. W.; Reed, D.; Ainscough, J. B. The Irradiation Performance of Magnesia-Doped UO<sub>2</sub> fuel. *J. Nucl. Mater.* **1980**, *95*, 119–128.
- (11) Arborelius, J.; Backman, K.; Hallstadius, L.; Limbäck, M.; Nilsson, J.; Rebensdorff, B.; Zhou, G.; Kitano, K.; Löfstrom, R.; Rönnerberg, G. Advanced Doped UO<sub>2</sub> Pellets in LWR Applications. *J. Nucl. Sci. Technol.* **2006**, *43*, 967–976.
- (12) Cooper, M. W. D.; Stanek, C. R.; Andersson, D. A. The Role of Dopant Charge State on Defect Chemistry and Grain Growth of Doped UO<sub>2</sub>. *Acta Mater.* **2018**, *150*, 403–413.
- (13) Cooper, M. W.; Pastore, G.; Che, Y.; Matthews, C.; Forslund, A.; Stanek, C. R.; Shirvan, K.; Tverberg, T.; Gamble, K. A.; Mays, B.; Andersson, D. A.; et al. Fission Gas Diffusion and Release for Cr<sub>2</sub>O<sub>3</sub>-Doped UO<sub>2</sub>: From the Atomic to the Engineering Scale. *J. Nucl. Mater.* **2021**, *545*, 152590.
- (14) Jovani-Abril, R.; Gibilaro, M.; Janssen, A.; Eloirdi, R.; Somers, J.; Spino, J.; Malmbeck, R. Synthesis of Nc-UO<sub>2</sub> by Controlled Precipitation in Aqueous Phase. *J. Nucl. Mater.* **2016**, *477*, 298–304.
- (15) Spino, J.; Santa Cruz, H.; Jovani-Abril, R.; Birtcher, R.; Ferrero, C. Bulk-Nanocrystalline Oxide Nuclear Fuels - An Innovative Material Option for Increasing Fission Gas Retention, Plasticity and Radiation-Tolerance. *J. Nucl. Mater.* **2012**, *422*, 27–44.
- (16) Zhou, W.; Zhou, W. Enhanced Thermal Conductivity Accident Tolerant Fuels for Improved Reactor Safety - A Comprehensive Review. *Ann. Nucl. Energy* **2018**, *119*, 66–86.
- (17) Gong, B.; Yao, T.; Lei, P.; Cai, L.; Metzger, K. E.; Lahoda, E. J.; Boylan, F. A.; Mohamad, A.; Harp, J.; Nelson, A. T.; et al. U<sub>3</sub>Si<sub>2</sub> and UO<sub>2</sub> Composites Densified by Spark Plasma Sintering for Accident-Tolerant Fuels. *J. Nucl. Mater.* **2020**, *534*, 152147.
- (18) Finkeldei, S. C.; Kiggans, J. O.; Hunt, R. D.; Nelson, A. T.; Terrani, K. A. Fabrication of UO<sub>2</sub>-Mo Composite Fuel with Enhanced Thermal Conductivity from Sol-Gel Feedstock. *J. Nucl. Mater.* **2019**, *520*, 56–64.
- (19) Li, B.; Yang, Z.; Jia, J.; Zhang, P.; Gao, R.; Liu, T.; Li, R.; Huang, H.; Sun, M.; Mazhao, D. High Temperature Thermal Physical Performance of SiC/UO<sub>2</sub> composites up to 1600 °C. *Ceram. Int.* **2018**, *44*, 10069–10077.
- (20) Yao, T.; Xin, G.; Scott, S. M.; Gong, B.; Lian, J. Thermally-Conductive and Mechanically-Robust Graphene Nanoplatelet Reinforced UO<sub>2</sub> Composite Nuclear Fuels. *Sci. Rep.* **2018**, *8*, 2987.
- (21) Li, B.; Yang, Z.; Jia, J.; Zhong, Y.; Liu, X.; Zhang, P.; Gao, R.; Liu, T.; Li, R.; Huang, H.; et al. High Temperature Thermal Physical Performance of BeO/UO<sub>2</sub> Composites Prepared by Spark Plasma Sintering (SPS). *Scr. Mater.* **2018**, *142*, 70–73.
- (22) Yang, J. H.; Kim, D.-J.; Kim, K. S.; Koo, Y.-H. UO<sub>2</sub>-UN Composites with Enhanced Uranium Density and Thermal Conductivity. *J. Nucl. Mater.* **2015**, *465*, 509–515.
- (23) Yeo, S.; Baney, R.; Subhash, G.; Tulenko, J. The Influence of SiC Particle Size and Volume Fraction on the Thermal Conductivity of Spark Plasma Sintered UO<sub>2</sub>-SiC Composites. *J. Nucl. Mater.* **2013**, *442*, 245–252.
- (24) Ishimoto, S.; Hirai, M.; Ito, K.; Korei, Y. Thermal Conductivity of UO<sub>2</sub>-BeO Pellet. *J. Nucl. Sci. Technol.* **1996**, *33*, 134–140.
- (25) Liu, X. Y.; Cooper, M. W. D.; McClellan, K. J.; Lashley, J. C.; Byler, D. D.; Bell, B. D. C.; Grimes, R. W.; Stanek, C. R.; Andersson, D. A. Molecular Dynamics Simulation of Thermal Transport in UO<sub>2</sub>

- Containing Uranium, Oxygen, and Fission-product Defects. *Phys. Rev. Appl.* **2016**, *6*, 044015.
- (26) Tonks, M. R.; Liu, X. Y.; Andersson, D.; Perez, D.; Chernatynskiy, A.; Pastore, G.; Stanek, C. R.; Williamson, R. Development of a Multiscale Thermal Conductivity Model for Fission Gas in  $\text{UO}_2$ . *J. Nucl. Mater.* **2016**, *469*, 89–98.
- (27) Pang, J. W.; Buyers, W. J.; Chernatynskiy, A.; Lumsden, M. D.; Larson, B. C.; Phillpot, S. R. Phonon Lifetime Investigation of Anharmonicity and Thermal Conductivity of  $\text{UO}_2$  by Neutron Scattering and Theory. *Phys. Rev. Lett.* **2013**, *110*, 157401.
- (28) Khafizov, M.; Riyad, M. F.; Wang, Y. Z.; Pakarinen, J.; He, L. F.; Yao, T. K.; El-Azab, A.; Hurley, D. Combining Mesoscale Thermal Transport and X-ray Diffraction Measurements to Characterize Early-Stage Evolution of Irradiation-Induced Defects in Ceramics. *Acta Mater.* **2020**, *193*, 61–70.
- (29) Dennett, C. A.; Hua, Z. L.; Khanolkar, A.; Yao, T. K.; Morgan, P. K.; Prusnick, T. A.; Poudel, N.; French, A.; Gofryk, K.; He, L. F.; et al. The Influence of Lattice Defects, Recombination, and Clustering on Thermal Transport in Single Crystal Thorium Dioxide. *APL Mater.* **2020**, *8*, 111103.
- (30) Klemens, P. G. The Scattering of Low-Frequency Lattice Waves by Static Imperfections. *Proc. Phys. Soc., London, Sect. A* **1955**, *A68*, 1113–1128.
- (31) Callaway, J.; von Baeyer, H. C. Effect of Point Imperfections on Lattice Thermal Conductivity. *Phys. Rev.* **1960**, *120*, 1149–1154.
- (32) Slack, G. A. Thermal Conductivity of Pure and Impure Silicon, Silicon Carbide, and Diamond. *J. Appl. Phys.* **1964**, *35*, 3460–3466.
- (33) Berman, R.; Foster, E. L.; Schneidmesser, B.; Tirmizi, S. M. A. Effects of Irradiation on the Thermal Conductivity of Synthetic Sapphire. *J. Appl. Phys.* **1960**, *31*, 2156–2159.
- (34) Broido, D. A.; Malorny, M.; Birner, G.; Mingo, N.; Stewart, D. A. Intrinsic Lattice Thermal Conductivity of Semiconductors from First Principles. *Appl. Phys. Lett.* **2007**, *91*, 231922.
- (35) Ward, A.; Broido, D. A.; Stewart, D. A.; Deinzer, G. Ab Initio Theory of the Lattice Thermal Conductivity in Diamond. *Phys. Rev. B: Condens. Matter Mater. Phys.* **2009**, *80*, 125203.
- (36) Esfarjani, K.; Chen, G.; Stokes, H. T. Heat Transport in Silicon from First-Principles Calculations. *Phys. Rev. B: Condens. Matter Mater. Phys.* **2011**, *84*, 085204.
- (37) Mingo, N.; Yang, L. Phonon Transport in Nanowires Coated with an Amorphous Material: An Atomistic Green's Function Approach. *Phys. Rev. B: Condens. Matter Mater. Phys.* **2003**, *68*, 245406.
- (38) Pernot, G.; Stoffel, M.; Savic, I.; Pezzoli, F.; Chen, P.; Savelli, G.; Jacquot, A.; Schumann, J.; Denker, U.; Mönch, I.; et al. Precise Control of Thermal Conductivity at the Nanoscale Through Individual Phonon-Scattering Barriers. *Nat. Mater.* **2010**, *9*, 491–495.
- (39) Protik, N. H.; Carrete, J.; Katcho, N. A.; Mingo, N.; Broido, D. Ab Initio Study of the Effect of Vacancies on the Thermal Conductivity of Boron Arsenide. *Phys. Rev. B: Condens. Matter Mater. Phys.* **2016**, *94*, 045207.
- (40) Delaire, O.; Ma, J.; Marty, K.; May, A. F.; McGuire, M. A.; Du, M.-H.; Singh, D. J.; Podlesnyak, A.; Ehlers, G.; Lumsden, M. D.; et al. Giant Anharmonic Phonon Scattering in  $\text{PbTe}$ . *Nat. Mater.* **2011**, *10*, 614–619.
- (41) Burkel, E. Phonon Spectroscopy by Inelastic X-ray Scattering. *Rep. Prog. Phys.* **2000**, *63*, 171–232.
- (42) Cahill, D. G.; Ford, W. K.; Goodson, K. E.; Mahan, G. D.; Majumdar, A.; Maris, H. J.; Merlin, R.; Phillpot, S. R. Nanoscale Thermal Transport. *J. Appl. Phys.* **2003**, *93*, 793–818.
- (43) Broido, D. A.; Ward, A.; Mingo, N. Lattice Thermal Conductivity of Silicon from Empirical Interatomic Potentials. *Phys. Rev. B: Condens. Matter Mater. Phys.* **2005**, *72*, 014308.
- (44) Omini, M.; Sparavigna, A. Beyond the Isotropic-Model Approximation in the Theory of Thermal Conductivity. *Phys. Rev. B: Condens. Matter Mater. Phys.* **1996**, *53*, 9064–9073.
- (45) Turney, J. E.; Landry, E. S.; McGaughey, A. J. H.; Amon, C. H. Predicting Phonon Properties and Thermal Conductivity from Anharmonic Lattice Dynamics Calculations and Molecular Dynamics Simulations. *Phys. Rev. B: Condens. Matter Mater. Phys.* **2009**, *79*, 064301.
- (46) Squires, G. L. *Introduction to the Theory of Thermal Neutron Scattering*; Cambridge University Press: Cambridge, U.K., 2012; p 25.
- (47) Kittel, C. *Introduction to Solid State Physics*; Wiley: New York, 1976; p 89.
- (48) Fultz, B. Vibrational Thermodynamics of Materials. *Prog. Mater. Sci.* **2010**, *55*, 247–352.
- (49) Dolling, G.; Cowley, R. A.; Woods, A. D. B. The Crystal Dynamics of Uranium Dioxide. *Can. J. Phys.* **1965**, *43*, 1397–1413.
- (50) Clausen, K.; Hayes, W.; Macdonald, J. E.; Osborn, R.; Schnabel, P. G.; Hutchings, M. T.; Magerl, A. Inelastic Neutron Scattering Investigation of the Lattice Dynamics of  $\text{ThO}_2$  and  $\text{CeO}_2$ . *J. Chem. Soc., Faraday Trans. 2* **1987**, *83*, 1109–1112.
- (51) Brockhouse, B. N.; Stewart, A. T. Scattering of Neutrons by Phonons in an Aluminum Single Crystal. *Phys. Rev.* **1955**, *100*, 756–757.
- (52) Woods, A. D. B.; Cochran, W.; Brockhouse, B. N. Lattice Dynamics of Alkali Halide Crystals. *Phys. Rev.* **1960**, *119*, 980–999.
- (53) Verbeni, R.; Sette, F.; Krisch, M. H.; Bergmann, U.; Gorges, B.; Halcoussis, C.; Martel, K.; Masciovecchio, C.; Ribois, J. F.; Ruocco, G.; et al. X-ray Monochromator with  $2 \times 10^8$  Energy Resolution. *J. Synchrotron Radiat.* **1996**, *3*, 62–64.
- (54) Sinn, H.; Alp, E. E.; Barraza, J.; Bortel, G.; Burkel, E.; Shu, D.; Sturhahn, W.; Sutter, J. P.; Toellner, T. S.; et al. An Inelastic X-ray Spectrometer with 2.2 meV Energy Resolution. *Nucl. Instrum. Methods Phys. Res., Sect. A* **2001**, *467–468*, 1545–1548.
- (55) Alatas, A.; Leu, B. M.; Zhao, J.; Yavas, H.; Toellner, T. S.; Alp, E. E. Improved Focusing Capability for Inelastic X-ray Spectrometer at 3-ID of the APS: A Combination of Toroidal and Kirkpatrick-Baez (KB) Mirrors. *Nucl. Instrum. Methods Phys. Res., Sect. A* **2011**, *649*, 166–168.
- (56) Toellner, T. S.; Alatas, A.; Said, A. H. Six-Reflection meV-Monochromator for Synchrotron Radiation. *J. Synchrotron Radiat.* **2011**, *18*, 605–611.
- (57) Manley, M. E.; Lander, G. H.; Sinn, H.; Alatas, A.; Hulst, W. L.; McQueeney, R. J.; Smith, J. L.; Willit, J. Phonon Dispersion in Uranium Measured using Inelastic X-ray Scattering. *Phys. Rev. B: Condens. Matter Mater. Phys.* **2003**, *67*, 052302.
- (58) Wong, J.; Krisch, M.; Farber, D. L.; Ocellini, F.; Schwartz, A. J.; Chiang, T.-C.; Wall, M.; Boro, C.; Xu, R. Phonon Dispersion of FCC d-Plutonium-Gallium by Inelastic X-ray Scattering. *Science* **2003**, *301*, 1078–1080.
- (59) Manley, M. E.; Jeffries, J. R.; Said, A. H.; Marianetti, C. A.; Cynn, H.; Leu, B. M.; Wall, M. A. Measurement of the Phonon Density of States of  $\text{PuO}_2(+2\% \text{ Ga})$ : A Critical Test of the Theory. *Phys. Rev. B: Condens. Matter Mater. Phys.* **2012**, *85*, 132301.
- (60) Maldonado, P.; Paolasini, L.; Oppeneer, P. M.; Forrest, T. R.; Prodi, A.; Magnani, N.; Bosak, A.; Lander, G. H.; Caciuffo, R. Crystal Dynamics and Thermal Properties of Neptunium Dioxide. *Phys. Rev. B* **2016**, *93*, 144301.
- (61) Stone, M. B.; Niedziela, J. L.; Abernathy, D. L.; DeBeer-Schmitt, L.; Ehlers, G.; Garlea, O.; Granroth, G. E.; Graves-Brook, M.; Kolesnikov, A. I.; Podlesnyak, A.; et al. A Comparison of Four Direct Geometry Time-of-Flight Spectrometers at the Spallation Neutron Source. *Rev. Sci. Instrum.* **2014**, *85*, 045113.
- (62) Janoschek, M.; Das, P.; Chakrabarti, B.; Abernathy, D. L.; Lumsden, M. D.; Lawrence, J. M.; Thompson, J. D.; Lander, G. H.; Mitchell, J. N.; Richmond, S.; et al. The Valence-Fluctuating Ground State of Plutonium. *Sci. Adv.* **2015**, *1*, No. e1500188.
- (63) Pang, J. W. L.; Chernatynskiy, A.; Larson, B. C.; Buyers, W. J. L.; Abernathy, D. L.; McClellan, K. J.; Phillpot, S. R. Phonon Density of States and Anharmonicity of  $\text{UO}_2$ . *Phys. Rev. B: Condens. Matter Mater. Phys.* **2014**, *89*, 115132.
- (64) Yin, Q.; Savrasov, S. Y. Origin of the Low Thermal Conductivity in Nuclear Fuels. *Phys. Rev. Lett.* **2008**, *100*, 225504.
- (65) Rennie, S.; Lawrence Bright, E.; Darnbrough, J. E.; Paolasini, L.; Bosak, A.; Smith, A. D.; Mason, N.; Lander, G. H.; Springell, R. Study of Phonons in Irradiated Epitaxial Thin Films of  $\text{UO}_2$ . *Phys. Rev. B: Condens. Matter Mater. Phys.* **2018**, *97*, 224303.

- (66) Weisensee, P. B.; Feser, J. P.; Cahill, D. G. Effect of Ion Irradiation on the Thermal Conductivity of  $\text{UO}_2$  and  $\text{U}_3\text{O}_8$  Epitaxial Layers. *J. Nucl. Mater.* **2013**, *443*, 212–217.
- (67) Bryan, M. S.; Fu, L.; Rickert, K.; Turner, D.; Prusnick, T. A.; Mann, J. M.; Abernathy, D. L.; Marianetti, C. A.; Manley, M. E. Nonlinear Propagating Modes Beyond the Phonons in Fluorite-Structured Crystals. *Commun. Phys.* **2020**, *3*, 217.
- (68) Manley, M. E.; Sievers, A. J.; Lynn, J. W.; Kiselev, S. A.; Agladze, N. I.; Chen, Y.; Llobet, A.; Alatas, A. Intrinsic Localized Modes Observed in the High-Temperature Vibrational Spectrum of NaI. *Phys. Rev. B: Condens. Matter Mater. Phys.* **2009**, *79*, 134304.
- (69) Hohenberg, P.; Kohn, W. Inhomogeneous Electron Gas. *Phys. Rev.* **1964**, *136*, B864–B871.
- (70) Kohn, W.; Sham, L. J. Self-Consistent Equations Including Exchange and Correlation Effects. *Phys. Rev.* **1965**, *140*, A1133–A1138.
- (71) Kohn, W. Nobel Lecture: Electronic Structure of Matter-Wave Functions and Density Functionals. *Rev. Mod. Phys.* **1999**, *71*, 1253–1266.
- (72) Jones, R. O.; Gunnarsson, O. The Density Functional Formalism, Its Applications and Prospects. *Rev. Mod. Phys.* **1989**, *61*, 689–746.
- (73) Jones, R. O. Density Functional Theory: Its Origins, Rise to Prominence, and Future. *Rev. Mod. Phys.* **2015**, *87*, 897–923.
- (74) Kummel, S.; Kronik, L. Orbital-Dependent Density Functionals: Theory and Applications. *Rev. Mod. Phys.* **2008**, *80*, 3–60.
- (75) Ernzerhof, M.; Scuseria, G. E. Assessment of the Perdew-Burke-Ernzerhof Exchange-Correlation Functional. *J. Chem. Phys.* **1999**, *110*, 5029–5036.
- (76) Adamo, C.; Barone, V. Toward Reliable Density Functional Methods Without Adjustable Parameters: The PBE0 model. *J. Chem. Phys.* **1999**, *110*, 6158–6170.
- (77) Oba, F.; Togo, A.; Tanaka, I.; Paier, J.; Kresse, G. Defect Energetics in ZnO: A Hybrid Hartree-Fock Density Functional Study. *Phys. Rev. B: Condens. Matter Mater. Phys.* **2008**, *77*, 245202.
- (78) Franchini, C.; Bayer, V.; Podloucky, R.; Paier, J.; Kresse, G. Density Functional Theory Study of MnO by a Hybrid Functional Approach. *Phys. Rev. B: Condens. Matter Mater. Phys.* **2005**, *72*, 045132.
- (79) Tran, F.; Blaha, P.; Schwarz, K.; Novak, P. Hybrid Exchange-Correlation Energy Functionals for Strongly Correlated Electrons: Applications to Transition-Metal Monoxides. *Phys. Rev. B: Condens. Matter Mater. Phys.* **2006**, *74*, 155108.
- (80) Franchini, C.; Podloucky, R.; Paier, J.; Marsman, M.; Kresse, G. Ground-State Properties of Multivalent Manganese Oxides: Density Functional and Hybrid Density Functional Calculations. *Phys. Rev. B: Condens. Matter Mater. Phys.* **2007**, *75*, 195128.
- (81) Rodl, C.; Fuchs, F.; Furthmüller, J.; Bechstedt, F. Quasiparticle Band Structures of the Antiferromagnetic Transition-Metal Oxides MnO, FeO, CoO, and NiO. *Phys. Rev. B: Condens. Matter Mater. Phys.* **2009**, *79*, 235114.
- (82) Paier, J.; Marsman, M.; Kresse, G. Why Does the b3lyp Hybrid Functional Fail for Metals? *J. Chem. Phys.* **2007**, *127*, 024103.
- (83) Heyd, J.; Scuseria, G. E.; Ernzerhof, M. Hybrid Functionals Based on a Screened Coulomb Potential. *J. Chem. Phys.* **2003**, *118*, 8207–8215.
- (84) Eyert, V. The Metal-Insulator Transitions of  $\text{VO}_2$ : A Band Theoretical Approach. *Ann. Phys.* **2002**, *11*, 650–702.
- (85) Grau-Crespo, R.; Wang, H.; Schwingenschloegl, U. Why the Heyd-Scuseria-Ernzerhof hybrid Functional Description of  $\text{VO}_2$  Phases is Not Correct. *Phys. Rev. B: Condens. Matter Mater. Phys.* **2012**, *86*, 081101.
- (86) Kosuge, K. The Phase Transition in  $\text{VO}_2$ . *J. Phys. Soc. Jpn.* **1967**, *22*, 551–557.
- (87) Qazilbash, M. M.; Burch, K. S.; Whisler, D.; Shrekenhamer, D.; Chae, B. G.; Kim, H. T.; Basov, D. N. Correlated Metallic State of Vanadium Dioxide. *Phys. Rev. B: Condens. Matter Mater. Phys.* **2006**, *74*, 205118.
- (88) Paier, J.; Hirschl, R.; Marsman, M.; Kresse, G. The Perdew-Burke-Ernzerhof Exchange-Correlation Functional Applied to the g2–1 Test Set using a Plane-Wave Basis Set. *J. Chem. Phys.* **2005**, *122*, 234102.
- (89) Anisimov, V. I.; Aryasetiawan, F.; Lichtenstein, A. I. First-Principles Calculations of the Electronic Structure and Spectra of Strongly Correlated Systems: The LDA+U Method. *J. Phys.: Condens. Matter* **1997**, *9*, 767–808.
- (90) Ivady, V.; Armiento, R.; Szasz, K.; Janzen, E.; Gali, A.; Abrikosov, I. A. Theoretical Unification of Hybrid-DFT and DFT Plus U Methods for the Treatment of Localized Orbitals. *Phys. Rev. B: Condens. Matter Mater. Phys.* **2014**, *90*, 035146.
- (91) Agapito, L. A.; Curtarolo, S.; Buongiorno Nardelli, M. Reformulation of DFT Plus U as a Pseudohybrid Hubbard Density Functional for Accelerated Materials Discovery. *Phys. Rev. X* **2015**, *5*, 011006.
- (92) Luttinger, J. M.; Ward, J. C. Ground-State Energy of a Many-Fermion System. II. *Phys. Rev.* **1960**, *118*, 1417–1427.
- (93) Baym, G.; Kadanoff, L. P. Conservation Laws and Correlation Functions. *Phys. Rev.* **1961**, *124*, 287–299.
- (94) Dedominicis, C.; Martin, P. C. Stationary Entropy Principle + Renormalization in Normal + Superfluid Systems. I. Algebraic Formulation. *J. Math. Phys.* **1964**, *5*, 14–30.
- (95) Chitra, R.; Kotliar, G. Effective-Action Approach to Strongly Correlated Fermion Systems. *Phys. Rev. B: Condens. Matter Mater. Phys.* **2001**, *63*, 115110.
- (96) Gutzwiller, M. C. Effect of Correlation on Ferromagnetism of Transition Metals. *Phys. Rev. Lett.* **1963**, *10*, 159–162.
- (97) Kanamori, J. Electron Correlation and Ferromagnetism of Transition Metals. *Prog. Theor. Phys.* **1963**, *30*, 275–289.
- (98) Hubbard, J. Electron Correlations in Narrow Energy Bands. *Proc. R. Soc., Ser. A* **1963**, *276*, 238–257.
- (99) Lieb, E. H.; Wu, F. Y. Absence of Mott Transition in an Exact Solution of Short-Range 1-Band Model in 1 Dimension. *Phys. Rev. Lett.* **1968**, *20*, 1445–1448.
- (100) Lieb, E. H.; Wu, F. Y. The One-Dimensional Hubbard Model: A Reminiscence. *Phys. A* **2003**, *321*, 1–27.
- (101) Georges, A.; Kotliar, G.; Krauth, W.; Rozenberg, M. J. Dynamical Mean-Field Theory of Strongly Correlated Fermion Systems and the Limit of Infinite Dimensions. *Rev. Mod. Phys.* **1996**, *68*, 13–125.
- (102) Kotliar, G.; Savrasov, S. Y.; Haule, K.; Oudovenko, V. S.; Parcollet, O.; Marianetti, C. A. Electronic Structure Calculations with Dynamical Mean-Field Theory. *Rev. Mod. Phys.* **2006**, *78*, 865–951.
- (103) Gull, E.; Millis, A. J.; Lichtenstein, A. I.; Rubtsov, A. N.; Troyer, M.; Werner, P. Continuous-Time Monte-Carlo Methods for Quantum Impurity Models. *Rev. Mod. Phys.* **2011**, *83*, 349.
- (104) Haule, K. Quantum Monte Carlo Impurity Solver for Cluster Dynamical Mean-Field Theory and Electronic Structure Calculations with Adjustable Cluster Base. *Phys. Rev. B: Condens. Matter Mater. Phys.* **2007**, *75*, 155113.
- (105) Troyer, M.; Wiese, U. J. Computational Complexity and Fundamental Limitations to Fermionic Quantum Monte Carlo Simulations. *Phys. Rev. Lett.* **2005**, *94*, 170201.
- (106) Park, H.; Millis, A. J.; Marianetti, C. A. Total Energy Calculations Using DFT Plus DMFT: Computing the Pressure Phase Diagram of the Rare Earth Nickelates. *Phys. Rev. B: Condens. Matter Mater. Phys.* **2014**, *89*, 245133.
- (107) Park, H.; Millis, A. J.; Marianetti, C. A. Computing Total Energies in Complex Materials Using Charge Self-Consistent DFT +DMFT. *Phys. Rev. B: Condens. Matter Mater. Phys.* **2014**, *90*, 235103.
- (108) Haule, K.; Birol, T. Free Energy from Stationary Implementation of the DFT+DMFT Functional. *Phys. Rev. Lett.* **2015**, *115*, 256402.
- (109) Delange, P.; Ayrat, T.; Simak, S. I.; Ferrero, M.; Parcollet, O.; Biermann, S.; Pourovskii, L. Large Effects of Subtle Electronic Correlations on the Energetics of Cacanics in Alpha-Fe. *Phys. Rev. B: Condens. Matter Mater. Phys.* **2016**, *94*, 100102.
- (110) Leonov, I.; Anisimov, V. I.; Vollhardt, D. First-Principles Calculation of Atomic Forces and Structural Distortions in Strongly Correlated Materials. *Phys. Rev. Lett.* **2014**, *112*, 146401.
- (111) Haule, K.; Pascut, G. L. Mott Transition and Magnetism in Rare Earth Nickelates and Its Fingerprint on the X-ray Scattering. *Sci. Rep.* **2017**, *7*, 10375.

- (112) Anisimov, V. I.; Zaanen, J.; Andersen, O. K. Band Theory and Mott Insulators - Hubbard-U Instead of Stoner-I. *Phys. Rev. B: Condens. Matter Mater. Phys.* **1991**, *44*, 943–954.
- (113) Fu, L.; Kornbluth, M.; Cheng, Z.; Marianetti, C. A. Group Theoretical Approach to Computing Phonons and Their Interactions. *Phys. Rev. B: Condens. Matter Mater. Phys.* **2019**, *100*, 014303.
- (114) Martin, R. M. *Electronic Structure: Basic Theory and Practical Methods*; Cambridge University Press: New York, 2008; p 52.
- (115) Baroni, S.; deGironcoli, S.; DalCorso, A.; Giannozzi, P. Phonons and Related Crystal Properties from Density-Functional Perturbation Theory. *Rev. Mod. Phys.* **2001**, *73*, 515–562.
- (116) Kunc, K.; Martin, R. M. Ab Initio Force Constants of GaAs: A New Approach to Calculation of Phonons and Dielectric Properties. *Phys. Rev. Lett.* **1982**, *48*, 406–409.
- (117) Parlinski, K.; Li, Z.; Kawazoe, Y. First-Principles Determination of the Soft Mode in Cubic ZrO<sub>2</sub>. *Phys. Rev. Lett.* **1997**, *78*, 4063–4066.
- (118) Ziman, J. M. *Electrons and Phonons: The Theory of Transport Phenomena in Solids*; Oxford University Press: London, 1960; p 264.
- (119) Fugallo, G.; Lazzeri, M.; Paulatto, L.; Mauri, F. Ab Initio Variational Approach for Evaluating Lattice Thermal Conductivity. *Phys. Rev. B: Condens. Matter Mater. Phys.* **2013**, *88*, 045430.
- (120) Fugallo, G.; Colombo, L. Calculating Lattice Thermal Conductivity: A Synopsis. *Phys. Scr.* **2018**, *93*, 043002.
- (121) Lindsay, L.; Katre, A.; Cepellotti, A.; Mingo, N. Perspective on Ab Initio Phonon Thermal Transport. *J. Appl. Phys.* **2019**, *126*, 050902.
- (122) Feng, T. L.; Ruan, X. L. Quantum Mechanical Prediction of Four-Phonon Scattering Rates and Reduced Thermal Conductivity of Solids. *Phys. Rev. B: Condens. Matter Mater. Phys.* **2016**, *93*, 045202.
- (123) Feng, T. L.; Lindsay, L.; Ruan, X. L. Four-Phonon Scattering Significantly Reduces Intrinsic Thermal Conductivity of Solids. *Phys. Rev. B: Condens. Matter Mater. Phys.* **2017**, *96*, 161201.
- (124) Ravichandran, N. K.; Broido, D. Unified First-Principles Theory of Thermal Properties of Insulators. *Phys. Rev. B: Condens. Matter Mater. Phys.* **2018**, *98*, 085205.
- (125) Ravichandran, N. K.; Broido, D. Phonon-Phonon Interactions in Strongly Bonded Solids: Selection Rules and Higher-Order Processes. *Phys. Rev. X* **2020**, *10*, 021063.
- (126) Carbogno, C.; Ramprasad, R.; Scheffler, M. Ab Initio Green–Kubo Approach for the Thermal Conductivity of Solids. *Phys. Rev. Lett.* **2017**, *118*, 175901.
- (127) Kang, J.; Wang, L. W. First-Principles Green–Kubo Method for Thermal Conductivity Calculations. *Phys. Rev. B: Condens. Matter Mater. Phys.* **2017**, *96*, 020302.
- (128) Lu, Y.; Yang, Y.; Zhang, P. Thermodynamic Properties and Structural Stability of Thorium Dioxide. *J. Phys.: Condens. Matter* **2012**, *24*, 225801.
- (129) Szpunar, B.; Szpunar, J. A. Theoretical Investigation of Structural and Thermo-Mechanical Properties of Thoria up to 3300 K Temperature. *Solid State Sci.* **2014**, *36*, 35–40.
- (130) Szpunar, B.; Szpunar, J. A.; Sim, K. S. Theoretical Investigation of Structural and Thermo-Mechanical Properties of Thoria. *J. Phys. Chem. Solids* **2016**, *90*, 114–120.
- (131) Malakkal, L.; Szpunar, B.; Zuniga, J. C.; Siripurapu, R. K.; Szpunar, J. A. First Principles Calculation of Thermo-Mechanical Properties of Thoria Using Quantum Espresso. *Int. J. Comput. Mater. Sci. Eng.* **2016**, *5*, 1650008.
- (132) Dennett, C. A.; Deskins, W. R.; Khafizov, M.; Hua, Z.; Khanolkar, A.; Bawane, K.; Fu, L.; Mann, J. M.; Marianetti, C. A.; He, L.; et al. An Integrated Experimental and Computational Investigation of Defect and Microstructural Effects on Thermal Transport in Thorium Dioxide. *Acta Mater.* **2021**, *213*, 116934.
- (133) Toropova, A.; Marianetti, C. A.; Haule, K.; Kotliar, G. One-Electron Physics of the Actinides. *Phys. Rev. B: Condens. Matter Mater. Phys.* **2007**, *76*, 155126.
- (134) Wen, X.; Martin, R. L.; Henderson, T. M.; Scuseria, G. E. Density Functional Theory Studies of the Electronic Structure of Solid State Actinide Oxides. *Chem. Rev.* **2013**, *113*, 1063–1096.
- (135) Boettger, J. C.; Ray, A. K. All-Electron LCGTO Calculations for Uranium Dioxide. *Int. J. Quantum Chem.* **2000**, *80*, 824–830.
- (136) Prodan, I. D.; Scuseria, G. E.; Martin, R. L. Assessment of Metageneralized Gradient Approximation and Screened Coulomb Hybrid Density Functionals on Bulk Actinide Oxides. *Phys. Rev. B: Condens. Matter Mater. Phys.* **2006**, *73*, 045104.
- (137) Prodan, I. D.; Scuseria, G. E.; Martin, R. L. Covalency in the Actinide Dioxides: Systematic Study of the Electronic Properties Using Screened Hybrid Density Functional Theory. *Phys. Rev. B: Condens. Matter Mater. Phys.* **2007**, *76*, 033101.
- (138) Laskowski, R.; Madsen, G. K. H.; Blaha, P.; Schwarz, K. Magnetic Structure and Electric-Field Gradients of Uranium Dioxide: An Ab Initio Study. *Phys. Rev. B* **2004**, *69*, 140408.
- (139) Zhou, F.; Ozolins, V. Crystal Field and Magnetic Structure of UO<sub>2</sub>. *Phys. Rev. B: Condens. Matter Mater. Phys.* **2011**, *83*, 085106.
- (140) Suzuki, M. T.; Magnani, N.; Oppeneer, P. M. Microscopic Theory of the Insulating Electronic Ground States of the Actinide Dioxides AnO<sub>2</sub> (An= U, Np, Pu, Am, and Cm). *Phys. Rev. B: Condens. Matter Mater. Phys.* **2013**, *88*, 195146.
- (141) Dudarev, S. L.; Liu, P.; Andersson, D. A.; Stanek, C. R.; Ozaki, T.; Franchini, C. Parametrization of LSDA Plus U for Noncollinear Magnetic Configurations: Multipolar Magnetism in UO<sub>2</sub>. *Phys. Rev. Mater.* **2019**, *3*, 083802.
- (142) Pi, S. T.; Nanguneri, R.; Savrasov, S. Calculation of Multipolar Exchange Interactions in Spin-Orbital Coupled Systems. *Phys. Rev. Lett.* **2014**, *112*, 077203.
- (143) Sanati, M.; Albers, R. C.; Lookman, T.; Saxena, A. Elastic Constants, Phonon Density of States, and Thermal Properties of UO<sub>2</sub>. *Phys. Rev. B: Condens. Matter Mater. Phys.* **2011**, *84*, 014116.
- (144) Wang, B. T.; Zhang, P.; Lizarraga, R.; Di Marco, I.; Eriksson, O. Phonon Spectrum, Thermodynamic Properties, and Pressure-Temperature Phase Diagram of Uranium Dioxide. *Phys. Rev. B: Condens. Matter Mater. Phys.* **2013**, *88*, 104107.
- (145) Kolorenc, J.; Shick, A. B.; Lichtenstein, A. I. Electronic Structure and Core-Level Spectra of Light Actinide Dioxides in the Dynamical Mean-Field Theory. *Phys. Rev. B: Condens. Matter Mater. Phys.* **2015**, *92*, 085125.
- (146) Pourvorskii, L. V.; Khmelevskiy, S. Quadrupolar Superexchange Interactions, Multipolar Order, and Magnetic Phase Transition in UO<sub>2</sub>. *Phys. Rev. B: Condens. Matter Mater. Phys.* **2019**, *99*, 094439.
- (147) Lanata, N.; Yao, Y. X.; Deng, X. Y.; Dobrosavljevic, V.; Kotliar, G. Slave Boson Theory of Orbital Differentiation with Crystal Field Effects: Application to UO<sub>2</sub>. *Phys. Rev. Lett.* **2017**, *118*, 126401.
- (148) Slack, G. A. Nonmetallic Crystals with High Thermal Conductivity. *J. Phys. Chem. Solids* **1973**, *34*, 321–335.
- (149) Lu, Y.; Yang, Y.; Zhang, P. Thermodynamic Properties and Structural Stability of Thorium Dioxide. *J. Phys.: Condens. Matter* **2012**, *24*, 225801.
- (150) Kaur, G.; Panigrahi, P.; Valsakumar, M. C. Thermal Properties of UO<sub>2</sub> with a Non-Local Exchange-Correlation Pressure Correction: A Systematic First Principles DFT Plus U Study. *Modell. Simul. Mater. Sci. Eng.* **2013**, *21*, 06S014.
- (151) Nakamura, H.; Machida, M. First-Principles Calculation Study on Phonon Thermal Conductivity of Thorium and Plutonium Dioxides: Intrinsic Anharmonic Phonon-Phonon and Extrinsic Grain-Boundary-Phonon Scattering Effects. *J. Nucl. Mater.* **2019**, *519*, 45–51.
- (152) Jin, M.; Khafizov, M.; Jiang, C.; Zhou, S.; Marianetti, C.; Bryan, M.; Manley, M. E.; Hurley, D. H. Assessment of Empirical Interatomic Potential to Predict Thermal Conductivity in ThO<sub>2</sub> and UO<sub>2</sub>. *J. Phys.: Condens. Matter* **2021**, *33*, 275402.
- (153) Liu, J. Y.; Dai, Z. H.; Yang, X. X.; Zhao, Y. C.; Meng, S. Lattice Thermodynamic Behavior in Nuclear Fuel ThO<sub>2</sub> from First Principles. *J. Nucl. Mater.* **2018**, *511*, 11–17.
- (154) Malakkal, L.; Prasad, A.; Jossou, E.; Ranasinghe, J.; Szpunar, B.; Bichler, L.; Szpunar, J. Thermal Conductivity of Bulk and Porous ThO<sub>2</sub>: Atomistic and Experimental Study. *J. Alloys Compd.* **2019**, *798*, 507–516.
- (155) Jones, W. M.; Gordon, J.; Long, E. A. The Heat Capacities of Uranium, Uranium Trioxide, and Uranium Dioxide from 15 to 300 K. *J. Chem. Phys.* **1952**, *20*, 695–699.

- (156) Osborne, D. W.; Westrum, E. F. Specific Heat of  $\text{NpO}_2$  at Low Temperature. *J. Chem. Phys.* **1953**, *21*, 1884–1887.
- (157) Frazer, B. C.; Shirane, G.; Cox, D. E.; Olsen, C. E. Neutron Diffraction Study of Antiferromagnetism in  $\text{UO}_2$ . *Phys. Rev.* **1965**, *140*, A1448–A1452.
- (158) Willis, B. T. M.; Taylor, R. J. Neutron Diffraction Study of Antiferromagnetism in  $\text{UO}_2$ . *Phys. Lett.* **1965**, *17*, 188–190.
- (159) Burel, P.; Rossat-Mignod, J.; Vuevel, S.; Vogt, O.; Spirlet, J. C.; Rebivant, J. Neutron Diffraction on Actinides. *J. Less-Common. Met.* **1986**, *121*, 121–139.
- (160) Blackburn, E.; Caciuffo, R.; Magnani, N.; Santini, P.; Brown, P. J.; Enderle, M.; Lander, G. H. Spherical Neutron Spin Polarimetry of Anisotropic Magnetic Fluctuations in  $\text{UO}_2$ . *Phys. Rev. B: Condens. Matter Mater. Phys.* **2005**, *72*, 184411.
- (161) Paixão, J. A.; Detlefs, C.; Longfield, M. J.; Caciuffo, R.; Santini, P.; Bernhoeft, N.; Rebizant, J.; Lander, G. H. Triple-q Octupolar Ordering in  $\text{NpO}_2$ . *Phys. Rev. Lett.* **2002**, *89*, 187202.
- (162) Wilkins, S. B.; Caciuffo, R.; Detlefs, C.; Rebizant, J.; Colineau, E.; Wastin, F.; Lander, G. H. Direct Observation of Electric-Quadrupolar Order in  $\text{UO}_2$ . *Phys. Rev.* **2006**, *73*, 060406.
- (163) Santini, P.; Carretta, S.; Amoretti, G.; Caciuffo, R.; Magnani, N.; Lander, G. H. Multipolar Interactions in  $f$ -Electron Systems: The Paradigm of Actinide Dioxides. *Rev. Mod. Phys.* **2009**, *81*, 807–863.
- (164) Caciuffo, R.; Santini, P.; Carretta, S.; Amoretti, G.; Hiess, A.; Magnani, N.; Regnault, L.-P.; Lander, G. H. Multipolar, Magnetic, and Vibrational Lattice Dynamics in the Low-Temperature Phase of Uranium Dioxide. *Phys. Rev. B: Condens. Matter Mater. Phys.* **2011**, *84*, 104409.
- (165) Carretta, S.; Santini, P.; Caciuffo, R.; Amoretti, G. Quadrupolar Waves in Uranium Dioxide. *Phys. Rev. Lett.* **2010**, *105*, 167201.
- (166) Lander, G. H.; Caciuffo, R. The Fifty Years It Has Taken to Understand the Dynamics of  $\text{UO}_2$  in Its Ordered State. *J. Phys.: Condens. Matter* **2020**, *32*, 374001.
- (167) Faber, J.; Lander, G. H. Neutron Diffraction Study of  $\text{UO}_2$ : Antiferromagnetic State. *Phys. Rev. B* **1976**, *14*, 1151–1164.
- (168) Bryan, M. S.; Pang, J. W. L.; Larson, B. C.; Chernatynskiy, A.; Abernathy, D. L.; Gofryk, K.; Manley, M. E. Impact of Anharmonicity on the Vibrational Entropy and Specific Heat of  $\text{UO}_2$ . *Phys. Rev. Mater.* **2019**, *3*, 065405.
- (169) Maldonado, P.; Paolasini, L.; Oppeneer, P. M.; Forrest, T. R.; Prodi, A.; Magnani, N.; Bosak, A.; Lander, G. H.; Caciuffo, R. Crystal Dynamics and Thermal Properties of Neptunium Dioxide. *Phys. Rev. B* **2016**, *93*, 144301.
- (170) Flotow, H. E.; Osborne, D. W.; Fried, S. M.; Malm, J. G. Heat Capacity of  $^{242}\text{PuO}_2$  from 12 to 3500 K and of  $^{244}\text{PuO}_2$  from 4 to 25 K. Entropy, Enthalpy, and Gibbs Energy of Formation of  $\text{PuO}_2$  at 298.15 K. *J. Chem. Phys.* **1976**, *65*, 1124–1129.
- (171) Sandenaw, Th. A. Heat Capacity of Plutonium Dioxide Below 325 K. *J. Nucl. Mater.* **1963**, *10*, 165–172.
- (172) Martel, L.; Hen, A.; Tokunaga, Y.; Kinnart, F.; Magnani, N.; Colineau, E.; Griveau, J.-C.; Caciuffo, R. Magnetization, Specific Heat,  $^{17}\text{O}$  NMR, and  $^{237}\text{Np}$  Mössbauer study of  $\text{U}_{0.15}\text{Np}_{0.85}\text{O}_2$ . *Phys. Rev. B: Condens. Matter Mater. Phys.* **2018**, *98*, 014410.
- (173) Willis, B. T. M.; Hazell, R. G. Re-analysis of Single-Crystal Neutron-Diffraction Data on  $\text{UO}_2$  Using Third Cumulants. *Acta Crystallogr., Sect. A: Cryst. Phys., Diffr., Theor. Gen. Crystallogr.* **1980**, *A36*, 582–584.
- (174) Santini, P.; Carretta, S.; Magnani, N.; Amoretti, G.; Caciuffo, R. Hidden Order and Low-Energy Excitations in  $\text{NpO}_2$ . *Phys. Rev. Lett.* **2006**, *97*, 207203.
- (175) Suzuki, M.-T.; Magnani, M.; Oppeneer, P. M. First-Principles Theory of Multipolar Order in Neptunium Dioxide. *Phys. Rev. B* **2010**, *82*, 241103R.
- (176) Walstedt, R. E.; Tokunaga, Y.; Kambe, S.; Sakai, H. NMR Evidence for  $f$ -Electron Excitations in the Multipolar Ground State of  $\text{NpO}_2$ . *Phys. Rev. B: Condens. Matter Mater. Phys.* **2018**, *98*, 144403.
- (177) Válu, O. S.; Beneš, O.; Konings, R. J. M.; Griveau, J.-C.; Colineau, E. The Low-Temperature Heat Capacity of the (Th, Pu) $\text{O}_2$  Solid Solution. *J. Phys. Chem. Solids* **2015**, *86*, 194–206.
- (178) Magnani, N.; Santini, P.; Amoretti, G.; Caciuffo, R. Perturbative Approach to  $J$  Mixing in  $f$ -Electron Systems: Application to Actinide Dioxide. *Phys. Rev. B: Condens. Matter Mater. Phys.* **2005**, *71*, 054405.
- (179) Mann, M.; Thompson, D.; Serivalsatit, K.; Triitt, T. M.; Ballato, J.; Kolis, J. Hydrothermal Growth and Thermal Property Characterization of  $\text{ThO}_2$  Single Crystals. *Cryst. Growth Des.* **2010**, *10*, 2146–2151.
- (180) Gofryk, K.; Du, S.; Stanek, C. R.; Lashley, J. C.; Liu, X. Y.; Schulze, R. K.; Smith, J. L.; Safarik, D. J.; Byler, D. D.; McClellan, K. J.; et al. Anisotropic Thermal Conductivity in Uranium Dioxide. *Nat. Commun.* **2014**, *5*, 4551.
- (181) Gevers, R.; De Batist, R.; De Coninck, R.; Denayer, M.; Nagels, P.; Penninck, R.; Van den Bosch, A.; Van Lierde, W. *Physical Properties of  $\text{UO}_2$  Single Crystals*; EURAEC Report 1776; European Atomic Energy Community - EURATOM, 1967.
- (182) Slack, G. R. Thermal Conductivity of  $\text{CaF}_2$ ,  $\text{MnF}_2$ ,  $\text{CoF}_2$ , and  $\text{ZnF}_2$  Crystals. *Phys. Rev.* **1961**, *122*, 1451–1464.
- (183) Moore, J.; McElroy, D. Thermal Conductivity of Nearly Stoichiometric Single Crystal and Polycrystalline  $\text{UO}_2$ . *J. Am. Ceram. Soc.* **1971**, *54*, 40–46.
- (184) Hofmann, M.; Lorenz, T.; Uhrig, G. S.; Kierspel, H.; Zabara, O.; Freimuth, A.; Kageyama, H.; Ueda, Y. Strong Damping of Phononic Heat Current by Magnetic Excitations in  $\text{SrCu}_2(\text{BO}_3)_2$ . *Phys. Rev. Lett.* **2001**, *87*, 047202.
- (185) Paolasini, L.; Chaney, D.; Bosak, A.; Lander, G. H.; Caciuffo, R. Anisotropy in Cubic  $\text{UO}_2$  Caused by Electronic-Lattice Interactions. *Phys. Rev. B: Condens. Matter Mater. Phys.* **2021**, *104*, 024305.
- (186) Macedo, P. M.; Capps, W.; Wachtman, J. O. Elastic Constants of Single Crystal  $\text{ThO}_2$  at 25 °C. *J. Am. Ceram. Soc.* **1964**, *47*, 651–651.
- (187) Wachtman, J. B.; Wheat, M. L.; Anderson, H. J.; Bates, J. L. Elastic Constants of Single Crystal  $\text{UO}_2$  at 25 °C. *J. Nucl. Mater.* **1965**, *16*, 39–41.
- (188) Brandt, O. G.; Walker, C. T. Temperature Dependence of Elastic Constants and Thermal Expansion for  $\text{UO}_2$ . *Phys. Rev. Lett.* **1967**, *18*, 11–13.
- (189) Brandt, O. G.; Walker, C. G. Ultrasonic Attenuation and Elastic Constants for Uranium Dioxide. *Phys. Rev.* **1968**, *170*, 528–541.
- (190) White, G. K.; Sheard, F. W. The Thermal Expansion at Low Temperatures of  $\text{UO}_2$  and  $\text{UO}_2/\text{ThO}_2$ . *J. Low Temp. Phys.* **1974**, *14*, 445–457.
- (191) Antonio, D. J.; Weiss, J. T.; Shanks, K. S.; Ruff, J. P. C.; Jaime, M.; Saul, A.; Swinburne, T.; Salamon, M.; Shrestha, K.; Lavina, B.; et al. Piezomagnetic Switching and Complex Phase Equilibria in Uranium Dioxide. *Commun. Mater.* **2021**, *2*, 17.
- (192) Sasaki, K.; Obata, Y. Studies of the Dynamical Jahn-Teller Effect on Static Magnetic Susceptibility. *J. Phys. Soc. Jpn.* **1970**, *28*, 1157–1167.
- (193) Caciuffo, R.; Amoretti, G.; Santini, P.; Lander, G. H.; Kulda, J.; Du Plessis, P. V. Magnetic Excitations and Dynamical Jahn-Teller Distortions in  $\text{UO}_2$ . *Phys. Rev. B: Condens. Matter Mater. Phys.* **1999**, *59*, 13892–13900.
- (194) Dolling, G.; Cowley, R. A. Observation of Magnon-Phonon Interaction at Short Wavelengths. *Phys. Rev. Lett.* **1966**, *16*, 683–685.
- (195) Cowley, R. A.; Dolling, G. Magnetic Excitations in Uranium Dioxide. *Phys. Rev.* **1968**, *167*, 464–477.
- (196) Jaime, M.; Saul, A.; Salamon, M.; Zapf, V. S.; Harrison, N.; Durakiewicz, T.; Lashley, J. C.; Andersson, D. A.; Stanek, C. R.; Smith, J. L.; et al. Piezomagnetism and Magnetoelastic Memory in Uranium Dioxide. *Nat. Commun.* **2017**, *8*, 99.
- (197) Bar'yakhtar, V. G.; Vitebskii, I. M.; Yablonskii, D. A. Magnetoelastic Effects in Noncollinear Antiferromagnets. *Zh. Eksp. Teor. Fiz.* **1985**, *89*, 189–202.
- (198) Ronchi, C.; Hiernaut, J. P. Experimental Measurement of Pre-Melting and Melting of Thorium Dioxide. *J. Alloys Compd.* **1996**, *240*, 179–185.
- (199) Manara, D.; Ronchi, C.; Sheindlin, M.; Lewis, M.; Brykin, M. Melting of Stoichiometric and Hyperstoichiometric Uranium Dioxide. *J. Nucl. Mater.* **2005**, *342*, 148–163.

- (200) De Bruycker, F.; Boboridis, K.; Manara, D.; Poml, P.; Rini, M.; Konings, R. J. M. Reassessing the Melting Temperature of PuO<sub>2</sub>. *Mater. Today* **2010**, *13*, 52–55.
- (201) Capriotti, L.; Quaini, A.; Bohler, R.; Boboridis, K.; Luzzi, L.; Manara, D. A Laser Heating Study of the CeO<sub>2</sub> Solid/Liquid Transition: Challenges Related to a Refractory Compound with a Very High Oxygen Pressure. *High Temp. - High Press.* **2014**, *44*, 69–82.
- (202) Neck, V.; Altmaier, M.; Muller, R.; Bauer, A.; Fanghanel, Th.; Kim, J. I. Solubility of Crystalline Thorium Dioxide. *Radiochim. Acta* **2003**, *91*, 253–262.
- (203) Neck, V.; Kim, J. I. Solubility and Hydrolysis of Tetravalent Actinides. *Radiochim. Acta* **2001**, *89*, 1–16.
- (204) Hayes, S. A.; Yu, P.; O'Keefe, T. J.; O'Keefe, M. J.; Stoffer, J. O. The Phase Stability of Cerium Species in Aqueous Systems - I. E-pH Diagram for the Ce-HClO<sub>4</sub>-H<sub>2</sub>O System. *J. Electrochem. Soc.* **2002**, *149*, C623–C630.
- (205) Yu, P.; Hayes, S. A.; O'Keefe, T. J.; O'Keefe, M. J.; Stoffer, J. O. The Phase Stability of Cerium Species in Aqueous Systems - II. The Ce(III/IV)-H<sub>2</sub>O-H<sub>2</sub>O<sub>2</sub>/O<sub>2</sub> Systems. Equilibrium Considerations and Pourbaix Diagram Calculations. *J. Electrochem. Soc.* **2006**, *153*, C74–C79.
- (206) Byrappa, K.; Yoshimura, M. *Handbook of Hydrothermal Technology: A Technology for Crystal Growth and Materials Processing*; Noyes Publications: Park Ridge, NJ, 2001; p 1.
- (207) Elwell, D.; Scheel, H. J. *Crystal Growth from High Temperature Solutions*; Academic Press: London, 1975; p 1.
- (208) Suresh, D.; Rohatgi, P. K.; Coutures, J. P. Use of Solar Furnaces - I Materials Research. *Sol. Energy* **1981**, *26*, 377–390.
- (209) Capper, P. Bulk Crystal Growth: Methods and Materials. In *Springer Handbook of Electronic and Photonic Materials*; Springer: Cham, Switzerland, 2017; p 1.
- (210) Rao, C. N. R.; Biswas, K. Arc and Skull Methods. In *Essentials of Inorganic Materials Synthesis*; John Wiley & Sons: Hoboken, NJ, 2015; p 37.
- (211) Scott, B. L.; Joyce, J. J.; Durakiewicz, T. D.; Martin, R. L.; McCleskey, T. M.; Bauer, E.; Luo, H.; Jia, Q. High Quality Epitaxial Thin Films of Actinide Oxides, Carbides, and Nitrides: Advancing Understanding of Electronic Structure of f-Element Materials. *Coord. Chem. Rev.* **2014**, *266–267*, 137–154.
- (212) Herrick, C. C.; Behrens, R. G. Growth of Large Uraninite And Thorianite Single Crystal from the Melt Using A Cold-Crucible Technique. *J. Cryst. Growth* **1981**, *51*, 183–189.
- (213) Rasmussen, J. J.; Nelson, R. P. Growth of UO<sub>2</sub> Single Crystals by Closed-Capsule Zone Melting. *J. Nucl. Mater.* **1970**, *36*, 237–240.
- (214) Chapman, A. T.; Clark, G. W. Growth of UO<sub>2</sub> Single Crystals Using the Floating-Zone Technique. *J. Am. Ceram. Soc.* **1965**, *48*, 494–495.
- (215) Yust, C. S.; McHargue, C. J. Dislocation Substructures in Deformed Uranium Dioxide Single Crystals. *J. Nucl. Mater.* **1969**, *31*, 121–137.
- (216) Scott, J. J.; Patchett, J. E. Preparation Methods and Quality Control of Fused Urania. Presented at the Meeting on Characterization of Uranium Dioxide Held at Oak Ridge National Laboratory, December 12–13, 1961.
- (217) Bard, R. J. *The Preparation of Uranium Dioxide Crystals*; Rep. LA-2076; Los Alamos Science Laboratory: Los Alamos, NM, 1957.
- (218) Brite, D. W.; Anderson, H. J. High Density UO<sub>2</sub> for Nuclear Fuel Applications. Presented at the Meeting on Characterization of Uranium Dioxide Held at Oak Ridge National Laboratory, December 12–13, 1961.
- (219) Childs, B. G.; Harvey, P. J.; Hallett, J. B. Color Centers and Point Defects in Irradiated Thoria. *J. Am. Ceram. Soc.* **1970**, *53*, 431–435.
- (220) Griffiths, T. R.; Dixon, J. Optical Absorption Spectroscopy of Thorium Dioxide. *J. Chem. Soc., Faraday Trans.* **1992**, *88*, 1149–1160.
- (221) Harvey, P. J.; Childs, B. G.; Moerman, J. Optical Absorbance and Fluorescence in Pure and Doped ThO<sub>2</sub>. *J. Am. Ceram. Soc.* **1973**, *56*, 134–136.
- (222) Harvey, P. J.; Hallett, J. B. Factors Influencing the Photoluminescence Behavior of Thoria. *J. Electrochem. Soc.* **1976**, *123*, 398–403.
- (223) Rodine, E. T.; Land, P. L. Electronic and Defect Structure of Single-Crystal ThO<sub>2</sub> by Thermoluminescence. *Phys. Rev. B* **1971**, *4*, 2701–2724.
- (224) Sakurai, T.; Kamada, O.; Ishigame, M. Uranium Dioxide Crystals Grown by A Solar Furnace. *J. Cryst. Growth* **1968**, *2*, 326–327.
- (225) Laszlo, T. S.; Sheehan, P. J.; Gannon, R. E. Thoria Single Crystals Grown by Vapor Deposition In A Solar Furnace. *J. Phys. Chem. Solids* **1967**, *28*, 313–316.
- (226) Hedley, W. H.; Roehrs, R. J. High Temperature Preparation of UO<sub>2</sub>. In *Uranium Dioxide: Properties and Nuclear Applications*; U.S. Government Printing Office: Washington DC, 1961.
- (227) Chapman, A. T.; Clark, G. W.; Hendrix, D. E.; Yust, C. S.; Cavin, O. B. Substructure and Perfection in UO<sub>2</sub> Single Crystals. *J. Am. Ceram. Soc.* **1970**, *53*, 46–51.
- (228) Naito, K.; Kamegashira, N.; Nomura, Y. Single Crystals of Uranium Oxides by Chemical Transport Reactions. *J. Cryst. Growth* **1971**, *8*, 219–220.
- (229) Singh, R. N.; Coble, R. L. Growth Of Uranium Dioxide Single Crystals By Chemical Vapor Deposition. *J. Cryst. Growth* **1974**, *21*, 261–266.
- (230) Nomura, Y.; Kamegashira, N.; Naito, K. Synthesis of Single Crystals of Nonstoichiometric Uranium Oxides by Chemical Transport Reactions. *J. Cryst. Growth* **1981**, *52*, 279–284.
- (231) Faile, S. P. Growth of Uranium Dioxide Crystals Using Tellurium Tetrachloride and Argon. *J. Cryst. Growth* **1978**, *43*, 133–134.
- (232) Kamegashira, N.; Ohta, K.; Naito, K. Growth of Single Crystals of U<sub>1-x</sub>Th<sub>x</sub>O<sub>2</sub> Solid Solutions by Chemical Transport Reactions. *J. Cryst. Growth* **1978**, *44*, 1–4.
- (233) Kolberg, D.; Wastin, F.; Rebizant, J.; Boulet, P.; Lander, G. H.; Schoenes, J. Magnetic Susceptibility and Spin-Lattice Interactions in U<sub>1-x</sub>Pu<sub>x</sub>O<sub>2</sub> single crystals. *Phys. Rev. B: Condens. Matter Mater. Phys.* **2002**, *66*, 214418.
- (234) Prohaska, J.; Tromel, M.; Rager, H. EPR Study of Fe<sup>3+</sup> and Mn<sup>2+</sup> in CeO<sub>2</sub> and ThO<sub>2</sub>. *Appl. Magn. Reson.* **1993**, *5*, 387–398.
- (235) Wanklyn, B. M.; Garrard, B. J. The Flux Growth of Large Thoria and Ceria Crystals. *J. Cryst. Growth* **1984**, *66*, 346–350.
- (236) Linares, R. C. Growth and Properties of CeO<sub>2</sub> and ThO<sub>2</sub> Single Crystals. *J. Phys. Chem. Solids* **1967**, *28*, 1285–1286.
- (237) Harari, M. A.; Thery, M. J.; Collongues, M. R. Sur La Preparation De Monocristaux D'Oxydes MO<sub>2</sub>. *Rev. Int. Hautes Temp. Refract.* **1967**, *4*, 207–209.
- (238) Grodkiewicz, W. H.; Nitti, D. J. Oxide Crystal Growth by Flux Evaporation. *J. Am. Ceram. Soc.* **1966**, *49*, 576–576.
- (239) Finch, C. B.; Clark, G. W. Single-Crystal Growth of Cerium Dioxide from Lithium Ditungstate Solvent. *J. Appl. Phys.* **1966**, *37*, 3910–3910.
- (240) Chaminade, J. P.; Olazcuaga, R.; Le Polles, G.; Le Flem, G.; Hagenmuller, P. Crystal Growth and Characterization of Ce<sub>1-x</sub>Pr<sub>x</sub>O<sub>2</sub> (x = 0.05) Single Crystals. *J. Cryst. Growth* **1988**, *87*, 463–465.
- (241) Baker, J. M.; Copland, G. M.; Wanklyn, B. M. Nuclear Moments and Hyperfine Structure Anomaly for Gadolinium. *J. Phys. C: Solid State Phys.* **1969**, *2*, 862–869.
- (242) Rizzoli, C.; Spirlet, J. C. Single Crystal Growth of Actinide Dioxides. *Inorg. Chim. Acta* **1984**, *94*, 112–113.
- (243) Finch, C. B.; Clark, G. W. Single-Crystal Growth of Thorium Dioxide from Lithium Ditungstate Solvent. *J. Appl. Phys.* **1965**, *36*, 2143–2145.
- (244) Kolopus, J. L.; Finch, C. B.; Abraham, M. M. ESR of Pb<sup>3+</sup> Centers in ThO<sub>2</sub>. *Phys. Rev. B* **1970**, *2*, 2040–2045.
- (245) Chase, A. B.; Osmer, J. A. Localized Cooling in Flux Crystal Growth. *J. Am. Ceram. Soc.* **1967**, *50*, 325–328.
- (246) Garton, G.; Smith, S. H.; Wanklyn, B. M. Crystal Growth from The Flux Systems PbO-V<sub>2</sub>O<sub>5</sub> and Bi<sub>2</sub>O<sub>3</sub>-V<sub>2</sub>O<sub>5</sub>. *J. Cryst. Growth* **1972**, *13–14*, 588–592.

- (247) Amoretti, G.; Giori, D. C.; Ori, O.; Schianchi, G.; Calestani, G.; Rizzoli, C.; Spirlet, J. C. Actinide and Rare Earth Ions in Single Crystals of ThO<sub>2</sub>: Preparation, EPR, Studies and Related Problems. *J. Less-Common Met.* **1986**, *122*, 35–45.
- (248) Amelinckx, S.; Bressers, J.; Nevelsteen, K.; Smets, E.; Van Lierde, W. *Growth of UO<sub>2</sub> Single Crystals*; EUR 345.e; European Atomic Energy Community - EURATOM, 1963.
- (249) Hillebrand, W. F. A Further Example of The Isomorphism of Thoria and Uranium Dioxide. *Bull. U. S. Geol. Soc.* **1893**, *113*, 41–43.
- (250) Phipps, K. D.; Sullenger, D. B. Plutonium Dioxide: Preparation of Single Crystals. *Science* **1964**, *145*, 1048–1049.
- (251) Finch, C. B.; Clark, G. W. High-Temperature Solution Growth of Single-Crystal Plutonium Dioxide. *J. Cryst. Growth* **1972**, *12*, 181–182.
- (252) Modin, A.; Yun, Y.; Suzuki, M.-T.; Vegelius, J.; Werme, L.; Nordgren, J.; Oppeneer, P. M.; Butorin, S. M. Indication of Single-Crystal PuO<sub>2</sub> Oxidation from O 1s X-ray Absorption Spectra. *Phys. Rev. B: Condens. Matter Mater. Phys.* **2011**, *83*, 075113.
- (253) Modin, A.; Suzuki, M.-T.; Vegelius, J.; Yun, Y.; Shuh, D. K.; Werme, L.; Nordgren, J.; Oppeneer, P. M.; Butorin, S. M. 5f-Shell Correlation Effects in Dioxides of Light Actinides Studied by O 1s X-ray Absorption and Emission Spectroscopies and First-Principles Calculations. *J. Phys.: Condens. Matter* **2015**, *27*, 315503.
- (254) Tani, E.; Yoshimura, M.; Somiya, S. Crystallization and Crystal Growth of CeO<sub>2</sub> Under Hydrothermal Conditions. *J. Mater. Sci. Lett.* **1982**, *1*, 461–462.
- (255) Sen, A.; Bachhav, M.; Vurpillot, F.; Mann, J. M.; Morgan, P. K.; Prusnick, T. A.; Wharry, J. P. Influence on Field Conditions on Quantitative Analysis of Single Crystal Thorium Dioxide by Atom Probe Tomography. *Ultramicroscopy* **2021**, *220*, 113167.
- (256) Knight, S.; Korlacki, R.; Dugan, C.; Petrosky, J. C.; Mock, A.; Dowben, P. A.; Mann, J. M.; Kimani, M. M.; Schubert, M. Infrared-Active Phonon Modes in Single-Crystal Thorium and Uranium Dioxide. *J. Appl. Phys.* **2020**, *127*, 125103.
- (257) Mock, A.; Dugan, C.; Knight, S.; Korlacki, R.; Mann, J. M.; Kimani, M. M.; Petrosky, J. C.; Dowben, P. A.; Schubert, M. Band-to-Band Transitions and Critical Points in the Near-Infrared to Vacuum Ultraviolet Dielectric Function of Single Crystal Urania and Thoria. *Appl. Phys. Lett.* **2019**, *114*, 211901.
- (258) Rickert, K.; Prusnick, T. A.; Kimani, M. M.; Moore, E. A.; Merriman, C. A.; Mann, J. M. Assessing UO<sub>2</sub> Sample Quality with  $\mu$ -Raman Spectroscopy. *J. Nucl. Mater.* **2019**, *514*, 1–11.
- (259) Kelly, T. D.; Petrosky, J. C.; McClory, J. W.; Mann, J. M.; Kolis, J. W. Analysis of Oxygen Shell Splitting in Hydrothermally Grown Single Crystal ThO<sub>2</sub> (200). *Phys. Status Solidi RRL* **2015**, *9*, 668–672.
- (260) Kelly, T. D.; Petrosky, J. C.; Turner, D.; McClory, J. W.; Mann, J. M.; Kolis, J. W.; Zhang, X.; Dowben, P. A. The Unoccupied Electronic Structure Characterization of Hydrothermally Grown ThO<sub>2</sub> Single Crystals. *Phys. Status Solidi RRL* **2014**, *8*, 283–286.
- (261) Kelly, T. D.; Petrosky, J. C.; McClory, J. W.; Zens, T.; Turner, D.; Mann, J. M.; Kolis, J. W.; Colon Santana, J. A.; Dowben, P. A. The Debye Temperature for Hydrothermally Growth ThO<sub>2</sub> Single Crystals. *Mater. Res. Soc. Symp. Proc.* **2013**, *1576*, 996.
- (262) Castilow, J.; Zens, T. W.; Mann, J. M.; Kolis, J. W.; McMillen, C. D.; Petrosky, J. Hydrothermal Synthesis and Characterization of ThO<sub>2</sub>, U<sub>x</sub>Th<sub>1-x</sub>O<sub>2</sub>, and UO<sub>x</sub>. *Mater. Res. Soc. Symp. Proc.* **2013**, *1576*, 973.
- (263) Turner, D. B.; Kelly, T. D.; Peterson, G. R.; Reding, J. D.; Hengehold, R. L.; Mann, J. M.; Kolis, J. W.; Zhang, X.; Dowben, P. A.; Petrosky, J. C. Electronic Structure of the Hydrothermally Synthesized Single Crystal U<sub>0.22</sub>Th<sub>0.78</sub>O<sub>2</sub>. *Phys. Status Solidi B* **2016**, *253*, 1970–1976.
- (264) Rickert, K.; Prusnick, T. A.; Hunt, E.; Kimani, M. M.; Chastang, S.; Brooks, D. L.; Moore, E. A.; Petrosky, J. C.; Mann, J. M. Inhibiting Laser Oxidation of UO<sub>2</sub> via Th Substitution. *J. Nucl. Mater.* **2019**, *517*, 254–262.
- (265) Dugan, C. L.; Peterson, G. G.; Mock, A.; Young, C.; Mann, J. M.; Nastasi, M.; Schubert, M.; Wang, L.; Mei, W.-N.; Tanabe, I.; et al. Electrical and Materials Properties of Hydrothermally Grown Single Crystal (111) UO<sub>2</sub>. *Eur. Phys. J. B* **2018**, *91*, 67.
- (266) Young, C.; Petrosky, J.; Mann, J. M.; Hunt, E. M.; Turner, D.; Dowben, P. A. The Lattice Stiffening Transition in UO<sub>2</sub> Single Crystals. *J. Phys.: Condens. Matter* **2017**, *29*, 035005.
- (267) Young, C.; Petrosky, J.; Mann, J. M.; Hunt, E. M.; Turner, D.; Kelly, T. The Work Function of Hydrothermally Synthesized UO<sub>2</sub> and the Implications for Semiconductor Device Fabrication. *Phys. Status Solidi RRL* **2016**, *10*, 687–690.
- (268) Meredith, N. A.; Wang, S.; Diwu, J.; Albrecht-Schmitt, T. E. Two Convenient Low-Temperature Routes to Single Crystals of Plutonium Dioxide. *J. Nucl. Mater.* **2014**, *454*, 164–167.
- (269) Kawabuchi, K.; Magari, S. Growth Morphology of UO<sub>2</sub>, ZrO<sub>2</sub>, HfO<sub>2</sub>, and ThO<sub>2</sub> Crystallites Grown from Oxide Plasmas. *J. Cryst. Growth* **1980**, *49*, 81–84.
- (270) Van Lierde, W.; Strumane, R.; Smets, E.; Amelinckx, S. The Preparation of Uranium Oxide Single Crystals By Sublimation. *J. Nucl. Mater.* **1962**, *5*, 250–253.
- (271) Schlechter, M. The Preparation Of Crystalline UO<sub>2</sub> Crystals By Thermal Decomposition of UOCl<sub>2</sub> Dissolved In Molten UCl<sub>4</sub>. *J. Nucl. Mater.* **1968**, *28*, 228–229.
- (272) Schlechter, M. The Preparation Of PuO<sub>2</sub> Crystals By Thermal Decomposition of Pu(SO<sub>4</sub>)<sub>2</sub> Dissolved In Chloride Melts. *J. Nucl. Mater.* **1970**, *37*, 82–88.
- (273) Robins, R. G. Uranium Dioxide Single Crystals by Electrodeposition. *J. Nucl. Mater.* **1961**, *3*, 294–301.
- (274) Scott, F. A.; Mudge, L. K. The Electrolytic Preparation of Single Crystals of Uranium Dioxide. *J. Nucl. Mater.* **1963**, *9*, 245–251.
- (275) Schlechter, M. The Preparation Of UO<sub>2</sub> By Electrolysis of UO<sub>2</sub>Cl<sub>2</sub> Dissolved In Molten NaCl-KCl-MgCl<sub>2</sub> Eutectic. *J. Nucl. Mater.* **1963**, *10*, 145–146.
- (276) Kordyukevich, V. O.; Kuznetsov, V. I.; Otstavnov, Y. D.; Smirnov, N. N. Electrochemical Preparation of Single Crystals of <sup>235</sup>UO<sub>2</sub>. *At. Energy* **1977**, *42*, 145–147.
- (277) Graham, J. T.; Zhang, Y. W.; Weber, W. J. Irradiation-Induced Defect Formation and Damage Accumulation in Single Crystal CeO<sub>2</sub>. *J. Nucl. Mater.* **2018**, *498*, 400–408.
- (278) Evans, W. R.; Allred, D. D. Determining Indices of Refraction for ThO<sub>2</sub> Thin Films Sputter Under Different Bias Voltages from 1.2 to 6.5 eV by Spectroscopic Ellipsometry. *Thin Solid Films* **2006**, *515*, 847–853.
- (279) Navinsek, B. Epitaxial Growth of UO<sub>2</sub> Thin Films Produced by Cathode Sputtering. *J. Nucl. Mater.* **1971**, *40*, 338–340.
- (280) Strehle, M. M.; Heuser, B. J.; Elbakshwan, M. S.; Han, X.; Gennardo, D. J.; Pappas, H. K.; Ju, H. Characterization of Single Crystal Uranium-Oxide Thin Films Grown via Reactive-Gas Magnetron Sputtering on Yttria-Stabilized Zirconia and Sapphire. *Thin Solid Films* **2012**, *520*, 5616–5626.
- (281) Bao, Z.; Springell, R.; Walker, H. C.; Leiste, H.; Kuebel, K.; Prang, R.; Nisbet, G.; Langridge, S.; Ward, R. C. C.; Gouder, T.; et al. Antiferromagnetism in UO<sub>2</sub> Thin Epitaxial Films. *Phys. Rev. B* **2013**, *88*, 134426.
- (282) Rennie, S.; Bright, E. L.; Sutcliffe, J. E.; Darnbrough, J. E.; Burrows, R.; Rawle, J.; Nicklin, C.; Lander, G. H.; Springell, R. The Role of Crystal Orientation in the Dissolution of UO<sub>2</sub> Thin Films. *Corros. Sci.* **2018**, *145*, 162–169.
- (283) Elbakshwan, M. S.; Miao, Y.; Stubbins, J. F.; Heuser, B. J. Mechanical Properties of UO<sub>2</sub> Thin Films Under Heavy Ion Irradiation Using Nanoindentation and Finite Element Modeling. *J. Nucl. Mater.* **2016**, *479*, 548–558.
- (284) Darnbrough, J. E.; Harker, R. M.; Griffiths, I.; Wermelle, D.; Lander, G. H.; Springell, R. Interaction Between U/UO<sub>2</sub> Bilayers and Hydrogen Studied by In-Situ X-ray Diffraction. *J. Nucl. Mater.* **2018**, *502*, 9–19.
- (285) Whapham, A. D.; Sheldon, B. E. Radiation Damage in Uranium Dioxide. *Philos. Mag.* **1965**, *12*, 1179–1102.
- (286) Weber, W. J. Alpha-Irradiation Damage in CeO<sub>2</sub>, UO<sub>2</sub> and PuO<sub>2</sub>. *Radiat. Eff.* **1984**, *83*, 145–156.
- (287) Weber, W. J. Thermal Recovery of Lattice-Defects in Alpha-Irradiated UO<sub>2</sub> Crystals. *J. Nucl. Mater.* **1983**, *114*, 213–221.

- (288) Weber, W. J. Ingrowth of Lattice-Defects in Alpha Irradiated UO<sub>2</sub> Single-Crystals. *J. Nucl. Mater.* **1981**, *98*, 206–215.
- (289) Matzke, H.J.; Blank, H.; Coquerelle, M.; Lassmann, K.; Ray, I. L. F.; Ronchi, C.; Walker, C. T. Oxide Fuel Transients. *J. Nucl. Mater.* **1989**, *166*, 165–178.
- (290) Evans, J. H.; Vanveen, A.; Westerduin, K. T. A TEM and TDS Study of Gas-Release from Bubbles in Krypton-Implanted Uranium-Dioxide. *J. Nucl. Mater.* **1992**, *195*, 250–59.
- (291) Whapham, A. D. Electron Microscope Observation of Fission-Gas Bubble Distribution in UO<sub>2</sub>. *Nucl. Applicat.* **1966**, *2*, 123–130.
- (292) Kashibe, S.; Une, K.; Nogita, K. Formation and Growth of Intragranular Fission-Gas Bubbles in UO<sub>2</sub> Fuels with Burnup of 6–83 GWd/T. *J. Nucl. Mater.* **1993**, *206*, 22–34.
- (293) Une, K.; Nogita, K.; Kashibe, S.; Imamura, M. Microstructural Change and Its Influence on Fission-Gas Release in High Burnup UO<sub>2</sub> Fuel. *J. Nucl. Mater.* **1992**, *188*, 65–72.
- (294) Rest, J.; Cooper, M. W. D.; Spino, J.; Turnbull, J. A.; Van Uffelen, P.; Walker, C. T. Fission Gas Release from UO<sub>2</sub> Nuclear Fuel: A Review. *J. Nucl. Mater.* **2019**, *513*, 310–45.
- (295) Ye, B.; Kirk, M. A.; Chen, W. Y.; Oaks, A.; Rest, J.; Yacout, A.; Stubbins, J. F. TEM Investigation of Irradiation Damage in Single Crystal CeO<sub>2</sub>. *J. Nucl. Mater.* **2011**, *414*, 251–256.
- (296) Ye, B.; Oaks, A.; Kirk, M.; Yun, D.; Chen, W. Y.; Holtzman, B.; Stubbins, J. F. Irradiation Effects in UO<sub>2</sub> and CeO<sub>2</sub>. *J. Nucl. Mater.* **2013**, *441*, 525–529.
- (297) Chauhan, V. S.; Pakarinen, J.; Yao, T.; He, L.; Hurley, D. H.; Khafizov, M. Indirect Characterization of Point Defects in Proton Irradiated Ceria. *Materialia* **2021**, *15*, 101019.
- (298) Miao, Y. B.; Aidhy, D.; Chen, W. Y.; Mo, K.; Oaks, A.; Wolf, D.; Stubbins, J. F. The Evolution Mechanism of the Dislocation Loops in Irradiated Lanthanum Doped Cerium Oxide. *J. Nucl. Mater.* **2014**, *445*, 209–217.
- (299) Matzke, H. Xenon Migration and Trapping in Doped ThO<sub>2</sub>. *J. Nucl. Mater.* **1967**, *21*, 190–198.
- (300) Ogawa, T.; Verrall, R. A.; Matzke, H.; Lucuta, P. G. Release of Ion-Implanted Kr from (Th, U)O<sub>2</sub> - Effect of Matrix Oxidation. *Solid State Ionics* **1991**, *49*, 211–216.
- (301) Jegadeesan, P.; Amirthapandian, S.; Panigrahi, B. K.; Kaur, G.; Kumar, D. S.; Magudapathy, P.; Ananthasivan, K. Aggregation and Ordering of Helium in Thoria. *J. Alloy. Compd.* **2018**, *743*, 196–202.
- (302) Jin, M.; Jiang, C.; Gan, J.; Hurley, D. H. Systematic Analysis on the Primary Radiation Damage in Th<sub>1-x</sub>U<sub>x</sub>O<sub>2</sub> Fluorite Systems. *J. Nucl. Mater.* **2020**, *536*, 152144.
- (303) Bawane, K.; Liu, X.; Yao, T.; Khafizov, M.; French, A.; Mann, J. M.; Shao, L.; Gan, J.; Hurley, D. H.; He, L. TEM Characterization of Dislocation Loops in Proton Irradiated Single Crystal ThO<sub>2</sub>. *J. Nucl. Mater.* **2021**, *552*, 152998.
- (304) Was, G. S.; Allen, T. R. Radiation Damage from Different Particle Types. In *Radiation Effects in Solids*; NATO Science Series, Vol. 235; Springer: Dordrecht, The Netherlands, 2007; pp 65–98.
- (305) Cureton, W. F.; Palomares, R. I.; Tracy, C. L.; O'Quinn, E. C.; Walters, J.; Zdrovets, M.; Ewing, R. C.; Toulemonde, M.; Lang, M. Effects of Irradiation Temperature on the Response of CeO<sub>2</sub>, ThO<sub>2</sub>, and UO<sub>2</sub> to Highly Ionizing Radiation. *J. Nucl. Mater.* **2019**, *525*, 83–91.
- (306) Cureton, W. F.; Palomares, R. I.; Walters, J.; Tracy, C. L.; Chen, C.-H.; Ewing, R. C.; Baldinozzi, G.; Lian, J.; Trautmann, C.; Lang, M. Grain Size Effects on Irradiated CeO<sub>2</sub>, ThO<sub>2</sub>, and UO<sub>2</sub>. *Acta Mater.* **2018**, *160*, 47–56.
- (307) Garcia, P.; Gilbert, E.; Martin, G.; Carlot, G.; Sabathier, C.; Sauvage, T.; Desgardin, P.; Barthe, M.-F. Helium Behaviour in UO<sub>2</sub> Through Low Fluence Ion Implantation Studies. *Nucl. Instrum. Methods Phys. Res., Sect. B* **2014**, *327*, 113–116.
- (308) Garcia, P.; Martin, G.; Sabathier, C.; Carlot, G.; Michel, A.; Martin, P.; Dorado, B.; Freyss, M.; Bertolus, M.; Skorek, R.; et al. Nucleation and Growth of Intragranular Defect and Insoluble Atom Clusters in Nuclear Oxide Fuels. *Nucl. Instrum. Methods Phys. Res., Sect. B* **2012**, *277*, 98–108.
- (309) Haddad, Y.; Delauche, L.; Gentils, A.; Garrido, F. In Situ Characterization of Irradiation-Induced Microstructural Evolution in Urania Single Crystals at 773 K. *Nucl. Instrum. Methods Phys. Res., Sect. B* **2018**, *435*, 25–30.
- (310) He, L.; Bai, X.M.; Pakarinen, J.; Jaques, B.J.; Gan, J.; Nelson, A.T.; El-Azab, A.; Allen, T.R. Bubble Evolution in Kr-Irradiated UO<sub>2</sub> During Annealing. *J. Nucl. Mater.* **2017**, *496*, 242–250.
- (311) He, L.; Valderrama, B.; Hassan, A.-R.; Yu, J.; Gupta, M.; Pakarinen, J.; Henderson, H. B.; Gan, J.; Kirk, M. A.; Nelson, A. T.; et al. Bubble Formation and Kr Distribution in Kr-Irradiated UO<sub>2</sub>. *J. Nucl. Mater.* **2015**, *456*, 125–132.
- (312) He, L. F.; Gupta, M.; Kirk, M. A.; Pakarinen, J.; Gan, J.; Allen, T. R. In Situ TEM Observation of Dislocation Evolution in Polycrystalline UO<sub>2</sub>. *JOM* **2014**, *66*, 2553–2561.
- (313) He, L. F.; Gupta, M.; Yablinsky, C. A.; Gan, J.; Kirk, M. A.; Bai, X.-M.; Pakarinen, J.; Allen, T. R. In Situ TEM Observation of Dislocation Evolution in Kr-Irradiated UO<sub>2</sub> Single Crystal. *J. Nucl. Mater.* **2013**, *443*, 71–77.
- (314) He, L.F.; Pakarinen, J.; Kirk, M.A.; Gan, J.; Nelson, A.T.; Bai, X.-M.; El-Azab, A.; Allen, T.R. Microstructure Evolution in Xe-Irradiated UO<sub>2</sub> at Room Temperature. *Nucl. Instrum. Meth. Phys. Res. B* **2014**, *330*, 55–60.
- (315) Khafizov, M.; Pakarinen, J.; He, L.; Hurley, D. H. Impact of Irradiation Induced Dislocation Loops on Thermal Conductivity in Ceramics. *J. Am. Ceram. Soc.* **2019**, *102*, 7533–7542.
- (316) Marchand, B.; Moncoffre, N.; Pison, Y.; Bererd, N.; Garnier, C.; Raimbault, L.; Sainsot, P.; Epicier, T.; Delafoy, C.; Fraczkiwicz, M.; et al. Xenon Migration in UO<sub>2</sub> Under Irradiation Studied by SIMS Profilometry. *J. Nucl. Mater.* **2013**, *440*, 562–567.
- (317) Onofri, C.; Sabathier, C.; Baumier, C.; Bachelet, C.; Palancher, H.; Warot-Fonrose, B.; Legros, M. Influence of Exogenous Xenon Atoms on the Evolution Kinetics of Extended Defects in Polycrystalline UO<sub>2</sub> Using In Situ TEM. *J. Nucl. Mater.* **2018**, *512*, 297–306.
- (318) Onofri, C.; Sabathier, C.; Palancher, H.; Carlot, G.; Miro, S.; Serruys, Y.; Desgranges, L.; Legros, M. Evolution of Extended Defects in Polycrystalline UO<sub>2</sub> Under Heavy Ion Irradiation: Combined TEM, XRD and Raman Study. *Nucl. Instrum. Methods Phys. Res., Sect. B* **2016**, *374*, 51–57.
- (319) Pakarinen, J.; He, L.; Gupta, M.; Gan, J.; Nelson, A.; El-Azab, A.; Allen, T. R. 2.6 MeV Proton Irradiation Effects on the Surface Integrity of Depleted UO<sub>2</sub>. *Nucl. Instrum. Methods Phys. Res., Sect. B* **2014**, *319*, 100–106.
- (320) Pakarinen, J.; Khafizov, M.; He, L.; Wetteland, C.; Gan, J.; Nelson, A. T.; Hurley, D. H.; El-Azab, A.; Allen, T. R. Microstructure Changes and Thermal Conductivity Reduction in UO<sub>2</sub> Following 3.9 MeV He<sup>2+</sup> Ion Irradiation. *J. Nucl. Mater.* **2014**, *454*, 283–289.
- (321) Palomares, R. I.; Shamblin, J.; Tracy, C. L.; Neufeind, J.; Ewing, R. C.; Trautmann, C.; Lang, M. Defect Accumulation in Swift Heavy Ion-Irradiated CeO<sub>2</sub> and ThO<sub>2</sub>. *J. Mater. Chem. A* **2017**, *5*, 12193–12201.
- (322) Tracy, C. L.; Lang, M.; Pray, J. M.; Zhang, F.; Popov, D.; Park, C.; Trautmann, C.; Bender, M.; Severin, D.; Skuratov, V. A.; et al. Redox Response of Actinide Materials to Highly Ionizing Radiation. *Nat. Commun.* **2015**, *6*, 6133.
- (323) Tracy, C. L.; McLain Pray, J.; Lang, M.; Popov, D.; Park, C.; Trautmann, C.; Ewing, R. C. Defect Accumulation in ThO<sub>2</sub> Irradiated With Swift Heavy Ions. *Nucl. Instrum. Methods Phys. Res., Sect. B* **2014**, *326*, 169–173.
- (324) Onofri, C.; Legros, M.; Lechelle, J.; Palancher, H.; Baumier, C.; Bachelet, C.; Sabathier, C. Full Characterization of Dislocations in Ion-Irradiated Polycrystalline UO<sub>2</sub>. *J. Nucl. Mater.* **2017**, *494*, 252–259.
- (325) Onofri, C.; Sabathier, C.; Baumier, C.; Bachelet, C.; Drouan, D.; Gerardin, M.; Legros, M. Extended Defect Change in UO<sub>2</sub> During In Situ TEM Annealing. *Acta Mater.* **2020**, *196*, 240–251.
- (326) Onofri, C.; Sabathier, C.; Baumier, C.; Bachelet, C.; Palancher, H.; Legros, M. Evolution of Extended Defects in Polycrystalline Au-Irradiated UO<sub>2</sub> Using In Situ TEM: Temperature and Fluence Effects. *J. Nucl. Mater.* **2016**, *482*, 105–113.

- (327) Onofri, C.; Sabathier, C.; Carlot, G.; Drouan, D.; Bachelet, C.; Baumier, C.; Gerardin, M.; Bricout, M. Changes in Voids Induced by Ion Irradiations in  $\text{UO}_2$ . In *Situ TEM Studies. Nucl. Instrum. Methods Phys. Res., Sect. B* **2020**, *463*, 76–85.
- (328) He, L.; Khafizov, M.; Jiang, C.; Tyburska-Puschel, B.; Jaques, B. J.; Xiu, P.; Xu, P.; Meyer, M. K.; Sridharan, K.; Butt, D. P.; et al. Phase and Defect Evolution in Uranium-Nitrogen-Oxygen System Under Irradiation. *Acta Mater.* **2021**, *208*, 116778.
- (329) Wiss, T. Radiation Effects in  $\text{UO}_2$ . In *Comprehensive Nuclear Materials*; Elsevier: Amsterdam, 2012; p 465.
- (330) De Bona, E.; Benedetti, A.; Dieste, O.; Staicu, D.; Wiss, T.; Konings, R. J. M. Radiation Effects in Alpha-Doped  $\text{UO}_2$ . *Nucl. Instrum. Methods Phys. Res., Sect. B* **2020**, *468*, 54–59.
- (331) Soullard, J. High-Voltage Electron-Microscope Observations of  $\text{UO}_2$ . *J. Nucl. Mater.* **1985**, *135*, 190–196.
- (332) Leinders, G.; Bes, R.; Pakarinen, J.; Kvashnina, K.; Verwerft, M. Evolution of the Uranium Chemical State in Mixed-Valence Oxides. *Inorg. Chem.* **2017**, *56*, 6784–6787.
- (333) Schmitt, R.; Nenning, A.; Kraynis, O.; Korobko, R.; Frenkel, A. I.; Lubomirsky, I.; Haile, S. M.; Rupp, J. L. M. A Review of Defect Structure and Chemistry in Ceria and Its Solid Solutions. *Chem. Soc. Rev.* **2020**, *49*, 554–592.
- (334) Amidani, L.; Vaughan, G. B. M.; Plakhova, T. V.; Romanchuk, A. Y.; Gerber, E.; Svetogorov, R.; Weiss, S.; Joly, Y.; Kalmykov, S. N.; Kvashnina, K. O. The Application of HEX and HERFD XANES for Accurate Structural Characterisation of Actinide Nanomaterials: The Case of  $\text{ThO}_2$ . *Chem. - Eur. J.* **2021**, *27*, 252–263.
- (335) Allen, G. C.; Tempest, P. A.; Garner, C. D.; Ross, I.; Jones, D. J. EXAFS - a New Approach to the Structure of Uranium-Oxides. *J. Phys. Chem.* **1985**, *89*, 1334–1339.
- (336) Jones, D. J.; Roziere, J.; Allen, G. C.; Tempest, P. A. The Structural Determination of Fluorite-Type Oxygen Excess Uranium-Oxides Using EXAFS Spectroscopy. *J. Chem. Phys.* **1986**, *84*, 6075–6082.
- (337) Conradson, S. D.; Manara, D.; Wastin, F.; Clark, D. L.; Lander, G. H.; Morales, L. A.; Rebizant, J.; Rondinella, V. V. Local Structure and Charge Distribution in the  $\text{UO}_2$ - $\text{U}_4\text{O}_9$  System. *Inorg. Chem.* **2004**, *43*, 6922–6935.
- (338) Conradson, S. D.; Begg, B. D.; Clark, D. L.; den Auwer, C.; Ding, M.; Dorhout, P. K.; Espinosa-Faller, F. J.; Gordon, P. L.; Haire, R. G.; Hess, N. J.; et al. Charge Distribution and Local Structure and Speciation in the  $\text{UO}_{2+x}$  and  $\text{PuO}_{2+x}$  Binary Oxides for  $x \leq 0.25$ . *J. Solid State Chem.* **2005**, *178*, 521–535.
- (339) Martin, P.; Ripert, M.; Petit, T.; Reich, T.; Hennig, C.; D'Acapito, F.; Hazemann, J. L.; Proux, O. A XAS Study of the Local Environments of Cations in  $(\text{U}, \text{Ce})\text{O}_2$ . *J. Nucl. Mater.* **2003**, *312*, 103–110.
- (340) Martin, P.; Grandjean, S.; Valot, C.; Carlot, G.; Ripert, M.; Blanc, P.; Hennig, C. XAS Study of  $(\text{U}_{1-x}\text{Pu}_x)\text{O}_2$  Solid Solutions. *J. Alloys Compd.* **2007**, *444*, 410–414.
- (341) Kvashnina, K. O.; Butorin, S. M.; Martin, P.; Glatzel, P. Chemical State of Complex Uranium Oxides. *Phys. Rev. Lett.* **2013**, *111*, 253002.
- (342) Shi, W. Q.; Yuan, L. Y.; Wang, C. Z.; Wang, L.; Mei, L.; Xiao, C. L.; Zhang, L.; Li, Z. J.; Zhao, Y. L.; Chai, Z. F. Exploring Actinide Materials Through Synchrotron Radiation Techniques. *Adv. Mater.* **2014**, *26*, 7807–7848.
- (343) Ramanantoanina, H.; Kuri, G.; Martin, M.; Bertsch, J. Study of Electronic Structure in the L-Edge Spectroscopy of Actinide Materials:  $\text{UO}_2$  as an Example. *Phys. Chem. Chem. Phys.* **2019**, *21*, 7789–7801.
- (344) Degueldre, C.; Bertsch, J.; Kuri, G.; Martin, M. Nuclear Fuel in Generation II and III Reactors: Research Issues Related to High Burn-Up. *Energy Environ. Sci.* **2011**, *4*, 1651–1661.
- (345) Lang, M.; Tracy, C. L.; Palomares, R. I.; Zhang, F.; Severin, D.; Bender, M.; Trautmann, C.; Park, C.; Prakapenka, V. B.; Skuratov, V. A.; et al. Characterization of Ion-Induced Radiation Effects in Nuclear Materials Using Synchrotron X-ray Techniques. *J. Mater. Res.* **2015**, *30*, 1366–1379.
- (346) Selim, F. A. Positron Annihilation Spectroscopy of Defects in Nuclear and Irradiated Materials - A Review. *Mater. Charact.* **2021**, *174*, 110952.
- (347) Schultz, P. J.; Lynn, K. G. Interaction of Positron Beams with Surfaces, Thin Films, and Interfaces. *Rev. Mod. Phys.* **1988**, *60*, 701–779.
- (348) Mills, A. P., Jr.; Platzman, P. M.; Brown, B. L. Slow-Positron Emission from Metal Surfaces. *Phys. Rev. Lett.* **1978**, *41*, 1076–1079.
- (349) Hugenschmidt, C. Positrons in Surface Physics. *Surf. Sci. Rep.* **2016**, *71*, 547–594.
- (350) Auguste, R.; Liedke, M. O.; Selim, F. A.; Uberuaga, B. P.; Wagner, A.; Hosemann, P. Measurement and Simulation of Vacancy Formation in 2-MeV Self-irradiated Pure Fe. *JOM* **2020**, *72*, 2436–2444.
- (351) Pells, G. P. Radiation-Damage Effects in Alumina. *J. Am. Ceram. Soc.* **1994**, *77*, 368–377.
- (352) Popov, A. I.; Kotomin, E. A.; Maier, J. Basic Properties of the F-Type Centers in Halides, Oxides and Perovskites. *Nucl. Instrum. Methods Phys. Res., Sect. B* **2010**, *268*, 3084–3089.
- (353) Lushchik, A.; Lushchik, C.; Schwartz, K.; Vasil'chenko, E.; Kaerner, T.; Kudryavtseva, I.; Isakhanyan, V.; Shugai, A. Stabilization and Annealing of Interstitials Formed by Radiation in Binary Metal Oxides and Fluorides. *Nucl. Instrum. Methods Phys. Res., Sect. B* **2008**, *266*, 2868–2871.
- (354) Griffiths, T. R.; Dixon, J. Fast-Neutron Radiation on Single-Crystal Thorium-Dioxide - An Optical-Absorption Spectroscopy Study of the F(O) Color Center. *J. Chem. Soc., Faraday Trans.* **1992**, *88*, 3475–3482.
- (355) Xiao, H. Y.; Weber, W. J. Oxygen Vacancy Formation and Migration in  $\text{Ce}_x\text{Th}_{1-x}\text{O}_2$  Solid Solution. *J. Phys. Chem. B* **2011**, *115*, 6524–6533.
- (356) Marabelli, F.; Wachtter, P. Covalent Insulator  $\text{CeO}_2$  - Optical Reflectivity Measurements. *Phys. Rev. B: Condens. Matter Mater. Phys.* **1987**, *36*, 1238–1243.
- (357) Patsalas, P.; Logothetidis, S.; Sygellou, L.; Kennou, S. Structure-Dependent Electronic Properties of Nanocrystalline Cerium Oxide Films. *Phys. Rev. B: Condens. Matter Mater. Phys.* **2003**, *68*, 035104.
- (358) Schoenes, J. Electronic-Transitions, Crystal-Field Effects and Phonons in  $\text{UO}_2$ . *Phys. Rep.* **1980**, *63*, 301–336.
- (359) Costantini, J. M.; Lelong, G.; Guillaumet, M.; Gourier, D.; Takaki, S.; Ishikawa, N.; Watanabe, H.; Yasuda, K. Optical Reflectivity of Ion-Irradiated Cerium Dioxide Sinters. *J. Appl. Phys.* **2019**, *126*, 175902.
- (360) Costantini, J.-M.; Lelong, G.; Guillaumet, M.; Weber, W. J.; Takaki, S.; Yasuda, K. Color Center Production and Recovery in Electron-Irradiated Magnesium Aluminate Spinel and Ceria. *J. Phys.: Condens. Matter* **2016**, *28*, 325901.
- (361) Schoenes, J. Optical-Properties and Electronic-Structure of  $\text{UO}_2$ . *J. Appl. Phys.* **1978**, *49*, 1463–1465.
- (362) Wang, J. W.; Ewing, R. C.; Becker, U. Electronic Structure and Stability of Hyperstoichiometric  $\text{UO}_{2+x}$  Under Pressure. *Phys. Rev. B: Condens. Matter Mater. Phys.* **2013**, *88*, 024109.
- (363) Andersson, D. A.; Uberuaga, B. P.; Nerikar, P. V.; Unal, C.; Stanek, C. R. U and Xe Transport in  $\text{UO}_{2+x}$ : Density Functional Theory Calculations. *Phys. Rev. B* **2011**, *84*, 054105.
- (364) Conradson, S. D.; Durakiewicz, T.; Espinosa-Faller, F. J.; An, Y. Q.; Andersson, D. A.; Bishop, A. R.; Boland, K. S.; Bradley, J. A.; Byler, D. D.; Clark, D. L.; et al. Possible Bose-Condensate Behavior in a Quantum Phase Originating in a Collective Excitation in the Chemically and Optically Doped Mott-Hubbard System  $\text{UO}_{2+x}$ . *Phys. Rev. B: Condens. Matter Mater. Phys.* **2013**, *88*, 115135.
- (365) Marlow, P. G.; Russell, J. P.; Hardy, J. R. Raman Scattering in Uranium Dioxide. *Philos. Mag.* **1966**, *14*, 409–410.
- (366) Keramidis, V. G.; White, W. B. Raman Spectra of Oxides with the Fluorite Structure. *J. Chem. Phys.* **1973**, *59*, 1561–1562.
- (367) Rao, R.; Bhagat, R. K.; Salke, N. P.; Kumar, A. Raman Spectroscopic Investigation of Thorium Dioxide-Uranium Dioxide ( $\text{ThO}_2$ - $\text{UO}_2$ ) Fuel Materials. *Appl. Spectrosc.* **2014**, *68*, 44–48.

- (368) Mohun, R.; Desgranges, L.; Lechelle, J.; Simon, P.; Guimbretiere, G.; Canizares, A.; Duval, F.; Jegou, C.; Magnin, M.; Clavier, N.; et al. Charged Defects During Alpha-Irradiation of Actinide Oxides as Revealed by Raman and Luminescence Spectroscopy. *Nucl. Instrum. Methods Phys. Res., Sect. B* **2016**, *374*, 67–70.
- (369) Weber, W. H.; Hass, K. C.; McBride, J. R. Raman-Study of CeO<sub>2</sub> - 2nd-Order Scattering, Lattice-Dynamics, and Particle-Size Effects. *Phys. Rev. B: Condens. Matter Mater. Phys.* **1993**, *48*, 178–185.
- (370) Nakajima, A.; Yoshihara, A.; Ishigame, M. Defect-Induced Raman-Spectra in Doped CeO<sub>2</sub>. *Phys. Rev. B: Condens. Matter Mater. Phys.* **1994**, *50*, 13297–13307.
- (371) McBride, J. R.; Hass, K. C.; Poindexter, B. D.; Weber, W. H. Raman and X-ray Studies of Ce<sub>1-x</sub>Re<sub>x</sub>O<sub>2-y</sub>, Where Re = La, Pr, Nd, Ee, Gd, and Tb. *J. Appl. Phys.* **1994**, *76*, 2435–2441.
- (372) Lacina, W. B.; Pershan, P. S. Phonon Optical Properties of Ca<sub>1-x</sub>Sr<sub>x</sub>F<sub>2</sub>. *Phys. Rev. B* **1970**, *1*, 1765–1786.
- (373) Haridasan, T. M.; Govindarajan, J.; Nerenberg, M. A.; Jacobs, P. W. M. Impurity Modes Due to Interstitials in CaF<sub>2</sub>. *Phys. Rev. B: Condens. Matter Mater. Phys.* **1979**, *20*, 3462–3473.
- (374) Haridasan, T. M.; Govindarajan, J.; Nerenberg, M. A.; Jacobs, P. W. M. Phonon Resonances Associated with a Vacancy in CaF<sub>2</sub>. *Phys. Rev. B: Condens. Matter Mater. Phys.* **1979**, *20*, 3474–3480.
- (375) Li, L.; Chen, F.; Lu, J. Q.; Luo, M. F. Study of Defect Sites in Ce<sub>1-x</sub>M<sub>x</sub>O<sub>2-δ</sub> (x = 0.2) Solid Solutions Using Raman Spectroscopy. *J. Phys. Chem. A* **2011**, *115*, 7972–7977.
- (376) Desgranges, L.; Baldinozzi, G.; Simon, P.; Guimbretiere, G.; Canizares, A. Raman Spectrum of U<sub>4</sub>O<sub>9</sub>: A New Interpretation of Damage Lines in UO<sub>2</sub>. *J. Raman Spectrosc.* **2012**, *43*, 455–458.
- (377) Talip, Z.; Wiss, T.; Raison, P. E.; Paillier, J.; Manara, D.; Somers, J.; Konings, R. J. M. Raman and X-ray Studies of Uranium-Lanthanum-Mixed Oxides Before and After Air Oxidation. *J. Am. Ceram. Soc.* **2015**, *98*, 2278–2285.
- (378) Mohun, R.; Desgranges, L.; Jégou, C.; Boizot, B.; Cavani, O.; Canizarès, A.; Duval, F.; He, C.; Desgardin, P.; Barthe, M. F.; et al. Quantification of Irradiation-Induced Defects in UO<sub>2</sub> Using Raman and Positron Annihilation Spectroscopies. *Acta Mater.* **2019**, *164*, 512–519.
- (379) Colmenares, C.; Howell, R.; McCreary, T. *Oxidation of Uranium Studied by Gravimetric and Positron Annihilation Techniques*; Technical Report UCRL-85549; Lawrence Livermore National Laboratory: Livermore, CA, 1981.
- (380) Upadhyaya, D.; Muraleedharan, R.; Sharma, B. Study of Positron Lifetime Spectra in UO<sub>2</sub> Powders. *J. Nucl. Mater.* **1982**, *105*, 219–222.
- (381) Upadhyaya, D. D.; Muraleedharan, R. V.; Sharma, B. D.; Prasad, K. G. Positron Lifetime Studies on Thorium Oxide Powders. *Philos. Mag. A* **1982**, *45*, 509–518.
- (382) Troev, T.; Penev, I.; Protochristov, H. Positron Annihilation in UO<sub>2</sub>. *Phys. Lett. A* **1984**, *100A*, 221–224.
- (383) Chollet, M.; Krsjak, V.; Cozzo, C.; Bertsch, J. Positron Annihilation Spectroscopy Study of Lattice Defects in Non-Irradiated Doped and Un-Doped Fuels. *EPJ Nucl. Sci. Technol.* **2017**, *3*, 3.
- (384) Mogensen, M.; Sammes, N. M.; Tompsett, G. A. Physical, Chemical and Electrochemical Properties of Pure and Doped Ceria. *Solid State Ionics* **2000**, *129*, 63–94.
- (385) Ohmichi, T.; Fukushima, S.; Maeda, A.; Watanabe, H. On the Relation Between Lattice-Parameter and O/M Ratio for Uranium-Dioxide Trivalent Rare-Earth-Oxide Solid-Solution. *J. Nucl. Mater.* **1981**, *102*, 40–46.
- (386) Shannon, R. D. Revised Effective Ionic-Radii and Systematics Studies of Interatomic Distances in Halides and Chalcogenides. *Acta Crystallogr., Sect. A: Cryst. Phys., Diffr., Theor. Gen. Crystallogr.* **1976**, *32*, 751–767.
- (387) Grieshammer, S.; Zacherle, T.; Martin, M. Entropies of Defect Formation in Ceria From First Principles. *Phys. Chem. Chem. Phys.* **2013**, *15*, 15935–15942.
- (388) Bruneval, F.; Freyss, M.; Crocombette, J. P. Lattice Constant in Nonstoichiometric Uranium Dioxide From First Principles. *Phys. Rev. Mater.* **2018**, *2*, 023801.
- (389) Manara, D.; Renker, B. Raman Spectra of Stoichiometric and Hyperstoichiometric Uranium Dioxide. *J. Nucl. Mater.* **2003**, *321*, 233–237.
- (390) Elorrieta, J. M.; Bonales, L. J.; Rodríguez-Villagra, N.; Baonza, V. G.; Cobos, J. A Detailed Raman and X-ray Study of UO<sub>2</sub><sup>+</sup>: X Oxides and Related Structure Transitions. *Phys. Chem. Chem. Phys.* **2016**, *18*, 28209–28216.
- (391) Guéneau, C.; Baichi, M.; Labroche, D.; Chatillon, C.; Sundman, B. Thermodynamic Assessment of the Uranium-Oxygen System. *J. Nucl. Mater.* **2002**, *304*, 161–175.
- (392) Agarwal, R.; Parida, S. C. Phase Diagrams and Thermodynamic Properties of Thoria, Thoria-Urania, and Thoria-Plutonia. In *Thoria-Based Nuclear Fuels*; Springer: London, 2013; pp 71–105.
- (393) Benz, R. Thorium-Thorium Dioxide Phase Equilibria. *J. Nucl. Mater.* **1969**, *29*, 43–49.
- (394) Darnell, A.; McCollum, W. A. *High Temperature Reactions of Thorium and Thoria and the Vapor Pressure of Thoria*; Report NAA-SR-6498; Office of Technical Services, U.S. Department of Commerce: Washington, DC, 1960.
- (395) Ackermann, R. J.; Rauh, E. G.; Thorn, R. J.; Cannon, M. C. A Thermodynamic Study of the Thorium-Oxygen System at High Temperatures. *J. Phys. Chem.* **1963**, *67*, 762–769.
- (396) Murphy, S.; Cooper, M. W. D.; Grimes, R. W. Point Defects and Non-Stoichiometry in Thoria. *Solid State Ionics* **2014**, *267*, 80–87.
- (397) Bergeron, A.; Manara, D.; Beneš, O.; Eloirdi, R.; Piro, M.; Corcoran, E. Point Defects and Non-Stoichiometry in Thoria: Description of the Th-U-Pu-O Quaternary System. *J. Nucl. Mater.* **2018**, *512*, 324–348.
- (398) Schmalzried, H. *Chemical Kinetics of Solids*; VCH: New York, 1995; p 19.
- (399) Piro, M.; Bergeron, A.; Corcoran, E. Thermodynamic Modelling of Thoria-Urania and Thoria-Plutonia Fuels. Presented at Materials Modelling and Simulations for Nuclear Fuels 2017. DOI: 10.13140/RG.2.2.34703.48809.
- (400) Wachsmann, E. Solid-State Ionic Devices. *Electrochem. Soc. Interface* **2007**, *16*, 27–28.
- (401) Hassan, A.-R.; El-Azab, A.; Yablinsky, C.; Allen, T. R. Defect Disorder in UO<sub>2</sub>. *J. Solid State Chem.* **2013**, *204*, 136–145.
- (402) Cooper, M. W. D.; Murphy, S.; Andersson, D. A. The Defect Chemistry of UO<sub>2±x</sub> From Atomistic Simulations. *J. Nucl. Mater.* **2018**, *504*, 251–260.
- (403) Soulié, A.; Bruneval, F.; Marinica, M.-C.; Murphy, S.; Crocombette, J.-P. Influence of Vibrational Entropy on the Concentrations of Oxygen Interstitial Clusters and Uranium Vacancies in Non-Stoichiometric UO<sub>2</sub>. *Phys. Rev. Mater.* **2018**, *2*, 083607.
- (404) Matzke, H. Radiation Damage in Crystalline Insulators, Oxides, and Ceramic Nuclear Fuels. *Radiat. Eff.* **1982**, *64*, 3–33.
- (405) Wiss, T.; Hiernaut, J.-P.; Roudil, D.; Colle, J.-Y.; Maugeri, E.; Talip, Z.; Janssen, A.; Rondinella, V.; Konings, R.; Matzke, H.-J.; et al. Evolution of Spent Nuclear Fuel in Dry Storage Conditions for Millennia and Beyond. *J. Nucl. Mater.* **2014**, *451*, 198–206.
- (406) Cahill, D. G. Thermal-Conductivity Measurement by Time-Domain Thermoreflectance. *MRS Bull.* **2018**, *43*, 782–788.
- (407) Khafizov, M.; Park, I.-W.; Chernatynskiy, A.; He, L.; Lin, J.; Moore, J. J.; Swank, D.; Lillo, T.; Phillipot, S. R.; El-Azab, A.; et al. Thermal Conductivity in Nanocrystalline Ceria Thin Films. *J. Am. Ceram. Soc.* **2014**, *97*, 562–569.
- (408) Was, G. S.; Busby, J. T.; Allen, T.; Kenik, E. A.; Jansson, A.; Bruemmer, S. M.; Gan, J.; Edwards, A. D.; Scott, P. M.; Andreson, P. L. Emulation of Neutron Irradiation Effects with Protons: Validation of Principle. *J. Nucl. Mater.* **2002**, *300*, 198–216.
- (409) Popel, A. J.; Spurgeon, S. R.; Matthews, B.; Olszta, M. J.; Tan, B. T.; Gouder, T.; Eloirdi, R.; Buck, E. C.; Farnan, I. An Atomic-Scale Understanding of UO<sub>2</sub> Surface Evolution During Anoxic Dissolution. *ACS Appl. Mater. Interfaces* **2020**, *12*, 39781–39786.
- (410) Clark, R. A.; Conroy, M. A.; Lach, T. G.; Buck, E. C.; Pellegrini, K. L.; McNamara, B. K.; Schwantes, J. M. Distribution of Metallic Fission-Product Particles in the Cladding Liner of Spent Nuclear Fuel. *npj Mater. Degrad.* **2020**, *4*, 4.

- (411) Feng, B.; Sugiyama, I.; Hojo, H.; Ohta, H.; Shibata, N.; Ikuhara, Y. Atomic Structures and Oxygen Dynamics of CeO<sub>2</sub> Grain Boundaries. *Sci. Rep.* **2016**, *6*, 20288.
- (412) Fortner, J. A.; Buck, E. C. The Chemistry of the Light Rare-Earth Elements as Determined by Electron Energy Loss Spectroscopy. *Appl. Phys. Lett.* **1996**, *68*, 3817–3819.
- (413) Garvie, L. A. J.; Buseck, P. R. Determination of Ce<sup>4+</sup>/Ce<sup>3+</sup> in Electron-Beam-Damaged CeO<sub>2</sub> by Electron Energy-Loss Spectroscopy. *J. Phys. Chem. Solids* **1999**, *60*, 1943–1947.
- (414) Pakarinen, J.; He, L. F.; Hassan, A. R.; Wang, Y. Q.; Gupta, M.; El-Azab, A.; Allen, T. R. Annealing-Induced Lattice Recovery in Room-Temperature Xenon Irradiated CeO<sub>2</sub>: X-ray Diffraction and Electron Energy Loss Spectroscopy Experiments. *J. Mater. Res.* **2015**, *30*, 1555–1562.
- (415) Colella, M.; Lumpkin, G. R.; Zhang, Z.; Buck, E. C.; Smith, K. L. Determination of the Uranium Valence State in the Brannerite Structure Using EELS, XPS, and EDX. *Phys. Chem. Miner.* **2005**, *32*, 52–64.
- (416) Fortner, J. A.; Buck, E. C.; Ellison, A. J. G.; Bates, J. K. EELS Analysis of Redox in Glasses for Plutonium Immobilization. *Ultramicroscopy* **1997**, *67*, 77–81.
- (417) Spurgeon, S. R.; Sassi, M.; Ophus, C.; Stubbs, J. E.; Ilton, E. S.; Buck, E. C. Nanoscale Oxygen Defect Gradients in UO<sub>2+x</sub> Surfaces. *Proc. Natl. Acad. Sci. U. S. A.* **2019**, *116*, 17181–17186.
- (418) Kellogg, G. L.; Tsong, T. T. Pulsed-Laser Atom-Probe Field-Ion Microscopy. *J. Appl. Phys.* **1980**, *51*, 1184–1193.
- (419) Vella, A. On the Interaction of an Ultra-Fast Laser with a Nanometric Tip by Laser Assisted Atom Probe Tomography: A Review. *Ultramicroscopy* **2013**, *132*, 5–18.
- (420) Valderrama, B.; Henderson, H. B.; Gan, J.; Manuel, M. V. Influence of Instrument Conditions on the Evaporation Behavior of Uranium Dioxide with UV Laser-Assisted Atom Probe Tomography. *J. Nucl. Mater.* **2015**, *459*, 37–43.
- (421) Devaraj, A.; Colby, R.; Hess, W. P.; Perea, D. E.; Thevuthasan, S. Role of Photoexcitation and Field Ionization in the Measurement of Accurate Oxide Stoichiometry by Laser-Assisted Atom Probe Tomography. *J. Phys. Chem. Lett.* **2013**, *4*, 993–998.
- (422) Kirchhofer, R.; Teague, M. C.; Gorman, B. P. Thermal Effects on Mass and Spatial Resolution During Laser Pulse Atom Probe Tomography of Cerium Oxide. *J. Nucl. Mater.* **2013**, *436*, 23–28.
- (423) Vella, A.; Mazumder, B.; Da Costa, G.; Deconihout, B. Field Evaporation Mechanism of Bulk Oxides Under Ultra Fast Laser Illumination. *J. Appl. Phys.* **2011**, *110*, 044321.
- (424) Verberne, R.; Saxey, D. W.; Reddy, S. M.; Rickard, W. D. A.; Fougereuse, D.; Clark, C. Analysis of Natural Rutile (TiO<sub>2</sub>) by Laser-Assisted Atom Probe Tomography. *Microsc. Microanal.* **2019**, *25*, 539–546.
- (425) Marquis, E. A.; Yahya, N. A.; Larson, D. J.; Miller, M. K.; Todd, R. I. Probing the Improbable: Imaging C Atoms in Alumina. *Mater. Today* **2010**, *13*, 34–36.
- (426) Valderrama, B.; Henderson, H. B.; Yablinsky, C. A.; Gan, J.; Allen, T. R.; Manuel, M. V. Investigation of Material Property Influenced Stoichiometric Deviations as Evidenced During UV Laser-Assisted Atom Probe Tomography in Fluorite Oxides. *Nucl. Instrum. Methods Phys. Res., Sect. B* **2015**, *359*, 107–114.
- (427) Silaeva, E. P.; Karahka, M.; Kreuzer, H. J. Atom Probe Tomography and Field Evaporation of Insulators and Semiconductors: Theoretical Issues. *Curr. Opin. Solid State Mater. Sci.* **2013**, *17*, 211–216.
- (428) Herbig, M. Spatially Correlated Electron Microscopy and Atom Probe Tomography: Current Possibilities and Future Perspectives. *Ser. Mater.* **2018**, *148*, 98–105.
- (429) Makineni, S. K.; Lenz, M.; Kontis, P.; Li, Z.; Kumar, A.; Felfer, P. J.; Neumeier, S.; Herbig, M.; Spiecker, E.; Raabe, D.; et al. Correlative Microscopy-Novel Methods and Their Applications to Explore 3D Chemistry and Structure of Nanoscale Lattice Defects: A Case Study in Superalloys. *JOM* **2018**, *70*, 1736–1743.
- (430) He, L.; Bachhav, M.; Keiser, D. D.; Madden, J. W.; Perez, E.; Miller, B. D.; Gan, J.; Van Renterghem, W.; Leenaers, A.; Van den Berghe, S. STEM-EDS/EELS and APT Characterization of ZrN Coatings on UMO Fuel Kernels. *J. Nucl. Mater.* **2018**, *511*, 174–182.
- (431) Lach, T. G.; Olszta, M. J.; Taylor, S. D.; Yano, K. H.; Edwards, D. J.; Byun, T. S.; Chou, P. H.; Schreiber, D. K. Correlative STEM-APT Characterization of Radiation-Induced Segregation and Precipitation of In-Service BWR 304 Stainless Steel. *J. Nucl. Mater.* **2021**, *549*, 152894.
- (432) Wang, X.; Hatzoglou, C.; Sneed, B.; Fan, Z.; Guo, W.; Jin, K.; Chen, D.; Bei, H. B.; Wang, Y. Q.; Weber, W. J.; et al. Interpreting Nanovoids in Atom Probe Tomography Data for Accurate Local Compositional Measurements. *Nat. Commun.* **2020**, *11*, 1022.
- (433) Oberdorfer, C.; Eich, S. M.; Lutkemeyer, M.; Schmitz, G. Applications of a Versatile Modelling Approach to 3D Atom Probe Simulations. *Ultramicroscopy* **2015**, *159*, 184–194.
- (434) Hofer, F.; Golob, P. Quantification of Electron Energy-Loss Spectra with K-Shell and L-Shell Ionization Cross-Sections. *Micron Microsc. Acta* **1988**, *19*, 73–86.
- (435) Amirifar, N.; Larde, R.; Talbot, E.; Pareige, P.; Rigutti, L.; Mancini, L.; Houard, J.; Castro, C.; Sallet, V.; Zehani, E.; et al. Quantitative Analysis of Doped/Undoped ZnO Nanomaterials Using Laser Assisted Atom Probe Tomography: Influence of the Analysis Parameters. *J. Appl. Phys.* **2015**, *118*, 215703.
- (436) Karahka, M.; Xia, Y.; Kreuzer, H. J. The Mystery of Missing Species in Atom Probe Tomography of Composite Materials. *Appl. Phys. Lett.* **2015**, *107*, 062105.
- (437) Graves, P. R. Raman Microprobe Spectroscopy of Uranium Dioxide Single Crystals and Ion Implanted Polycrystals. *Appl. Spectrosc.* **1990**, *44*, 1665–1667.
- (438) Guimbretière, G.; Desgranges, L.; Canizarès, A.; Carlot, G.; Caraballo, R.; Jégou, C.; Duval, F.; Raimboux, N.; Ammar, M. R.; Simon, P. Determination of In-Depth Damaged Profile by Raman Line Scan in a Pre-Cut He<sup>2+</sup> Irradiated UO<sub>2</sub>. *Appl. Phys. Lett.* **2012**, *100*, 251914.
- (439) Desgranges, L.; Guimbretière, G.; Simon, P.; Jégou, C.; Caraballo, R. A Possible New Mechanism for Defect Formation in Irradiated UO<sub>2</sub>. *Nucl. Instrum. Meth. Phys. Res. B* **2013**, *315*, 169–172.
- (440) Nakae, N.; Iwata, Y.; Kirihaara, T. Thermal Recovery of Defects in Neutron-Irradiated UO<sub>2</sub>. *J. Nucl. Mater.* **1979**, *80*, 314–322.
- (441) Roudil, D.; Barthe, M. F.; Jégou, C.; Gavazzi, A.; Vella, F. Investigation of Defects in Actinide-Doped UO<sub>2</sub> by Positron Annihilation Spectroscopy. *J. Nucl. Mater.* **2012**, *420*, 63–68.
- (442) Yamamoto, Y.; Kishino, T.; Ishiyama, T.; Iwase, A.; Hori, F. Study on Lattice Defects in CeO<sub>2</sub> by Means of Positron Annihilation Measurements. *J. Phys. Conf. Ser.* **2016**, *674*, 012015.
- (443) Wiktor, J.; Barthe, M. F.; Jomard, G.; Torrent, M.; Freyss, M.; Bertolus, M. Coupled Experimental and DFT+U Investigation of Positron Lifetimes in UO<sub>2</sub>. *Phys. Rev. B: Condens. Matter Mater. Phys.* **2014**, *90*, 184101.
- (444) Djourelou, N.; Marchand, B.; Marinov, H.; Moncoffre, N.; Piron, Y.; Nédélec, P.; Toulhoat, N.; Sillou, D. Variable Energy Positron Beam Study of Xe-Implanted Uranium Oxide. *J. Nucl. Mater.* **2013**, *432*, 287–293.
- (445) Evans, H.; Evans, J.; Rice-Evans, P.; Smith, D.; Smith, C. A Slow Positron Study Into the Recovery Behaviour of As-Polished and Krypton-Implanted Uranium Dioxide. *J. Nucl. Mater.* **1992**, *199*, 79–83.
- (446) Barthe, M.; Labrim, H.; Gentils, A.; Desgardin, P.; Corbel, C.; Esnouf, S.; Piron, J. P. Positron Annihilation Characteristics in UO<sub>2</sub>: For Lattice and Vacancy Defects Induced by Electron Irradiation. *Phys. Status Solidi C* **2007**, *4*, 3627–3632.
- (447) Labrim, H.; Barthe, M.; Desgardin, P.; Sauvage, T.; Blondiaux, G.; Corbel, C.; Piron, J. P. Vacancy Defects Induced in Sintered Polished UO<sub>2</sub> Disks by Helium Implantation. *Appl. Surf. Sci.* **2006**, *252*, 3256–3261.
- (448) Labrim, H.; Barthe, M.; Desgardin, P.; Sauvage, T.; Corbel, C.; Blondiaux, G.; Piron, J. P. Thermal Evolution of the Vacancy Defects Distribution in 1MeV Helium Implanted Sintered UO<sub>2</sub>. *Nucl. Instrum. Methods Phys. Res., Sect. B* **2007**, *261*, 883–887.
- (449) Djourelou, N.; Marchand, B.; Marinov, H.; Moncoffre, N.; Piron, Y.; Berer, N.; Nédélec, P.; Raimbault, L.; Epicier, T. Study of

the Temperature and Radiation Induced Microstructural Changes in Xe-Implanted  $\text{UO}_2$  by TEM, STEM, SIMS and Positron Spectroscopy. *J. Nucl. Mater.* **2013**, *443*, 562–569.

(450) Nogita, K.; Une, K. High Resolution TEM Observation and Density Estimation of Xe Bubbles in High Burnup  $\text{UO}_2$  Fuels. *Nucl. Instrum. Methods Phys. Res., Sect. B* **1998**, *141*, 481–486.

(451) Sabathier, C.; Vincent, L.; Garcia, P.; Garrido, F.; Carlot, G.; Thome, L.; Martin, P.; Valot, C. In Situ TEM of Temperature-Induced Fission Product Precipitation in  $\text{UO}_2$ . *Nucl. Instrum. Methods Phys. Res., Sect. B* **2008**, *266*, 3027–3032.

(452) Michel, A.; Sabathier, C.; Carlot, G.; Kaitasov, O.; Bouffard, S.; Garcia, P.; Valot, C. An In Situ TEM Study of the Evolution of Xe Bubble Populations in  $\text{UO}_2$ . *Nucl. Instrum. Methods Phys. Res., Sect. B* **2012**, *272*, 218–221.

(453) Michel, A.; Sabathier, C.; Carlot, G.; Cabie, M.; Bouffard, S.; Garcia, P. A TEM Study of Bubbles Growth with Temperature in Xenon and Krypton Implanted Uranium Dioxide. *Defect Diffus. Forum* **2012**, *323–325*, 191–196.

(454) Lamontagne, J.; Desgranges, L.; Valot, C.; Noirot, J.; Blay, T.; Roure, L.; Pasquet, B. Fission Gas Bubble Characterisation in Irradiated  $\text{UO}_2$  Fuel by SEM, EPMA and SIMS. *Microchim. Acta* **2006**, *155*, 183–187.

(455) Martin, P. M.; Vathonne, E.; Carlot, G.; Delorme, R.; Sabathier, C.; Freyss, M.; Garcia, P.; Bertolus, M.; Glatzel, P.; Proux, O. Behavior of Fission Gases in Nuclear Fuel: XAS Characterization of Kr in  $\text{UO}_2$ . *J. Nucl. Mater.* **2015**, *466*, 379–392.

(456) Garcia, P.; Martin, P.; Carlot, G.; Castelier, E.; Ripert, M.; Sabathier, C.; Valot, C.; D'Acapito, F.; Hazemann, J.-L.; Proux, O.; et al. A Study of Xenon Aggregates in Uranium Dioxide Using X-ray Absorption Spectroscopy. *J. Nucl. Mater.* **2006**, *352*, 136–143.

(457) Martin, P.; Garcia, P.; Carlot, G.; Sabathier, C.; Valot, C.; Nassif, V.; Proux, O.; Hazemann, J. L. XAS Characterisation of Xenon Bubbles in Uranium Dioxide. *Nucl. Instrum. Methods Phys. Res., Sect. B* **2008**, *266*, 2887–2891.

(458) Sabathier, C.; Martin, G.; Michel, A.; Carlot, G.; Maillard, S.; Bachelet, C.; Fortuna, F.; Kaitasov, O.; Oliviero, E.; Garcia, P. In-Situ TEM Observation of Nano-Void Formation in  $\text{UO}_2$  Under Irradiation. *Nucl. Instrum. Methods Phys. Res., Sect. B* **2014**, *326*, 247–250.

(459) Perrin-Pellegrino, C.; Dumont, M.; Keita, M. F.; Neisius, T.; Mikaelian, G.; Manginck, D.; Carlot, G.; Maugis, P. Characterization by APT and TEM of Xe Nano-Bubbles in  $\text{CeO}_2$ . *Nucl. Instrum. Meth. Phys. Res. B* **2020**, *469*, 24–27.

(460) Asoka-Kumar, P.; Alatalo, M.; Ghosh, V. J.; Kruseman, A. C.; Nielsen, B.; Lynn, K. G. Increased Elemental Specificity of Positron Annihilation Spectr. *Phys. Rev. Lett.* **1996**, *77*, 2097–2100.

(461) Nagai, Y.; Hasegawa, M.; Tang, T.; Hempel, A.; Yubuta, K.; Shimamura, T.; Kawazoe, Y.; Kawai, A.; Kano, F. Positron Confinement in Ultrafine Embedded Particles: Quantum-Dot-Like State in an Fe-Cu Alloy. *Phys. Rev. B: Condens. Matter Mater. Phys.* **2000**, *61*, 6574–6578.

(462) Agarwal, S.; Liedke, M. O.; Jones, A. C. L.; Reed, E.; Kohnert, A. A.; Uberuaga, B. P.; Wang, Y. Q.; Cooper, J.; Kaoumi, D.; Li, N.; et al. A New Mechanism for Void-Cascade Interaction From Nondestructive Depth-Resolved Atomic-Scale Measurements of Ion Irradiation-Induced Defects in Fe. *Sci. Adv.* **2020**, *6*, No. eaba8437.

(463) Jiang, J.; Wu, Y. C.; Liu, X. B.; Wang, R. S.; Nagai, Y.; Inoue, K.; Shimizu, Y.; Toyama, T. Microstructural Evolution of RPV Steels Under Proton and Ion Irradiation Studied by Positron Annihilation Spectroscopy. *J. Nucl. Mater.* **2015**, *458*, 326–334.

(464) Jiang, W.; Conroy, M. A.; Kruska, K.; Overman, N. R.; Droubay, T. C.; Gigax, J.; Shao, L.; Devanathan, R. Nanoparticle Precipitation in Irradiated and Annealed Ceria Doped with Metals for Emulation of Spent Fuel. *J. Phys. Chem. C* **2017**, *121*, 22465–22477.

(465) Kuri, G.; Mieszczynski, C.; Martin, M.; Bertsch, J.; Borca, C. N.; Delafoy, C. Local Atomic Structure of Chromium Bearing Precipitates in Chromia Doped Uranium Dioxide Investigated by Combined Micro-Beam X-ray Diffraction and Absorption Spectroscopy. *J. Nucl. Mater.* **2014**, *449*, 158–167.

(466) Yun, D.; Oaks, A. J.; Chen, W.-y.; Kirk, M. A.; Rest, J.; Insopov, Z. Z.; Yacout, A. M.; Stubbins, J. F. Kr and Xe Irradiations in Lanthanum (La) Doped Ceria: Study at the High Dose Regime. *J. Nucl. Mater.* **2011**, *418*, 80–86.

(467) Bachhav, M.; Gan, J.; Keiser, D.; Giglio, J.; Jadernas, D.; Leenaers, A.; Van den Berghe, S. A Novel Approach to Determine the Local Burnup in Irradiated Fuels using Atom Probe Tomography (APT). *J. Nucl. Mater.* **2020**, *528*, 151853.

(468) Bachhav, M.; He, L.; Kane, J.; Liu, X.; Gan, J.; Vurpilot, F. Atom Probe Tomography for Burnup and Fission Product Analysis for Nuclear Fuels. *Microsc. Microanal.* **2020**, *26*, 3086–3088.

(469) Ryazanov, A. I.; Kinoshita, C. Growth Kinetics of Dislocation Loops in Irradiated Ceramic Materials. *Nucl. Instrum. Methods Phys. Res., Sect. B* **2002**, *191*, 65–73.

(470) Kiritani, M.; Yoshida, N.; Takata, H.; Maehara, Y. Growth of Interstitial Type Dislocation Loops and Vacancy Mobility in Electron-Irradiated Metals. *J. Phys. Soc. Jpn.* **1975**, *38*, 1677–1686.

(471) Kinoshita, C.; Hayashi, K.; Kitajima, S. Kinetics of Point-Defects in Electron-Irradiated  $\text{MgO}$ . *Nucl. Instrum. Methods Phys. Res., Sect. B* **1984**, *1*, 209–218.

(472) Mansur, L. K. Theory and Experimental Background on Dimensional Changes in Irradiated Alloys. *J. Nucl. Mater.* **1994**, *216*, 97–123.

(473) Ghoniem, N. M.; Cho, D. D. The Simultaneous Clustering of Point Defects during Irradiation. *Phys. Status Solidi A* **1979**, *54*, 171–178.

(474) Dunn, A.; Capolungo, L. Simulating Radiation Damage Accumulation in  $\alpha\text{-Fe}$ : A Spatially Resolved Stochastic Cluster Dynamics Approach. *Comput. Mater. Sci.* **2015**, *102*, 314–326.

(475) Dunn, A.; Dingreville, R.; Martínez, E.; Capolungo, L. Synchronous Parallel Spatially Resolved Stochastic Cluster Dynamics. *Comput. Mater. Sci.* **2016**, *120*, 43–52.

(476) Wirth, B. D.; Hu, X.; Kohnert, A.; Xu, D. Modeling Defect Cluster Evolution in Irradiated Structural Materials: Focus on Comparing to High-Resolution Experimental Characterization Studies. *J. Mater. Res.* **2015**, *30*, 1440–1455.

(477) Blondel, S.; Bernholdt, D. E.; Hammond, K. D.; Wirth, B. D. Continuum-Scale Modeling of Helium Bubble Bursting Under Plasma-Exposed Tungsten Surfaces. *Nucl. Fusion* **2018**, *58*, 126034.

(478) Matthews, C.; Perriot, R.; Cooper, M. W. D.; Stanek, C. R.; Andersson, D. A. Cluster Dynamics Simulation of Uranium Self-Diffusion During Irradiation in  $\text{UO}_2$ . *J. Nucl. Mater.* **2019**, *527*, 151787.

(479) Matthews, C.; Perriot, R.; Cooper, M. W. D.; Stanek, C. R.; Andersson, D. A. Cluster Dynamics Simulation of Xenon Diffusion During Irradiation in  $\text{UO}_2$ . *J. Nucl. Mater.* **2020**, *540*, 152326.

(480) Cooper, M. W. D.; Pastore, G.; Che, Y.; Matthews, C.; Forslund, A.; Stanek, C. R.; Shirvan, K.; Tverberg, T.; Gamble, K. A.; Mays, B.; et al. Fission Gas Diffusion and Release for  $\text{Cr}_2\text{O}_3$ -Doped  $\text{UO}_2$ : From the Atomic to the Engineering Scale. *J. Nucl. Mater.* **2021**, *545*, 152590.

(481) Gokhman, A.; Bergner, F. Cluster Dynamics Simulation of Point Defect Clusters in Neutron Irradiated Pure Iron. *Radiat. Eff. Defects Solids* **2010**, *165*, 216–226.

(482) Pokor, C.; Brechet, Y.; Dubuisson, P.; Massoud, J. P.; Barbu, A. Irradiation Damage in 304 and 316 Stainless Steels: Experimental Investigation and Modeling. Part I: Evolution of the Microstructure. *J. Nucl. Mater.* **2004**, *326*, 19–29.

(483) Brimbal, C.; Fournier, L.; Barbu, A. Cluster Dynamics Modeling of the Effect of High Dose Irradiation and Helium on the Microstructure of Austenitic Stainless Steels. *J. Nucl. Mater.* **2016**, *468*, 124–139.

(484) Christien, F.; Barbu, A. Effect of Self-Interstitial Diffusion Anisotropy in Electron-Irradiated Zirconium: A Cluster Dynamics Modelling. *J. Nucl. Mater.* **2005**, *346*, 272–281.

(485) Clouet, E.; Barbu, A.; Laé, L.; Martin, G. Precipitation Kinetics of  $\text{Al}_3\text{Zr}$  and  $\text{Al}_3\text{Sc}$  in Aluminum Alloys Modeled with Cluster Dynamics. *Acta Mater.* **2005**, *53*, 2313–2325.

- (486) Bai, X. M.; Ke, H.; Zhang, Y.; Spencer, B. W. Modeling Copper Precipitation Hardening and Embrittlement in a Dilute Fe-0.3 at.% Cu Alloy Under Neutron Irradiation. *J. Nucl. Mater.* **2017**, *495*, 442–454.
- (487) Skorek, R.; Maillard, S.; Michel, A.; Carlot, G.; Gilbert, E.; Jourdan, T. Modelling Fission Gas Bubble Distribution in UO<sub>2</sub>. *Defect Diffus. Forum* **2012**, *323–325*, 209–214.
- (488) Khalil, S.; Allen, T. R.; El-Azab, A. Off-stoichiometric Defect Clustering in Irradiated Oxides. *Chem. Phys.* **2017**, *487*, 1–10.
- (489) Kohnert, A. A.; Wirth, B. D.; Capolungo, L. Modeling Microstructural Evolution in Irradiated Materials with Cluster Dynamics Methods: A review. *Comput. Mater. Sci.* **2018**, *149*, 442–45.
- (490) Vincent-Aublant, E.; Delaye, J.-M.; Van Brutzel, L. Self-Diffusion Near Symmetrical Tilt Grain Boundaries in UO<sub>2</sub> Matrix: A Molecular Dynamics Simulation Study. *J. Nucl. Mater.* **2009**, *392*, 114–120.
- (491) Symington, A. R.; Molinari, M.; Brincat, N. A.; Williams, N. R.; Parker, S. C. Defect Segregation Facilitates Oxygen Transport at Fluorite UO<sub>2</sub> Grain Boundaries. *Philos. Trans. R. Soc., A* **2019**, *377*, 20190026.
- (492) Perriot, R.; Dholabhai, P. P.; Uberuaga, B. P. Disorder-Induced Transition from Grain Boundary to Bulk Dominated Ionic Diffusion in Pyrochlores. *Nanoscale* **2017**, *9*, 6826–6836.
- (493) Williams, N. R.; Molinari, M.; Parker, S. C.; Storr, M. T. Atomistic Investigation of the Structure and Transport Properties of Tilt Grain Boundaries of UO<sub>2</sub>. *J. Nucl. Mater.* **2015**, *458*, 45–55.
- (494) Murphy, S. T.; Jay, E. E.; Grimes, R. W. Pipe Diffusion at Dislocations in UO<sub>2</sub>. *J. Nucl. Mater.* **2014**, *447*, 143–149.
- (495) Galvin, C. O.; Cooper, M. W. D.; Fossati, P. C. M.; Stanek, C. R.; Grimes, R. W.; Andersson, D. A. Pipe and Grain Boundary Diffusion of He in UO<sub>2</sub>. *J. Phys.: Condens. Matter* **2016**, *28*, 405002.
- (496) Andersson, D. A.; Tonks, M. R.; Casillas, L.; Vyas, S.; Nerikar, P.; Uberuaga, B. P.; Stanek, C. R. Multiscale Simulation of Xenon Diffusion and Grain Boundary Segregation in UO<sub>2</sub>. *J. Nucl. Mater.* **2015**, *462*, 15–25.
- (497) Nerikar, P. V.; Parfitt, D. C.; Casillas Trujillo, L. A.; Andersson, D. A.; Unal, C.; Sinnott, S. B.; Grimes, R. W.; Uberuaga, B. P.; Stanek, C. R. Segregation of Xenon to Dislocations and Grain Boundaries in Uranium Dioxide. *Phys. Rev. B: Condens. Matter Mater. Phys.* **2011**, *84*, 174105.
- (498) Vincent-Aublant, E.; Delaye, J. M.; Van Brutzel, L. Self-diffusion Near Symmetrical Tilt Grain Boundaries in UO<sub>2</sub> Matrix: A Molecular Dynamics Simulation Study. *J. Nucl. Mater.* **2009**, *392*, 114–120.
- (499) Valderrama, B.; He, L.; Henderson, H. B.; Pakarinen, J.; Jaques, B.; Gan, J.; Butt, D. P.; Allen, T. R.; Manuel, M. V. Effect of Grain Boundaries on Krypton Segregation Behavior in Irradiated Uranium Dioxide. *JOM* **2014**, *66*, 2562–2568.
- (500) Zacharie, I.; Lansart, S.; Combette, P.; Trotabas, M.; Coster, M.; Groos, M. Microstructural Analysis and Modelling of Intergranular Swelling of Irradiated UO<sub>2</sub> Fuel Treated at High Temperature. *J. Nucl. Mater.* **1998**, *255*, 92–104.
- (501) Millett, P. C.; Tonks, M. R. Meso-Scale Modeling of the Influence of Intergranular Gas Bubbles on Effective Thermal Conductivity. *J. Nucl. Mater.* **2011**, *412*, 281–286.
- (502) Millett, P. C.; Zhang, Y.; Andersson, D. A.; Tonks, M. R.; Biner, S. B. Random-Walk Monte Carlo Simulation of Intergranular Gas Bubble Nucleation in UO<sub>2</sub> Fuel. *J. Nucl. Mater.* **2012**, *430*, 44–49.
- (503) Millett, P. C.; Tonks, M. R.; Biner, S. B.; Zhang, L.; Chockalingam, K.; Zhang, Y. Phase-Field Simulation of Intergranular Bubble Growth and Percolation in Bicrystals. *J. Nucl. Mater.* **2012**, *425*, 130–135.
- (504) Dholabhai, P. P.; Aguiar, J. A.; Wu, L.; Holesinger, T. G.; Aoki, T.; Castro, R. H. R.; Uberuaga, B. P. Structure and Segregation of Dopant-Defect Complexes at Grain Boundaries in Nanocrystalline Doped Ceria. *Phys. Chem. Chem. Phys.* **2015**, *17*, 15375–15385.
- (505) Li, F.; Ohkubo, T.; Chen, Y. M.; Kodzuka, M.; Hono, K. Quantitative Atom Probe Analyses of Rare-Earth-Doped Ceria by Femtosecond Pulsed Laser. *Ultramicroscopy* **2011**, *111*, 589–594.
- (506) Li, F.; Ohkubo, T.; Chen, Y. M.; Kodzuka, M.; Ye, F.; Ou, D. R.; Mori, T.; Hono, K. Laser-Assisted Three-Dimensional Atom Probe Analysis of Dopant Distribution in Gd-doped CeO<sub>2</sub>. *Scripta Mater.* **2010**, *63*, 332–335.
- (507) Sun, L.; Marrocchelli, D.; Yildiz, B. Edge Dislocation Slows Down Oxide Ion Diffusion in Doped CeO<sub>2</sub> by Segregation of Charged Defects. *Nat. Commun.* **2015**, *6*, 6294.
- (508) Barney, W. K.; Wemple, B. D. *Metallography of Irradiated UO<sub>2</sub> Containing Fuel Elements*; Report KAPL-1836; Knolls Atomic Power Laboratory: Schenectady, NY, 1958.
- (509) Belle, J. *Uranium Dioxide: Properties and Nuclear Applications*; Naval Reactors Handbooks; U.S. Atomic Energy Commission: Washington, D.C., 1961.
- (510) Matzke, H.; Turos, A.; Linker, G. Polygonization of Single Crystals of the Fluorite-Type Oxide UO<sub>2</sub> Due to High Dose Ion Implantation. *Nucl. Instrum. Methods Phys. Res., Sect. B* **1994**, *91*, 294–300.
- (511) Spino, J.; Papaioannou, D. Lattice Parameter Changes Associated with the Rim-Structure Formation in High Burn-Up UO<sub>2</sub> Fuels by Micro X-ray Diffraction. *J. Nucl. Mater.* **2000**, *281*, 146–162.
- (512) Bai, X.-M.; Tonks, M. R.; Zhang, Y.; Hales, J. D. Multiscale Modeling of Thermal Conductivity of High Burnup Structures in UO<sub>2</sub> Fuels. *J. Nucl. Mater.* **2016**, *470*, 208–215.
- (513) Wiss, T.; Rondinella, V. V.; Konings, R. J. M.; Staicu, D.; Papaioannou, D.; Bremier, S.; Poml, P.; Benes, O.; Colle, J.-Y.; Van Uffelen, P.; et al. Properties of the High Burnup Structure in Nuclear Light Water Reactor Fuel. *Radiochim. Acta* **2017**, *105*, 893–906.
- (514) Matzke, H.; Wang, L. M. High Resolution Transmission Electron Microscopy of Ion Irradiated Uranium Oxide. *J. Nucl. Mater.* **1996**, *231*, 155–158.
- (515) Hayashi, K.; Kikuchi, H.; Fukuda, K. Radiation Damage of UO<sub>2</sub> by High Energy Heavy Ions. *J. Nucl. Mater.* **1997**, *248*, 191–195.
- (516) Sonoda, T.; Kinoshita, M.; Ishikawa, N.; Sataka, M.; Iwase, A.; Yasunaga, K. Clarification of High Density Electronic Excitation Effects on the Microstructural Evolution of UO<sub>2</sub>. *Nucl. Instrum. Methods Phys. Res., Sect. B* **2010**, *268*, 3277–3281.
- (517) Baranov, V. G.; Lunev, A. V.; Reutov, V. F.; Tenishev, A. V.; Isaenkova, M. G.; Khulunov, A. V. An Attempt to Reproduce High Burn-Up Structure by Ion Irradiation of SIMFUEL. *J. Nucl. Mater.* **2014**, *452*, 147–157.
- (518) Miao, Y.; Yao, T.; Lian, J.; Zhu, S.; Bhattacharya, S.; Oaks, A.; Yacout, A. M.; Mo, K. Nano-Crystallization Induced by High-Energy Heavy Ion Irradiation in UO<sub>2</sub>. *Scr. Mater.* **2018**, *155*, 169–174.
- (519) Gerczak, T. J.; Parish, C. M.; Edmondson, P. D.; Baldwin, C. A.; Terrani, K. A. Restructuring in High Burnup UO<sub>2</sub> Studied Using Modern Electron Microscopy. *J. Nucl. Mater.* **2018**, *509*, 245–259.
- (520) Ferry, S. E.; Dennett, C. A.; Woller, K. B.; Short, M. P. Inferring Radiation-Induced Microstructural Evolution in Single-Crystal Niobium Through Changes in Thermal Transport. *J. Nucl. Mater.* **2019**, *523*, 378–382.
- (521) Cinbiz, M. N.; Wiesenack, W.; Yagnik, S.; Terrani, K. A. In-Pile Thermal Conductivity of Uranium Dioxide at Low Burnup. *J. Nucl. Mater.* **2020**, *538*, 152210.
- (522) Dennett, C. A.; Buller, D. L.; Hattar, K.; Short, M. P. Real-Time Thermomechanical Property monitoring During Ion Beam Irradiation Using In Situ Transient Grating Spectroscopy. *Nucl. Instrum. Methods Phys. Res., Sect. B* **2019**, *440*, 126–138.
- (523) Wang, Y. Z.; Sha, G. F.; Harlow, C.; Yazbeck, M.; Khafizov, M. Impact of Nuclear Reactor Radiation on the Performance of AlN/Sapphire Surface Acoustic Wave Devices. *Nucl. Instrum. Methods Phys. Res., Sect. B* **2020**, *481*, 35–41.
- (524) Schley, R. S.; Hua, Z.; Hurley, D. H. *Status Report: Design and Fabricate Installation-Ready Test Capsule for the In-Situ Measurement of Elastic Properties Using an Optical Fiber-Based Measurement Technique*; Report INL/EXT-19-53123; Idaho National Laboratory: Idaho Falls, ID, 2019.
- (525) Guimbretiere, G.; Desgranges, L.; Canizares, A.; Caraballo, R.; Duval, F.; Raimboux, N.; Omnee, R.; Ammar, M. R.; Jegou, C.; Simon, P. In Situ Raman Monitoring of He<sup>2+</sup> Irradiation Induced Damage in a UO<sub>2</sub> Ceramic. *Appl. Phys. Lett.* **2013**, *103*, 041904.

- (526) Petrie, C. M.; Blue, T. E. In Situ Reactor Radiation-Induced Attenuation in Sapphire Optical Fibers Heated up to 1000 degrees C. *Nucl. Instrum. Methods Phys. Res., Sect. B* **2015**, *342*, 91–97.
- (527) Pena-Rodriguez, O.; Crespillo, M. L.; Diaz-Nunez, P.; Perlado, J. M.; Rivera, A.; Olivares, J. In Situ Monitoring the Optical Properties of Dielectric Materials During Ion Irradiation. *Opt. Mater. Express* **2016**, *6*, 734–742.
- (528) Dennett, C. A.; Dacus, B. R.; Barr, C. M.; Clark, T.; Bei, H.; Zhang, Y.; Short, M. P.; Hattar, K. The Dynamic Evolution of Swelling in Nickel Concentrated Solid Solution Alloys Through In Situ Property Monitoring. *Appl. Mater. Today* **2021**, *25*, 101187.
- (529) Khafizov, M.; Chauhan, V.; Wang, Y.; Riyad, F.; Hang, N.; Hurley, D. H. Investigation of Thermal Transport in Composites and Ion Beam Irradiated Materials for Nuclear Energy Applications. *J. Mater. Res.* **2017**, *32*, 204–216.
- (530) Lucuta, P. G.; Matzke, H.; Hastings, I. J. A Pragmatic Approach to Modelling Thermal Conductivity of Irradiated UO<sub>2</sub> Fuel: Review and Recommendations. *J. Nucl. Mater.* **1996**, *232*, 166–180.
- (531) Geelhood, K.; Luscher, W. G.; Beyer, C. E. FRAPCON-3.4: A Computer Code for the Calculation of Steady State Thermal-Mechanical Behavior of Oxide Fuel Rods for High Burnup; NUREG-CR-7022, Vol. 1; U.S. Nuclear Regulatory Commission: Richland, WA, 2011.
- (532) Lassmann, K. TRANSURANUS - A Fuel-Rod Analysis Code Ready For Use. *J. Nucl. Mater.* **1992**, *188*, 295–302.
- (533) Van Uffelen, P.; Hales, J.; Li, W.; Rossiter, G.; Williamson, R. A Review of Fuel Performance Modeling. *J. Nucl. Mater.* **2019**, *516*, 373–412.
- (534) Williamson, R.; Hales, J.; Novascone, S.; Tonks, M.; Gaston, D.; Permann, C.; Andrs, D.; Martineau, R. Multidimensional Multiphysics Simulation of Nuclear Fuel Behavior. *J. Nucl. Mater.* **2012**, *423*, 149–163.
- (535) Williamson, R. L.; Hales, J. D.; Novascone, S. R.; Pastore, G.; Gamble, K. A.; Spencer, B. W.; Jiang, W.; Pitts, S. A.; Casagrande, A.; Schwen, D.; et al. BISON: A Flexible Code for Advanced Simulation of the Performance of Multiple Nuclear Fuel Forms. *Nucl. Technol.* **2021**, *207*, 954–980.
- (536) Klemens, P. G. Thermal Conductivity and Lattice Vibrational Modes. *Solid State Phys.* **1958**, *7*, 1–98.
- (537) Berman, R. *Thermal Conduction in Solids*; Clarendon Press: Oxford, U.K., 1976; p 11.
- (538) Staicu, D. Thermal Properties of Irradiated UO<sub>2</sub> and MOX. In *Comprehensive Nuclear Materials*; Elsevier: Amsterdam, 2012; p 439.
- (539) Wiesenack, W.; Tverberg, T. The OECD Halden Reactor Project Fuels Testing Programme: Methods, Selected Results and Plans. *Nucl. Eng. Des.* **2001**, *207*, 189–197.
- (540) Fujii, H.; Teshima, H.; Kanasugi, K.; Sendo, T. MOX Fuel Performance Experiment Specified for Japanese PWR Utilisation in the HBWR. *J. Nucl. Sci. Technol.* **2006**, *43*, 998–1005.
- (541) Nakamura, J.; Amaya, M.; Nagase, F.; Fuketa, T. Thermal Conductivity Change in High Burnup MOX Fuel Pellet. *J. Nucl. Sci. Technol.* **2009**, *46*, 944–952.
- (542) Nakae, N.; Akiyama, H.; Miura, H.; Baba, T.; Kamimura, K.; Kurematsu, K.; Kosaka, Y.; Yoshino, A.; Kitagawa, T. Thermal Property Change of MOX and UO<sub>2</sub> Irradiated up to High Burnup of 74 GWd/t. *J. Nucl. Mater.* **2013**, *440*, S15–S23.
- (543) Minato, K.; Shiratori, T.; Serizawa, H.; Hayashi, K.; Une, K.; Nogita, K.; Hirai, M. Thermal Conductivities of Irradiated UO<sub>2</sub> and (U,Gd)O<sub>2</sub>. *J. Nucl. Mater.* **2001**, *288*, 57–65.
- (544) Fink, J. K. Thermophysical Properties of Uranium Dioxide. *J. Nucl. Mater.* **2000**, *279*, 1–18.
- (545) Bakker, K.; Cordfunke, E. H. P.; Konings, R. J. M.; Schram, R. P. C. Critical Evaluation of the Thermal Properties of ThO<sub>2</sub> and Th<sub>1-y</sub>U<sub>y</sub>O<sub>2</sub> and a Survey of the Literature Data on Th<sub>1-y</sub>Pu<sub>y</sub>O<sub>2</sub>. *J. Nucl. Mater.* **1997**, *250*, 1–12.
- (546) Pastore, G.; Swiler, L. P.; Hales, J. D.; Novascone, S. R.; Perez, D. M.; Spencer, B. W.; Luzzi, L.; Van Uffelen, P.; Williamson, R. L. Uncertainty and Sensitivity Analysis of Fission Gas Behavior in Engineering-Scale Fuel Modeling. *J. Nucl. Mater.* **2015**, *456*, 398–408.
- (547) Tonks, M. R.; Andersson, D.; Phillpot, S. R.; Zhang, Y.; Williamson, R.; Stanek, C. R.; Uberuaga, B. L.; Hayes, S. L. Mechanistic Materials Modeling for Nuclear Fuel Performance. *Ann. Nucl. Energy* **2017**, *105*, 11–24.
- (548) Chockalingam, K.; Millett, P. C.; Tonks, M. R. Effects of Intergranular Gas Bubbles on Thermal Conductivity. *J. Nucl. Mater.* **2012**, *430*, 166–170.
- (549) Biancheria, A. Effect of Porosity on Thermal Conductivity of Ceramic Bodies. *Trans. Am. Nucl. Soc.* **1966**, *9*, 1.
- (550) Tonks, M. R.; Bhawe, C.; Wu, X.; Zhang, Y. 10 - Uncertainty Quantification of Mesoscale Models of Porous Uranium Dioxide. In *Uncertainty Quantification of Multiscale Materials Modeling*; Woodhead Publishing, 2020; pp 329–354.
- (551) White, J. T.; Nelson, A. T. Thermal Conductivity of UO<sub>2+x</sub> and U<sub>4</sub>O<sub>9-y</sub>. *J. Nucl. Mater.* **2013**, *443*, 342–350.
- (552) Watanabe, T.; Sinnott, S. B.; Tulenko, J. S.; Grimes, R. W.; Schelling, P. K.; Phillpot, S. R. Thermal Transport Properties of Uranium Dioxide by Molecular Dynamics Simulations. *J. Nucl. Mater.* **2008**, *375*, 388–396.
- (553) Nichenko, S.; Staicu, D. Thermal Conductivity of Porous UO<sub>2</sub>: Molecular Dynamics Study. *J. Nucl. Mater.* **2014**, *454*, 315–322.
- (554) Chen, W.; Bai, X.-M. Unified Effect of Dispersed Xe on the Thermal Conductivity of UO<sub>2</sub> Predicted by Three Interatomic Potentials. *JOM* **2020**, *72*, 1710–1718.
- (555) Deskins, W. R.; Hamed, A.; Kumagai, T.; Dennett, C. A.; Peng, J.; Khafizov, M.; Hurley, D. H.; El-Azab, A. Thermal Conductivity of ThO<sub>2</sub>: Effect of Point Defect Disorder. *J. Appl. Phys.* **2021**, *129*, 075102.
- (556) Lucuta, P. G.; Matzke, H.; Verrall, R. A.; Tasman, H. A. Thermal-Conductivity of SIMFUEL. *J. Nucl. Mater.* **1992**, *188*, 198–204.
- (557) Ishimoto, S.; Hirai, M.; Ito, I.; Korei, Y. Effects of Soluble Fission-Products on Thermal-Conductivities of Nuclear-Fuel Pellets. *J. Nucl. Sci. Technol.* **1994**, *31*, 796–802.
- (558) Gibby, R. L. Effect of Plutonium Content on Thermal Conductivity of (U, Pu)O<sub>2</sub> Solid Solutions. *J. Nucl. Mater.* **1971**, *38*, 163–177.
- (559) Hirai, M.; Ishimoto, S. Thermal Diffusivities and Thermal-Conductivities of UO<sub>2</sub>-Gd<sub>2</sub>O<sub>3</sub>. *J. Nucl. Sci. Technol.* **1991**, *28*, 995–1000.
- (560) Lucuta, P. G.; Matzke, H.; Verrall, R. A. Thermal Conductivity of Hyperstoichiometric SIMFUEL. *J. Nucl. Mater.* **1995**, *223*, 51–60.
- (561) Cozzo, C.; Staicu, D.; Somers, J.; Fernandez, A.; Konings, R. J. M. Thermal Diffusivity and Conductivity of Thorium-Plutonium Mixed Oxides. *J. Nucl. Mater.* **2011**, *416*, 135–141.
- (562) Duriez, C.; Alessandri, J. P.; Gervais, T.; Philipponneau, Y. Thermal Conductivity of Hypostoichiometric Low Pu Content (U, Pu)O<sub>2-x</sub> Mixed Oxide. *J. Nucl. Mater.* **2000**, *277*, 143–158.
- (563) Suzuki, K.; Kato, M.; Sunaoshi, T.; Uno, H.; Carvajal-Nunez, U.; Nelson, A. T.; McClellan, K. J. Thermal and Mechanical Properties of CeO<sub>2</sub>. *J. Am. Ceram. Soc.* **2019**, *102*, 1994–2008.
- (564) Dennett, C. A.; Choens, R. C.; Taylor, C. A.; Heckman, N. M.; Ingraham, M. D.; Robinson, D.; Boyce, B. L.; Short, M. P.; Hattar, K. Listening to Radiation Damage In Situ: Passive and Active Acoustic Techniques. *JOM* **2020**, *72*, 197–209.
- (565) Hofmann, F.; Short, M. P.; Dennett, C. A. Transient Grating Spectroscopy: An Ultrarapid, Nondestructive Materials Evaluation Technique. *MRS Bull.* **2019**, *44*, 392–402.
- (566) Hofmann, F.; Mason, D. R.; Eliason, J. K.; Maznev, A. A.; Nelson, K. A.; Dudarev, S. L. Non-Contact Measurement of Thermal Diffusivity in Ion-Implanted Nuclear Materials. *Sci. Rep.* **2015**, *5*, 16042.
- (567) Reza, A.; Yu, H.; Mizohata, K.; Hofmann, F. Thermal Diffusivity Degradation and Point Defect Density in Self-Ion Implanted Tungsten. *Acta Mater.* **2020**, *193*, 270–279.
- (568) Capinski, W. S.; Maris, H. J.; Bauser, E.; Silier, I.; Asen-Palmer, M.; Ruf, T.; Cardona, M.; Gmelin, E. Thermal Conductivity of Isotopically Enriched Si. *Appl. Phys. Lett.* **1997**, *71*, 2109–2111.
- (569) Braun, J. L.; Hopkins, P. E. Upper Limit to the Thermal Penetration Depth During Modulated Heating of Multilayer Thin

- Films with Pulsed and Continuous Wave Lasers: a Numerical Study. *J. Appl. Phys.* **2017**, *121*, 17S107.
- (570) Weisensee, P. B.; Feser, J. P.; Cahill, D. G. Effect of Ion Irradiation on the Thermal Conductivity of  $\text{UO}_2$  and  $\text{U}_3\text{O}_8$  Epitaxial Layers. *J. Nucl. Mater.* **2013**, *443*, 212–217.
- (571) Cheaito, R. C.; Gorham, C. S.; Misra, A.; Hattar, K.; Hopkins, P. E. Thermal Conductivity Measurements via Time-Domain Thermoreflectance for the Characterization of Radiation-Induced Damage. *J. Mater. Res.* **2015**, *30*, 1403–1412.
- (572) Chauhan, V.; Riyad, M. F.; Du, X. P.; Wei, C. D.; Tyburska-Puschel, B.; Zhao, J. C.; Khafizov, M. Thermal Conductivity Degradation and Microstructural Damage Characterization in Low-Dose Ion Beam-Irradiated 3C-SiC. *Metall. Mater. Trans. E* **2017**, *4*, 61–69.
- (573) Scott, E. A.; Hattar, K.; Rost, C. M.; Gaskins, J. T.; Fazli, M.; Ganski, C.; Li, C.; Bai, T.; Wang, Y.; Esfarjani, K.; et al. Phonon Scattering Effects from Point and Extended Defects on Thermal Conductivity Studied via Ion Irradiation of Crystals with Self-Imputities. *Phys. Rev. Mater.* **2018**, *2*, 095001.
- (574) Abdullaev, A.; Chauhan, V. S.; Muminov, B.; O'Connell, J.; Skuratov, V. A.; Khafizov, M.; Utegulov, Z. N. Thermal Transport Across Nanoscale Damage Profile in Sapphire Irradiated by Swift Heavy Ions. *J. Appl. Phys.* **2020**, *127*, 035108.
- (575) Scott, E. A.; Hattar, K.; Braun, J. L.; Rost, C. M.; Gaskins, J. T.; Bai, T.; Wang, Y.; Ganski, C.; Goorsky, M.; Hopkins, P. E. Orders of Magnitude Reduction in the Thermal Conductivity of Polycrystalline Diamond Through Carbon, Nitrogen, and Oxygen Ion Implantation. *Carbon* **2020**, *157*, 97–105.
- (576) Hurley, D. H.; Telschow, K. L. Simultaneous Microscopic Imaging of Elastic and Thermal Anisotropy. *Phys. Rev. B: Condens. Matter Mater. Phys.* **2005**, *71*, 241410.
- (577) Hurley, D. H.; Wright, O. B.; Matsuda, O.; Shinde, S. L. Time Resolved Imaging of Carrier and Thermal Transport in Silicon. *J. Appl. Phys.* **2010**, *107*, 023521.
- (578) Khafizov, M.; Hurley, D. H. Measurement of Thermal Transport Using Time-Resolved Thermal Wave Microscopy. *J. Appl. Phys.* **2011**, *110*, 083525.
- (579) Feser, J. P.; Cahill, D. G. Probing Anisotropic Heat Transport Using Time-Domain Thermoreflectance With Offset Laser Spots. *Rev. Sci. Instrum.* **2012**, *83*, 104901.
- (580) Fournier, D.; Marangolo, M.; Fretigny, C. Measurement of Thermal Properties of Bulk Materials and Thin Films by Modulated Thermoreflectance (MTR). *J. Appl. Phys.* **2020**, *128*, 241101.
- (581) Tang, L.; Dames, C. Anisotropic Thermal Conductivity Tensor Measurements Using Beam-Offset Frequency Domain Thermoreflectance (BO-FDTR) for Materials Lacking In-Plane Symmetry. *Int. J. Heat Mass Transfer* **2021**, *164*, 120600.
- (582) Hurley, D. H.; Schley, R. S.; Khafizov, M.; Wendt, B. L. Local Measurements of Thermal Conductivity and Diffusivity. *Rev. Sci. Instrum.* **2015**, *86*, 123901.
- (583) Khafizov, M.; Yablinsky, C.; Allen, T. R.; Hurley, D. H. Measurement of Thermal Conductivity in Proton Irradiation Silicon. *Nucl. Instrum. Methods Phys. Res., Sect. B* **2014**, *325*, 11–14.
- (584) Chauhan, V. S.; Abdullaev, A.; Utegulov, Z. N.; O'Connell, J.; Skuratov, V.; Khafizov, M. Simultaneous Characterization of Cross- and In-Plane Thermal Transport in Insulator Patterned by Directionally Aligned Nano-Channels. *AIP Adv.* **2020**, *10*, 015304.
- (585) Hua, Z.; Fleming, A.; Ban, H. The Study of Using Multi-Layered Model to Extract Thermal Property Profiles of Ion-Irradiated Materials. *Int. J. Heat Mass Transfer* **2019**, *131*, 206–216.
- (586) Riyad, M. F.; Chauhan, V.; Khafizov, M. Implementation of a Multilayer Model for Measurement of Thermal Conductivity in Ion Beam Irradiated Samples Using a Modulated Thermoreflectance Approach. *J. Nucl. Mater.* **2018**, *509*, 134–144.
- (587) Adkins, C. A.; Pavlov, T. R.; Middlemas, S. C.; Schley, R. S.; Marshall, M. C.; Cole, M. R. *Demonstrate Thermal Property Measurement on Irradiated Fuel in IMCL*; Report INL/EXT-19-55902; Idaho National Laboratory: Idaho Falls, ID, 2019.
- (588) Togo, A.; Chaput, L.; Tanaka, I. Distributions of Phonon Lifetimes in Brillouin Zones. *Phys. Rev. B: Condens. Matter Mater. Phys.* **2015**, *91*, 094306.
- (589) Ohashi, K. Scattering of Lattice Waves by Dislocations. *J. Phys. Soc. Jpn.* **1968**, *24*, 437–445.
- (590) Klemens, P. G. Some Scattering Problems in Conduction Theory. *Can. J. Phys.* **1957**, *35*, 441–450.
- (591) Turk, L. A.; Klemens, P. G. Phonon Scattering by Impurity Platelet Precipitates in Diamond. *Phys. Rev. B* **1974**, *9*, 4422–4428.
- (592) Snead, L. L.; Zinkle, S. J.; White, D. P. Thermal Conductivity Degradation of Ceramic Materials Due to Low Temperature, Low Dose Neutron Irradiation. *J. Nucl. Mater.* **2005**, *340*, 187–202.
- (593) Morelli, D. T.; Perry, T. A.; Farmer, J. W. Phonon-Scattering in Lightly Neutron-Irradiated Diamond. *Phys. Rev. B: Condens. Matter Mater. Phys.* **1993**, *47*, 131–139.
- (594) Kim, W.; Majumdar, A. Phonon Scattering Cross Section of Polydispersed Spherical Nanoparticles. *J. Appl. Phys.* **2006**, *99*, 084306.
- (595) Fukushima, S.; Ohmichi, T.; Maeda, A.; Handa, M. Thermal Conductivity of Stoichiometric  $(\text{Pu}, \text{Nd})\text{O}_2$  and  $(\text{Pu}, \text{Y})\text{O}_2$  Solids Solutions. *J. Nucl. Mater.* **1983**, *114*, 260–266.
- (596) Gurunathan, R.; Hanus, R.; Dylla, M.; Katre, A.; Snyder, G. J. Analytical Models of Phonon-Point-Defect Scattering. *Phys. Rev. Appl.* **2020**, *13*, 034011.
- (597) Tamura, S. Isotope Scattering of Dispersive Phonons in Ge. *Phys. Rev. B: Condens. Matter Mater. Phys.* **1983**, *27*, 858–866.
- (598) Callaway, J. Model for Lattice Thermal Conductivity at Low Temperatures. *Phys. Rev.* **1959**, *113*, 1046–1051.
- (599) Cahill, D. G.; Braun, P. V.; Chen, G.; Clarke, D. R.; Fan, S.; Goodson, K. E.; Keblinski, P.; King, W. P.; Mahan, G. D.; Majumdar, A.; et al. Nanoscale Thermal Transport. II. 2003–2012. *Appl. Phys. Rev.* **2014**, *1*, 011305.
- (600) Srivastava, G. P. *The Physics of Phonons*; Taylor and Francis: New York, 1990; p 122.
- (601) Reissland, J. A. *The Physics of Phonons*; Wiley: London, 1973; p 83.
- (602) Torres, E.; CheikNjifon, I.; Kaloni, T. P.; Pencer, J. A. Comparative Analysis of the Phonon Properties in  $\text{UO}_2$  Using the Boltzmann Transport Equation Coupled with DFT Plus U and Empirical Potentials. *Comput. Mater. Sci.* **2020**, *177*, 109594.
- (603) Cooper, M. W. D.; Middleburgh, S. C.; Grimes, R. W. Modelling the Thermal Conductivity of  $(\text{U}_x\text{Th}_{1-x})\text{O}_2$  and  $(\text{U}_x\text{Pu}_{1-x})\text{O}_2$ . *J. Nucl. Mater.* **2015**, *466*, 29–35.
- (604) Muta, H.; Murakami, Y.; Uno, M.; Kurosaki, K.; Yamanaka, S. Thermophysical Properties of  $\text{Th}_{1-x}\text{U}_x\text{O}_2$  Pellets Prepared by Spark Plasma Sintering Technique. *J. Nucl. Sci. Technol.* **2013**, *50*, 181–187.
- (605) Yue, S.-Y.; Zhang, X.; Qin, G.; Phillpot, S. R.; Hu, M. Metric for Strong Intrinsic Four-Order Phonon Anharmonicity. *Phys. Rev. B* **2017**, *95*, 195203.
- (606) Verlet, L. Computer 'Experiments' on Classical Fluids. I. Thermodynamical Properties of Lennard-Jones Molecules. *Phys. Rev.* **1967**, *159*, 98–103.
- (607) Schelling, P. K.; Phillpot, S. R.; Keblinski, P. Comparison of Atomic-Level Simulation Methods for Computing Thermal Conductivity. *Phys. Rev. B: Condens. Matter Mater. Phys.* **2002**, *65*, 144306.
- (608) Müller-Plathe, F. A Simple Nonequilibrium Molecular Dynamics Method for Calculating the Thermal Conductivity. *J. Chem. Phys.* **1997**, *106*, 6082.
- (609) Poetzsch, R. H. H.; Bottger, H. Interplay of Disorder and Anharmonicity in Heat Conduction: Molecular-Dynamics Study. *Phys. Rev. B* **1994**, *50*, 15757–15763.
- (610) Oligschleger, C.; Schon, J. C. Simulation of Thermal Conductivity and Heat Transport in Solids. *Phys. Rev. B: Condens. Matter Mater. Phys.* **1999**, *59*, 4125–4133.
- (611) Sellan, D. P.; Landry, E. S.; Turney, J. E.; Mcgaughey, A. J. H.; Amon, C. H. Size Effects in Molecular Dynamics Thermal Conductivity Predictions. *Phys. Rev. B: Condens. Matter Mater. Phys.* **2010**, *81*, 214305.

- (612) Buckingham, R. A. The Classical Equation of State of Gaseous Helium, Neon and Argon. *Proc. Math. Phys. Eng. Sci.* **1938**, *168*, 264–283.
- (613) Morse, P. M. Diatomic Molecules According to the Wave Mechanics. II. Vibrational Levels. *Phys. Rev.* **1929**, *34*, 57–64.
- (614) Basak, C. B.; Sengupta, A. K.; Kamath, H. S. Classical Molecular Dynamics Simulation of  $\text{UO}_2$  to Predict Thermophysical Properties. *J. Alloys Compd.* **2003**, *360*, 210–216.
- (615) Yakub, E.; Ronchi, C.; Staicu, D. Molecular Dynamics Simulation of Premelting and Melting Phase Transitions in Stoichiometric Uranium Dioxide. *J. Chem. Phys.* **2007**, *127*, 094508.
- (616) Morelon, N.-D.; Ghaleb, D.; Delaye, J.-M.; Van Brutzel, L. A New Empirical Potential for Simulating the Formation of Defects and Their Mobility in Uranium Dioxide. *Philos. Mag.* **2003**, *83*, 1533–1555.
- (617) Jackson, R. A.; Catlow, C. R. A. Trapping and Solution of Fission Xe in  $\text{UO}_2$ . *J. Nucl. Mater.* **1985**, *127*, 161–166.
- (618) Govers, K.; Lemehov, S.; Hou, M.; Verwerft, M. Comparison of Interatomic Potentials for  $\text{UO}_2$ . *J. Nucl. Mater.* **2007**, *366*, 161–177.
- (619) Soulie, A.; Crocombette, J.-P.; Kraych, A.; Garrido, F.; Sattonnay, G.; Clouet, E. Atomistically-Informed Thermal Glide Model for Edge Dislocations in Uranium Dioxide. *Acta Mater.* **2018**, *150*, 248–261.
- (620) Sattonnay, G.; Tetot, R. Bulk, Surface and Point Defect Properties of  $\text{UO}_2$  From a Tight-Binding Variable-Charge Model. *J. Phys.: Condens. Matter* **2013**, *25*, 125403.
- (621) Li, Y.; Liang, T.; Sinnott, S. B.; Phillpot, S. R. A Charge-Optimized Many-Body Potential for the U- $\text{UO}_2$ - $\text{O}_2$  System. *J. Phys.: Condens. Matter* **2013**, *25*, 505401.
- (622) Govers, K.; Lemehov, S.; Hou, M.; Verwerft, M. Comparison of Interatomic Potentials for  $\text{UO}_2$ : Part II: Molecular Dynamics Simulations. *J. Nucl. Mater.* **2008**, *376*, 66–77.
- (623) Dacus, B.; Beeler, B.; Schwen, D. Calculation of Threshold Displacement Energies in  $\text{UO}_2$ . *J. Nucl. Mater.* **2019**, *520*, 152–164.
- (624) Murphy, S. T.; Rushton, M. J. D.; Grimes, R. W. A Comparison of Empirical Potential Models for the Simulation of Dislocations in Uranium Dioxide. *Prog. Nucl. Energy* **2014**, *72*, 27–32.
- (625) Zhang, Y.; Millett, P. C.; Tonks, M. R.; Bai, X.-M.; Biner, S. B. Molecular Dynamics Simulations of Intergranular Fracture in  $\text{UO}_2$  with Nine Empirical Interatomic Potentials. *J. Nucl. Mater.* **2014**, *452*, 296–303.
- (626) Arima, T.; Yamasaki, S.; Inagaki, Y.; Idemitsu, K. Evaluation of Thermal Properties of  $\text{UO}_2$  and  $\text{PuO}_2$  by Equilibrium Molecular Dynamics Simulations from 300 to 2000K. *J. Alloys Compd.* **2005**, *400*, 43–50.
- (627) Maxwell, C. I.; Pencer, J. Molecular Dynamics Modelling of the Thermal Conductivity of Off-Stoichiometric  $\text{UO}_{2\pm x}$  and  $(\text{U}_y\text{Pu}_{1-y})\text{-O}_{2\pm x}$  Using Equilibrium Molecular Dynamics. *Ann. Nucl. Energy* **2019**, *131*, 317–324.
- (628) Cooper, M. W. D.; Murphy, S. T.; Rushton, M. J. D.; Grimes, R. W. Thermophysical Properties and Oxygen Transport in the  $(\text{U}_x\text{Pu}_{1-x})\text{O}_2$  Lattice. *J. Nucl. Mater.* **2015**, *461*, 206–214.
- (629) Lunev, A. V.; Tarasov, B. A. A Classical Molecular Dynamics Study of the Correlation Between the Bredig Transition and Thermal Conductivity of Stoichiometric Uranium Dioxide. *J. Nucl. Mater.* **2011**, *415*, 217–221.
- (630) Park, J.; Farfan, E. B.; Enriquez, C. Thermal Transport in Thorium Dioxide. *Nucl. Eng. Technol.* **2018**, *50*, 731–737.
- (631) Behera, R. K.; Deo, C. S. Atomistic Models to Investigate Thorium Dioxide ( $\text{ThO}_2$ ). *J. Phys.: Condens. Matter* **2012**, *24*, 215405.
- (632) Chernatynskiy, A.; Flint, C.; Sinnott, S. B.; Phillpot, S. R. Critical Assessment of  $\text{UO}_2$  Classical Potentials for Thermal Conductivity Calculations. *J. Mater. Sci.* **2012**, *47*, 7693–7702.
- (633) Hyland, G. J. Thermal Conductivity of Solid  $\text{UO}_2$ : Critique and Recommendation. *J. Nucl. Mater.* **1983**, *113*, 125–132.
- (634) Arima, T.; Yamasaki, S.; Idemitsu, K.; Inagaki, Y. Equilibrium and Nonequilibrium Molecular Dynamics Simulations of Heat Conduction in Uranium Oxide and Mixed Uranium - Plutonium Oxide. *J. Nucl. Mater.* **2008**, *376*, 139–145.
- (635) Qin, M. J.; Middleburgh, S. C.; Cooper, M. W. D.; Rushton, M. J. D.; Puide, M.; Kuo, E. Y.; Grimes, R. W.; Lumpkin, G. R. Thermal Conductivity Variation in Uranium Dioxide with Gadolinia Additions. *J. Nucl. Mater.* **2020**, *540*, 152258.
- (636) Watanabe, T.; Srivilliputhur, S. G.; Schelling, P. K.; Tulenko, J. S.; Sinnott, S. B.; Phillpot, S. R. Thermal Transport in Off-Stoichiometric Uranium Dioxide by Atomic Level Simulation. *J. Am. Ceram. Soc.* **2009**, *92*, 850–856.
- (637) Deng, B.; Chernatynskiy, A.; Shukla, P.; Sinnott, S. B.; Phillpot, S. R. Effects of Edge Dislocations on Thermal Transport in  $\text{UO}_2$ . *J. Nucl. Mater.* **2013**, *434*, 203–209.
- (638) Phillpot, S. R.; El-Azab, A.; Chernatynskiy, A.; Tulenko, J. S. Thermal Conductivity of  $\text{UO}_2$  Fuel: Predicting Fuel Performance from Simulation. *JOM* **2011**, *63*, 73–79.
- (639) Watanabe, T.; Sinnott, S. B.; Tulenko, J. S.; Grimes, R. W.; Schelling, P. K.; Phillpot, S. R. Thermal Transport Properties of Uranium Dioxide by Molecular Dynamics Simulations. *J. Nucl. Mater.* **2008**, *375*, 388–396.
- (640) Chen, T.; Chen, D.; Sencer, B. H.; Shao, L. Molecular Dynamic Simulation of Grain Boundary Thermal Resistance in  $\text{UO}_2$ . *J. Nucl. Mater.* **2014**, *452*, 364–369.
- (641) Deng, B.; Chernatynskiy, A.; Sinnott, S. B.; Phillpot, S. R. Thermal Transport at (001) Twist Grain Boundary in  $\text{UO}_2$ . *J. Nucl. Mater.* **2016**, *479*, 167–173.
- (642) Chen, W.; Cooper, M. W. D.; Xiao, Z.; Andersson, D. A.; Bai, X. Effect of Xe Bubble Size and Pressure on the Thermal Conductivity of  $\text{UO}_2$  - A Molecular Dynamics Study. *J. Mater. Res.* **2019**, *34*, 2295–2305.
- (643) Lee, C.; Chernatynskiy, A.; Shukla, P.; Stoller, R. E.; Sinnott, S. B.; Phillpot, S. R. Effect of Pores and He Bubbles on the Thermal Transport Properties of  $\text{UO}_2$  by Molecular Dynamics Simulation. *J. Nucl. Mater.* **2015**, *456*, 253–259.
- (644) Swartz, E. T.; Pohl, R. O. Thermal Boundary Resistance. *Rev. Mod. Phys.* **1989**, *61*, 605–668.
- (645) Tonks, M. R.; Millett, P. C.; Nerikar, P.; Du, S.; Andersson, D.; Stanek, C. R.; Gaston, D.; Andrs, D.; Williamson, R. Multiscale Development of a Fission Gas Thermal Conductivity Model: Coupling Atomic, Meso, and Continuum Level Simulations. *J. Nucl. Mater.* **2013**, *440*, 193–200.
- (646) Zhu, X.; Gong, H.; Zhao, Y.-F.; Lin, D.-Y.; Han, G.; Liu, T.; Song, H. Effect of Xe Bubbles on the Thermal Conductivity of  $\text{UO}_2$ : Mechanisms and Model Establishment. *J. Nucl. Mater.* **2020**, *533*, 152080.
- (647) Hua, Z.; Spackman, J.; Ban, H. Characterization of Kapitza Resistances of Natural Grain Boundaries in Cerium Oxide. *Materialia* **2019**, *5*, 100230.
- (648) Hurley, D. H.; Khafizov, M.; Shinde, S. L. Measurement of the Kapitza Resistance Across a Bicrystal Interface. *J. Appl. Phys.* **2011**, *109*, 083504.
- (649) Deng, B.; Chernatynskiy, A.; Khafizov, M.; Hurley, D. H.; Phillpot, S. R. Kapitza Resistance of Si/SiO<sub>2</sub> Interface. *J. Appl. Phys.* **2014**, *115*, 084910.
- (650) Shrestha, K.; Yao, T.; Lian, J.; Antonio, D.; Sessim, M.; Tonks, M. R.; Gofryk, K. The Grain-Size Effect on Thermal Conductivity of Uranium Dioxide. *J. Appl. Phys.* **2019**, *126*, 125116.
- (651) Katre, A.; Carrete, J.; Dongre, B.; Madsen, G. K. H.; Mingo, N. Exceptionally Strong Phonon Scattering by B Substitution in Cubic SiC. *Phys. Rev. Lett.* **2017**, *119*, 075902.
- (652) Polanco, C. A.; Lindsay, L. Thermal Conductivity of InN with Point Defects from First Principles. *Phys. Rev. B: Condens. Matter Mater. Phys.* **2018**, *98*, 014306.
- (653) Kundu, A.; Mingo, N.; Broido, D. A.; Stewart, D. A. Role of Light and Heavy Embedded Nanoparticles on the Thermal Conductivity of SiGe alloys. *Phys. Rev. B: Condens. Matter Mater. Phys.* **2011**, *84*, 125426.
- (654) Wang, T.; Carrete, J.; van Roekeghem, A.; Mingo, N.; Madsen, G. K. H. Ab Initio Phonon Scattering by Dislocations. *Phys. Rev. B: Condens. Matter Mater. Phys.* **2017**, *95*, 245304.